Contributions of hydroclimate variability and associated North-African riverine fluxes to eastern-Mediterranean sapropel formation and related seawater circulation

Jiawang Wu

Utrecht Studies in Earth Sciences

No. 146

ISBN 978-90-6266-493-1
USES No. 146

Author contact: Jiawang Wu (j.w.wu@uu.nl or jwwu99@126.com)

Cover illustration: Sapropels S1 to S9 in the marine sediment piston-core CP11PC (34°32.7'N, 16°34.0'E; 1501 m water-depth), collected from the Libyan-Tunisian margin in the Mediterrnean Sea via the cruise of RV *Pelagia* CORTADO 2011. The photos were taken with an Avaatech XRF core scanner at NIOZ in November 2013.
Cover and lay-out design: Margot Stoete, Xin Wang, and Jiawang Wu.

Printed in the Netherlands by Proefschriftmaken.

Contributions of hydroclimate variability and associated North-African riverine fluxes to eastern-Mediterranean sapropel formation and related seawater circulation

Bijdragen van hydro-klimaat variabiliteit en bijbehorende Noord-Afrikaanse rivier-fluxen aan sapropel vorming in de oostelijke Middellandse Zee en daarmee verwante zeewater circulatie
(met een samenvatting in het Nederlands)

水文气候变化以及相关的北非河流输入对
东地中海腐泥层的形成机制及其海洋环流的影响和贡献
（附带中文摘要）

PROEFSCHRIFT

ter verkrijging van de graad van doctor aan de Universiteit Utrecht
op gezag van de rector magnificus, prof. dr. G.J. van der Zwaan,
ingevolge het besluit van het college voor promoties in het openbaar te verdedigen op

maandag 18 december 2017 des middags te 6.00 uur

door

Jiawang Wu

geboren op 14 mei 1987 te Hainan, China

Promotor:

Prof. dr. Gert J. de Lange

This thesis was accomplished with financial support from the China Scholarship Council (CSC).

Members of the dissertation committee:

Prof. dr. Zhifei Liu
Tongji University, China

Dr. Katharina Pahnke
ICBM & University of Oldenburg, Germany

Prof. dr. Jack J. Middelburg
Utrecht University, the Netherlands

Prof. dr. Caroline P. Slomp
Utrecht University, the Netherlands

Prof. dr. Gert-Jan Reichart
Royal NIOZ & Utrecht University, the Netherlands

The study was carried out at Department of Earth Sciences–Geochemistry, Faculty of Geosciences, Utrecht University (Princetonplein 9, 3584 CC Utrecht, the Netherlands).

This book is dedicated to the memory of my father

CONTENTS

CHAPTER 1

Introduction and Synopsis

1 General background

The Mediterranean Sea is a semi-enclosed basin surrounded by catchment areas characterized by different climate regimes, as it lies at the interface between the African sub-tropical and the European temperate zones (Tzedakis, 2007; Magny et al., 2013; Rohling et al., 2015). Moreover, the Mediterranean has a dynamic thermohaline circulation (Pinardi and Masetti, 2000; Pinardi et al., 2015; Rolison et al., 2015), making it particularly sensitive to changes in the hydrological cycle. This sensitivity is best witnessed by the rhythmic occurrence of sapropel – organic-rich sedimentary units, particularly in Mediterranean Sea, at an astronomically determined cyclicity throughout the last 13.5 million years (see reviews by Cramp and O'Sullivan, 1999; Rohling et al., 2015). Sapropels occurred more frequently in the eastern Mediterranean Sea (EMS) rather than the western basin, and only during the precession-forced summer insolation maxima in the northern hemisphere, coupled with increased seasonal contrast and river runoff (Rossignol-Strick, 1983; Hilgen, 1991; Lourens et al., 1996; Tuenter et al., 2003; Ziegler et al., 2010). The enhanced freshwater and nutrients brought in by the runoff stimulated a pronounced density stratification of the water column and/or an increased primary productivity in the surface waters, which ultimately led to stagnant deep-water conditions and sapropel formation (e.g. Rossignol-Strick et al., 1982; De Lange and Ten Haven, 1983; Rohling, 1994; Emeis et al., 2000; 2003; De Lange et al., 2008; Rohling et al., 2015; Tesi et al., 2017).

Regardless of the relative importance of deep-water stagnation versus surface-ocean productivity, sapropel deposition can thus be viewed as directly related to freshwater forcing and its hydrographic response (Rohling, 1994; Emeis et al., 2003; Rohling et al., 2015, and reference therein). Moreover, it has been shown that with increasing strength of the freshwater forcing, the strength of the deep-water stagnation is increased; and the changes in the freshwater sources will modulate this effect (Myers et al., 1998; Myers, 2002). This is in line with the interplay between physical circulation and deep-water oxygen consumption, as suggested by ocean-biogeochemical modeling (Stratford et al., 2000; Bianchi et al., 2006; Grimm et al., 2015).

However, the exact sources of freshwater and associated hydroclimate changes, including precipitation/evaporation balance and changes in regional convection, remain unresolved. Moreover, the complex interactions between paleoclimatic and paleoceanographic processes for sapropel formation are still highly debated.

2 Freshwater sources and hydroclimate changes

Increased rainfall and related riverine inputs around the Northern Borderlands of the Eastern Mediterranean (NBEM) concurred with sapropel deposition, as shown by speleothem data (e.g. Bar-Matthews et al., 2000, 2003; Zanchetta et al., 2007; Zhornyak et al., 2011) and marine sediment records (e.g. Kallel et al., 1997; Emeis et al., 2000; Toucanne et al., 2015; Filippidi et al., 2016). Being seasonally specified, palynological studies suggest that enhanced winter precipitation was responsible for the NBEM wet conditions at times of sapropel deposition (e.g. S1: Kotthoff et al., 2008; Peyron et al., 2011; S5: Milner et al., 2012). Recent work has also revealed north–south contrasts of precipitation seasonality in the Holocene central Mediterranean, which can reconcile the discrepancies from various proxies (see review by Magny et al., 2013). In addition, possible impacts of the Black Sea overflow and meltwater runoff of European ice-sheets during sapropel deposition have been excluded (Sperling et al., 2003).

The monsoon-fuelled Nile discharge is recognized as a key freshwater source for sapropel formation (Rossignol-Strick et al., 1982; Rossignol-Strick, 1983; Emeis et al., 2000; Hennekam et al., 2014; 2015; Weldeab et al., 2014). Apart from the Nile flooding, intensification of African monsoon precipitation had a profound and more widespread influence on the EMS during sapropel times, as it could reactivate the fossil river/wadi systems (presently buried beneath sand dunes) along the wider North-African margin (Rohling et al., 2002). This scenario has been proposed for last interglacial sapropel S5 based on $\delta^{18}O$ data and Nd isotopes of planktonic foraminifera (Rohling et al., 2002; 2004; Osborne et al., 2008, 2010)). Satellite mapping as well as paleohydrological and hydraulic modeling have revealed the existence of paleodrainage networks (Vörösmarty et al., 2000; Paillou et al., 2009, 2012; Coulthard et al., 2013). These routes may have rivaled the Nile runoff in magnitude (Scrivner et al., 2004) and functioned for a majority of Quaternary sapropels (e.g. S1: Fontugne et al., 1994; Freydier et al., 2001; S6: Emeis et al., 2003). This hypothesis is also supported by reconstructed dust variations from a long-term perspective (Larrasoaña et al., 2003; 2013), and may also occur for the humid-climate episodes without sapropel deposition (Hoffmann et al., 2016). Archaeological surveys also suggest human occupation and dispersal over the Libyan-Saharan desert along the interlinked river-lake-wetland systems during such so-called African Humid Period (e.g. Drake et al., 2011; Lézine et al., 2011; Manning and Timpson, 2014).

Therefore, the knowledge of the North-African paleodrainage systems and associated networks is very important as such paleodrainage fluxes and associated networks may have: 1) constituted a considerable freshwater source for sapropel formation, 2) played a key role in the nonlinear feedbacks to insolation forcing, and 3) had a major influence on the human migrations out of Africa. However, limited information is available on the origin, distribution, and intensity of this North-African paleodrainage contribution. In particular, there is no marine evidence whether the fossil river/wadi route was active during the Holocene sapropel S1.

For the first time, robust and consistent evidence is given for important riverine supplies from the Libyan-Tunisian margin into the central Mediterranean during S1 time. The specific source and distribution of such detrital supplies have been further evaluated by the records along a west–east transect throughout the EMS (Chapter 2). Moreover, in comparison with published results from both local and regional core-sites, we not only give new insights in the fluvial discharge from the North-African margin, but also propose a forcing and modulation mechanism controlling the paleodrainage delivery (Chapter 3).

3 Detrital sediment provenance and proxies

To reconstruct the riverine supplies into the EMS and associated hydroclimate changes over the catchment areas, the detrital composition of marine sediment appears to be a very valuable archive. The EMS sediments contain significant terrigenous detrital components, with aeolian and riverine origin, driven by competing climatic processes. A strong east–west gradient in geochemical signatures has been reported for surface sediments in the EMS (Venkatarathnam and Ryan, 1971; Krom et al., 1999a; Weldeab et al., 2002a). This is due to mixing between two endmembers: “young and mafic” Nile sediment is diluted towards the west by “old and felsic” Saharan dust, while riverine contributions derived from basalts and ultramafic rocks over the NBEM have also been proposed. Such a recent provenance pattern can generally explain the variability of sediment composition in the eastern part of the EMS (e.g. Krom et al., 1999b; Nijenhuis and De Lange, 2000; Wehausen and Brumsack, 1999; 2000; Hamann et al., 2009; Revel et al., 2010). For the western section, however, the system is much more complex (e.g. Freydier et al., 2001; Weldeab et al., 2002b; Goudeau et al., 2013; Klaver et al., 2015).

This is, on one hand, because existing geochemical datasets do not adequately cover the Ionian Sea, and in particular information is lacking for the broad Libyan margin. On the other hand, only a few multiproxy studies on the marine detrital component exist, and most of these are focused on the Nile discharge variability.

Coupled Sr and Nd isotopic ratios in detrital sediments have been widely used as fingerprints for source areas in the EMS, as there appears to be little effect of transport processes and diagenesis. In the Levantine Basin, a simple mixing model between Nile sediment and Saharan dust is sufficient to explain the variability of detrital supplies, in terms of Sr and Nd isotopes (Krom et al., 1999b; Freydier et al., 2001; Revel et al., 2010). The Sr-Nd isotope data also suggest that the Late-Quaternary sediments deposited in the areas around Crete are a mixture of Saharan dust and Aegean/Nile river-borne materials (Weldeab et al., 2002b; Ehrmann et al., 2007b); while the Aegean and Nile inputs cannot be differentiated using these isotopes alone (Weldeab et al., 2002a; 2002b; Klaver et al., 2015).

This thesis demonstrates that an important component needs to be involved for the western section of the EMS, central Mediterranean, using Sr and Nd isotopes (Chapter 2). This has been related to fluvial contributions from the wider North-African margin, derived from reactivated paleodrainage systems during sapropel periods (Chapters 2–4). Moreover, the mixture of Nile and Aegean riverine contributions can be unraveled by elemental geochemistry, using a ternary diagram of Ti, K, and Mg contents in particular (Chapters 3 and 4). Furthermore, most studies suggest that sediment provenance plays a dominant role in determining the composition of rare earth elements (REE), as they are very are resistant to chemical weathering (e.g. Taylor and McLennan, 1985; Moreno et al., 2006; Padoan et al., 2011; Révillon at al., 2011; Wu et al., 2013). Unfortunately, only few REE relevant studies have been reported for EMS sediments (c.f. Martinez-Ruiz et al., 2015). The sedimentary REE pattern and associated parameters are shown to be able to give robust constraints for EMS provenance determination (Chapter 4).

In addition to the geochemical tracers, clay mineralogy is a useful provenance indicator, in particular for the circum-Mediterranean region. Moreover, the end-member modeling technique of Weltje (1997) applied to grain-size distributions is a powerful tool for unmixing of different components in detrital sediments (e.g. Stuut et al., 2002; Hamann et al., 2008; Tjallingii et al., 2008; McGee et al., 2013). Not only the detrital riverine fluxes can be detected but also the relative freshwater input using planktonic foraminiferal $d^{18}O$ data (e.g. Kallel et al., 1997; Rohling et al., 2002; Hennekam et al., 2014, 2015) (Chapter 3).

This study demonstrates the effectiveness of a multiproxy approach. In particular, the elemental fingerprints of detrital sediment have shown to be very practical for EMS provenance studies, not only due to their ease-of-analysis compared to isotope data, but also offering essential complementary information (Chapters 3 and 4).

By carrying out the provenance studies, the applications of various proxies have also been examined. One of the most critical problems is the potential Sr remaining in barite after traditional carbonate removal. The Sr concentration and isotopes of carbonate-free sediments have been widely used for provenance studies. However, the authigenic Sr associated with marine barite may still remain in the decarbonated sediments, which could have largely affected the detrital Sr signatures. This problem is expected to be very prominent in regions with high productivity, while it was overlooked somehow in most – if not all – studies. The Mediterranean Sea is probably the best area to examine such an impact of barite-bearing Sr. On the one hand, in the Mediterranean successful detrital provenance studies have been done based on Sr isotopes and concentrations. On the other hand, enhanced levels of barite occur in Mediterranean sediments during sapropel formation. Chapter 5 of this thesis is therefore dedicated to evaluate the effect of potentially remaining barite-Sr using Mediterranean sediments, and demonstrate that this barite-Sr must be taken into account for all provenance studies using detrital Sr composition.

4 Seawater circulation and freshwater forcing

An important characteristic of the present-day Mediterranean is that it has an anti-estuarine circulation pattern. The surface inflow of relatively fresh, low-density water flows eastward with increasing salinity and in a counter-clockwise pathway. Strong evaporation causes the Mediterranean to function as a concentration basin, converting the surface water into deeper outflow of salty, denser water (Pinardi and Masetti, 2000). In other words, there is a basin-averaged excess of evaporation (X) over total freshwater input (i.e. X = E (evaporation) – P (precipitation) – R (runoff); X > 0), in particular for the EMS. Consequently, the aridity and, more generally speaking, the hydroclimate over the Mediterranean region, strongly influences the physical parameters of the surface waters, which play a central role in the functioning of the thermohaline circulation (Rohling et al., 2015, and references therein).

Such pattern may have not always been as it is today, especially at times of sapropel formation. To date, the spatially estimate for the changes in freshwater forcing and consequent circulation pattern is mostly based on planktonic foraminiferal oxygen isotopes ($\delta^{18}O$). However, three different hypotheses exist for the Holocene sapropel S1 period, suggesting that the present-day west–east surface-water salinity gradient was 1) reversed to an estuarine-type condition (Thunell and Williams, 1989), 2) changed to a flat field, i.e. no gradient but not reversed (Kallel et al., 1997), and 3) similar to that of today but a weaker gradient (Rohling and De Rijk, 1999). This is mainly because of the uncertainties in the use of salinity:$\delta^{18}O$ relationships (Rohling, 1999).

It has been proposed that a reduction of intermediate and deep-water formation as a consequence of surface hydrological changes acted as a precondition for S1 formation by limiting the oxygen supply to the bottom waters (Rohling, 1994; De Lange et al., 2008; Rohling et al., 2015; Tachikawa et al., 2015). Faunal- and stable-isotope records of benthic foraminifera suggest a collapse of the intermediate waters synchronous with the sapropel S1 deposition, in contrast to the well-ventilated conditions before the S1 (e.g. Jorissen et al., 1999; Kuhnt et al., 2008; Schmiedl et al., 2010). Nevertheless, the use of this approach for deep-sea sapropels is hampered by the paucity of epibenthic species under low-oxygen conditions. Bulk sediment geochemistry, in particular redox-sensitive elements, can be used to indicate the re-ventilation of the water column, but only if post-depositional diffusion is carefully considered (Van Santvoort et al. 1996; Thomson et al., 1999; Reitz et al., 2006). Ocean-biogeochemical modeling studies, which attempted to address the interplay between physical circulation and deep-water oxygen consumption, have concluded that stagnating deep-water circulation, combined with a large external nutrient input, is a prerequisite for the S1 formation (Stratford et al., 2000; Bianchi et al., 2006; Grimm et al., 2015). This is supported by a compilation study, indicating the presence of an anoxic boundary at a water-depth of ~1,800 m (De Lange et al., 2008).

However, proxy reconstructions that can be compared with simulations are still scarce for the Holocene sapropel S1, in particular a systematic reconstruction of the Mediterranean thermohaline circulation using appropriate tracer is hitherto lacking.

Neodymium (Nd) isotopes have proven to be an adequate tracer for modern ocean circulation and have great potential to trace past circulation of water masses (see review by Frank, 2002). Its composition is conventionally expressed as: $\varepsilon Nd = [(^{143}Nd/^{144}Nd)_{sample} / (^{143}Nd/^{144}Nd)_{CHUR} - 1] \times 10^4$ where CHUR (chondritic uniform reservoir) is 0.512638 (Jacobsen and Wasserburg, 1980). The application of Nd isotopes seems particularly appropriate to study paleoceanographic deepwater processes, provided that an appropriate archive can be identified (see review by Tachikawa et al., 2014).

As the last part of the thesis (Chapter 6), we present, for the first time, a basin-wide reconstruction of seawater εNd signatures for the Holocene sapropel S1. The reconstruction is based on the reliable seawater-εNd archives of fish debris and foraminiferal shells. The samples are taken from 9 carefully selected cores representing a geographical and bathymetric coverage of the EMS. Additional εNd data of sediment HCl-leachate from the EMS and the western Mediterranean Sea (WMS) are also provided. Our results will be discussed with existing data of seawater εNd for both the present-day and sapropel S1 period, and for the whole

Mediterranean Sea in a wider perspective. Important implications emerge for the Mediterranean water circulation during the sapropel S1 period, and for the processes leading to sapropel formation.

5 Sapropels S1 and S5

The knowledge of sapropel formation mechanisms is mostly based on the latest, Holocene sapropel S1 deposited in the EMS between ~10.8 and 6.1 ka cal. BP (hereafter referred to as “ka”) (c.f. De Lange et al., 2008). This is because it is more easily accessible and also is the only sapropel within the range of precise radiocarbon dating.

Although the general principles are similar, all individual sapropels show their own specific features (see reviews by Cramp and O'Sullivan, 1999; Rohling et al., 2015). In particular, the last interglacial sapropel S5 is one of the most intensely developed sapropels of the Late Quaternary. Sapropels S1 and S5 formed during insolation-driven monsoon maxima of the current (Holocene) and last interglacial periods, respectively. Both monsoon maxima were interrupted by a dry interlude of several centuries, with concomitant cooling over the NBEM (Northern Borderlands of the Eastern Mediterranean; i.e. Aegean and Adriatic regions) (e.g. S1: Emeis et al., 2000; Hennekam et al., 2014; Filippidi et al., 2016; S5: Rohling et al., 2002; 2004; Schmiedl et al., 2003; Scrivner et al., 2004).

An important aim of this thesis is also to provide better analogues for the present-day climate. This is needed to comprehend paleoclimate variability to distinguish between natural climatic change and human induced changes. With a similar but more extraordinary astronomical setting during the last interglacial insolation maximum (Berger and Loutre, 1991), overall, sapropel S5 has far more runoff than the Holocene sapropel S1 (e.g. Rossignol-Strick, 1983; Bar-Matthews et al., 2000; 2003). As a result, the period of sapropel S5 deposition in the EMS (~128 to 121 ka; c.f. Rohling et al., 2015) – last interglacial insolation maximum – Marine Isotope sub-Stage 5e (MIS 5e), has long been regarded as a potential candidate for such an analogue (e.g. Kukla et al., 1997; Rohling et al., 2002; Marino et al., 2007).

Therefore, part of this thesis focuses on the riverine supplies into the EMS during sapropel S5 time, in comparison to those of sapropel S1 and the present-day (Chapter 4).

6 Scope of the thesis

Focusing on the problems and challenges discussed above, this thesis deals with the hydroclimate variability and associated changes in riverine fluxes and seawater

circulation during eastern-Mediterranean sapropel formation. Overall, the PhD study is done via three research routes, being 1) “freshwater sources and associated hydroclimate changes”, 2) “evaluation of detrital provenance proxies”, and 3) “complex interplay between the paleoceanographic and paleoclimatic processes”.

First of all, under “***the freshwater sources and associated hydroclimate changes***”, we aim to reconstruct the riverine supplies into the EMS (**Chapters 2–4**). The approaches involve the combined use of major and trace elements, Sr and Nd isotopes, clay mineralogy, grain size end-member modeling, etc., which are mostly done on the terrigenous detrital component of the marine sediments. The samples are taken from a geographical and bathymetric coverage of the EMS, including the sediments of Holocene sapropel S1 and of last interglacial sapropel S5. Specifically, our study is started from the sapropel S1 period, mainly focusing on a well-dated sediment core in the central Mediterranean (**Chapter 2**). Then it is extended to the past 18,000 years in comparison with existing North-African hydroclimate records on a sub-continental scale (**Chapter 3**). After that, the knowledge is applied to last interglacial sapropel S5 to investigate the distribution of river-borne materials on a basin-wide EMS scale (**Chapter 4**).

During this study it appears necessary to “***evaluate and examine the applications of various detrital provenance proxies***”. One of the most prominent problems is the potential barite-associated Sr remaining in decarbonated sediments, as the not fully removed barite-Sr may largely affect the assumed detrital Sr composition. However, this problem was ignored or just overlooked in published studies. The intention and set-up for **Chapter 5** is thus to evaluate the contribution of barite-associated Sr for provenance studies using Sr isotopes and concentration.

Apart from the studies on marine detrital sediments, we use seawater-derived fractions to explore the changes in the thermohaline circulation and water column of the Mediterranean Sea during sapropel formation. For the purpose of a better understanding of “***the complex interplay between the paleoceanographic and paleoclimatic processes***”, for the first time, a basin-wide EMS reconstruction of seawater Nd isotopic ratios during sapropel S1 deposition is given (**Chapter 6**).

7 Summary of the chapters

To be more specific, the highlights and contents for each chapter are summarized as follows:

In **Chapter 2**, Sr and Nd isotopes and high-resolution elemental data are used to constrain different riverine and eolian supplies to the central Mediterranean during the Holocene sapropel S1 period. For the first time, robust and consistent evidence

is given for important detrital supplies from fossil river/wadi systems along the Libyan-Tunisian margin, which was activated by intensified African monsoon precipitation. These freshwater routes had a major influence on the settlement of Neolithic communities and may have favored modern human migrations out of Africa. Furthermore, the specific source and distribution of such riverine supplies have been evaluated by the records along a west–east transect throughout the EMS.

In **Chapter 3**, using elemental geochemistry, clay mineralogy, grain size end-member modeling, and planktonic foraminiferal oxygen isotopes, a multiproxy study not only allows us to constrain the variability of detrital supplies to the EMS, but also to reveal and characterize the (paleo-) fluvial discharges along the wider North-African margin. On a sub-continental scale, we find a remarkable similarity between different paleodrainage systems with runoff towards the North-African and the Atlantic West-African margins. This indicates a common headwater region in the central Saharan mountains, and a similar climate mechanism. Our results suggest a dominant control of Saharan humid surface on the paleodrainage delivery over North Africa, modulated by groundwater level, in response to the insolation-driven West-African monsoon precipitation.

In **Chapter 4**, the studied scope is expanded to a basin-wide EMS scale, and focused on a different but analogous sapropel S5 that deposited during the last interglacial maximum. A geochemical view of riverine inputs to the EMS is not only provided for sapropel S5 period, but also to be compared with those of Holocene sapropel S1 and the present-day. This detailed knowledge of hydroclimate changes and associated riverine supplies to the EMS further contributes to a better understanding of sapropel formation, paleoclimate variability, and human migration. On the other hand, our approach demonstrates the potential of a combined use of major elements, rare earth elements, and Sr and Nd isotopes. In particular, the elemental fingerprints of detrital sediment have shown to be very practical for EMS provenance studies.

The potential problem of barite-Sr remaining in decarbonated sediment was overlooked in most – if not all – studies using Sr concentration and isotopes as provenance proxies. Using Mediterranean sediment for an exemplary study, in **Chapter 5**, we demonstrate the existence of Sr remaining in barite after traditional carbonate removal and must be considered for provenance studies using detrital Sr composition. We estimate that the correction is required for marine sediments with >400 ppm barite content. Such a correction is strongly needed if there is also a $^{87}Sr/^{86}Sr$ signature >0.713 and low Sr/Al ratio (e.g. <0.0010) for the detrital sediments. For the marine sediments with extremely high barite content (>1500 ppm), additional NH_4Cl leaching after a decarbonation is necessary.

In **Chapter 6**, for the first time, we present a basin-wide reconstruction of seawater Nd isotopic ratios at the time of Holocene sapropel S1 deposition. As reliable archives for the deep-water εNd signal, fish debris and foraminiferal tests from nine cores are obtained to provide a geographical and bathymetric coverage of the EMS. Additional εNd data of Mediterranean sediment HCl-leachate from two cores are also used. This allows us to constrain the mixing and sources of water masses and to evaluate the thermohaline circulation of the Mediterranean Sea. Our results suggest deep-water stagnation below ~800 m depth in the EMS, which persisted over the whole S1 period. This deep-water stagnation might have been preconditioned two thousand years earlier than S1 formation started, whereas it terminated synchronously with the S1 ending. Moreover, a reduction in hydrological exchange between EMS and WMS across the Strait of Sicily is evidently suggested. It appears that diminished intermediate-water production and ceased deep-water formation occurred for the EMS during S1 period, while the WMS water circulation must have persistently functioned. This EMS–WMS difference supports the vision that deep-water stagnation is a prerequisite for sapropel formation.

CHAPTER 2

Unraveling North-African riverine and eolian contributions to central Mediterranean sediments during Holocene sapropel S1 formation

Jiawang Wu [a*], Philipp Böning [b], Katharina Pahnke [b], Kazuyo Tachikawa [c], and Gert J. de Lange [a]

[a] Department of Earth Sciences – Geochemistry, Faculty of Geosciences, Utrecht University, Princetonplein 9, 3584 CC Utrecht, The Netherlands
[b] Max Planck Research Group for Marine Isotope Geochemistry, Institute for Chemistry and Biology of the Marine Environment (ICBM), University of Oldenburg, Carl-von-Ossietzky-Strasse 9-11, 26129 Oldenburg, Germany
[c] CEREGE, Aix-Marseille Université, CNRS, IRD, Collège de France, CEREGE UM34, 13545 Aix en Provence, France

[*] Corresponding author: j.w.wu@uu.nl (J. Wu).

Published in Quaternary Science Reviews 152, 31–48, 2016

Abstract

Hydroclimate variability has exerted a fundamental control on the alternating deposition of organic-lean marl and organic-rich sapropel sediments in the eastern Mediterranean Sea (EMS). However, the exact mechanisms regarding the freshwater sources and related changes are still debated. Here, Sr and Nd isotopes and high-resolution elemental data are used to constrain different riverine and eolian supplies to the central Mediterranean over the past 9.8 ka. The detrital sediments in core CP10BC, taken at the margin of the Libyan shelf in the southwestern Ionian Sea, can be described by a three-endmember mixing system based on Sr and Nd isotopic compositions. The same systematics can also be deduced from Ti and K compositional variability. The endmembers comprise: Saharan Dust, Aegean/Nile, and Libyan Soil, representing the eolian supply from North Africa, the riverine inputs from the Aegean/Nile areas, as well as the riverine and shelf-derived fluxes from the Libyan-Tunisian margin. For the sapropel S1 period in particular, we find important detrital supplies from fossil river/wadi systems along the Libyan-Tunisian margin, activated by intensified African monsoon precipitation. Combining the temporal profiles with the consistent variability observed in the $^{87}Sr/^{86}Sr$–1000/Sr diagram, such Libyan contribution has been most prominent during the uppermost period of sapropel S1 in core CP10BC. This observation is in agreement with hydroclimate reconstructions of northwestern Libya. Comparison of the Sr-Nd isotope data between core CP10BC and four cores taken along a west–east transect throughout the EMS shows that this detrital supply originated mainly from western Libya/Tunisia, and was transported as far eastward as ~25°E while being diluted by an increasing Nile contribution.

Keywords

sapropel S1; Sr isotopes; Nd isotopes; elemental geochemistry; provenance; Libya; North Africa

1 Introduction

The Mediterranean lies at the interface between the European temperate and African tropical zones. In addition, the semi-enclosed basin setting makes it particularly sensitive to changes in the hydrological cycle (Tzedakis, 2007; Magny et al., 2013; Rohling et al., 2015). This sensitivity is best witnessed by the rhythmic occurrence of sapropels, organic-rich sedimentary units deposited in the eastern Mediterranean Sea (EMS) at an astronomically determined cyclicity (Rossignol-Strick et al., 1982; Hilgen, 1991; Tuenter et al., 2003). The knowledge of sapropel formation mechanisms mostly relies on the last, Holocene, sapropel S1 (Rohling, 1994; Rohling et al., 2015; and references therein), because it is more easily accessible and also is the only sapropel within the range of precise radiocarbon dating. Warm and humid conditions between ~10.8 and 6.1 ka cal. BP (hereafter referred to as "ka") have caused a pronounced density stratification of the water column and high primary productivity in the surface waters, ultimately resulting in deepwater stagnation and the basin-wide S1-formation in the EMS (e.g. Emeis et al., 2000; Mercone et al., 2000; Slomp et al., 2004; De Lange et al., 2008; Tachikawa et al., 2015; Van Helmond et al., 2015). Enhanced freshwater influx at sapropel times has been demonstrated through $\delta^{18}O$ of planktonic foraminifera (e.g. Fontugne et al., 1994; Kallel et al., 1997; Emeis et al., 2000; 2003; Rohling et al., 2002; 2004; Hennekam et al., 2014; Toucanne et al., 2015) and of cave speleothems (e.g. Bar-Matthews et al., 2000; 2003; Bard et al., 2002; Zanchetta et al., 2007; Spötl et al., 2010; Zhornyak et al., 2011). Although the general principles are clear, the exact mechanisms with regard to freshwater sources and associated hydroclimate changes in the circum-Mediterranean remain highly debated.

Pioneering studies have proposed increased precipitation around the Northern Borderlands of the Eastern Mediterranean (NBEM) concurrent with sapropel depositions (Rossignol-Strick, 1987; Rohling and Hilgen, 1991). This increase is corroborated by speleothem $\delta^{18}O$ data from the NBEM (e.g. Zanchetta et al., 2007; Spötl et al., 2010; Zhornyak et al., 2011) and by their correspondence with the records of Soreq Cave (Bar-Matthews et al., 2000; 2003). Marine records from the eastern and central Mediterranean also confirm that increased rainfall was widespread over the NBEM during sapropel formation (e.g. Kallel et al., 1997; Emeis et al., 2000; Toucanne et al., 2015; Filippidi et al., 2016). Being seasonally specified, palynological studies demonstrate that enhanced winter precipitation was responsible for the NBEM wet conditions at times of sapropel deposition (e.g. S1: Kotthoff et al., 2008; Peyron et al., 2011; S5: Milner et al., 2012). Summer rainfall was thought to have been increased too, but this is questioned by Tzedakis (2007). Recent work has revealed north–south contrasts of precipitation seasonality in the Holocene central Mediterranean, which can reconcile the discrepancies from various proxies (e.g. Magny et al., 2011; Peyron et al., 2011; 2013; Giraudi et al., 2013;

Goudeau et al., 2014; 2015). The evidence suggests that, there were also increases in 1) winter precipitation in the NBEM and 2) summer and winter precipitation in the southern EMS borderlands during S1 period, in addition to the enhanced Nile discharge (see review by Magny et al., 2013). Possible impacts of the Black Sea overflow and meltwater runoff of European ice-sheets during sapropel deposition have been excluded (Sperling et al., 2003).

Sapropels occurred at times of Northern Hemisphere insolation maxima related to the orbital cycle of precession, when the African monsoon was intensified (Rossignol-Strick et al., 1982; Rossignol-Strick, 1987; Hilgen, 1991; Tuenter et al., 2003). Even though the African monsoon precipitation did not directly extend to the EMS, the monsoon-fuelled Nile discharge is recognized as a key freshwater source for sapropel formation. This has been explicitly illustrated by the temporal coincidence between the S1 deposition and Nile discharge (e.g. Rossignol-Strick et al., 1982; Mercone et al., 2000; De Lange et al., 2008; Revel et al., 2010; Box et al., 2011; Hennekam et al., 2014).

Apart from the Nile flooding, intensification of African monsoon precipitation had a profound and more widespread influence on the EMS at sapropel times. Based on planktonic foraminiferal $\delta^{18}O$ data, Rohling et al. (2002; 2004) suggested that the summer monsoon penetrated northward beyond the central Saharan drainage basin at ~21°N during sapropel S5 deposition. As a consequence, activated fossil river/wadi systems along the wider North-African margin that are now buried beneath sand dunes could have debouched into the EMS. Major paleo-river systems have been revealed via satellite imagery (Paillou et al., 2009; 2012) and paleohydrological modeling (Coulthard et al., 2013). Influence of runoff from the central Saharan mountains towards the Gulf of Sirte during sapropel S5 period is also shown in Nd isotopes of planktonic foraminifera (Osborne et al., 2008; 2010). This freshwater route into the EMS may have rivaled the Nile runoff in magnitude (Scrivner et al., 2004), favored human migrations out of Africa (Osborne et al., 2008; Coulthard et al., 2013), and possibly operated for a majority of Quaternary sapropels (e.g. S1: Fontugne et al., 1994; S6: Emeis et al., 2003). Although the origin of Nd recorded in planktonic foraminifera is still controversial (see review by Tachikawa et al., 2014), this scenario is supported by dust variations over the past 3 Ma in combination with other Saharan data (Larrasoaña et al., 2003; 2013). Indeed, archaeological surveys suggest human occupation and dispersal over the Libyan-Saharan desert along the interlinked river-lake-wetland systems during the African Humid Period (AHP; ~11–5 ka) (e.g. Mandel and Simmons, 2001; Drake et al., 2011; Lézine et al., 2011; Manning and Timpson, 2014). However, so far there is no marine evidence whether the fossil river/wadi route was active during sapropel S1

time. In this paper we focus on such riverine contribution by analyzing the detrital component of EMS sediments.

It has been suggested that clay minerals of surface sediments over most of the EMS can be described by a simple two-endmember mixing model, with Saharan dust and Nile sediment as the dominant sources (e.g. Venkatarathnam and Ryan, 1971; Ehrmann et al., 2007a; Hamann et al., 2009). From a long-term perspective, various records of clay minerals and major elements reflect consistent sapropel-related alternations between riverine and eolian endmembers (e.g. Wehausen and Brumsack, 1999; 2000; Foucault and Mélière, 2000; Lourens et al., 2001; Zhao et al., 2012; 2016). However, only a few high-resolution studies on the detrital composition of marine sediments exist, and most of these are focused on the Nile-dominated region (e.g. Hamann et al., 2009; Revel et al., 2010; 2015; Box et al., 2011; Hennekam et al., 2014; 2015). Very little is known about the supplies of numerous small rivers from other sources through time. In particular, potential riverine supplies from the wider North-African margin may have been underestimated, or even neglected.

Paired Sr and Nd isotopes have shown to be a powerful tool for provenance studies. Their isotopic ratios in lithogenic sediments have characteristic fingerprints of source rocks, with little effect of transport processes and diagenesis (e.g. Freydier et al., 2001; Weldeab et al., 2002a; 2002b; Revel et al., 2010; 2015; Rodrigo-Gámiz et al., 2015; Castañeda et al., 2016). In addition to radiogenic isotopic tracers, elemental geochemistry of marine sediments can be used to track changes in detrital inputs (e.g. Wehausen and Brumsack, 1999; 2000; Bout-Roumazeilles et al., 2013; Wu et al., 2013; Klaver et al., 2015). Lower Ti/Al and Zr/Al values and higher K/Al ratios during humid sapropel periods are generally interpreted as a sign of reduced eolian and enhanced riverine fluxes, and vice versa for more arid conditions (see review by Martinez-Ruiz et al., 2015). Here, combining Sr and Nd isotopes with major elements, we present a high-resolution record of the origin of detrital sediments over the past 9.8 ka using a well-dated boxcore. Core CP10BC was strategically retrieved from the southwestern Ionian Sea, at the margin of the Libyan shelf (Figure 1). The sediment provenance for this area is thought to be influenced by Saharan dust and riverine sources from northern and southern EMS borderlands, with a presumably limited Nile contribution. Therefore, this core represents an excellent location to understand the nature and importance of rivers flowing north out of the Sahara during sapropel S1 time. Furthermore, by comparing the Sr-Nd isotope data of core CP10BC with four cores taken along a west–east transect throughout the EMS, a detailed evaluation can be made of the potential distribution of detrital material.

2 Recent regional settings

2.1 Hydroclimate

The Mediterranean climate is characterized by marked seasonality in rainfall (Magny et al., 2013; Rohling et al., 2015 and references therein; Castañeda et al. 2016). General features are summarized as follows (Figure 1a). During summer, the Mediterranean is dominated by the subtropical high-pressure belt resulting in dry and hot conditions, especially in the southeastern sector (Lolis et al., 2002). In winter, the high-pressure belt migrates southward and the Mediterranean comes under the control of the westerlies, which drive an eastward transport of Atlantic depressions, bringing enhanced precipitation over the NBEM (Rohling and Hilgen, 1991; Lolis et al., 2002).

2.2 Water masses and circulation

The climate strongly influences the physical parameters of the surface waters, which play a central role in controlling the thermohaline circulation in the EMS (Pinardi and Masetti, 2000; Pinardi et al., 2015; and references therein) (Figure 1b). Inflowing surface waters occupying the upper 200 m depth, called Modified Atlantic Water (MAW), flow eastward along the North-African coast. The MAW splits into two branches; one turns southward into a broad anticyclonic pattern in the Gulf of Sirte, while the other continues in an easterly direction with increasing salinity, following a large-scale counter-clockwise pathway (Pinardi and Masetti, 2000; Béranger et al., 2005; Pinardi et al., 2015). The eastern-most MAW cools in winter and consequently forms the Levantine Intermediate Water (LIW). The LIW flows westward at 200–600 m depth as the salty outflow waters, and also contributes to the formation of Adriatic Deep Water (AdDW) and Aegean Deep Water (AeDW) below 800 m (Roether et al., 1996; Pinardi and Masetti, 2000; Pinardi et al., 2015).

2.3 Detrital sediment provenance

The amount and composition of riverine supply depends on the extent of catchment areas, exposed rocks, and weathering conditions (Figure 1b). The Nile is the longest river on Earth, comprising two different systems: 1) the White Nile and 2) the Blue Nile and Atbara (Williams et al., 2000). The latter drains the Ethiopian highlands that predominantly consist of continental flood basalts of Tertiary age, affected by the East African monsoon in summer, resulting in the annual Nile flood (Hennekam et al 2014; Castañeda et al., 2016). As the Sudd swamps in Sudan filter out most of the suspension load of the White Nile, the Blue Nile and Atbara account for >50% of the water flow and >95% of the sediment load (~230 Mt/yr) (Foucault and Stanley, 1989; Williams et al., 2000; Padoan et al., 2011). The coarser fraction of Nile sediments is mostly deposited on the delta, and the finer fraction is transported in a counter-clockwise gyre within the Levantine Basin. At present, only a small fraction of Nile-derived particulates is thought to be transported to areas west of Crete (Krom et al., 1999a; Weldeab et al., 2002a).

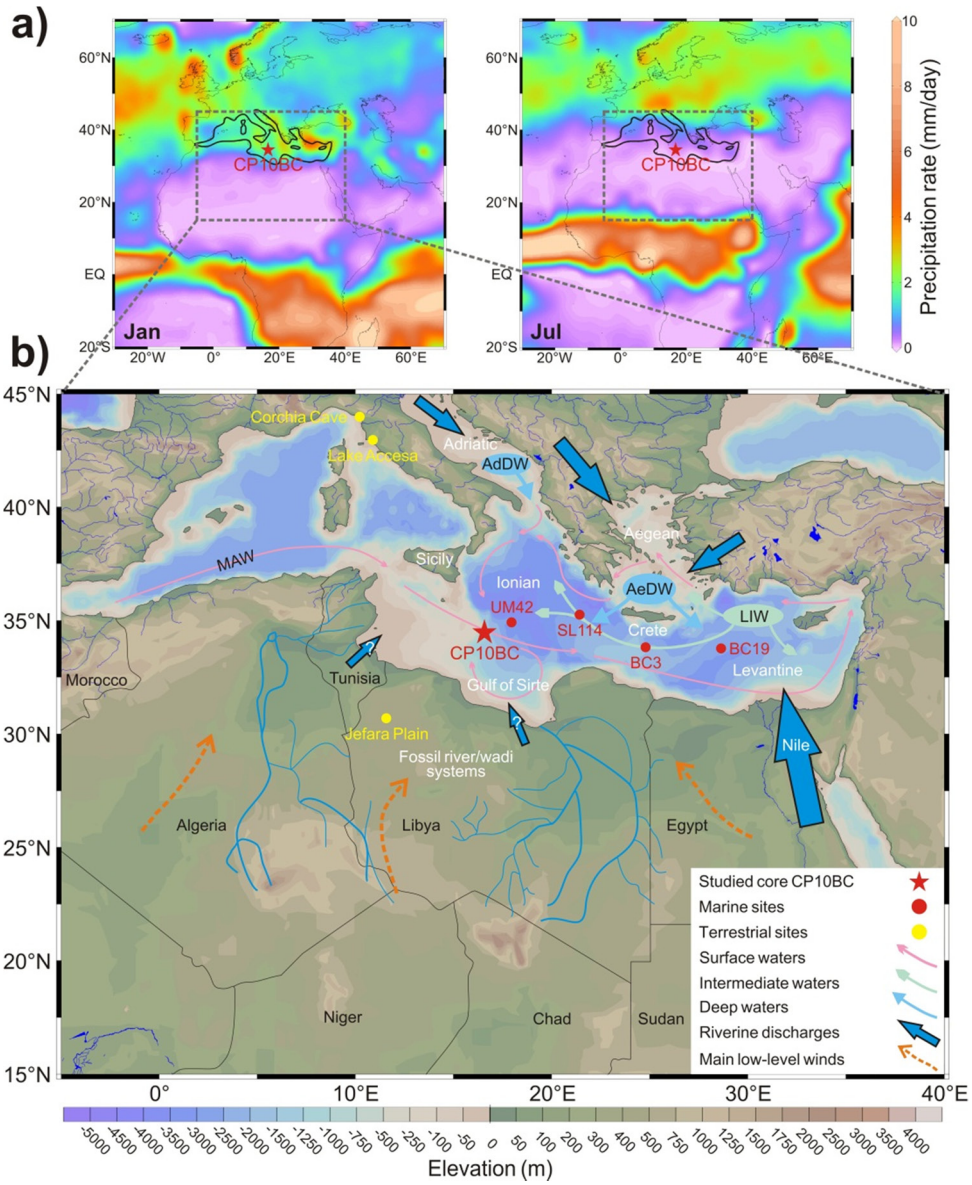

Figure 1 Map of the eastern Mediterranean Sea and adjacent areas, with location of core CP10BC (star) shown and four cores (red circles) with Sr and Nd isotope data used for comparison. a) Long-term mean precipitation rate in January (winter) and July (summer) (www.esrl.noaa.gov/psd/data). b) Large-scale oceanography after Pinardi and Masetti (2000), including the general surface-water circulation, i.e. Modified Atlantic Water (MAW), formation sites and pathways of Levantine Intermediate Water (LIW), as well as Adriatic Deep Water (AdDW) and Aegean Deep Water (AeDW). Potential route of fossil river/wadi systems over the western Libyan-Tunisian areas after Coulthard et al. (2013), and that in eastern Libya and Egypt after Rohling et al. (2002). Main low-level winds after Israelevich et al. (2003).

Numerous small rivers in the NBEM are major contributors to detrital deposition in the Ionian Sea (Figure 1b). The Turkish rivers (~17 Mt/yr), southeastern European rivers (~30 Mt/yr), and the Po (~17 Mt/yr) yield substantial sediment loads into the Aegean and Adriatic Sea (after Bout-Roumazeilles et al., 2013). Part of this may subsequently be transported to the Ionian Sea by oceanic currents (Venkatarathnam and Ryan; 1971; Ehrmann et al., 2007a; Goudeau et al., 2013). This river-borne material reflects the weathering and erosion products of basalts and ultramafic rocks in relation to the lithology of the catchments (Weldeab et al., 2002a; Klaver et al., 2015).

Present-day riverine contribution to the Ionian Sea from the North-African margin is limited because of small catchments and sparse rainfall. Because of the regional topography and precipitation seasonality, nevertheless, the ephemeral rivers draining northward from the central Saharan mountains may have been a considerable supplier of detrital material, especially during the humid sapropel times (Drake et al., 2011; Lézine et al., 2011; Scheuvens et al., 2013) (Figure 1b). The river channels dissipate in the desert, but some converge forming the main river/wadi systems. The Irharhar, for instance, is associated with dry/salt lakes in Tunisia and Algeria, fed by rainfall and groundwater, flowing towards the Libyan-Tunisian coast (Paillou et al., 2009; 2012; Drake et al., 2011; Coulthard et al., 2013). Moreover, the irregularly active river/wadi systems can provoke turbid flows associated with high detrital fluxes into the Ionian Sea (Weldeab et al., 2002a; Zielhofer et al., 2008).

Saharan dust is the dominant source of the EMS detrital sediment (~25–100 Mt/yr) (see compilations in Goudie and Middleton, 2001), notably for the Ionian Sea receiving low riverine input (Guerzoni et al., 1997; Rutten et al., 2000). Dust from the northern and eastern EMS borderlands is quantitatively negligible (Guerzoni et al., 1997; Ehrmann et al., 2007a). The source areas consist mainly of Precambrian granitoid rocks in the central Sahara, and of limestone in the North (Moreno et al., 2006). Major dust production for the EMS originates from hyperarid areas with little/no vegetation (see Scheuvens et al., 2013) (Figure 1b). The Bodélé Depression in Chad is the largest dust source in the world; other productive sources include western Sahara, Tunisia/northern Algeria, and central Libya. The northward delivery of Saharan dust is primarily via low-level winds (Goudie and Middleton, 2001; Stuut et al., 2009; Israelevich et al., 2012), which can be related to the coupling of sea-surface temperature to atmospheric pressure over the Mediterranean Sea (Jilbert et al., 2010).

3 Material and methods

Core CP10BC (34°32.7'N, 16°34.0'E; 1501 m water-depth) was collected during the RV *Pelagia* cruise CORTADO in 2011 (Figure 1). This 35.5 cm long boxcore consists of foraminifera and pteropod marl ooze, with a distinct S1 unit. The olive-grey S1 is ~10 cm thick at the bottom; a diffuse dark band occurs at ~16–24 cm depth, well above the visual S1. Normal yellowish-brown sediments are intercalated between the two layers. Two subcores were sampled so as to have enough material for all analyses. For subcore CP10BC#1 every 0.25 cm were sampled resulting in a total of 142 samples, which were freeze-dried and finely ground for subsequent geochemical analyses. Subcore CP10BC#3 was sampled at intervals of 0.5 cm for foraminiferal radiocarbon dating.

3.1 Age model

The chronology of core CP10BC is based on 4 Accelerator Mass Spectrometry (AMS) ^{14}C dates on planktonic foraminifers, done at the Poznan Radiocarbon Laboratory (Table 1). Approximately 15 mg of mixed planktonic foraminifers (*Globigerinoides ruber* and *Globigerinoides sacculifer*) in the 150–600 µm fractions was picked. All ^{14}C dates were converted into calendar ages using the Marine13 calibration curve (Reimer et al., 2013) implemented in the program Calib 7.0 (Stuiver et al., 2005), with no regional reservoir correction (i.e. $\Delta R=0$) that is valid for the modern Mediterranean (Siani et al., 2000). Inventories and activities of ^{210}Pb and ^{137}Cs were determined for 9 samples of bulk sediment (see Barsanti et al., 2011), showing that minor bioturbation affected the top 3 cm at most; thus the age of core-top is assessed to be the present-day.

The age model was developed by linear interpolation between these 5 tie-points, yielding a highly consistent depth-age curve, with the basal age of 9.8 ka that refers to the start of S1 here (Figure 2). The average sedimentation rate is 3.6 cm/ka.

Table 1 Core CP10BC radiocarbon chronology

Lab code	Depth (cm)	^{14}C age ± 2σ (yr BP)	Calibrated age ± 2σ (yr cal. BP) [a]
Poz-55177	6–6.5	2280 ± 30	1893 ± 85
Poz-55178	18.5–19	5130 ± 40	5486 ± 99
Poz-55179	28–28.5	7330 ± 40	7795 ± 107
Poz-55180	34–34.5	8770 ± 50	9423 ± 101

[a] Using Marine13 calibration curve (Reimer et al., 2013), implemented in program Calib 7.0 (Stuiver et al., 2005), with no regional offset ($\Delta R=0$) (Siani et al., 2000).

3.2 Total organic carbon

Total organic carbon (TOC) was measured on decarbonated samples following the protocol described in Van Santvoort et al. (1996). Powdered bulk sediments were decarbonated by shaking in 1 M HCl for 4 hours firstly, then for 12 hours. Subsequently, samples were rinsed twice with deionized water, oven-dried at 80 °C,

and ground. Replicate analyses of in-house standards and selected samples show that the relative deviations are <3%.

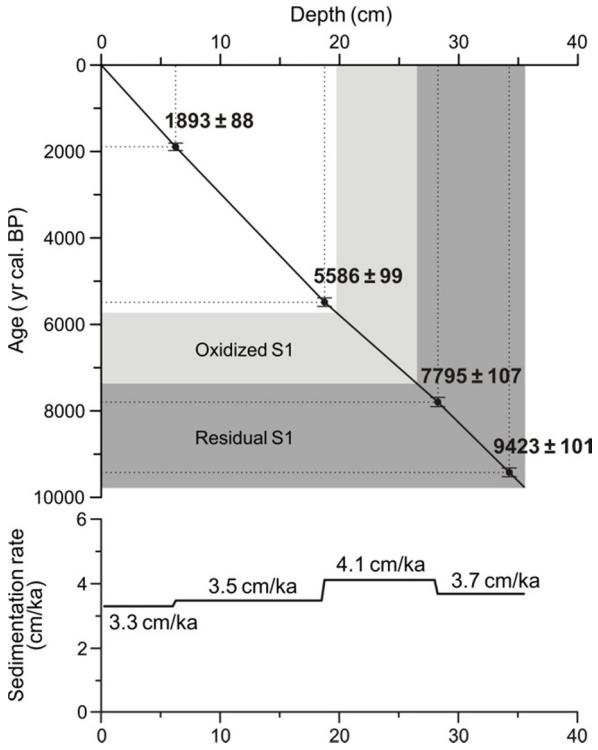

Figure 2 Age model and inferred sedimentation rate for core CP10BC, with dark and light shadings showing the residual and oxidized parts of sapropel S1, respectively. The 2σ errors are specified. Data sources refer to Table 1.

3.3 Major and minor elements

Elemental composition was analyzed by Inductively Coupled Plasma-Optical Emission Spectroscopy (ICP-OES) on a Perkin-Elmer Optima 3000 after a three-step total digestion (Reitz et al., 2006). First, ~125 mg of powdered sediments was digested in a mixture of 2.5 ml concentrated HF and 2.5 ml pre-mixed acid (3:2 concentrated $HClO_4$ and HNO_3), and heated at 90 °C in a gastight Teflon vessel for 12 hours. Subsequently, the solution was evaporated at 160 °C to near dryness, and then the residue was dissolved in 25 ml of 4.5% HNO_3 at 90 °C for 6 hours. For the samples with very high Mn concentrations, the procedure was applied to ~30 mg sediment with additional peroxide steps (see Reitz et al., 2006). Reported concentrations are on bulk sediment basis, expect for Sr content that was determined on the decarbonated fraction so as to represent the detrital phase alone (c.f. Section 3.2). Analytical uncertainties were monitored by international standard

(ISE-921), replicates, and blanks, showing that the relative deviations are <5% for all targeted elements.

3.4 Sr and Nd radiogenic isotopes

A selection of 27 samples was processed for Sr and Nd isotopic compositions at the Institute for Chemistry and Biology of the Marine Environment (ICBM) in Oldenburg. Decarbonation (c.f. Section 3.2) and Fe-Mn oxyhydroxide leaching were done to ensure that the analyses represent the detrital component alone. To remove the authigenic Fe-Mn oxyhydroxides, decarbonated samples were leached for 2 hours with a solution of 0.02 M hydroxylamine hydrochloride in 25% acetic acid. This was repeated for 6 hours twice, followed by three times rinsing with deionized water. The remaining siliciclastic fraction was dissolved using a routine three-step total digestion (c.f. Section 3.3).

Briefly, Sr and rare earth elements (REE) were separated using 100 µl Teflon columns filled with Eichrom TRU-Spec resin. Sr and Rb were collected in 1 M HNO_3 and REE in 1 M HCl. Subsequently, 30 µl Teflon columns with Eichrom Sr-Spec resin were used to isolate Sr from the Sr-Rb cuts, via washing out Rb in 3 M HNO_3 and then collecting Sr in Milli-Q water. Separation of Nd from other REE was performed on 250 µl Teflon columns using Eichrom Ln-Spec resin and 0.25 M HCl as eluent.

Isotope measurements were done by Multi-Collector Inductively Coupled Plasma-Mass Spectrometry (MC-ICP-MS) using the Thermo Scientific Neptune Plus at the ICBM. The measured $^{87}Sr/^{86}Sr$ and $^{143}Nd/^{144}Nd$ ratios were corrected for mass fractionation by normalizing to $^{86}Sr/^{88}Sr = 0.1194$ and $^{146}Nd/^{144}Nd = 0.7219$ and the exponential law, and are reported relative to the standards NBS-SRM 987 ($^{87}Sr/^{86}Sr = 0.710248$; Thirlwall, 1991) and JNdi ($^{143}Nd/^{144}Nd = 0.512115$; Tanaka et al., 2000), respectively. The 2σ external reproducibility was checked by repeated analysis of standards NBS-SRM 987 (40 ppm, n = 12) and JNdi (24 ppm, n = 17) (Table 2). The Nd isotopic ratio is expressed as: $\varepsilon_{Nd(0)} = [(^{143}Nd/^{144}Nd)_{measured} / (^{143}Nd/^{144}Nd)_{CHUR} -1] \times 10^4$, while CHUR (chondritic uniform reservoir) is 0.512638 (Jacobsen and Wasserburg, 1980). Blank levels were negligible in all cases. Krypton “gas blanks” as well as Rb and Ba levels in the measured Sr solutions were also negligible.

The Sr and Nd isotope data of four additional cores have been analyzed at CEREGE and are used for a west–east comparison throughout the EMS. The data of cores UM42, BC3, and BC19 have been published (Freydier et al., 2001), while the data from boxcore SL114 (35°17.2'N, 21°24.5'E; 3390 m depth) obtained during the RV *Logachev* cruise SMILABLE in 1999, are new. The analytical procedures for these four cores are the same and were given in Freydier et al. (2001).

Table 2 Sr and Nd isotopic compositions of detrital sediments in core CP10BC

Depth (cm)	Age (ka)	Sr (ppm)	$^{87}Sr/^{86}Sr$ [a]	$^{143}Nd/^{144}Nd$ [b]	$\varepsilon_{Nd(0)} \pm 2\sigma$ [c]
0–0.25	0.1	130.6	0.719740	0.512027	-11.9 ± 0.31
3–3.25	1.0	124.1	0.719847	0.512022	-12.0 ± 0.22
6–6.25	1.9	186.8	0.714879	0.512029	-11.9 ± 0.29
9–9.25	2.8	166.2	0.715315	0.512029	-11.9 ± 0.22
12–12.25	3.6	140.1	0.718365	0.512016	-12.1 ± 0.23
15–15.25	4.5	120.2	0.719703	0.512039	-11.7 ± 0.23
17–17.25	5.1	120.1	0.717723	0.512047	-11.5 ± 0.28
17.5–17.75	5.2	113.9	0.718582	0.512046	-11.5 ± 0.22
18.25–18.5	5.4	118.0	0.718113	0.512043	-11.6 ± 0.22
19–19.25	5.6	110.3	0.717853	0.512054	-11.4 ± 0.22
19.75–20	5.8	111.1	0.717317	0.512066	-11.2 ± 0.24
21.25–21.5	6.2	118.1	0.716946	0.512061	-11.3 ± 0.17
22–22.25	6.4	131.6	0.716631	0.512071	-11.1 ± 0.38
22.75–23	6.5	133.8	0.716065	0.512071	-11.1 ± 0.21
24–24.25	6.8	138.0	0.715476	0.512076	-11.0 ± 0.26
24.5–24.75	7.0	142.0	0.715471	0.512079	-10.9 ± 0.22
26–26.25	7.3	141.9	0.714622	0.512092	-10.6 ± 0.22
27.5–27.75	7.7	135.0	0.714916	0.512001	-11.0 ± 0.26
28–28.25	7.8	126.9	0.714915	0.512069	-11.1 ± 0.22
28.5–28.75	7.9	127.5	0.715166	0.512084	-10.8 ± 0.27
29.25–29.5	8.1	138.5	0.714822	0.512074	-11.1 ± 0.21
30–30.25	8.3	123.1	0.716075	0.512067	-11.1 ± 0.35
30.75–31	8.6	120.8	0.716393	0.512066	-11.2 ± 0.22
32.25–32.5	9.0	122.8	0.716694	0.511989	-11.6 ± 0.22
33.5–33.75	9.3	119.0	0.716986	0.512044	-11.6 ± 0.31
34–34.25	9.4	114.4	0.717473	0.512049	-11.5 ± 0.22
34.5–34.75	9.6	117.9	0.718064	0.512044	-11.7 ± 0.17

[a] Errors (2σ) are always <0.00004, normalized to the NBS-SRM 987 value of $^{87}Sr/^{86}Sr = 0.705248$ (Thirlwall, 1991).
[b] Normalized to the JNdi value of $^{143}Nd/^{144}Nd = 0.512115$ (Tanaka et al., 2000).
[c] Highest errors of internal and external errors are reported.

4 Results

4.1 Sapropel geochemistry (TOC, Ba, Mn) in core CP10BC

Sedimentation rates are relatively high during S1 period and low for the more recent, arid interval (Figure 2). The low TOC content in the uppermost 5 ka reflects the overall low productivity and oxic conditions in the EMS (Figure 3a). In the lower part, the residual S1 is characterized by 1.2–1.7% TOC content, while the full extent of S1 is recognized by the elevated Ba/Al zone (Figure 3b). This difference is due to post-depositional oxidation that removed most of the TOC but not biogenic Ba from the upper-most S1 interval (De Lange et al., 1989; Van Santvoort et al., 1996). Biogenic Ba (mainly barite, refer to as "Ba") was corrected by the equation: $Ba = Ba_{blk} - [Al_{blk} \times (Ba/Al)_{det}]$, where Ba_{blk} and Al_{blk} are concentrations in bulk sediments, and $(Ba/Al)_{det}$ represents the average Ba/Al ratio of EMS detrital sediments (0.0033 g/g) (Rutten and De Lange, 2002). Due to its conservative behavior, Al is adopted as a

normalizing parameter to assess the relative enrichment/depletion of specific elements (Martinez-Ruiz et al., 2015; and references therein).

The two separated Mn-rich zones at ~7.3 and 5.8 ka correspond to the upper boundary of the residual and the initial S1, respectively (Figure 3c). It has been demonstrated that the lower Mn-peak is forming actively, whereas the upper one is related to reventilation of the water column during S1 termination (Van Santvoort et al., 1996; Reitz et al., 2006). Defined by the Ba/Al ratio reflecting initial TOC accumulation rates, and the upper Mn/Al peak signaling the conversion from anoxic to oxic conditions, the S1 formation ended at ~5.8 ka in core CP10BC (Figure 3). This is within the range of previous studies (~6.1 ± 0.5 ka) (Mercone et al., 2000; De Lange et al., 2008). Note that bulk Ba associated with MnO_x may be enhanced at the major Mn-peak, causing a seemingly younger S1-ending age according to the Ba/Al profile (see Reitz et al., 2006). Sapropel S1 is split into S1a and S1b at ~8.0 ka, based on the ends of increasing trends of TOC and Ba/Al, as well as of decreasing (increasing) trend of $^{87}Sr/^{86}Sr$ ($\varepsilon_{Nd(0)}$) (Figure 3 and 4). This timing is close to the well-known 8.2 ka event (Rohling and Pälike, 2005).

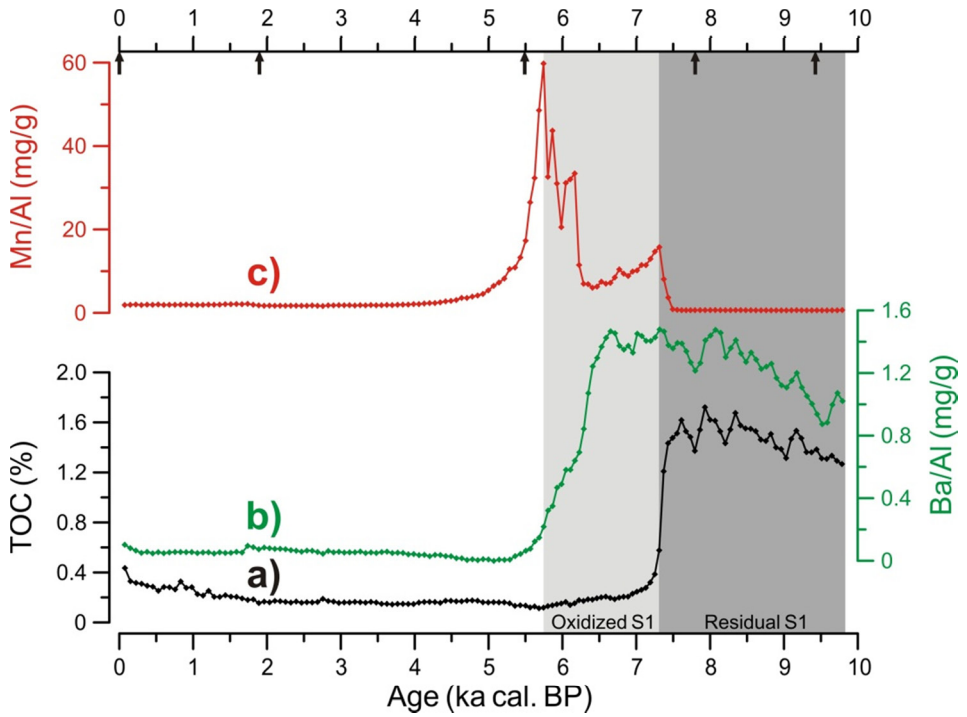

Figure 3 Sapropel S1 geochemistry of core CP10BC. a) TOC (total organic carbon). b) Ba/Al (biogenic Ba/bulk Al) (c.f. Section 4.1). c) Mn/Al. Age tie-points are indicated by arrows at upper axis. Dark and light shadings show the residual and oxidized parts of sapropel S1, respectively.

4.2 Detrital elements (Ti, Zr, K) in core CP10BC

There is a strong similarity between Ti/Al and Zr/Al profiles obtained for the bulk sediments, showing lower values in the S1 section and higher values in the upper part of the core, with a minimum at ~7.0–6.0 ka (Figure 4b,c). By contrast, K/Al is highest in the lower and upper parts, showing a rather broad minimum at ~5.0–4.0 ka (Figure 4d). In the plot of Ti/Al vs. K/Al (Figure 5a), the sapropel samples have lower Ti/Al ratios relative to the non-sapropel samples. The S1a samples report generally higher K/Al ratios, while the S1b samples show lowest Ti/Al values and a major decrease in K/Al.

4.3 Sr contents, and Sr-, Nd- isotopes of detrital sediments in cores CP10BC and SL114

After removing the carbonate, the remaining detrital Sr content in core CP10BC is relatively low (~110–187 ppm) (Table 2; Figure 4e). The $^{87}Sr/^{86}Sr$ ratio of the detrital fractions has a large variation (0.7146–0.7199), whereas the $\varepsilon_{Nd(0)}$ values vary within a narrow range (-12.0 to -10.8) (Table 2; Figure 4f,g). A strong negative correlation between detrital $^{87}Sr/^{86}Sr$ and $\varepsilon_{Nd(0)}$ values is displayed (Figure 4 and 6). The Sr content expressed as 1000/Sr also co-varies with (R^2 = 0.30) (Figure 4 and 7). The $^{87}Sr/^{86}Sr$ ratios in core SL114 are similar to those in core CP10BC, whereas during S1 the $\varepsilon_{Nd(0)}$ values of SL114 are higher than for CP10BC (Table 3; Figure 8).

Table 3 Sr and Nd isotopic compositions of detrital sediments in core SL114 [a]

Depth (cm)	Sample [b]	$^{87}Sr/^{86}Sr$	$^{143}Nd/^{144}Nd$	$\varepsilon_{Nd(0)}$
0.25	non-S1	0.718895	0.512019	-12.1
15.55	non-S1	0.718905	0.512013	-12.2
24.05	S1	0.716694	0.512111	-10.3
28.05	S1	0.715441	0.512123	-10.1
32.05	S1	0.715743	0.512113	-10.2
34.05	S1	0.716405	0.512083	-10.8
39.05	non-S1	0.716243	0.512072	-11.0
49.2	non-S1	0.718041	0.512074	-11.0

[a] Uncertainty (2σ) of $^{87}Sr/^{86}Sr$ and $^{143}Nd/^{144}Nd$ are 0.000015 and 0.000010, respectively. See Freydier et al. (2001) for analytical details.
[b] Identification of S1 is based on Ba/Al profile.

The interval of ~3.0–1.5 ka is deviating in geochemical compositions (e.g. Ti/Al, K/Al, Sr contents, and $^{87}Sr/^{86}Sr$) (Figure 4), which is related to dispersed tephra occurrence as identified in several samples. As tephra is not our focus here, we will disregard this interval hereafter.

5 Discussion

Characterization of detrital supplies and their attribution to different sources are prerequisites for hydroclimate reconstruction. Previous studies on modern EMS sediments have shown a clear geochemical west–east gradient because of mixing between distinct endmembers: “young and mafic” Nile sediment is diluted towards the west by “old and felsic” Saharan dust, while riverine contributions derived from basalts and ultramafic rocks over the NBEM have also been proposed (e.g. Venkatarathnam and Ryan, 1971; Krom et al., 1999a; Weldeab et al., 2002a; Klaver et al., 2015). It has been suggested that this recent provenance pattern was also present in the Quaternary (Krom et al., 1999b; Freydier et al., 2001; Weldeab et al., 2002b; Revel et al., 2010; 2015), Pliocene (Wehausen and Brumsack, 1999; 2000; Nijenhuis and De Lange, 2000), and even pre-Pliocene (Klaver et al., 2015) sediments. The reported sources have well-defined Sr-Nd isotopic signatures (Table 4; and references therein), but the underlying datasets do not adequately cover the Ionian Sea, especially the key margin areas (see Ayache et al., 2016).

Here, we combine detrital Sr and Nd isotopic compositions with high-resolution elemental ratios (Ti/Al, Zr/Al, and K/Al) from bulk sediments to unravel the provenance of sediments in the central Mediterranean during the Holocene. We first propose a three-endmember mixing hypothesis, which will be examined by a west–east comparison throughout the EMS, and finally reconstruct the changes in different detrital contributions with implications for hydroclimate over the circum-Mediterranean.

5.1 A three-endmember mixing system for detrital sediments in core CP10BC

In terms of Sr-Nd isotopic and elemental compositions, a simple mixing model between Nile sediment and Saharan dust has been used to describe the variability of detrital supplies to the Levantine Basin for the present-day (Krom et al., 1999a; Weldeab et al., 2002a) and for the last 100 ka (Krom et al., 1999b; Freydier et al., 2001; Revel et al., 2010; 2015). Using Sr-Nd isotope data, the late-Quaternary detrital sediments deposited in the Aegean Sea have also been reported to be a mixture of Aegean/Nile river-borne materials and Saharan dust (Weldeab et al., 2002b; Ehrmann et al., 2007b).

For the central Mediterranean, the system seems to be more complex. Based on the surface distribution of Sr-Nd isotopes, not only the Saharan dust and the NBEM riverine supplies have been reported, but also a potential influence from the Libyan margin has been inferred for the present-day Ionian Sea (Weldeab et al., 2002a). Moreover, a local riverine source to the Ionian Sea has been suggested for the S1 time, but with unspecified origin and geochemical signature (Fontugne et al., 1994; Krom et al., 1999b; Freydier et al., 2001; Scrivner et al., 2004).

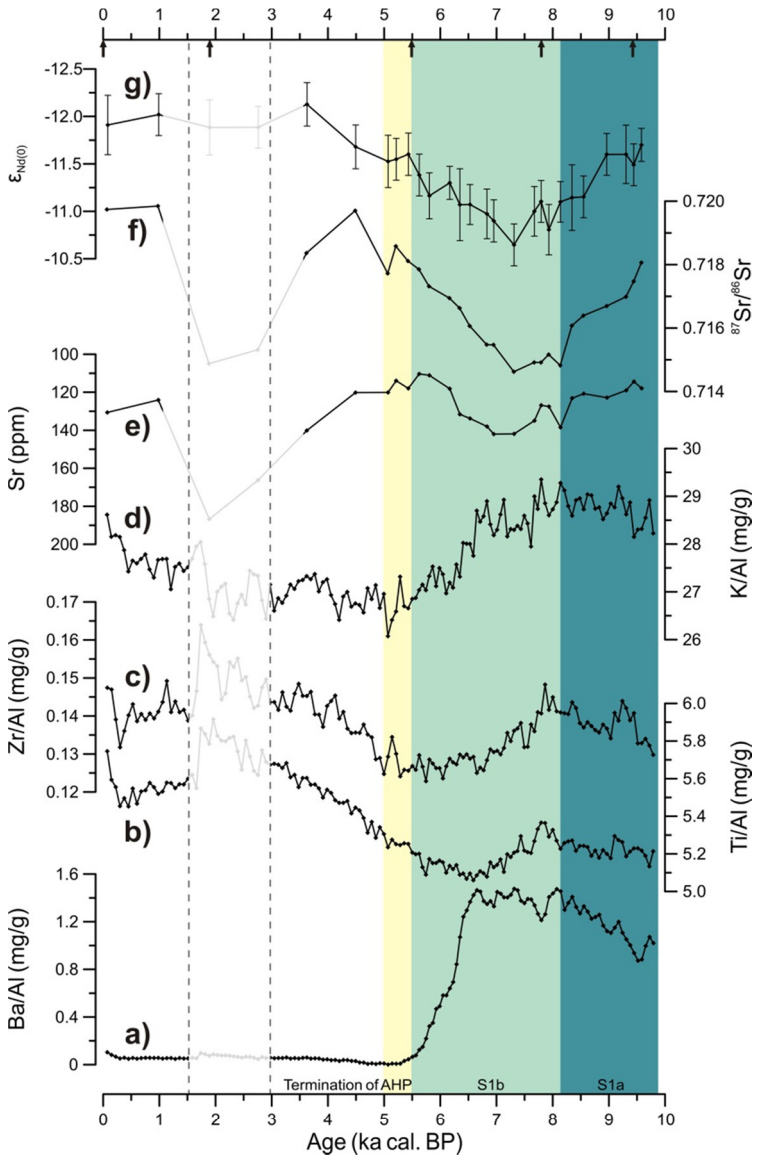

Figure 4 Geochemical records for core CP10BC over the past 9.8 ka. a) Ba/Al (biogenic Ba/bulk Al). b) Ti/Al. c) Zr/Al. d) K/Al. e) Sr content. f) $^{87}Sr/^{86}Sr$. g) $\varepsilon_{Nd(0)}$. Data for Sr, $^{87}Sr/^{86}Sr$, and $\varepsilon_{Nd(0)}$ are determined on detrital (decarbonated) sediments. Age tie-points are indicated by arrows at upper axis. Note descending axis of Sr content and $\varepsilon_{Nd(0)}$. Dashed lines indicate the tephra-related interval mentioned in Section 4.3, to be disregarded in this contribution. Sapropel S1a, S1b, and termination of AHP (African Humid Period) are specified.

For our data, it is clear that a third component is required to explain the Holocene deposition in the Ionian Sea (Figure 5–7). With reference to the published isotopic

and elemental data over the circum-Mediterranean (Table 4), we will show that for the past 9.8 ka the Ionian sediment composition can be represented by a three-endmember mixture of detrital supplies derived from Saharan Dust, Aegean/Nile, and Libyan Soil.

5.1.1 Definition of the two traditional endmembers

Dust derived from North Africa is a significant component to the EMS. Our radiogenic isotope results yield a “Saharan Dust” endmember, with values that are typical for central Sahara-derived dust/aerosols collected over the EMS (see reviews by Grousset and Biscaye, 2005; Scheuvens et al., 2013) (Table 4; Figure 6 and 7). Consistent low Ti/Al and Zr/Al values during the humid climate, sapropel S1 interval, and high values for the arid periods, are in agreement with a dominant Saharan dust input (e.g. Wehausen and Brumsack, 1999; 2000; Nijenhuis and De Lange, 2000; Lourens et al., 2001). Titanium and Zr mainly reside in heavy minerals and can be transported with coarse quartz in wind-blown Saharan materials (see Scheuvens et al., 2013).

At present, riverine supplies to the central Mediterranean are low compared to eolian fluxes (Guerzoni et al., 1997; Rutten et al., 2000). Using Sr and Nd isotopes, it has been shown that minor amounts of Nile sediments—if any—may be deposited in the areas west of Crete (Krom et al., 1999a; Weldeab et al., 2002a) (c.f. Section 2). At sapropel times, the enhanced Nile sediment load has been geographically limited. Comparisons across the Nile delta show that higher sedimentation rates during sapropel S1 occurred only for cores taken close to the delta (Hennekam et al., 2015), indicating that the offshore spread of Nile particulate matter was not larger. Based on the Nd isotopes and concentrations on both leachable and residual fractions from sapropel S1 sediments, the Nile influence can be observed as farthest west as the south of Crete (Freydier et al., 2001). Moreover, increased precipitation is thought to have generated denser vegetation causing reduced physical erosion in the Ethiopian highlands (Blue Nile source), which yields most of the Nile particulates (Krom et al., 1999b; Weldeab et al., 2002b). This is supported by the systematically lower Ti/Al ratios observed in the Levantine Basin during sapropel times (e.g. Krom et al., 1999b; Wehausen and Brumsack, 1999; 2000; Box et al., 2011; Hennekam et al., 2014). The higher Ti/Al in sapropels for the western Nile-delta (Revel et al., 2010; see also Hennekam et al., 2015) has been interpreted by Box et al. (2011) as overbank flood deposits from turbidity flows, which mainly reflect the magnitude of water flow. Box et al. (2011) also suggested that during S1 time the Nile sediment reaching distal locations within the Levantine Basin, was mainly from the White Nile, since the Sudd swamps no longer acted as a giant sediment trap (Williams et al., 2000). However, a simple dichotomy between riverine inputs from the Blue Nile and Atbara and Saharan dust fluxes has been recently shown by the $^{87}Sr/^{86}Sr$ and $\varepsilon_{Nd(0)}$

ratios of two cores from the Nile upper continental slope (Revel et al., 2015). This confirms that the sediment contribution from the White Nile has been minor for the last 25 ka (Revel et al., 2015).

In any case, the White Nile should not have constituted a considerable source for sapropel S1 sediment of core CP10BC in the distant southwestern Ionian, as explicitly discounted by the diagram of $^{87}Sr/^{86}Sr$ vs. 1000/Sr (Figure 7). Particularly, the surface-water pathway (Figure 1) strongly argues against contributions from the White Nile source. Considering the position of core CP10BC along the MAW pathway, rivers from the NBEM should be more important than the Nile as potential detrital source during humid sapropel periods (Figure 1).

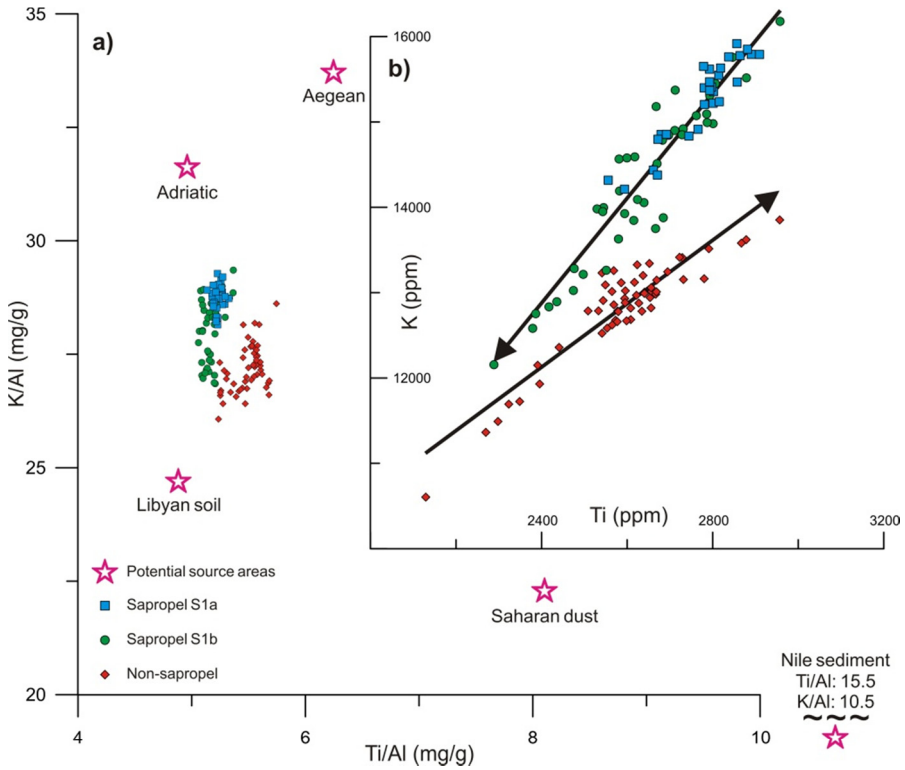

Figure 5 Data of Ti and K in core CP10BC are distinguished between three hydroclimate conditions of sediment deposition, indicating a ternary mixing system presented in elemental compositions. a) Plot of Ti/Al vs. K/Al. Potential source areas are shown, with Libyan Soil deduced from the evolution of CP10BC data, suggesting a minor Nile influence. b) Plot of Ti vs. K concentrations with arrows indisputably indicate the changes in sediment composition over the Holocene. The tephra-related data is excluded. Data of Saharan dust and Nile sediment after Krom et al. (1999a; 1999b); surface sediment data of Aegean (Karageorgis et al., 1998) and Adriatic (Dolenec et al., 1999) seas reported as average values.

Here, we refer to the endmember with lowest $^{87}Sr/^{86}Sr$ and highest $\varepsilon_{Nd(0)}$ ratios as "Aegean/Nile" in core CP10BC (Table 4; Figure 6 and 7). Its Sr and Nd isotopic compositions and Sr contents are taken from average values of Balkan and Aegean basalt and main Nile, representing river-borne particulates from the NBEM- and/or Nile (Table 4; Figure 6 and 7). This is because riverine inputs from Nile and Aegean regions cannot be differentiated due to the similar Sr-Nd isotopic signatures (Weldeab et al., 2002a; 2002b). In addition, this signature is quite similar for the Aegean and most other NBEM areas (Klaver et al., 2015).

The elemental composition of sediments in core CP10BC can, nevertheless, shed light on the relative contributions. The pattern of lower (higher) Ti/Al values in sapropel S1 (non-sapropel) and the similarity between Ti/Al and Zr/Al profiles in core CP10BC indicate that most of the Ti/Al signal is derived from Saharan dust, rather than from Nile sediment (Figure 4). From the plot of Ti/Al vs. K/Al (Figure 5a) it is also clear that only the NBEM (i.e. Aegean and Adriatic) riverine inputs can account for the increased K/Al ratio during sapropel S1 time in the Ionian Sea; an increased Nile sediment contribution can be rule out as this is characterized by very low K/Al. This means that during sapropel S1, the NBEM riverine input is a major component of the Aegean/Nile endmember, whereas the Nile contribution is minor.

The enhanced K/Al associated with NBEM riverine input for sapropel layers has been report to correspond with a higher illite content (see Martinez-Ruiz et al., 2015). The clay mineral assemblage is known to be related to provenance and hydrological environmental conditions (e.g. Chamley, 1989; Wu et al., 2012; Bout-Roumazeilles et al., 2013). A north–south contrast in hydroclimate conditions has been proposed for the Holocene central Mediterranean (see review by Magny et al., 2013). The K/Al profile of core CP10BC displays good correspondence with the precipitation reconstructions north of 40°N (Figure 1 and 9): speleothem $\delta^{18}O$ data of Corchia Cave reflecting regional precipitation (Zanchetta et al., 2007) and pollen-based estimates of winter precipitation in Lake Accesa (Peyron et al., 2011). On the other hand, the areas south of 40°N (e.g. Lake Pergusa in Sicily) are characterized by persistently humid winters and summers until ~5.0 ka (see Magny et al., 2013), coinciding with the K/Al minima in core CP10BC. Taken together, the K/Al in core CP10BC is considered to be related to winter precipitation and associated riverine inputs from the NBEM during S1 deposition.

5.1.2 Evidence for the Libyan endmember

In the diagnostic plot of $^{87}Sr/^{86}Sr$ vs. $\varepsilon_{Nd(0)}$ for the central Mediterranean sediments and in particular those of core CP10BC, a third component with a Sr-Nd isotopic composition different from the traditional provenance fields is expected (Figure 6). A similar observation can be made on the basis of the $^{87}Sr/^{86}Sr$–1000/Sr diagram; that

is, the data cannot be described by a simple two-endmember mixing model (Figure 7).

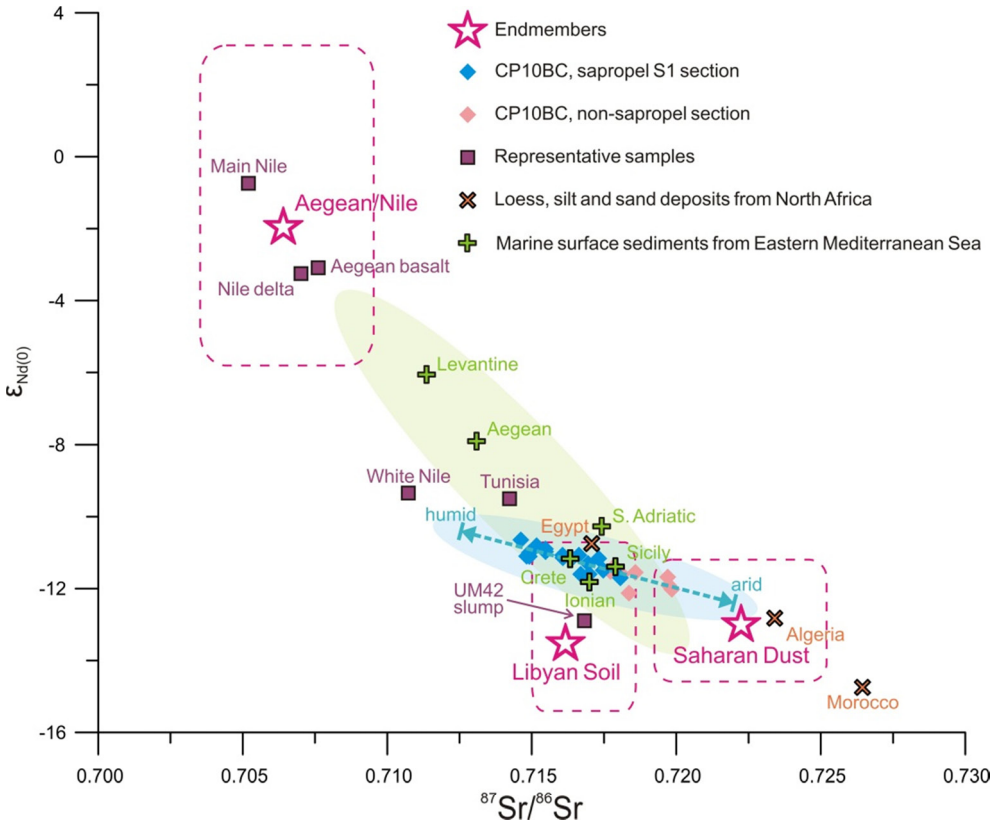

Figure 6(*) $^{87}Sr/^{86}Sr$ vs. $\varepsilon_{Nd(0)}$ isotopic compositions for core CP10BC detrital sediments and for potential source areas, with endmembers (star) and their ranges (dashed rectangle) shown. A distinct trend in CP10BC data (blue ellipse-shading) is clearly different from the domain of the eastern Mediterranean basins (green ellipse-shading), indicating the existence of Libyan Soil endmember. The signatures for Aegean and Nile rivers are similar and cannot be differentiated here (c.f. Section 5.1.1). For data sources refer to Table 3 and 4.

As shown in Figure 6, the Sr and Nd isotopic values of detrital sediments within core CP10BC display a distinctive trend. The non-sapropel samples would still fit along the two-endmember mixing trend between Saharan Dust and Aegean/Nile. However, the samples deposited during the humid S1-interval clearly indicate an additional source with a relatively low $^{87}Sr/^{86}Sr$ and $\varepsilon_{Nd(0)}$. The Sr-Nd isotopic array also reveals that enhanced contributions from this source and that of Aegean/Nile occurred at the same time, relative to a reduced supply of Saharan Dust, further suggesting the riverine-origin for the inferred source. Comparing the Sr-Nd isotopic ratios for all

potential source areas (Table 4; Figure 1 and 6), this endmember can only be attributed to “Libyan Soil” (Grousset and Biscaye, 2005; Revel et al., 2010).

A ternary mixing system is also present for the elemental compositions of sediments in core CP10BC. The data of Ti and K suggest three different hydroclimate conditions of sediment transport and deposition, and this compositional variability can only be explained by mixing between at least three endmembers (Figure 5). As discussed above, Saharan dust and NBEM riverine supplies are amongst the endmembers, with negligible Nile influence (c.f. Section 5.1.1). As indicated by decreasing Ti/Al and K/Al ratios, the evolution trend of CP10BC data from S1a to S1b suggests the existence of a third endmember (Figure 4 and 5). Despite the lack of adequate elemental data for the Libyan hinterland, this observation and the concurrent higher sedimentation rate (Figure 2) is interpreted here to indicate an enhanced contribution of Libyan Soil material during the S1b interval. This contribution is characterized by relatively low Ti/Al and K/Al ratios. Note that in general a spurious correlation may be discerned when using a plot of normalized elements (see Van der Weijden, 2002). In core CP10BC, however, the evolution trend in the indisputable Ti vs. K plot (Figure 5b) confirms and even better visualizes the pattern observed in the plot of Ti/Al vs. K/Al (Figure 5a), which justifies the evaluation of potential source areas made above.

Although the detrital Sr isotopic composition could be influenced by grain-sized sorting and possible barite-Sr, plotting of $^{87}Sr/^{86}Sr$ ratios against 1000/Sr concentrations has been widely used for provenance discrimination, especially in the circum-Mediterranean area (e.g. Grousset et al., 1992; 1998; Krom et al., 1999a; 1999b; Grousset and Biscaye, 2005; Box et al., 2011). Indeed, the patterns of trend and timing presented in the $^{87}Sr/^{86}Sr$–1000/Sr diagram (Figure 7) do corroborate this interpretation, showing the highest contribution of Libyan Soil between ~6.3 and 5.5 ka. It seems that during the onset (~9.8 to 8.3 ka) and ending (~6.3 to 5.5 ka) of S1, the relative contribution from Libyan rivers was more pronounced, whereas during mid-S1 it is rather the NBEM contribution that dominated (Figure 7). Further work is required to verify and quantify this observation, but a Libyan riverine supply during S1b must have been considerable. This increased detrital supply could be related to the simultaneously intensified dynamics of river/wadi systems draining Tunisia and western Libya (Zielhofer et al., 2008). An enhanced detrital input of Sr-rich aragonite from the Libyan coastal areas during S1 has also been suggested (Reitz and De Lange, 2006).

Our observations are consistent with previous reconstructions of North-African monsoon precipitation. Stratigraphic surveys and pollen analysis on palustrine and eolian sediments for the Jefara Plain suggest a wet Holocene until ~5.0 ka,

interrupted by two arid spells dated ~8.2 and 5.4 ka, with the most humid conditions occurring between ~6.8 and 5.5 ka (Giraudi et al., 2013) (Figure 1 and 9h). Archaeological surveys also indicate the same pattern. Persistently denser population in Libya between ~7.5 and 6.0 ka and densest population around 6.0 ka have been shown (Manning and Timpson, 2014), coherent with the Libyan hydroclimate evolution and the changes in Libyan Soil observed in core CP10BC. The steady humid phase (~6.7–5.4 ka) in northwestern Libya is also identified through the presence of large ponds and marshes (Barich, 2014).

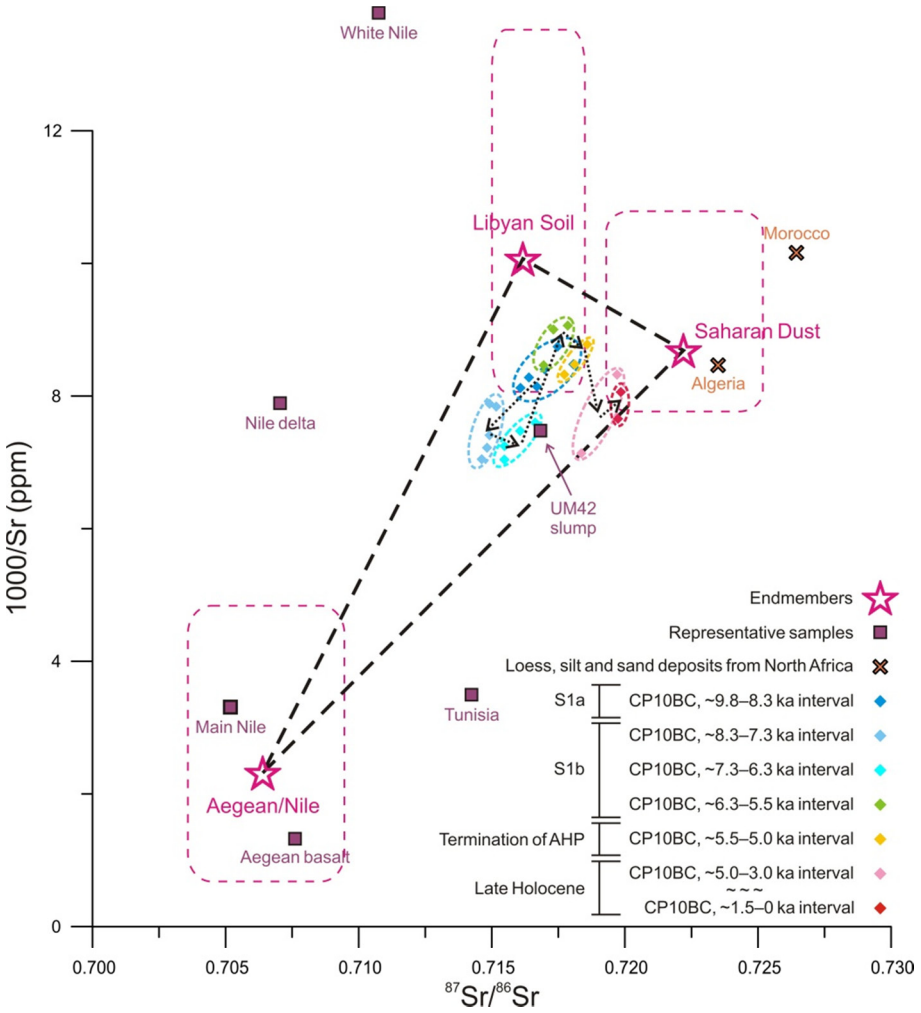

Figure 7(*) Evolution of different detrital contributions for core CP10BC on the basis of $^{87}Sr/^{86}Sr$ vs. 1000/Sr diagram. Endmembers (star) and their ranges (dashed rectangle), and potential source areas are shown. The UM42 slump is in line with enhanced fluvial activity in Tunisia during ~7.3–6.3 ka (c.f. Section 5.3). The tephra-related interval is not shown. For data sources see Table 3 and 4.

In conclusion, our results evidently indicate important riverine supplies from Libya to the Ionian Sea, accompanied by a simultaneous increase in the NBEM contribution. This riverine detrital supply is characterized by relatively low $^{87}Sr/^{86}Sr$ (~0.716) and $\varepsilon_{Nd(0)}$ (-13.5) values, as well as low Ti/Al (< 0.05) and K/Al (< 0.25) ratios. The riverine contribution from the Libyan margin is controlled by North-African monsoon precipitation. It was most enhanced during sapropel S1b in particular, with the highest contribution between ~6.3 and 5.5 ka.

5.2 A west–east comparison throughout the eastern Mediterranean Sea

At sapropel times, enhanced African monsoon precipitation can activate fossil river/wadi systems along the wider North-African margin, which could deliver substantial amounts of freshwater and detrital material to the EMS. This has been proposed previously for the sapropel S5 (Rohling et al. 2002; c.f. Section 1). We demonstrate that such scenario has occurred also for sapropel S1. The fossil river/wadi channel network in eastern Libya towards the Gulf of Sirte has been considered as an important detrital source during deposition of sapropel S5 (Rohling et al. 2002; 2004; Osborne et al., 2008; 2010) (Figure 1). The satellite imagery of its major paleo-river channels lends support to the idea of a humid corridor (Paillou et al., 2009, 2012). Yet, this consideration on the origin of the riverine supply may not be fully adequate due to the limited spatial coverage of the studied sites. In other words, none of the reported sites can distinguish between the supplies from western and eastern Libya. In fact, with three major paleo-river systems identified, Coulthard et al. (2013) have revealed that it is the most-western paleo-river system flowing over western Libya and Tunisia that represents the most likely route for human migration across the Sahara (Figure 1).

To evaluate the potential distribution of the Libyan detrital supply and to locate potential riverine sources, we compare the Sr and Nd isotope data of core CP10BC with those of four cores taken along a west–east transect throughout the EMS.

5.2.1 Distribution of the Libyan detrital supply

Cores UM42, SL114, BC3, and BC 19 were collected in the western, eastern Ionian Sea, the south of Crete, and the Levantine Basin, respectively (Freydier et al., 2001) (Figure 1). The Sr and Nd isotope data for these cores display distinct trends (Figure 8). For the recent sediments, the values of $^{87}Sr/^{86}Sr$ and $\varepsilon_{Nd(0)}$ in cores UM42, SL114, and BC3 are similar to those of core CP10BC, indicating a similar predominant Saharan dust source. It must be noted that a slight west–east decrease in dust $^{87}Sr/^{86}Sr$ ratio may occur (see Krom et al., 1999a).

It has been suggested that increased riverine flux and decreased eolian flux must have occurred together during sapropel deposition (e.g. Krom et al., 1999b;

Wehausen and Brumsack, 1999; 2000; Freydier et al., 2001). Indeed, the Sr-Nd isotopic arrays all show that during S1 time, contributions from Aegean/Nile and Libyan Soil increased, relative to a concomitantly reduced Saharan Dust supply (Figure 8). Specifically, cores CP10BC and UM42 point to a Libyan Soil dominated contribution, whereas SL114 shows a higher contribution from an Aegean/Nile source. This is in agreement with the location of core SL114, being more distant from the Libyan margin and more proximal to the NBEM area. Moreover, the overall higher $^{87}Sr/^{86}Sr$ -$\varepsilon_{Nd(0)}$ signatures for core SL114 compared to eastern sites BC3 and BC19 indicates a NBEM source rather than the Nile for the Aegean/Nile endmember (Figure 8c). In the Levantine Basin, the variability of Sr-Nd isotopic compositions has been attributed to a binary mixing between Saharan dust and Nile sediment (e.g. Krom et al., 1999b; Revel et al., 2010; 2015). This can be clearly seen in core BC19, the easternmost site. This confirms the predominant Aegean/Nile riverine inputs while the potential Libyan contribution seems to have nearly disappeared.

The overall trend towards the humid-most sapropel phase, indicates a decreasing Libyan Soil contribution from southern to northern Ionian (i.e. from CP10BC towards UM42, SL114), and from the Ionian eastward to Levantine (i.e. from CP10BC towards BC3 and BC19) (Figure 8). The decreasing contribution of Libyan Soil may be due to a decreasing flux, and/or relatively increasing fluxes from other provenances (i.e. NBEM and Nile).

The systematic west–east increase in the slope of Sr-Nd isotopic arrays within each of these five cores throughout the EMS is estimated to reflect a higher contribution from Libya in the western section and a more pronounced Nile contribution in the eastern part (Figure 8b). If this holds true, this feature points to the eastward flowing of suspended Libyan riverine material (presumably with MAW) and/or the westward transport of Nile-derived particulates (presumably with LIW).

5.2.2 Origin of the Libyan detrital supply

The Libyan detrital supply could originate from 1) eastern Libya as suggested for sapropel S5 (Rohling et al., 2002; Osborne et al., 2008), redistributed by the anticyclonic surface-currents on the Libyan shelf, or 2) from the west, transported by the MAW from the broad Libyan-Tunisian shelf (Figure 1). The lower contribution of Libyan Soil for core BC3 relative to CP10BC suggests that the major source is western Libya rather than eastern Libya; but this could also be related to a more prominent Aegean/Nile influence for BC3, and depends on the transport pathways (Figure 1 and 8).

Table 4 Published Sr contents, $^{87}Sr/^{86}Sr$ ratios, and $\varepsilon_{Nd(0)}$ values of samples from the circum-Mediterranean

Sample [a]	Sample type	Sample number	Sr (ppm)		$^{87}Sr/^{86}Sr$		$\varepsilon_{Nd(0)}$		Source [b]
			Average	Range	Average	Range	Average	Range	
Saharan Dust [c]	Loess, silt and sand deposits	9	115.1	92.5–128.6	0.722243	0.719251–0.725225	-13.0	-14.6–-11.2	1
Aegean/Nile [d]			528.5	206.0–1426.0	0.706394	0.703527–0.709529	-1.9	-5.8–3.1	
Aegean basalt	Tertiary basalt rocks	33	754.7	206.0–1426.0	0.707610	0.703527–0.709529	-3.1	-5.8–3.1	2
Main Nile	Levee mud	10	302.2	269.0–331.0	0.705177	0.704690–0.705660	-0.7	-2.9–1.7	3
White Nile [e]	Bank mud	3	72.5		0.710750	0.710450–0.710970	-9.4	-10.4–-8.6	3, 4
Nile delta	Delta sediments	3	126.7	116.6–140.3	0.707043	0.706470–0.707530	-3.3		after 5
UM42 slump [f]	Libyan-Tunisian shelf slump	1	133.7		0.716830		-12.9		6
Levantine	Marine surface sediments	17			0.711363	0.707531–0.714959	-6.1	-10.3–-1.0	5, 6, 7, 8
Aegean	Marine surface sediments	8			0.713090	0.710380–0.713831	-7.9	-8.8–-5.8	5, 8, 9
Crete	Marine surface sediments	5			0.716329	0.715968–0.716950	-11.2	-11.5–-10.9	5
Ionian	Marine surface sediments	7			0.716998	0.715924–0.718895	-11.8	-12.5–-11.0	5, 8
S. Adriatic	Marine surface sediments	4			0.717427	0.716887–0.718342	-10.3	-11.8–-9.6	5, 8
Sicily	Marine surface sediments	3			0.717906	0.715700–0.720086	-11.4	-12.1–-10.9	5
Libyan Soil [g]	Loess, silt and sand deposits	10	99.3	73.8–124.1	0.716165	0.715000–0.718597	-13.5	-15.4–-10.7	1, 7
Tunisia	Loess, silt and sand deposits	1	286.0		0.714239		-9.5		10
Egypt	Loess, silt and sand deposits	2			0.717072	0.715874–0.718270	-10.8	-11.0–-10.5	1

Algeria	Loess, silt and sand deposits	3	118.1	21.1–168.6	0.723500	0.721000–0.726000	-12.8	-12.1–-13.5	after 11
Morocco	Loess, silt and sand deposits	4	98.4	87.2–111.6	0.726441	0.716593–0.734041	-14.8	-17.1–-11.8	12

[a] All samples are decarbonated, except Aegean basalt, main Nile and White Nile, of which carbonate content <2%; endmembers are in bold.
[b] 1= Grousset and Biscaye (2005), 2= Güleç (1991), 3= Padoan et al. (2011), 4= Box et al. (2011),
5= Weldeab et al. (2002a), 6= Freydier et al. (2001), 7= Revel et al. (2010), 8= Tachikawa et al. (2004), 9= Ehrmann et al. (2007b), 10= Grousset et al. (1992), 11= Scheuvens et al. (2013), 12= Grousset et al. (1998).
[c] Sr is taken from modern Saharan aerosols collected in Corsica (~42°N, 9°E).
[d] Average of Aegean basalt and Main Nile.
[e] $^{87}Sr/^{86}Sr$ and $\varepsilon_{Nd(0)}$ from 3, while Sr after 4.
[f] Identified by the inversion of depth–AMS ^{14}C ages.
[g] Sr from 7 alone, while $^{87}Sr/^{86}Sr$ and $\varepsilon_{Nd(0)}$ from 1 and 7. Only the plotted data in 6 are used.

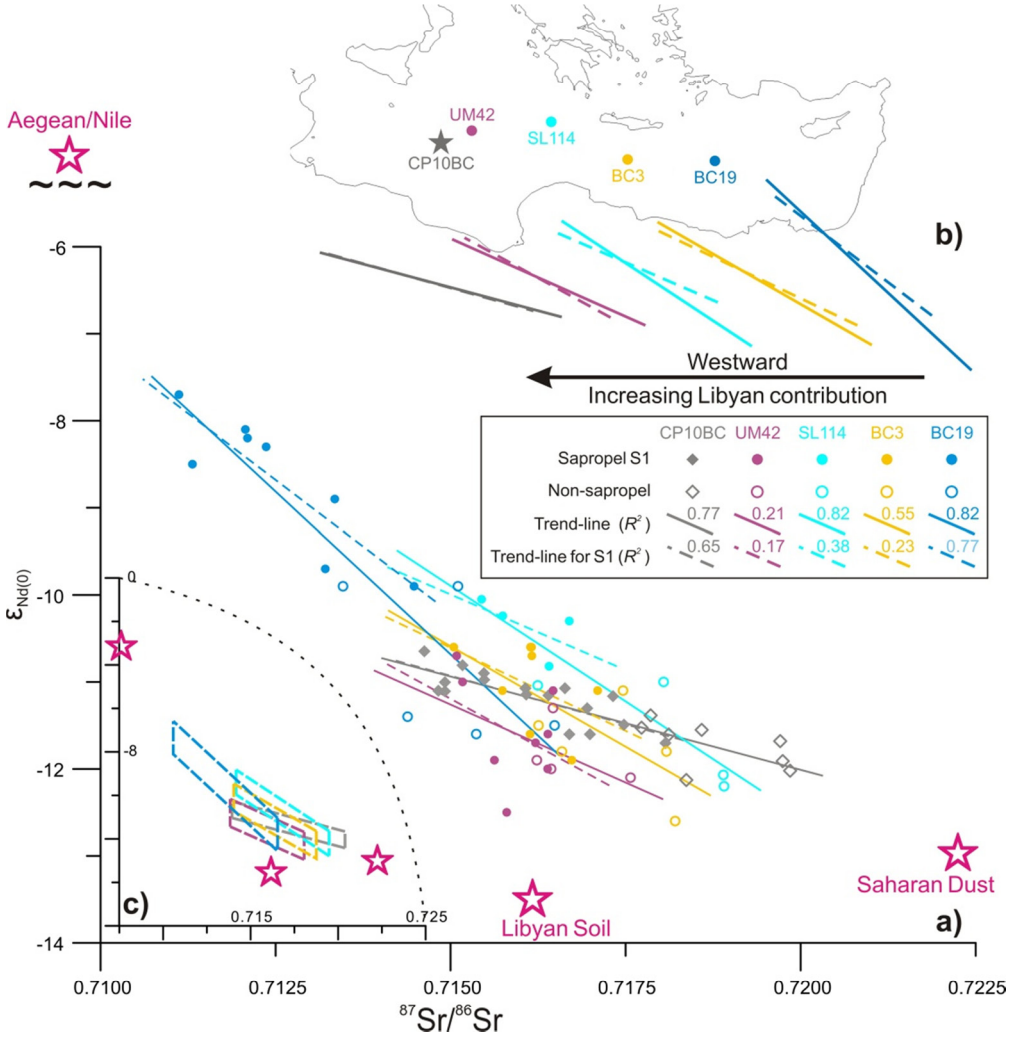

Figure 8(*) Comparisons of $^{87}Sr/^{86}Sr$ vs. $\varepsilon_{Nd(0)}$ isotopic compositions between core CP10BC and four cores UM42, BC3, BC19 (Freydier et al., 2001), and SL114, taken along a west–east transect throughout the eastern Mediterranean Sea for the Holocene. The data are differentiated between S1-samples (solid symbols) and nonsapropel-samples (open symbols). The trend-lines are specified for all-samples (solid lines) and for S1-samples alone (dashed lines). The trend-lines from a) are displayed in b), suggesting a westward increasing Libyan Soil contribution. c) Dashed parallelograms profile the data range for each core.

Comparison between cores CP10BC and UM42 can give more precise constraints. The Sr-Nd isotope data of core UM42 are generally closer to the Libyan Soil endmember (Figure 8), suggesting that the Libyan detrital supply has affected core UM42 more than others. In contrast to the other four cores, the UM42 data,

especially for S1-samples, including an identified slump, are characterized by a scattered distribution, implying a more dynamic depositional condition (Table 4; Figure 6 and 8). Moreover, core UM42 has a flatter $^{87}Sr/^{86}Sr–\varepsilon_{Nd(0)}$ trend-line for all-samples than for S1-samples alone; this is different from the pattern in the other cores, having trend-lines that are flatter for S1-samples than for all-samples (Figure 8b). Taken together, it seems that such detrital supply may not only be related to direct riverine sources but could as well be derived from shelf deposits. With similar water-depths (1501 vs. 1375 m for CP10BC and UM42 respectively), and given the locations of these two cores relative to the potential pathways (i.e. anticyclonic currents vs. MAW) (Figure 1), we suggest that the Libyan detrital supply is mainly from the west, including riverine inputs and shelf-derived fluxes from the Libyan-Tunisian margin.

This concept is consistent with the Sr-Nd isotopic signature of Tunisia (Figure 6), and supported by several lines of evidence. 1) Paleohydrological and hydraulic modeling have emphasized the paleo-river system (Irharhar) draining western Libya and Tunisia as a key humid corridor (Coulthard et al., 2013). 2) Based on >3000 calibrated ^{14}C dates from >1000 archaeological sites over North Africa, Manning and Timpson (2014) revealed a denser population and more frequent migration during the AHP in western than in eastern Libya, concordant with enhanced river-lake systems. 3) A hydroclimate reconstruction of northwestern Libya (Giraudi et al., 2013) appears to be consistent with the changes in the Libyan detrital supply revealed by the $^{87}Sr/^{86}Sr–1000/Sr$ diagram (Figure 7 and 9; c.f. Section 5.3). Nevertheless, in view of a potentially different eastern-Mediterranean circulation system during sapropel S1, an (additional) east-Libyan source area cannot be fully excluded.

5.3 Temporal changes in different detrital contributions in core CP10BC

Changes in different detrital contributions for core CP10BC associated with hydroclimate conditions can be discerned if detailed information is combined. Overall, the $^{87}Sr/^{86}Sr$ ($\varepsilon_{Nd(0)}$) and K/Ti profiles exhibit a close correspondence with lake records over North Africa (10–28°N) (Lézine et al., 2011), indicating that the North-African hydroclimate must have dominated the detrital supplies to the central Mediterranean (Figure 9a,g). During S1a, riverine inputs from the northern and southern borderlands both increased, as reflected by the decreasing $^{87}Sr/^{86}Sr$ and high K/Ti, corresponding with the North-African lake records and NBEM precipitation proxies, respectively (Figure 9c,d,f).

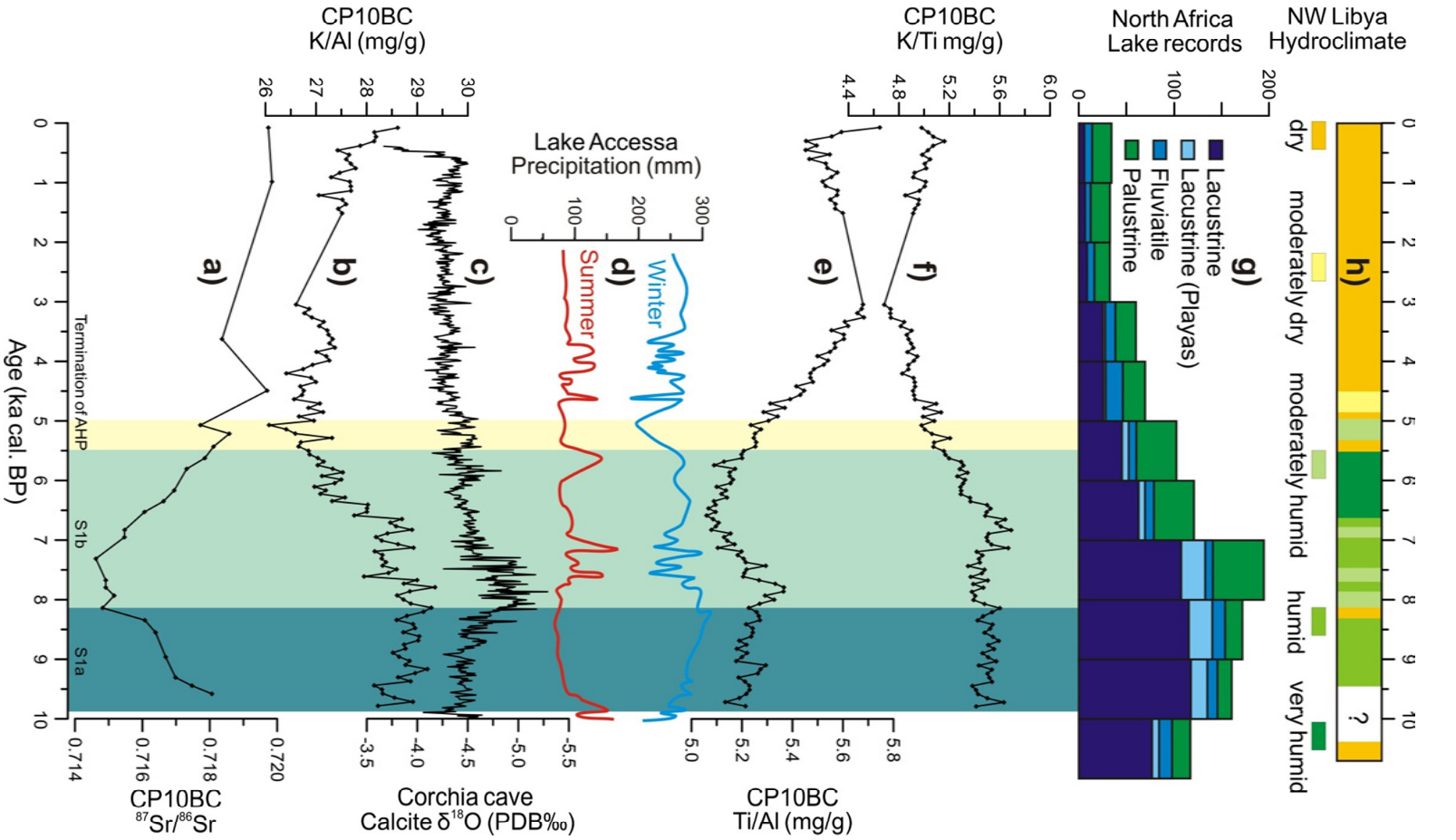

Figure 9 Comparisons of proxy records over the circum-Mediterranean. a) $^{87}Sr/^{86}Sr$ in core CP10BC. b) K/Al in core CP10BC. c) Speleothem $\delta^{18}O$ data of Corchia Cave (Zanchetta et al., 2007). d) Pollen-based estimations of seasonal precipitation for Lake Accesa (Peyron et al., 2011). e) Ti/Al in core CP10BC. f) K/Ti in core CP10BC. g) North-African (20–28°N) hydroclimate reconstruction according to lake records (Lézine et al., 2011). h) Hydroclimate evolution of Jefara Plain in northwestern Libya (Giraudi et al., 2013). The data of the deviating interval (~3.0–1.5 ka) are removed for core CP10BC. Sapropel S1a, S1b, and termination of AHP (African Humid Period) are indicated.

Between ~8.3 and 7.3 ka the most humid conditions occurred in the central Mediterranean (Figure 9), as indicated by various hydroclimate proxy records (e.g. Bar-Matthews et al., 2000; Zanchetta et al., 2007; Peyron et al., 2011; Magny et al., 2013). This can be deduced from the lowest $^{87}Sr/^{86}Sr$ and persistent high K/Ti, and from the $^{87}Sr/^{86}Sr$–1000/Sr diagram that indicates increased riverine and decreased eolian contributions for this period (Figure 7).

From ~7.3 to 5.5 ka, riverine inputs from the NBEM decreased while these from the south increased, as indicated by a progressive increase in $^{87}Sr/^{86}Sr$ associated with a decline in K/Al and lowest Ti/Al (Figure 9a,b,e). This is consistent with the wettest phase from ~6.5 to 5.5 ka in northwestern Libya (Figure 9h).

The deduced decrease in Libyan Soil contribution between ~7.3 and 6.3 ka (Figure 7) seems in conflict with the increasing Ti/Al and the wetter conditions in northwestern Libya (Figure 9e,h). This paradox is thought to be related to additional inputs from Tunisia associated with enhanced fluvial activity between ~6.7 and 6.0 ka (Zielhofer et al., 2008), in line with the signature of the UM42 slump (Figure 7). The large shift observed from intervals ~7.3–6.3 ka to ~6.3–5.5 ka reflects the abrupt withdrawal of the Tunisian inputs and a substantial increase in Libyan Soil contribution, coinciding with the wettest phase in northwestern Libya (Giraudi et al., 2013) (Figure 7 and 9).

After ~5.5 ka, dust supply increased with decreasing riverine inputs (Figure 7 and 9), associated with the AHP termination; reduced monsoon precipitation resulted in less vegetation cover and the wide occurrence of dry/salt lakes (Lézine et al., 2011; Bard, 2013). The ceasing riverine input from the Libyan-Tunisian margin is shown to be after ~5.0 ka (Figure 7). Accordingly, after ~1.5 ka the data can be represented by a two-endmember mixing model, analogous to that of the present-day.

6 Conclusions

Using Sr and Nd isotopes supported by major elements (Ti, Zr, K, and Al) from core CP10BC, eolian and riverine contributions from North Africa and NBEM to central Mediterranean sediments have been unraveled. For the first time, robust and consistent evidence is given for important riverine supplies from the Libyan-Tunisian margin into the central Mediterranean during sapropel S1 time. Considerable amounts of detrital materials and freshwater must have been delivered into the EMS through the fossil river/wadi systems, which were activated by intensified African monsoon precipitation. The riverine supplies appear to originate mainly from western Libya and Tunisia and were transported as far eastward as ~25°E. Variations in this riverine contribution show a tight correspondence with hydroclimate evolution of

northwestern Libya, with the strongest contribution between ~6.3 and 5.5 ka, indicating a control of the North-African monsoon precipitation on the regional sediment provenance. In addition, it is shown that the Nile influence to the central Mediterranean was negligible whereas a prominent NBEM riverine contribution occurred during sapropel S1 formation, particularly ~8.3–7.3 ka.

Acknowledgments

We thank crew and scientists on board the cruises of RV *Pelagia* CORTADO 2011 and RV *Logachev* SMILABLE 1999 for collecting cores CP10BC and SL114BC, respectively. We thank Dineke van de Meent-Olieman for laboratory assistance, Arnold van Dijk for TOC measurements, Ton Zalm and Helen de Waard for ICP-OES analyses in Utrecht. We are also grateful to Martina Schulz who assisted with column extractions in Oldenburg. Many thanks are given to Antonio Schirone for ^{210}Pb and ^{137}Cs determinations at ENEA, La Spezia. Two anonymous reviewers are thanked for their constructive comments and suggestions on a previous version of this manuscript. The China Scholarship Council–Utrecht University PhD Program is acknowledged for financial support (CSC No. 201206260116). JW dedicates this paper to his father, who recently passed away unexpectedly.

Note (*) *The potential barite-associated Sr remaining in the decarbonated sediments may have affected the Sr isotopes and concentration of cores CP10, and the Sr isotope data published/used in this paper (Chapter 2). For core CP10, this barite-Sr effect doesn't change the Sr-Nd isotopic array (Figure 6), but rather cause an overall data shift in the $^{87}Sr/^{86}Sr$–1000/Sr diagram (Figure 7). For core SL114, the remaining barite-Sr has considerably changed the Sr-Nd isotopic composition (Figure 8), but this does not largely influenced the associated interpretations in this contribution. For the rest cores (UM42, BC03, and BC19), the impacts from the potential barite-Sr remaining in decarbonated sediments are limited (Figure 8).*

CHAPTER 3

North-African paleodrainage discharges to the central Mediterranean during the last 18,000 years: a multiproxy characterization

Jiawang Wu [a*], Zhifei Liu [b], Jan-Berend W. Stuut [c,d], Yulong Zhao [b], Antonio Schirone [e], and Gert J. de Lange [a]

[a] Department of Earth Sciences – Geochemistry, Utrecht University, 3584 CC Utrecht, The Netherlands

[b] State Key Laboratory of Marine Geology, Tongji University, 200092 Shanghai, China

[c] NIOZ, Royal Netherlands Institute for Sea Research, and Utrecht University, 1790 AB Den Burg, The Netherlands

[d] MARUM, Center for Marine Environmental Sciences, Bremen University, 28359 Bremen, Germany

[e] ENEA, Marine Environment Research Centre, P.O. Box 224, 19100 La Spezia, Italy

[*] Corresponding author: j.w.wu@uu.nl (J. Wu).

Published in Quaternary Science Reviews 163, 95–113, 2017

Abstract

Using elemental geochemistry, clay mineralogy, grain size end-member modeling, and planktonic foraminiferal $\delta^{18}O$, we characterize the provenance of central-Mediterranean sediments over the past 18 ka. The provenance is dust-dominated before and after the African Humid Period (AHP). By contrast, during the AHP (~11–5 ka), largely concurrent with organic-rich sapropel S1 formation, it is predominantly riverine from North-African sources. Such fluvial supply is suggested to come from paleodrainage networks that were reactivated by intensified monsoon precipitation during the AHP. The supply is characterized by high Mg/Al and smectite contents, and has been accompanied by considerable freshwater influx, as indicated by the enhanced grain size and lighter foraminiferal $\delta^{18}O$. The clay-mineral assemblages in our core and in nearby cores correspond with a provenance from the Libyan-Tunisian margin, mainly via the paleo-river Irharhar. The inferred fluvial discharge is strongest during the late-AHP (~8–5.5 ka), coinciding with reported enhanced fluvial dynamics and wettest conditions over western Libya and Tunisia/Algeria. This period is not only synchronous with the largest extension of open-water bodies in North Africa and lowest Saharan dust inputs, but also consistent with precipitation records of the West-African monsoon. Moreover, our records show a remarkable correspondence with that of a paleodrainage system towards the Atlantic West-African margin, inferring a common headwater region in the central Saharan mountains, and a similar climate mechanism. Taken together, we suggest a dominant control of North-African humid surfaces on the paleodrainage delivery, modulated by groundwater level, in response to the insolation-driven West-African monsoon precipitation.

Keywords

Quaternary; paleoclimatology; North Africa; inorganic geochemistry; clay minerals; grain size end-member modeling; African Humid Period; sapropel S1; provenance; paleodrainage systems

1 Introduction

In North Africa, a humid episode occurred between ~11 and 5 ka cal. BP (hereafter referred to as “ka”), which led to the development of a savannah-type vegetation cover and extensive fluvial networks over the presently hyperarid Saharan desert (e.g. Hoelzmann et al., 1998; Jolly et al., 1998; Drake et al., 2011; Lézine et al., 2011; Armitage et al., 2015). This so-called African Humid Period (AHP; c.f. deMenocal et al., 2000) not only had a major influence on the settlement of Neolithic communities (e.g. Kuper and Kröpelin, 2006; Drake et al., 2011; Manning and Timpson, 2014; Timmermann and Friedrich, 2016), but also resulted in enhanced fluvial discharge to the surrounding ocean margins, such as the equatorial Atlantic (Schefuß et al., 2005; Weldeab et al., 2007), western Sahara (Zühlsdorff et al., 2007; Tjallingii et al., 2008; Niedermeyer et al., 2010; Skonieczny et al., 2015), and northeastern Africa (Almogi-Labin et al., 2009; Hennekam et al., 2014; 2015; Weldeab et al., 2014). Such enhanced freshwater influx to the eastern Mediterranean Sea (EMS) stimulated density stratification of the water column and was associated with higher productivity in the surface water. This ultimately caused deep-water stagnation and a basin-wide formation of the most-recent organic-rich unit, sapropel S1 (~10.8–6.1 ka) (Rohling, 1994; De Lange et al., 2008; Grimm et al., 2015; Filippidi et al., 2016). It is well understood that humid climatic conditions such as those during the AHP occurred repeatedly, in response to boreal precessional insolation maxima, associated with the strengthening of the African monsoon and the northward migration of the Intertropical Convergence Zone (ITCZ). This resulted in the rhythmic occurrence of sapropel units over the EMS (Rossignol-Strick et al., 1982; Tuenter et al., 2003; Zhao et al., 2012; Rohling et al., 2015).

Nevertheless, the exact mechanisms and sources for fluvial delivery and related changes are still insufficiently known. The monsoon-fed Nile discharge has been reported as the major freshwater source during sapropel formation (e.g. Rossignol-Strick et al., 1982; Freydier et al., 2001; Revel et al., 2010; Zhao et al., 2012; Hennekam et al., 2014). Increased precipitation and associated runoff from the Northern Borderlands of the Eastern Mediterranean (NBEM) may also constitute a considerable input (e.g. Kallel et al., 1997; Zanchetta et al., 2007; Magny et al., 2013). However, the potential fluvial contribution from the wider North-African margin is largely unknown.

At sapropel times, intensified monsoon precipitation could reactivate North-African fossil river/wadi systems (presently buried beneath sand dunes), transporting substantial amounts of detrital material and freshwater to the EMS. This scenario has been proposed for sapropel S5 (i.e. MIS 5e, ~125 ka) based on planktonic foraminiferal $\delta^{18}O$, indicating a northward shift of the ITCZ beyond the central Saharan watershed at ~21°N (Rohling et al., 2002; 2004). The inferred runoff from

the Saharan mountains is also reflected in Nd isotopes of planktonic foraminifera at the same site, ODP971, off NE Libya (Osborne et al., 2008; 2010) (Figure 1). Moreover, satellite mapping (Paillou et al., 2009; 2012) as well as paleohydrological and hydraulic modeling (Coulthard et al., 2013) have revealed the existence of paleodrainage networks. These routes into the EMS may have rivaled the Nile runoff in magnitude (Scrivner et al., 2004) and functioned for a majority of Quaternary sapropels (e.g. S1: Krom et al., 1999b; Freydier et al., 2001; S6: Emeis et al., 2003). This hypothesis is also supported by derived dust variations over the past 3 Ma (Larrasoaña et al., 2003; 2013). A similar case has been found off West Africa. The findings of a large submarine canyon (Krastel et al., 2004; Antobreh and Krastel, 2006), deposition of river-borne material (Zühlsdorff et al., 2007; Tjallingii et al., 2008), and the associated subaerial paleodrainage system Tamanrasett (Vörösmarty et al., 2000; Skonieczny et al., 2015) have revealed recurrent fluvial discharge to the Atlantic margin during late-Quaternary sapropel periods (core GeoB7920) (Figure 1).

Based on Sr and Nd isotopes and supported by major elements, Wu et al. (2016) recently demonstrated that such a scenario occurred also for the Holocene sapropel S1. However, several critical issues about the North-African fluvial contribution remain elusive. Their geochemical and mineralogical composition has not been specified. The transport processes are also unknown: what/how the depositional environment was and whether the detrital supply was accompanied by considerable freshwater inputs. In particular, the origin of such paleodrainage discharge is not clear. With three major paleodrainage systems identified, Coulthard et al. (2013) suggested that the Irharhar flowing over the central Sahara represents the most likely route for human migration out of Africa. Although the Irharhar is mostly non-discharging under the present climate regime, it has been recognized as a large (paleo) river system in the world (Vörösmarty et al., 2000). Moreover, fluvial evidence has been widely inferred from lake and cave deposits as well as anthropogenic sequences over its headwater region (Cremaschi and Zerboni, 2009; Drake et al., 2011; Zerboni et al., 2015). By contrast, the presently buried fluvial networks over eastern Libya (i.e. Kufrah and Sahabi), as revealed by satellite imagery (Paillou et al., 2009, 2012), are reported to be the potential primary deliverers during sapropel S5 deposition (Rohling et al. 2002; 2004; Osborne et al., 2008; 2010) (Figure 1).

To shed light on this gap in our knowledge, a multiproxy study – coupling major elements, clay minerals, grain-size distribution, and $\delta^{18}O$ of planktonic foraminifera – is employed to distinguish and characterize the terrigenous detrital supplies to the Libyan-Tunisian margin during the last 18 ka. Elemental geochemistry and clay mineralogy of marine sediments have been widely used to track changes in detrital

supply over the circum-Mediterranean (Bout-Roumazeilles et al., 2007; Scheuvens et al., 2013; Martinez-Ruiz et al., 2015; and references therein). The end-member modeling technique of Weltje (1997) applied to grain-size distributions is a powerful tool for unmixing of different components in detrital sediments (e.g. Stuut et al., 2002; Hamann et al., 2008; Tjallingii et al., 2008; McGee et al., 2013). Planktonic foraminiferal $\delta^{18}O$ data can indicate freshwater input (e.g. Kallel et al., 1997; Rohling et al., 2002; Hennekam et al., 2014; 2015). In comparison with published results from other core-sites (Figure 1), we not only constrain the variability of detrital supplies into the central Mediterranean Sea, but also give new insights in the fluvial discharge from the North-African margin, with implications for the mechanism controlling the paleodrainage delivery.

2 Material and methods

Cores CP10BC and CP11PC were collected at the same site (34°32.7'N, 16°34.0'E; 1,501 m water-depth) in the SE Ionian Sea, central Mediterranean, during the RV *Pelagia* CORTADO cruise in 2011 (Figure 1). This site is strategically located at the Libyan-Tunisian slope, underneath the eastward pathway of surface waters, thereby offering a sensitive monitor for the North-African fluvial discharge (Figure 1a). The 35.5-cm long boxcore CP10BC was sampled every 0.25 cm for geochemical and grain-size analyses, and every 0.5 cm for clay mineral and foraminiferal studies. The description and sampling of core CP10BC was given in Wu et al. (2016). For obtaining the whole sapropel S1 related interval, piston core CP11PC (total length: 10.8 m) was sliced at 0.5 cm intervals for the upper 50 cm. The two cores were correlated using absolute radiocarbon dates and the well-established criteria of sapropel S1 boundaries (10.8–6.1 ± 0.5 ka) (De Lange et al., 2008; see Supplementary material). Hereafter, these combined cores from the same site are referred to as “core CP10/11”.

The chronology for core CP10/11 was developed by means of 8 radiocarbon dates on mixed planktonic foraminifers, and 9 measurements of ^{210}Pb and ^{137}Cs on sediment samples. Around 15 mg of mixed planktonic foraminifera (*G. ruber* and *G. sacculifer*) in the 150–600 μm fractions was picked for ^{14}C analyses at the Poznan Radiocarbon Laboratory (Table 1). Inventories and activities of ^{210}Pb and ^{137}Cs on bulk sediments were determined via gamma spectrometry at ENEA, La Spezia (c.f. Barsanti et al., 2011), indicating that the age of CP10BC core-top can be assessed as the present-day (see Supplementary material). Taken together, linear interpolations between the tie-points result in a highly consistent depth-age curve with a basal age of ~18 ka for the sampled CP10/11 intervals (see Supplementary material).

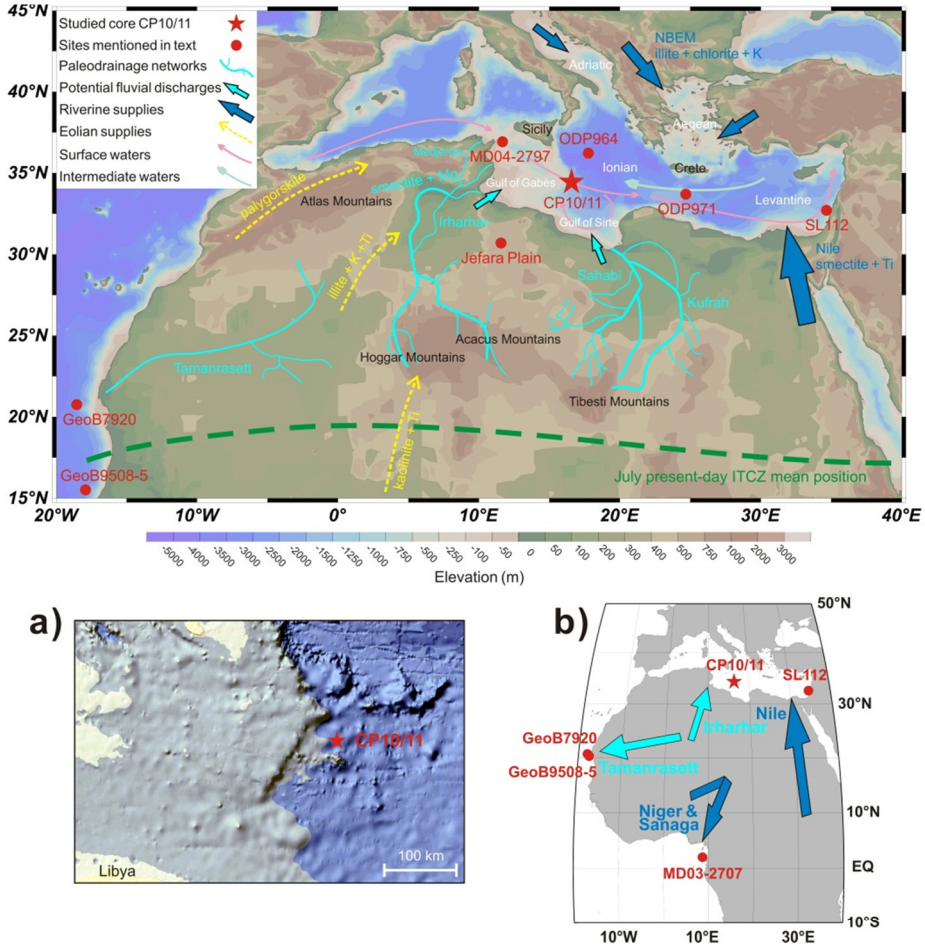

Figure 1 Topographic map of North Africa and the Mediterranean Sea with a hydrological context, showing the locations of core CP10/11 (red star) and other sites mentioned in text (red circles): MD04-2797 (Essallami et al., 2007; Bout-Roumazeilles et al., 2013), ODP 964 (Zhao et al., 2016), ODP 971 (Rohling et al., 2002; 2004; Osborne et al., 2008; 2010), SL112 (Weldeab et al., 2014), GeoB7920 (Tjallingii et al., 2008; Skonieczny et al., 2015), GeoB9508-5 (Niedermeyer et al., 2010), MD03-2707 (Weldeab et al., 2007), and Jefara Plain (Giraudi et al., 2013). Potential paleodrainage networks derived from central Saharan mountains along the wider North-African margins (i.e. Kufrah, Sahabi, and Irharhar including the Medjerda) are outlined (Vörösmarty et al., 2000; Rohling et al., 2002; Paillou et al., 2009; Coulthard et al., 2013). The Tamanrasett paleodrainage system toward the West-African coast is also drawn (Skonieczny et al., 2015), which has the same headwater region of the Hoggar-Acacus mountains as the Irharhar. The present-day perennial riverine discharges (blue arrows) and major dust emission paths (yellow dotted arrow-headed lines) to the central Mediterranean are indicated. The characteristic signatures for different detrital contributions are labeled (see text). The general circulations of surface-water and of intermediate-water are after Pinardi and Masetti (2000). a) Detailed bathymetric map of the Libyan-Tunisian margin. b) Zoom-out view of the different fluvial discharges, showing core MD03-2707 (Weldeab et al., 2007) receiving the Niger and Sanaga runoff.

Table 1 Radiocarbon chronology of core-site CP10/11

Core	Lab code	Depth (cm)	^{14}C age ± 2σ (yr BP)	Calibrated age ± 2σ (yr cal. BP) [a]
CP10BC	Poz-55177 [b]	6–6.5	2280 ± 30	1893 ± 85
CP10BC	Poz-55178 [b]	18.5–19	5130 ± 40	5486 ± 99
CP10BC	Poz-74802	25.5–26	6920 ± 40	7422 ± 89
CP10BC	Poz-55179 [b]	28–28.5	7330 ± 40	7795 ± 107
CP10BC	Poz-55180 [b]	34–34.5	8770 ± 50	9423 ± 101
CP11PC	Poz-82843	4–4.5	2680 ± 30	2385 ± 85
CP11PC	Poz-74666	30–30.5	11190 ± 60	12691 ± 116
CP11PC	Poz-74667	47–47.5	14530 ± 70	17201 ± 253

[a] Using Marine13 calibration curve (Reimer et al., 2013), implemented in program Calib 7.0 (Stuiver and Reimer, 1993), with no regional offset (ΔR=0) (Siani et al., 2000).
[b] Data from Wu et al. (2016).

Stable isotopes were analyzed on the sea-surface dwelling foraminifera *G. ruber* (white) (Hennekam et al., 2014). Clean and intact tests were picked from the 250–300 µm size range. Approximately 20–80 µg of foraminifera (i.e. 2–5 shells) was analyzed with a Kiel-III carbonate preparation device connected to a Finnigan MAT-253 mass spectrometer. The average standard deviation for $\delta^{18}O$ is 0.08‰, based on the regular measurements of duplicates and the NBS-19 standard. The *G. ruber* $\delta^{18}O$ ($\delta^{18}O_{ruber}$) values are reported in per mil (‰) relative to the Vienna PeeDee Belemnite (VPDB).

Following the protocol in Van Santvoort et al. (1996), freeze-dried, powdered bulk sediments were decarbonated by shaking in 1 M HCl for 4+12 hours. Subsequently, the residues were rinsed twice with distilled water, oven-dried at 80 °C, and ground. Elemental compositions were analyzed on a Spectro Arcos Inductively Coupled Plasma-Optical Emission Spectroscopy (ICP-OES) after a three-step total digestion (Reitz et al., 2006). Powdered samples were digested in a mixture of HF-$HClO_4$-HNO_3 and heated at 90 °C in a gastight Teflon vessel for at least 12 hours. The solution was evaporated at 160 °C to near dryness, and then the residue was dissolved in 4.5% HNO_3 at 90 °C. Reported concentrations were determined on the carbonate-free samples, thus representing the non-biogenic, "detrital" sediment alone, except for the Ba/Al data that are for bulk sediment samples. Analytical uncertainties were monitored by blanks, duplicates, and standards (ISE 921), showing that accuracy is better than 6% and precision better than 3% for all targeted elements. Given its conservative behavior, Al is adopted for normalizations here to assess the relative enrichment/depletion of specific elements (c.f. Martinez-Ruiz et al., 2015).

Clay minerals were identified by X-ray diffraction (XRD) using a PANalytical X'Pert Pro diffractometer, with a 0.03°2Θ/s rate under CuKα radiation and Ni filter, at Tongji University (Wu et al., 2012; Schroeder et al., 2015). The analysis was conducted on oriented mounts of non-calcareous, clay-sized particles (<2 µm), which were

obtained after the protocol described by Liu et al. (2004). The XRD runs were performed under three conditions: untreated, glycolated (in ethylene-glycol vapor for 24 hours), and heated (490 °C for 2 hours). Identification of clay minerals was done according to a comprehensive comparison of the three XRD diagrams. For the main clay-mineral groups, the relative abundances were calculated by measuring the peak areas on glycolated curve using MacDiff 4.2 software (Petschick, 2000); i.e. smectite (including mixed layers) (15–17 Å), illite (10 Å), and kaolinite/chlorite (7 Å). Relative proportions of kaolinite and chlorite were determined using the ratio of 3.57/3.54 Å peak areas. Palygorskite (10.6 Å) was also detected. Following the laboratory routine, the weighing factors introduced by Biscaye (1965) are not applied. Additionally, illite parameters were calculated to track provenance (Petschick et al., 1996). On the glycolated curve, the illite chemistry index refers to the ratio of the 5 Å and 10 Å peak areas, and illite crystallinity was obtained from half height width of the 10 Å peak. The reproducibility error of this method is <5%.

For grain-size analyses of the detrital fraction, bulk sediment was treated with 10% H_2O_2 at 80 °C using a water-bath, until reaction stopped to remove organic matter, and subsequently with 1 M HCl for 6 hours to remove marine carbonates. Microscope observations confirmed that this procedure successfully eliminated all biogenic constituents. After boiling briefly with a dispersing agent ($Na_4P_2O_7$), the CP10BC and CP11PC samples were measured on the Malvern Mastersizer-S and -2000 instruments, respectively, resulting in 64 size classes (0.06–879 µm) (Stuut et al., 2002). As the very fine fraction (<0.5 µm) has no meaning sedimentologically and accounts for a negligible proportion, the number of input variables is routinely reduced to 49 size classes (0.5–879 µm) for the subsequent end-member modeling (c.f. Stuut et al., 2002). The end-member modeling algorithm (EMMA) of Weltje (1997) is used to decompose the measured grain-size distribution into proportional contributions of an optimal set of end members (i.e. EMs). The inversion algorithm approximates a theoretical grain-size distribution by iterative calculation of the least-square fit between the measured grain-size distribution and the mixture of the calculated EMs. To estimate the minimum number of EMs required for a satisfactory approximation of the data (n=141), the coefficients of determination (r^2) of each size class, and the mean coefficient of determination (r^2_{mean}) were calculated. These coefficients represent the proportion of variance that can be reproduced by the approximated data (Weltje, 1997).

3 Results

3.1 *G. ruber* $\delta^{18}O$ and bulk Ba/Al

The $\delta^{18}O_{ruber}$ record in core CP10/11 shows a shift from enriched values (~4‰) around the Heinrich event 1 (H1), to much more depleted values of ~0.5‰ at ~10 ka. The profile maintains the depleted $\delta^{18}O_{ruber}$ ratios over the AHP, followed by a

gradual increase to ~1‰ today (Figure 2a). As post-depositional oxidation removed most of the organic carbon, but not the co-settling biogenic Ba from the upper-most part of sapropels, the full extent of sapropel S1 is recognized by the elevated zone of bulk Ba/Al (Van Santvoort et al., 1996; De Lange et al., 2008). For core CP10/11 this is between ~10.8–5.8 ka (Figure 2b), in agreement with previous studies (~10.8–6.1 ± 0.5 ka) (c.f. De Lange et al., 2008). Sapropel S1, largely coeval with the AHP, can be split into S1a and S1b periods, divided by the 8.2 ka interruption, visible here in Ba/Al at ~8.2–7.8 ka (Rohling and Pälike, 2005; Wu et al., 2016). The sedimentation rates are between 2.8 and 4.1 cm/ka, and is relatively high during the S1 period, S1b in particular, and lower for the arid intervals (Wu et al., 2016) (see Supplementary material).

The interval of ~3.0–1.5 ka is affected by dispersed tephra as identified in several samples (Wu et al., 2016), thus we will disregard this interval from hereon. In the following, data are grouped into four different periods of sediment transport and deposition: pre-AHP (~18.0–10.8 ka), S1a (~10.8–8.0 ka), S1b (~8.0–5.5 ka), and post-AHP (~5.5–0 ka).

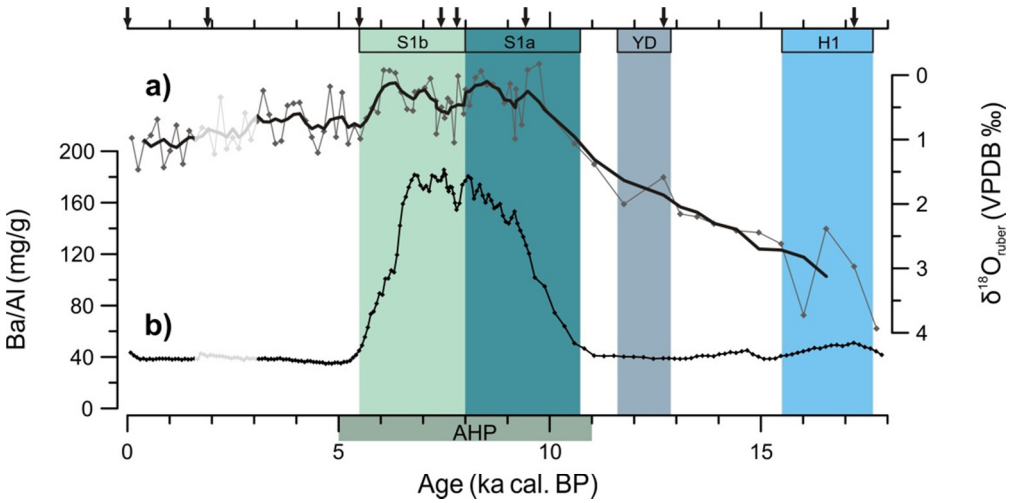

Figure 2 Geochemical records for core CP10/11 over the past 18 ka. a) Planktonic foraminiferal *G. ruber* $\delta^{18}O$, with 5-point moving average superimposed. b) Ba/Al of bulk sediment basis (Wu et al., 2016). Age tie-points are indicated by arrows at the upper axis. The tephra-related interval (~3.0–1.5 ka) mentioned in Section 3.1 is disregarded in this contribution. Sapropel S1a and S1b intervals, Heinrich event 1 (H1), Younger Dryas (YD), and African Humid Period (AHP) are specified (see Section 3).

3.2 Grain size end-member modeling

The mean grain-size distribution of core CP10/11 has a modal value near 5 µm (Figure 3a). For the total set of distributions (n=141), the coefficients of

determination (r^2) are plotted against grain size for models with 2–10 EMs (Figure 3b). The mean coefficient of determination (r^2_{mean}) of the grain-size classes increases when the number of EMs increases (Figure 3c). End-member modeling (EMMA) of the CP10/11 grain-size data results in two contrasting components in the 2-EM model (i.e. the model with 2 end members; and so on), which are consistent with the varying climatic conditions (Figures 3d; 4b). However, this model has a low r^2_{mean} (0.46) and especially low r^2 (<0.4) for the ranges of ~10–16 µm and >90 µm (Figure 3b,c). The 3-EM model reports a higher but still unsatisfactory fit (r^2_{mean}=0.66). The 4-EM model explains more than 75% of the variance in the total dataset, and considerably improves the ranges of ~10–16 µm (r^2 >0.8), and of ~90–200 µm (r^2=0.5–0.8) to an adequate extent (Figure 3b,c). The coarse tail (>90 µm) can only be sufficiently addressed with ≥5 EMs, but this fraction can be ignored because it comprises <4% of the total weight-mass of the samples (Figure 3b). This is justified by 1) the limited improvement of the goodness-of-fit with the use of ≥5 EMs and 2) the clear separation of aeolian supplies that mainly occupy the coarse-particle fraction by using a 4-EM model (Figures 3d; 4b). By contrast, the range of ~10–16 µm should be well reproduced by the mixing model, as this range contains a large proportion of the total mass. In brief, the goodness-of-fit statistics, combined with the grain-size distributions of the EMs, demonstrate that the 4-EM model provides the best balance between minimum number of EMs and maximum r^2.

Accordingly, the modeled grain-size distribution (Figure 3d) and downcore variability (Figure 4b–e) of the EMs are shown for the 4-EM model, with those of the 2-EM model for comparison. The end member 2-EM1 (i.e. the 2-EM model's 1st end member; and so on) has a dominant mode of ~40 µm, and 2-EM2 of ~4 µm (Figure 3d). For the 4-EM model, all end members have a well-defined distribution. The 4-EM1 has a major peak near 6 µm, with two minor bulges at ~12 and 40 µm. The 4-EM2 shows a poorly sorted, bimodal distribution with modes at ~6 and 35 µm. The 4-EM3 has a well sorted, dominant mode at ~3 µm. The 4-EM4 shows a modal grain size of ~5 µm, and a minor peak near 150 µm (Figure 3d).

The median grain size in core CP10/11 varies between 4–11 µm, displaying generally lower values during the AHP, except for the S1b interval (Figure 4a). Likewise, the 2-EM1 proportion is lower during the AHP; and vice versa for 2-EM2 (Figure 4b). Two different components (i.e. 4-EM1 + 4EM-2, 4-EM3 + 4EM-4) are clearly presented in the 4-EM model (Figure 4c). A high proportion (~80%) of 4-EM1 occurs only before sapropel S1, whereas the 4-EM2 proportion steadily increases up to 80% after the AHP (Figure 4d). An enhanced proportion of 4-EM3 corresponds with the Ba/Al within sapropel S1 (~10–6 ka), followed by a peculiar increase around 5 ka. The 4-EM4 also shows elevated contributions during the AHP, but is different from 4-EM3 in variability. The 4-EM4 proportions are highest during S1b, in contrast

to the simultaneously decreasing trend observed for 4-EM3 (Figure 4e). Moreover, humidity indexes are calculated for the North-African continent and eastern-Mediterranean region (after Tjallingii et al., 2008) (Figure 4f,g; see Section 4.3).

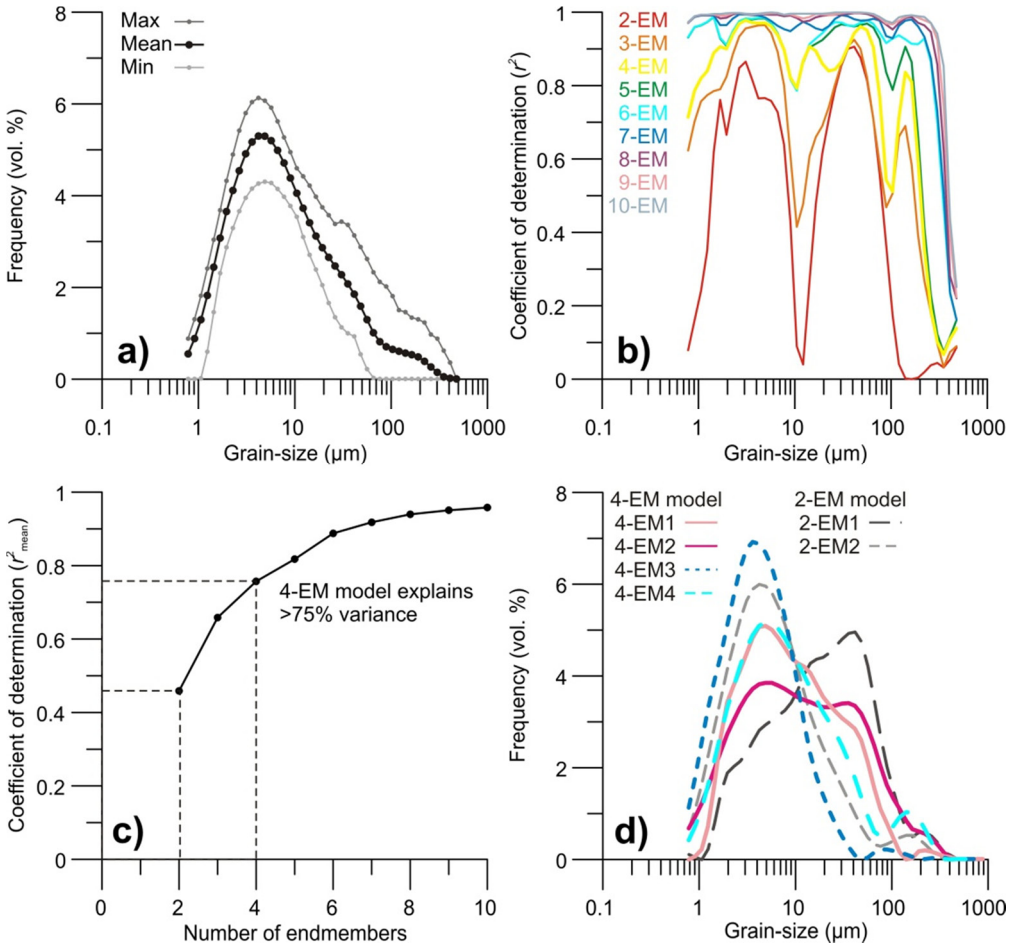

Figure 3 End-member modeling results of core CP10/11 grain-size data. a) Summary statistics of raw data (n=141); maximum, mean, and minimum frequency recorded in each size class. b) Coefficients of determination (r^2) per size class for models with 2–10 end members. c) Mean coefficient of determination (r^2_{mean}) of all size classes for each model. d) Modeled grain-size distributions of end members for the 4-EM and 2-EM models. The goodness-of-fit statistics suggest that the 4-EM model is an adequately reliable choice (see Section 3.2). Data of the tephra-related interval (~3.0–1.5 ka) were removed for the modeling (see Section 3.1).

3.3 Detrital elemental ratios and clay minerals

The Ti/Al ratio is recognized as a proxy for Saharan dust, while higher values of K/Al and detrital Mg/Al are generally interpreted as enhanced fluvial inputs to the EMS (Wehausen and Brumsack, 2000; Martinez-Ruiz et al., 2015, and references therein). In core CP10/11, the Ti/Al record displays a descending trend from H1 to the Younger Dryas (YD), with relatively low values for S1a. The Ti/Al reaches a minimum value at ~6.5 ka, followed by a steady increase (Figure 5a). The K/Al profile displays a similar evolution as that of Ti/Al before the AHP, but differs in two aspects for the Holocene: 1) having generally higher values in the AHP and 2) reaching the lowest value much later (~5 ka) (Figure 5b). The Mg/Al record shows very distinctive changes. After a slight decrease from H1 to YD, Mg/Al increases and shows the highest value during the S1b, followed by a decline till the present (Figure 6e). Additionally, transition elements Ni and Cr are typically concentrated in mafic igneous rocks, and thus high Ni/Al and Cr/Al suggest more mafic provenance (c.f. Wu et al., 2013). The Ni/Al and Cr/Al profiles show close relationships with Mg/Al (Figure 6e–g).

The clay-mineral assemblage of core CP10/11 over the past 18 ka is composed of dominant smectite (42–56%), moderate kaolinite (16–25%) and illite (15–21%), and minor chlorite (8–13%) and palygorskite (1–3%). The major clay minerals exhibit striking similarities to elemental ratios, i.e. smectite – Mg/Al (Figure 6e,h), kaolinite – Ti/Al (Figure 5a,c), and illite – K/Al (Figure 5b,e) (see Section 4). Chlorite is generally higher (lower) during the period before (after) ~8 ka (Figure 5g), while the palygorskite has low values and displays no discernible pattern (Figure 6l). The illite to kaolinite (I/K) ratio varies within a narrow range before ~10 ka; after a slight increase during S1a, a steady decline occurs (Figure 5i). The chlorite to kaolinite (C/K) and smectite/kaolinite (S/K) ratios have a variability similar to that of I/K, but with a more pronounced increase during S1a for C/K and more enhanced values during S1b for S/K (Figure 5k; 6j).

3.4 Estimated elemental ratios of grain-size end members

Via combining the results of grain size end-member modeling, with the elemental data, which are both derived from the detrital sediment fraction, a quantitative estimation of the elemental fingerprints for the 4-EM end members was made. For a certain element, the Al-normalized ratios were calculated using the equation: $Element/Al_{sample} = Proportion_{4\text{-}EM1} \times Element/Al_{4\text{-}EM1} + Proportion_{4\text{-}EM2} \times Element/Al_{4\text{-}EM2} + Proportion_{4\text{-}EM3} \times Element/Al_{4\text{-}EM3} + Proportion_{4\text{-}EM4} \times Element/Al_{4\text{-}EM4}$, where $Element/Al_{sample}$ is the measured elemental ratio in detrital sediment, $Proportion_{4\text{-}EM1}$ is the proportion of end member 4-EM1 (and so on), and $Element/Al_{4\text{-}EM1}$ is the (unknown) elemental ratio of end member 4-EM1 (and so on). This equation was applied for the four periods with different climatic conditions (i.e. pre-AHP, S1a, S1b, and post-AHP). Thus with four equations, the unknown elemental ratios for the four

end members can be determined. Note that the proportions of grain-size end members and the measured elemental ratios are taken as average values for a certain interval. This calculation was done for the three characteristic elements (i.e. Ti, K, and Mg). The results are presented in Table 2.

4 Discussion

A strong west–east gradient has been reported for surface sediments in the EMS, caused by mixing between two end members: Saharan dust vs. Nile sediments (Venkatarathnam and Ryan, 1971; Krom et al., 1999a; Weldeab et al., 2002a). This two-end-member model is usually adequate to explain the variability of sediment composition in the eastern section of the EMS (e.g. Krom et al., 1999b; Wehausen and Brumsack, 2000; Freydier et al., 2001; Weldeab et al., 2002b; Revel et al., 2010). For the central Mediterranean, however, detrital sediments can only be assigned to a ternary mixing system based on Sr and Nd isotopes, including 1) Saharan dust, 2) riverine inputs from the Nile and NBEM (i.e. Northern Borderlands of the Eastern Mediterranean), and 3) fluvial/shelf-derived fluxes from the Libyan-Tunisian margin (Wu et al., 2016). Therefore, although there is a general agreement on the overall systematics and provenance, several important controversies and unresolved issues remain.

1) Sources of Saharan dust are not evenly distributed over North Africa, have different elemental and mineralogical composition and may change substantially through time (Krom et al., 1999a; McGee et al., 2013; Scheuvens et al., 2013).
2) Riverine inputs from the NBEM and Nile have a similar Sr-Nd isotopic signature, thus cannot be differentiated using these isotopes alone (Weldeab et al., 2002a; 2002b; Wu et al., 2016).
3) Past detrital supply from the Libyan-Tunisian margin is poorly known for its composition and origin (see Section 1).

The complex controls on the provenance of central-Mediterranean sediments urge for a multi-proxy approach. We have done so on the well-dated CP10/11 core. The EMMA technique (Weltje, 1997) is applied to the grain-size data to distinguish aeolian and fluvial contributions. Different contributions are further characterized using major elements, clay minerals, and foraminiferal $\delta^{18}O_{ruber}$. In this way, the sediment provenance, especially for the North-African paleodrainage runoff, is unraveled. In a wider perspective, we compare our data with those published for cores MD04-2797 at the Strait of Sicily (Essallami et al., 2007; Bout-Roumazeilles et al., 2013), ODP964 in the Ionian Sea (Zhao et al., 2016), and GeoB7920 off West Africa (Tjallingii et al., 2008; Skonieczny et al., 2015). Finally, we discuss our findings in relation to paleo-hydroclimate changes over North Africa.

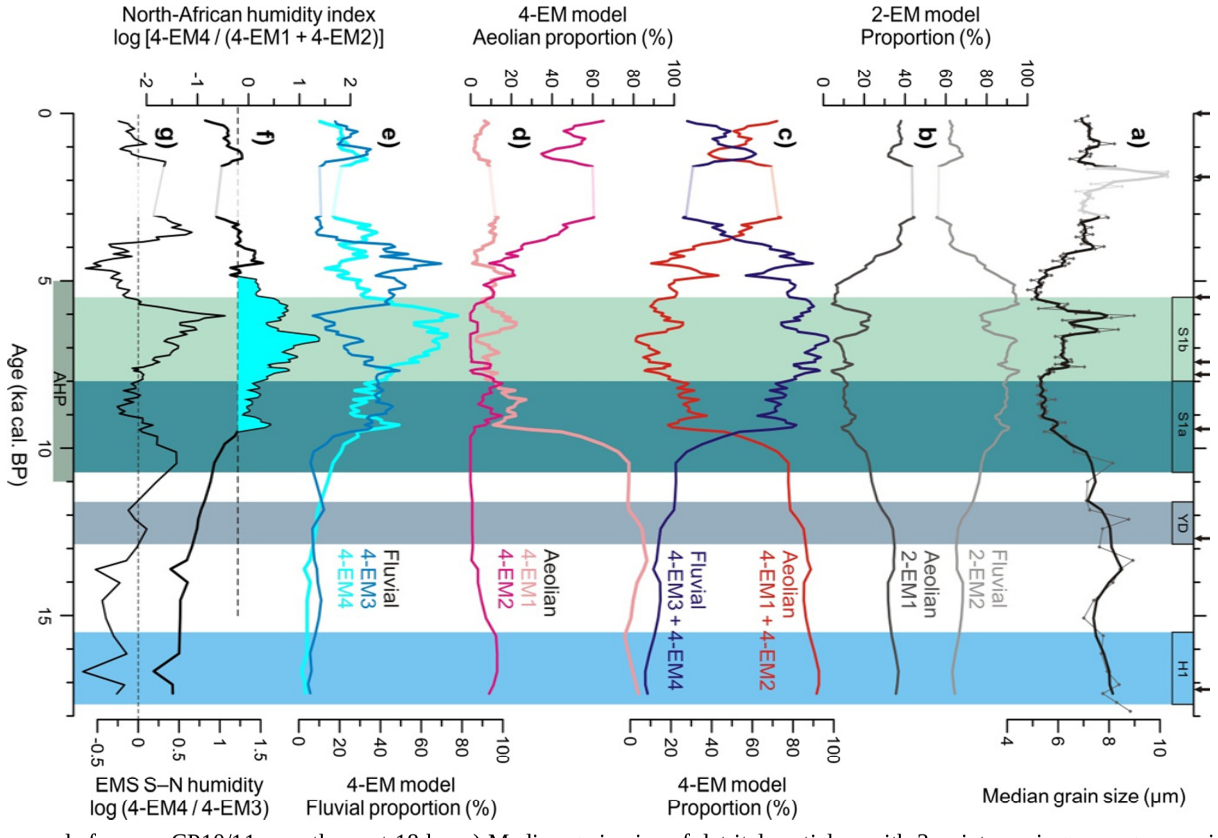

Figure 4 Grain-size records for core CP10/11 over the past 18 ka. a) Median grain size of detrital particles, with 3-point moving average superimposed. Aeolian and fluvial components presented in b) 2-EM model and c) 4-EM model, respectively. d) Proportions of aeolian end members for 4-EM model, which dominated the arid periods before (4-EM1) and after (4-EM2) sapropel S1, respectively. e) Proportions of fluvial end members for 4-EM model, which are interpreted to indicate the NBEM riverine inputs and the North-African paleodrainage discharges, respectively. f) Continental humidity index of North Africa, expressed as a log-ratio of the North-African fluvial (4-EM4) and aeolian (4-EM1 + 4-EM2) end members. g) Log-ratio of the North-African (4-EM4) and the NBEM riverine (4-EM3) fluvial end members, is thought to reflect relative S–N humidity of the eastern Mediterranean. Note that the grain-size modeled data are reported as 5-point moving average. Age tie-points are indicated by arrows at the upper axis. The tephra-related interval (~3.0–1.5 ka) is disregarded (see Section 3.1). Sapropel S1a and S1b intervals, Heinrich event 1 (H1), Younger Dryas (YD), and African Humid Period (AHP) are specified (see Section 3).

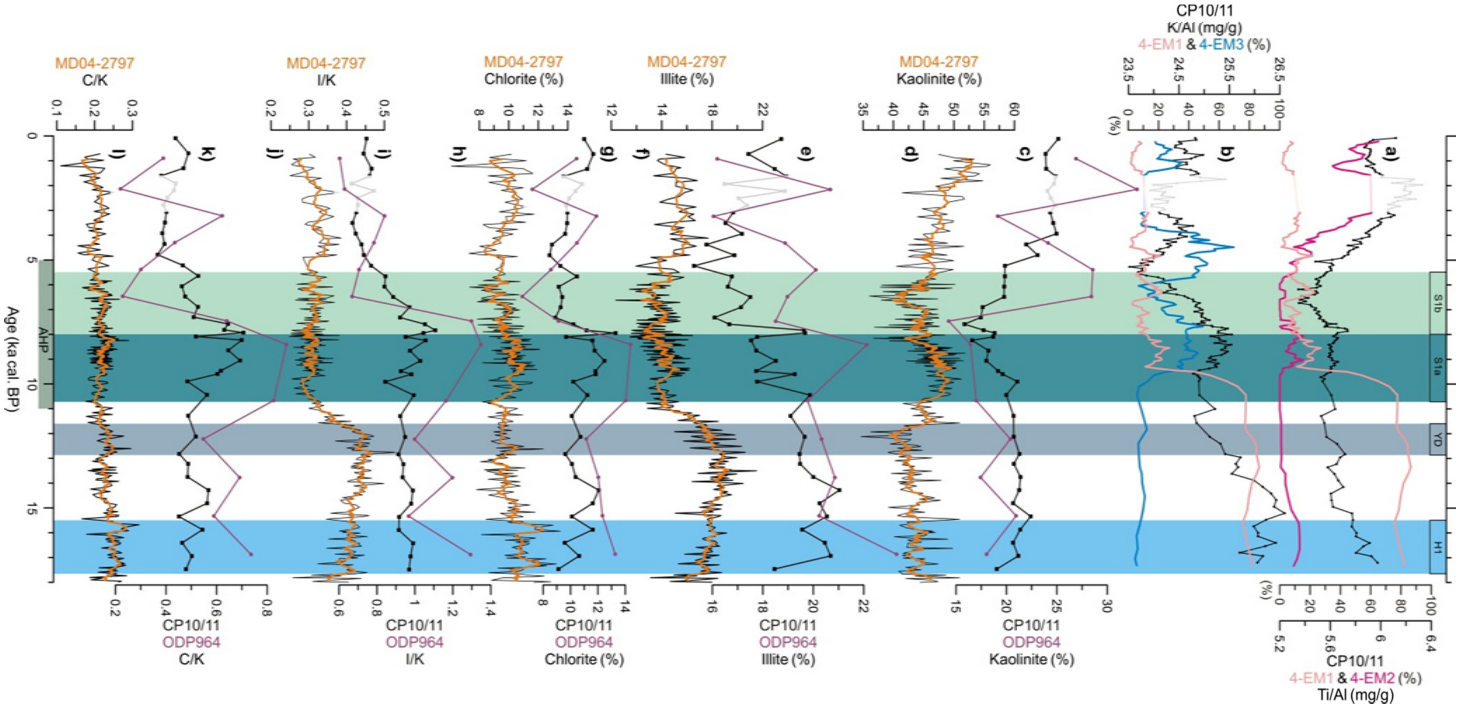

Figure 5 Comparison of detrital records between cores CP10/11, MD04-2797 (Bout-Roumazeilles et al., 2013), and ODP964 (Zhao et al., 2016) to distinguish aeolian and riverine supplies. a) Ti/Al (black), and proportions of Saharan dust end members 4-EM1 (pink) and 4-EM2 (magenta) in CP10/11. b) K/Al (black), and proportions of aeolian end member 4-EM1 (pink) and of NBEM riverine end member 4-EM3 (blue) in CP10/11. c) Kaolinite for CP10/11 and ODP964. d) Kaolinite in MD04-2797. e) Illite for CP10/11 and ODP964. f) Illite in MD04-2797. g) Chlorite for CP10/11 and ODP964. h) Chlorite in MD04-2797. i) I/K (illite/kaolinite) for CP10/11 and ODP964. j) I/K in MD04-2797. k) C/K (chlorite/kaolinite) for CP10/11 and for ODP964. l) C/K in MD04-2797. The profiles of grain-size derived data are reported as 5-point moving average. Note that the elemental and clay mineralogy records of CP10/11 are shown in black, ODP964 records in purple, and 5-point moving average (orange line) is also superimposed for MD04-2797. The tephra-related interval (~3.0–1.5 ka) is disregarded (see Section 3.1). Sapropel S1a and S1b intervals, Heinrich event 1 (H1), Younger Dryas (YD), and African Humid Period (AHP) are specified (see Section 3).

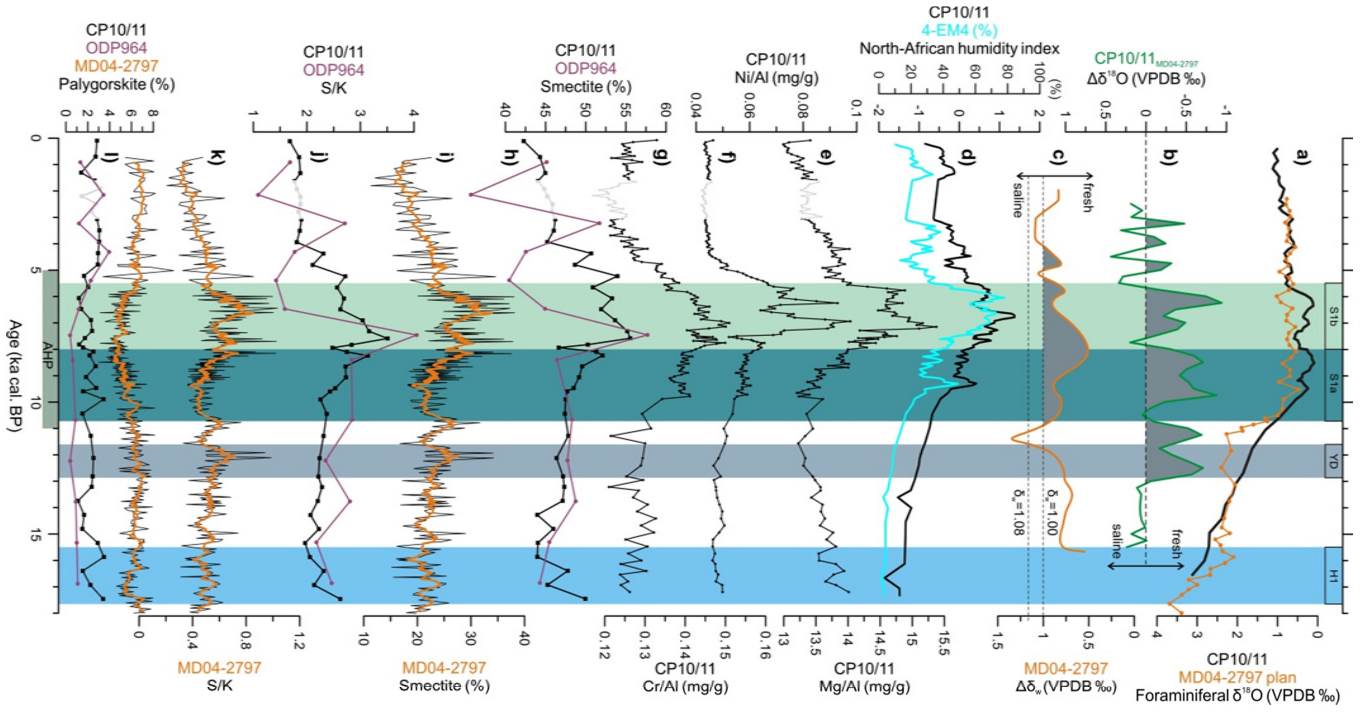

Figure 6 A tight correspondence between various proxy records from cores CP10/11, MD04-2797 (Essallami et al., 2007; Bout-Roumazeilles et al., 2013), and ODP964 (Zhao et al., 2016) indicates the reactivated paleodrainage systems (mainly Irharhar) along the Libyan-Tunisian margin transported considerable Mg- and smectite-rich detrital materials and freshwater into the Gulf of Gabès. Such fluvial discharge is strongest during the late-AHP, S1b interval (~8.0–5.5 ka), related to an enhanced fluvial dynamics and the most humid conditions in western Libya and Tunisia/Algeria. a) Planktonic foraminiferal $\delta^{18}O$ of *G. ruber* for CP10/11 (black, 5-point moving average) and of *G. bulloides* for MD04-2797 (orange). b) Difference of planktonic foraminiferal $\delta^{18}O$ ($\Delta\delta^{18}O$) between CP10/11 and MD04-2797, i.e. lower value is thought to indicate more freshwater supply to CP10/11 relative to MD04-2797; data were resampled at 250-yr resolution for calculation. c) $\Delta\delta_w$ for MD04-2797, a proxy for salinity, calculated using alkenones-derived SST; modern and S1 background δ_w (local seawater $\delta^{18}O$) values of 1.08 and 1.00 are shown (dash lines). d) Proportion of end member 4-EM4 (cyan), indicative of North-African paleodrainage discharge; North-African humidity index, expressed as a log-ratio of the North-African fluvial and aeolian end members in CP10/11. e) Detrital Mg/Al in CP10/11. f) Ni/Al in CP10/11. g) Cr/Al in CP10/11. h) Smectite for CP10/11 and ODP964. i) Smectite in MD04-2797. j) S/K (smectite/kaolinite) for CP10/11 and ODP964. k) S/K in MD04-2797. l) Palygorskite for CP10/11, ODP964, and MD04-2797. The profiles of grain-size derived data are reported as 5-point moving average. Note that the elemental and clay mineralogy records of CP10/11 are shown in black, ODP964 and MD04-2797 (5-point moving average) records are in purple and orange, respectively. The tephra-related interval (~3.0–1.5 ka) is disregarded (see Section 3.1). Sapropel S1a and S1b intervals, Heinrich event 1 (H1), Younger Dryas (YD), and African Humid Period (AHP) are specified (see Section 3).

4.1 Distinguishing aeolian and riverine inputs to the central Mediterranean

Terrigenous detrital deposits on continental margins represent mixtures of components brought in by wind and delivered by rivers. For the CP10/11 grain-size data, two contrasting components are generated by the 2-EM model, i.e. 2-EM1 is interpreted as aeolian and 2-EM2 as fluvial sediments (Figures 3d; 4b). Similarly but much more distinctly, aeolian (4-EM1 + 4EM-2) and fluvial (4-EM3 + 4EM-4) contributions are characterized by the 4-EM model, showing that their variation corresponds with the AHP-associated arid and humid conditions (Figures 4c).

The grain size of aeolian particles deposited in deep-sea sediments depends on the distance to the source and the capacity of the transporting agent. Aeolian contributions to deep-sea sediments are usually coarser grained than riverine, hemipelagic components. As a result, terrigenous detrital particles with a median grain size >6 μm are generally attributed to aeolian transport, and hemipelagic deposition is often assumed for the <6 μm particles. This is based on deep-sea sediment studies (e.g. Sarnthein et al., 1981; Sirocko et al., 1991; Prins et al., 2000) as well as modern-dust studies during which dust was collected at sea in various areas (e.g. Clemens, 1998; Ratmeyer et al., 1999; Stuut et al., 2005). Moreover, this concept has often been adopted to tentatively separate the eolian and fluvial contributions (e.g. Stuut et al., 2002; Tjallingii et al., 2008; McGee et al., 2013).

Here, our 4-EM1 and 4-EM2 are considered to be of aeolian origin, and the 4-EM3 and 4-EM4 are thought to be hemipelagic (Figures 3d; 4c). Specifically, the aeolian character of 4-EM1 and 4-EM2 is corroborated by their downcore variations, displaying high proportions only during non-AHP intervals dominated by an arid Saharan regime (Figure 4d). The enhanced contributions of 4-EM3 and 4-EM4 during the AHP are interpreted as non-aeolian hemipelagic mud associated with fluvially transported material (Figure 4e). As discussed below, we will examine these interpretations combined with the results of detrital elements and clay minerals.

4.1.1 Saharan dust

Today Saharan dust is the dominant component of central-Mediterranean sediments (Guerzoni et al., 1997; Rutten et al., 2000; Scheuvens et al., 2013). Dust from the northern and eastern borderlands of the Mediterranean is quantitatively negligible (Guerzoni et al., 1997; Ehrmann et al., 2007a). Because Ti principally resides in heavy minerals and is enriched in modern Saharan aerosols, the Ti/Al ratio has been widely used as a proxy for Saharan dust (e.g. Wehausen and Brumsack, 2000; Lourens et al., 2001; Wu et al., 2016). Part of the variability of Ti/Al may also result from a change in the grain size of aeolian particles, related to wind strength (Sarnthein et al., 1981; Stuut et al., 2002).

Illite and kaolinite together are reported to constitute a large fraction (usually >50%) of the clay-mineral assemblages of Saharan dust (Guerzoni et al., 1997; Scheuvens et al., 2013). Due to the different efficiency of weathering processes in soils at different latitudes, illite, usually enriched in K, is dominant in the NW sector of the Sahara. By contrast, abundant kaolinite is found at low latitudes, being preferentially formed under humid and warm conditions. As shown in the compilation by Scheuvens et al. (2013), these result in illite (kaolinite) contents for North-African soils to decrease (increase) southward. Furthermore, the I/K ratio in mineral dust exhibits a slight W–E decreasing gradient over North Africa and is considered to be conservative during long-range transport (Caquineau et al., 1998). Consequently, the I/K ratio has been used as a dust-source indicator for the tropical Atlantic (Caquineau et al., 1998; Skonieczny et al., 2013) and the Mediterranean (Bout-Roumazeilles et al., 2007; 2013; Zhao et al., 2016).

In core CP10/11, the evolution of Ti/Al, K/Al, kaolinite, and illite all show a similar pattern, with higher values during non-AHP intervals (Figure 5a,b,c,e). Given that these aeolian parameters are derived from different size fractions, this suggests that the coherent changes therein mainly result from dust fluxes. Variations in dust flux have been attributed to Saharan lake surface area and vegetation cover (e.g. Claussen et al., 1999; deMenocal et al., 2000; Cockerton et al., 2014; Armitage et al., 2015; Egerer et al., 2016). Indeed, during the AHP, North Africa was perennially covered by dense vegetation and extensive fluvial systems, leading to 70–80% lower dust emissions than today (deMenocal et al., 2000; McGee et al., 2013; Egerer et al., 2016).

4.1.1a Pre- and post-AHP dust

Aeolian contributions in core CP10/11 are neatly separated in terms of grain-size distribution. Different supplies of Saharan dust dominate during the pre-AHP (4-EM1) and post-AHP (4-EM2) (Figure 4d). In fact, for various parameters there is a difference in value before and after the AHP, observed for cores CP10/11, ODP964, and MD04-2797 (Figure 5a–f). The post-AHP dust seems to have a larger contribution of coarse components and has a higher Ti/Al. Moreover, compared to the pre-AHP, the post-AHP dust contains more kaolinite and less illite. The resulting I/K ratio explicitly indicates a more predominant NW-Saharan dust source for the pre-AHP, and a more SE-Saharan oriented provenance for the post-AHP (Figure 5i,j). Considering the poor sorting of the aeolian EMs (Figure 3d), Saharan dust deposited in the central Mediterranean is thought to be multiple-sourced, likely to have proximal and distal contributions. The presence of palygorskite is diagnostic for dust derived from NW Africa (i.e. Morocco, Algeria, and Tunisia) (Bout-Roumazeilles et al., 2007; Scheuvens et al., 2013; Skonieczny et al., 2013). Given the low

contents and lack of clear trends in variability for palygorskite (Figures 6l), the dust from these proximal regions must be minor, but may be persistently active. Taken together, for the pre-AHP compared to the post-AHP interval, our clay-mineral data refer to a more NW-Saharan provenance, while the smaller grain size of the dominant 4-EM1 and the lower Ti/Al values may signify a longer distance to dust sources or weaker wind strength.

Our I/K data for the non-AHP samples generally match with the domain of southern Algeria and Mali, one of the major dust production areas in North Africa nowadays (Bout-Roumazeilles et al., 2007; Scheuvens et al., 2013). However, it must be realized that although kaolinite is considered as a predominantly eolian signal (Venkatarathnam and Ryan, 1971; Bout-Roumazeilles et al., 2007), part of the illite may also originate from non-dust sources. Using I/K alone, this provenance domain is thus difficult to attribute with more certainty.

4.1.1b Contrasting AHP versus non-AHP

During the AHP and the nearly coincident sapropel S1, the dust contribution is small, whereas riverine inputs, and associated enhanced illite and K/Al, are more dominant. The decline of the I/K ratio after the YD observed for the Strait of Sicily and on the Iberian shelf (Stumpf et al., 2011), has been attributed to a southward shift of the Saharan dust sources, caused by a southward migration of the ITCZ (Bout-Roumazeilles et al., 2013). Cores CP10/11 and ODP964 in the Ionian Sea display a similar variability, but with a much delayed decrease, i.e. after S1a (Figure 5i,j). The different timing can be attributed to the influences of enhanced NBEM riverine inputs (enriched in illite and chlorite) during S1a on cores CP10/11 and ODP964, but not for MD04-2797 (Figure 5e–h; see Section 4.1.2).

The different illite sources for the Ionian Sea can be discriminated by mineralogical parameters. Lower values of illite chemistry index and illite crystallinity both indicate a weaker chemical hydrolysis formation, and thus a higher latitude environment; and vice versa (Petschick et al., 1996; Zhao et al., 2012; 2016). Accordingly, the high values for chemistry index and crystallinity of illite in non-AHP sediments correspond to the more humid and warm conditions of its formation in subtropical regions, and subsequent transportation as Saharan dust. By contrast, the low values for the illite parameters in the AHP samples point to a high-latitude illite source, characterized by relatively arid and cold conditions (i.e. NBEM riverine inputs) (Figure 7).

4.1.2 NBEM riverine inputs

Clay-sized particles represent the major component transported by rivers to the Mediterranean Sea. During the late-Quaternary, the Nile sediment is mainly derived from Cenozoic basaltic rocks in the Ethiopian Highlands. This is reflected in the

characteristic elemental compositions (high Ti, low K and Mg) (e.g. Krom et al., 1999a; 1999b; Hennekam et al., 2014) and the overwhelming smectite in clay-mineral assemblages of the Nile sediments (e.g. Venkatarathnam and Ryan, 1971; Hamann et al., 2009; Zhao et al., 2012). The Sr and Nd isotopes in surface sediments reveal that the recent Nile contribution rapidly decreases westward from the river-mouth to being negligible south of Crete (Krom et al., 1999a; Weldeab et al., 2002a).

Substantially enhanced sedimentation rates during sapropel S1 occurred only for cores taken within/near the Nile delta (Hennekam et al., 2015). This indicates that during the AHP the offshore spread of Nile sediments was not larger than before or after. Meanwhile, observations of the detrital Sr- and Nd- isotopes and concentrations on leachable and residual fractions of sapropel S1 sediments, taken from cores along a west–east transect throughout the EMS, show that the enhanced Nile discharge (i.e. dissolved and particulate) can only be detected westward until south of Crete (Krom et al., 1999b; Freydier et al., 2001). In accordance, the compositional variability of Ti and K data in core CP10BC clearly indicates a minor–if any–Nile contribution to the central Mediterranean during sapropel S1 (Wu et al., 2016). Taking all evidence together, this means that for the central Mediterranean no appreciable Nile contribution can be expected and in any case there will be no difference for sapropel and non-sapropel periods.

The NBEM is considered an important contributor of illite and chlorite to the Ionian Sea, mainly via rivers flowing into the Adriatic Sea (Po and other rivers) and Aegean Sea (southeastern European and Turkish rivers) (Venkatarathnam and Ryan, 1971; Guerzoni et al., 1997; Bout-Roumazeilles et al., 2007; Ehrmann et al., 2007a). Consequently, for central-Mediterranean sediments, increased NBEM riverine inputs may be documented by higher illite and chlorite contents, and illite-associated K/Al ratios (e.g. Nijenhuis and De Lange, 2000; Wehausen and Brumsack, 2000; Martinez-Ruiz et al., 2015).

In core CP10/11, illite is thought to be mostly aeolian in origin during non-AHP intervals. By contrast, during the S1a period, the relatively high contents of illite (and associated K/Al) and chlorite, as well as synchronous changes therein are interpreted to reflect enhanced NBEM riverine inputs (Figure 5b,e,g). This interpretation is supported by the wettest conditions over the NBEM during the S1a interval, as indicated by speleothem $\delta^{18}O$ data and pollen-based precipitation estimates (e.g. Zanchetta et al., 2007; Magny et al., 2013). Moreover, the profiles of K/Al and illite show a close relationship with that of the end member 4-EM3 (modal grain size 3 μm), which represents fine, fluvial particles (Figures 5b). The narrow grain-size distribution, i.e. good sorting of 4-EM3, suggests a long-range delivery of

river-borne material (Figure 3d). This characterization is similar but more prominent at site ODP964 (Zhao et al., 2016), which is likely to be due to a higher, more proximal riverine contribution enriched in both illite and chlorite (i.e. NBEM) (Figure 5e,g). By contrast, the NBEM riverine inputs during the AHP, had little effect on the MD04-2797 sediments in the Strait of Sicily (Bout-Roumazeilles et al., 2013), potentially due to the eastward flowing surface waters (Figures 1; 5f,h).

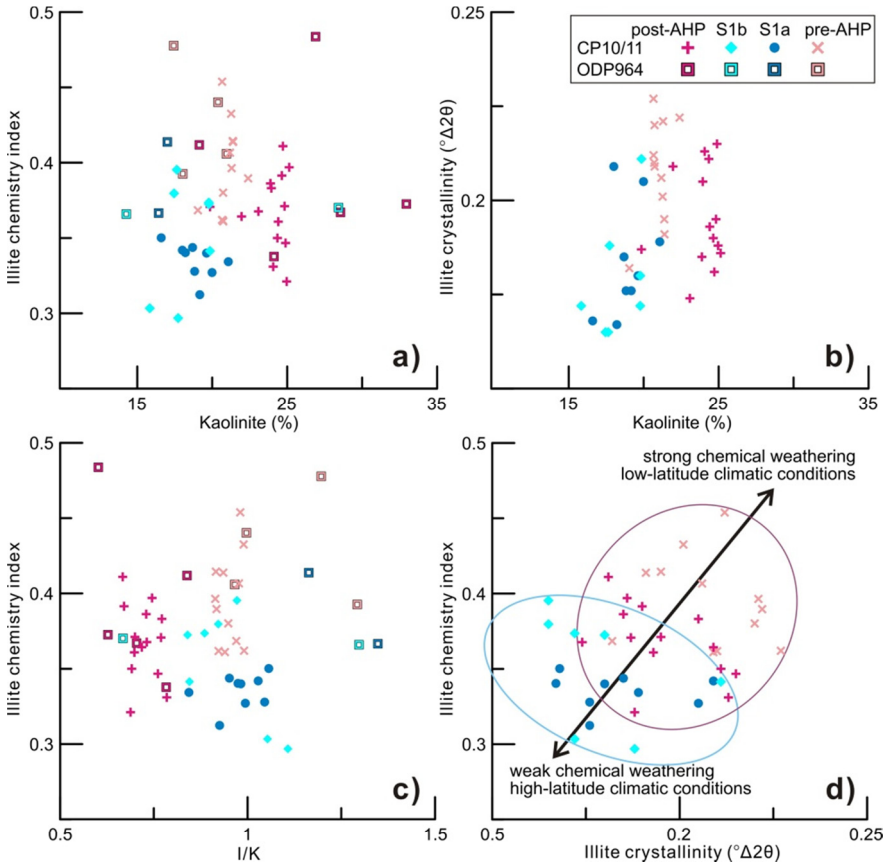

Figure 7 Plots of illite chemistry index, illite crystallinity, I/K (illite/kaolinite) ratio, and kaolinite content to discriminate different sources of illite for core CP10/11 (also ODP964; Zhao et al., 2016). During non-AHP intervals, the illite is mostly aeolian-origin derived from low latitudes (Saharan dust), whereas during sapropel S1 the illite was mainly delivered by high-latitude (NBEM) riverine inputs. The tephra-related interval (~3.0–1.5 ka) is excluded (see Section 3.1).

A peculiar interval (~6–4 ka) occurs with enhanced 4-EM3 and a low but subsequently increasing K/Al (Figure 5b). This increase can also be seen in the grain-size records of MD04-2797 (c.f. Bout-Roumazeilles et al., 2013). This may be

linked to the onset of enforced circulation because of renewed deepwater formation at the end of sapropel S1 formation (Rohling, 1994; Rohling et al., 2015; Filippidi et al., 2016). The renewed circulation may have caused an intensified flow of surface waters, thereby transporting more shelf-derived material eastward. This material is fine-grained and relatively well-sorted, thus for grain size is assigned to 4-EM3, but its elemental composition, e.g. K/Al, is rather mixed and unrelated to NBEM.

4.2 Characterization of past fluvial discharge from the Libyan-Tunisian margin

We have now distinguished Saharan dust and NBEM riverine inputs for core CP10/11 and attributed these to the first three end members. The 4th end member, 4-EM4, exhibits a close correspondence with the smectite content and Mg/Al (and Ni/Al, Cr/Al) ratios (Figure 6d–h). This reveals the existence of an important fluvial contribution during the AHP, particularly during the late-AHP, S1b phase. Below, we suggest that this is indicative for paleodrainage discharges from the Libyan-Tunisian margin.

4.2.1 Geochemical and clay-mineral composition

Detrital Mg and K are often associated with chlorite and illite, respectively. This association and the parallel variability of Mg/Al and K/Al in various EMS records have been related to the NBEM riverine inputs enriched in both illite and chlorite (Martinez-Ruiz et al., 2015, and references therein). Such river-borne material is thought to result from weathering of ultramafic rocks (e.g. Wehausen and Brumsack, 2000). In addition, other minerals such as palygorskite and smectite could significantly contribute to the sedimentary Mg content (e.g. Bout-Roumazeilles et al., 2007; Scheuvens et al., 2013; Martinez-Ruiz et al., 2015).

A combination of 1) higher Mg/Al during the AHP and 2) contrasting patterns between Mg/Al and K/Al suggests that the majority of Mg in core CP10/11 was derived from a different riverine source than the NBEM (Figures 5b; 6e). Above, we discussed that dust and Nile sources can be discounted. Consequently, two potential source areas remain: redeposition from the Strait of Sicily and North-African fluvial discharge. The low detrital Mg/Al ratio observed in sediments from the Strait of Sicily excludes this area as a source (0.11: after Böttcher et al., 2003; 0.110±0.005: G.J. de Lange, unpublished data for Holocene sediments at ODP Site 963).

Instead, the striking similarity between Mg/Al and smectite profiles in core CP10/11 seems to signify that the Mg input is associated with a smectite-rich detrital supply (Figure 6e,h). Increases in smectite content during sapropel S1 in core CP10/11, and less clearly in ODP964, can also be seen in core MD04-2797 (Bout-

Roumazeilles et al., 2013; Zhao et al., 2016) (Figure 6h,i). Therefore, the correspondence between the Mg/Al and smectite in core CP10/11, and the smectite in cores MD04-2797 and ODP964 is interpreted here to indicate that these multiple-phased changes are controlled by a similar, nearby provenance (Figure 8e–g). Given the limited supply of Saharan dust during the AHP and the absence of major rivers in this area today, we suggest that the inferred Mg- and smectite-rich detrital supply were delivered via paleodrainage systems from the wider North-African margin. Presently buried under younger aeolian deposits, the paleodrainage systems should have been reactivated during the most-intense humid phase of the AHP (i.e. the S1b). This is in agreement with the deduced composition (low Ti/Al and K/Al) for the detrital supplies from fossil river/wadi systems along the Libyan-Tunisian margin (Wu et al., 2016). In addition, this corresponds with the derived fluvial grain-size end member 4-EM4 (see Section 4.2.2).

In view of the eastward flowing surface waters in the southern central Mediterranean, i.e. across sites MD04-2797 and subsequently CP10/11 and ODP964 (Figure 1), the coherent changes recorded in these cores may indicate that such paleodrainage-related supplies mainly originated from the west. The most-obvious region is at the Libyan-Tunisian margin, along the Gulf of Gabès. Accordingly, the most-likely route is the Irharhar, which is a large topography-deduced subaerial system interlinked with diverse ephemeral/fossil networks over west Libya and Tunisia/Algeria, with an catchment area of 842,000 km^2 and a length of 1482 km (Vörösmarty et al., 2000; Coulthard et al., 2013) (Figure 1). Particularly, the Irharhar includes the present-day ephemeral river Medjerda draining Tunisia. Such pathway is supported by the Sr-Nd isotopes gradient of detrital material along a W–E transect in the EMS (Wu et al., 2016), and the extensive geoarchaeological data suggesting more human occupation during the late-AHP in western than in eastern Libya (Manning and Timpson, 2014). Nevertheless, alternative fluvial contributions from eastern Libya towards the Gulf of Sirte, as suggested for sapropel S5, cannot be fully excluded.

The co-varying Mg/Al, Ni/Al, and Cr/Al profiles in core CP10/11 reflect an ultramafic/mafic rock provenance (Figure 6e–g). There are many ophiolitic and basaltic rocks over the catchment areas of the North-African paleodrainage systems, such as the Hoggar-Acacus Mountains over Algeria and Libya, Tunisian Central Atlas, Tibesti Massif in Libya, and Nafusa Mountains in NE Libya and extending into Tunisia (e.g. Allègre et al., 1981; Kurtz, 1983; Augé et al., 2012; Al-Hafdh and Gafeer, 2015). During the AHP, the reactivated rivers draining catchment areas with occurrences of erodible ultramafic/mafic rock, may have delivered this weathered soil material enriched in Mg, Ni, and Cr to the EMS.

Concurrently, soil deposits over west Libya and Tunisia/Algeria, under recent climatic settings acting as dust source, are characterized by Mg-rich material with a predominance of smectite and palygorskite in the clay-mineral assemblages (Bout-Roumazeilles et al., 2007; 2013). Accordingly, the ephemeral river Medjerda draining western Libya/Tunisia, an important constituent of the Irharhar paleodrainage system (Vörösmarty et al., 2000; Coulthard et al., 2013), is enriched in smectite (up to 50 %) in suspended loads (Claude et al., 1977). This river system is thought to have contributed to the high smectite content reported for central-Mediterranean sediments (c.f. Bout-Roumazeilles et al., 2007). During fluvial transport, the initial clay-mineral assemblages may have been modified, as the fragile fibrous palygorskite is mostly destroyed (Chamley, 1989; Bout-Roumazeilles et al., 2007). Such discrepancy of clay-mineral assemblages between the source area and downstream alluvial sediment has also been reported for the Atlas watersheds (Elmouden et al., 2005).

In short, the most likely pathways for the North-African fluvial discharge to the central Mediterranean during the AHP are those through western Libya and Tunisia/Algeria, mainly via the Irharhar paleodrainage system towards the Gulf of Gabès. The provenance of this river-borne material reflects an important component of ultramafic/mafic rock weathering products (i.e. high Mg/Al, Ni/Al, Cr/Al ratios, and smectite content).

4.2.2 Transport processes and depositional environments

Fine-grained fluvial sediments are typically between 4–6 µm, and mostly deposited on the continental slope, but can reach the deep basin by nepheloid-layer sedimentation and low-density turbidity (Prins et al., 2000; Stuut et al., 2002). Located at the margin of the Libyan slope, core CP10/11 may have been affected by both processes (Figure 1a). The hemipelagic end member 4-EM4, having a dominant mode at ~5 µm (Figure 4d), is inferred as having been settled out of suspension, along with downslope sediment transport.

The downcore profile of 4-EM4 exhibits a close relationship with that of Mg/Al and smectite, suggesting that the 4-EM4 component originates from Libyan-Tunisian paleodrainage systems (Figure 6d,e,h). Similar grain-size distributions have been proposed as fluvial end members for the West-African margin (e.g. Zühlsdorff et al., 2007; Tjallingii et al., 2008). Besides, the 4-EM4 appears to comprise additional shelf-derived sediments, as seen from a minor peak near 150 µm in the modeled grain-size distribution (Figure 3d). For the nearby core MD04-2797, a combination of decreases of wind-blown clay minerals (palygorskite and illite) and higher Zr/Al ratios during the S1b interval has been interpreted as an enhanced transport of riverine-sourced sediments to the shelf (Bout-Roumazeilles et al., 2013). Intensified

fluvial dynamics over western Libya and Tunisia is likely responsible for those changes. Increased flooding and aggradation of relatively coarse overbank deposits during ~7–6 ka have been reported for the Medjerda alluvial sequences (Zielhofer et al., 2004; 2008). Thus, the increased median grain size of detrital material observed during S1b could be explained by elevated contributions of fluvial component 4-EM4, representing a mixture of fine fluvial particles in particular and of some coarse shelf-derived sediments (Figure 4a,e).

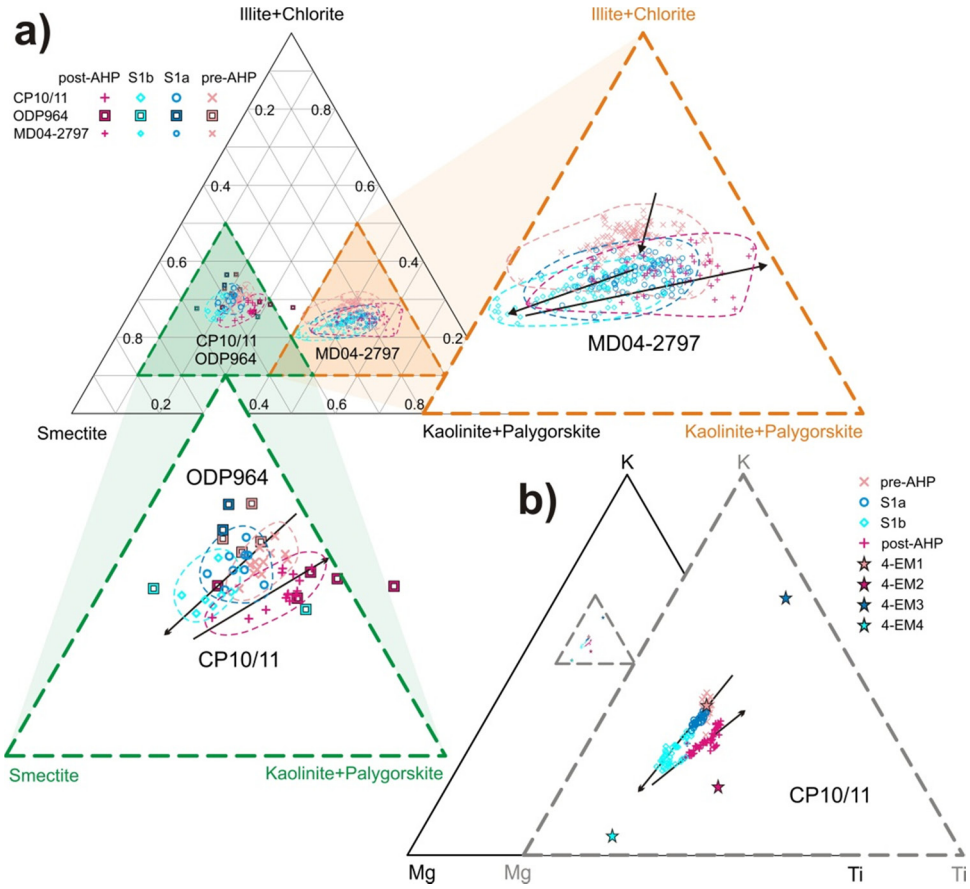

Figure 8 Ternary diagrams of a) clay minerals and b) detrital elements for central Mediterranean cores. The end members comprise: 1) Saharan dust (kaolinite+palygorskite, Ti), 2) NBEM riverine inputs (illite+chlorite, K), and 3) Libyan-Tunisian fluvial discharge (smectite, Mg). The trends of the clay-mineral data for cores CP10/11, ODP964 (Zhao et al., 2016), and MD04-2797 (Bout-Roumazeilles et al., 2013) are consistent, suggesting enhanced paleodrainage contributions from west Libya and Tunisia/Algeria, during sapropel S1b particularly. For core CP10/11, the detrital-element data not only shows similar trends with those of clay minerals, but also well corresponds with the estimated elemental composition of the grain-size 4-EM end members (Table 2). Note that the elemental pattern is identical whether using Al-normalized or not. The tephra-affected data are excluded (see Section 3.1).

During the humid climate periods, the reactivated paleodrainage systems could have provoked floods more frequently, because of strong precipitation seasonality (c.f. Zahar et al., 2008). Even during the last few millennia, extreme seasonal flooding is known for the Medjerda, e.g. in the year of 1973, suspension load ~170 g/liter and 10^8 ton of sediment deposited (Jebari et al., 2012). In the headwater region of the Irharhar paleodrainage system, co-existing evidence for freshwater environments and high evaporation rate suggests strong seasonal fluctuations of lake levels during the period of ~6.8–5.7 ka (Cremaschi and Zerboni, 2009; Zerboni et al., 2015). Persistently high winter- and decreased summer-rainfall have also been shown for the southern Mediterranean areas (e.g. Lake Pergusa) during ~7–5 ka (Magny et al., 2013). Also, simulations have shown a most-enhanced monsoon precipitation during S1b resulting from abundant late-summer moisture, which extended the Saharan rainy season into October (Skinner and Poulsen, 2016). These all are in line with the wettest conditions over NW Libya occurring between ~6.8 and 5.5 ka (Giraudi et al., 2013).

The enhanced precipitation and consequent flooding is consistent with the decreased $\delta^{18}O$ ratio of planktonic foraminifera during sapropel S1 observed in cores CP10/11 and MD04-2797 (Figure 6a). The more negative $\delta^{18}O$ observed for core CP10/11 during the AHP, as indicated by the $\Delta\delta^{18}O$ between CP10/11 and MD04-2797, points to a stronger freshening of surface waters for the former site (Figure 6b). For core MD04-2797, the negative $\Delta\delta_w$ values (i.e. lower than local seawater $\delta^{18}O$) were calculated using the alkenones-based sea surface temperatures (SST). These $\delta^{18}O$ data suggest a relatively low sea surface salinity for the whole sapropel S1 period (Figure 6c). Given the proximity and the anticipated eastward flowing surface waters across MD04-2797 towards CP10/11 site (Figure 1), the observed lower $\delta^{18}O$ for the latter may indicates additional excess freshwater supplies relative to the former. This coincides with the Irharhar runoff discussed above. These observations confirm that the fluvial discharge not only transports the detrital material, but also considerable freshwater.

4.3 Controls on the paleodrainage reactivation and delivery over North Africa

4.3.1 Integrating central-Mediterranean sediment provenance

To summarize, the grain-size data of core CP10/11 can best be described by two aeolian and two fluvial end members, in good agreement with the characterizations based on elemental geochemistry and clay mineralogy. The quantitative estimation of the elemental ratios for the four grain-size end members lends strong supports to our interpretations above, revealing generally high Ti/Al ratios for the aeolian 4-EM1 and 4-EM2, relatively high K/Al for the NBEM riverine inputs (4-EM3), and

particularly high Mg/Al for the North-African paleodrainage discharge (4-EM4) (Table 2).

Table 2 Estimated elemental ratios of the grain-size end members for core CP10/11 [a]

Modeled grain-size end members	Ti/Al (mg/g)	K/Al (mg/g)	Mg/Al (mg/g)
4-EM1	57.1	262	137
4-EM2	65.2	234	138
4-EM3	54.7	258	101
4-EM4	54.6	238	172

[a] For calculation refers to Section 3.4.

The results from clay minerals and major detrital-elements are presented in adjoining ternary diagrams to further integrate the above-discussed characteristics (Figure 8). The end members comprise: 1) Saharan dust (high Ti and kaolinite, and palygorskite), 2) NBEM riverine inputs (high K, illite and chlorite), and 3) fluvial discharge from the Libyan-Tunisian margin (high Mg and smectite). Note that the two aeolian end members are considered as one single end member of Saharan dust, as they both have generally high Ti and kaolinite contents, with detectable palygorskite.

Derived from different size fractions, the clay-mineral (Figure 8a) and elemental (Figure 8b) data are highly consistent, both displaying a trend towards smectite- and Mg-rich from the pre-AHP to S1b intervals, followed by a trend more towards kaolinite- and Ti-rich signals for the post-AHP. This evolutionary pattern also well corresponds with the estimated elemental composition of the grain-size 4-EM end members (Table 2; Figure 8b). Together, the remarkable similarity in the data evolution between clay minerals, major detrital-elements, and grain-size distribution strongly corroborates our interpretations above.

After the provenance characterization for central-Mediterranean sediments, critical proxies are extracted to assess the hydroclimate changes over North Africa. Following comparable studies on sediments deposited offshore continental margins (e.g. Stuut et al., 2002; Tjallingii et al., 2008), we use the log-ratio of the North-African fluvial end member (4-EM4) and aeolian end members (4-EM1 + 4-EM2) to indicate relative changes of continental humidity and surface cover in North Africa (Figure 9j). The use of this proxy is validated by the co-varying S/K ratio for the clay-sized fraction (Figure 9h), which is interpreted to indicate the relative contribution of North-African fluvial vs. aeolian inputs. Similarly, we use the log-ratio of 4-EM4 and 4-EM3 to evaluate the relative humidity between North Africa and the NBEM regions (Figure 4g).

4.3.2 Forcing and modulation of North-African paleodrainage discharges

The Libyan-Tunisian fluvial discharge appears to be most pronounced during the sapropel S1b interval, delivering considerable Mg- and smectite-rich detrital material and freshwater to the central Mediterranean Sea (Figure 9d–j). The strongest discharge can be related to intensified fluvial dynamics and the wettest conditions in western Libya and Tunisia/Algeria (Zielhofer et al., 2004; 2008; Giraudi et al., 2013) (Figure 9c). Moreover, variability of this North-African fluvial discharge to the central Mediterranean Sea has a tight correspondence with that of a large paleodrainage system towards the West-African margin. Today, the Atlantic continental margin of West Africa between 15 and 25°N is dominated by Saharan arid conditions and receives little fluvial input (Ratmeyer et al., 1999; deMenocal et al., 2000). For this area, several lines of evidence have shown that during late-Quaternary sapropel times reactivation of the Tamanrasett paleodrainage system contributed to canyon formation and sediment deposition offshore the Mauritania margin (e.g. core GeoB7920; Krastel et al., 2004; Antobreh and Krastel, 2006; Zühlsdorff et al., 2007; Tjallingii et al., 2008; Skonieczny et al., 2015) (Figure 1; see Section 1). There is a remarkable similarity in the humidity and detrital records between our Mediterranean core CP10/11 and the Atlantic core GeoB7920 (Figure 9f–j), which seems to indicate a common headwater region, the Hoggar-Acacus Mountains (Figure 1). Indeed, the central Saharan mountains have been reported to play a crucial role in favoring fluvial supplies to the lowlands over the AHP, which acted as a “water tower” receiving the earlier rainfall/water supply from elevated areas (Hoelzmann et al., 1998; Lézine et al., 2011).

Apart from a common headwater region, such close correspondence between the paleodrainage records from the North- and West-African margins may signify a similar climate forcing and modulation mechanism (Figure 9). A strengthening of the African monsoon driven by an early Holocene precessional insolation maximum, with associated increases in summer precipitation, is the primary forcing of the AHP (Kutzbach, 1981; Claussen et al., 1999). The co-varying humidity indexes and detrital records for cores CP10/11 and GeoB7920 (Figure 9f–j) are concurrent with changes in the extension of open-water bodies over North Africa (Figure 9a), and in contrast to Saharan dust inputs (Figure 9h). It has been suggested that the North-African surface characteristics exerts a fundamental control on dust emission (Claussen et al., 1999; deMenocal et al., 2000; Egerer et al., 2016). Based on the above-observed correspondence, our results further suggest a similar control on paleodrainage delivery. All of these records show a maximum humidity in the late-AHP, S1b interval (i.e. ~8.0–5.5 ka) (Figure 9). However, there is a lag of ~3–5 ka with the precessional insolation maxima (Figure 9a), and records are asynchronous with the precipitation proxy data of the African monsoon (Figure 9k,l).

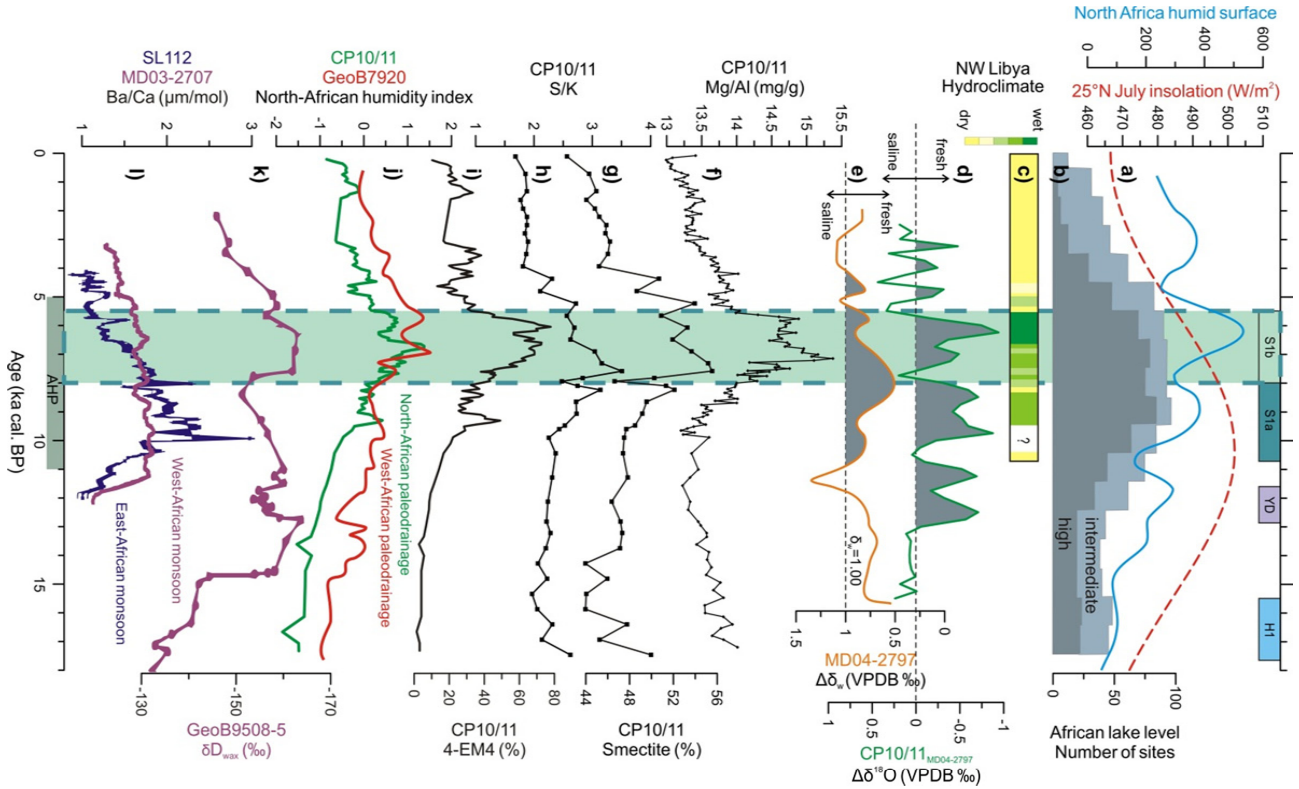

Figure 9 Hydroclimate proxy records from the central Mediterranean and North Africa display a tight correspondence during late-AHP, S1b interval, inferring a dominant control of North-African humid surface on the paleodrainage delivery, modulated by groundwater level, in response to the insolation-driven West-African monsoon precipitation. a) Mean March insolation at 25°N (Laskar et al., 2004); evolution of estimated (0.85 probability) humid surface over North Africa (10–28°N) (Lézine et al., 2011). b) Lake level status and number of sites in North Africa (after deMenocal and Tierney, 2012). c) Hydroclimate reconstruction of Jefara Plain in NW Libya (Giraudi et al., 2013). d) Planktonic foraminiferal $\Delta\delta^{18}O$ between CP10/11 and MD04-2797. e) Salinity changes recorded by $\Delta\delta_w$ from core MD04-2797 (Essallami et al., 2007). f) Detrital Mg/Al for core CP10/11. g) Smectite in CP10/11. h) S/K (smectite/kaolinite) in CP10/11. i) 4-EM4 proportion, indicative of North-African paleodrainage discharge. j) North-African humidity index derived from grain-size data, expressed as a log-ratio of the North-African fluvial and aeolian end members in CP10/11 and GeoB7920 (Tjallingii et al., 2008; Skonieczny et al., 2015), providing an integrated measure of changes in paleodrainage discharges. k) Hydrogen isotopic composition of leaf waxes (δD_{wax}) in core GeoB9508-5, taken as a direct indicator of changes in West-African monsoon precipitation (Niedermeyer et al., 2010). l) Ba/Ca in planktonic foraminiferal calcite, a proxy for regional riverine runoff and associated monsoon precipitation, retrieved from the Levantine Basin (SL112) and Gulf of Guinea (MD03-2797), respectively (Weldeab et al., 2007; 2014).

This contrast can be best explained by a modulating role of groundwater level, which has been recently highlighted by Lézine et al. (2011) on the basis of a comprehensive examination of >1500 paleohydrological dated records over North Africa. The highest number of lake initiations, associated with enhanced African monsoon precipitation, is recorded in the S1a interval. At that time, however, the geographical extension of open-water bodies was more fragmented and the groundwater was at a relatively low level, resulting in limited paleodrainage-related supplies (Figure 9a,b). Once the continuously high precipitation has replenished the groundwater to a sufficient level, i.e. after ~8 ka, the fluvial systems including lakes, wetlands, and rivers, were interlinked and fully developed at ~6 ka (Lézine et al., 2011) (Figure 9a,b). This largest geographical extension of open-water bodies for the late-AHP (i.e. ~8–6 ka) have also been deduced from dust studies, as discussed below (McGee et al., 2013; Cockerton et al., 2014; Egerer et al., 2016). Specifically, lakes and wetlands were widespread up to 30°N and covered ~7.6% of North Africa (Hoelzmann et al., 1998; Jolly et al., 1998). The largest water body was Lake Mega-Chad, which attained an area of 361,000 km^2 and a depth of up to 160 m (c.f. Armitage et al., 2015). There may be even a most-enhanced Saharan precipitation during the late-AHP (Niedermeyer et al., 2010; Skinner and Poulsen, 2016) (Figure 9k). Therefore, such extensive humid surfaces and persistently wet conditions during the late-AHP, S1b phase should have promoted the paleodrainage-related runoff to the greatest extent (Figure 9).

Coherently, the largest humid surfaces (Figure 9a) coincides with the lowest dust input occurred in the late-AHP, S1b interval, as indicated by the S/K ratio (Figure 9h). This point is also visible in various aeolian parameters (e.g. Ti/Al, kaolinite, 4-EM1, 4-EM2) (Figures 4b–d; 5a,c). This coincidence reflects the control of North-African humid surfaces on Saharan dust emission. In fact, the most diminished fluxes of Saharan dust (i.e. 2–5 times lower than pre-industrial fluxes) have been systematically reported for the period of ~8–6 ka, in relation to the wettest Saharan landscape (McGee et al., 2013; Cockerton et al., 2014; Egerer et al., 2016). In addition, this inference is in line with the relative humidity between the southern and northern borderlands of the EMS (Figure 4g). During the AHP and particularly during S1b, climatic conditions were more humid in North Africa (Giraudi et al., 2013), whereas during non-AHP intervals, those in the NBEM were wetter. The former is suggested to be due to a southward shift of the ITCZ during AHP, and the latter is related to sustained high winter precipitation (Magny et al., 2013).

In a broader perspective, we compare our results with precipitation proxy records for the East- and West-African monsoon (Figure 1b). The record of hydrogen isotopic composition of leaf waxes (δD_{wax}) offshore Senegal (close to GeoB7920), has been interpreted to directly reflect the variability of West-African monsoon precipitation

(Niedermeyer et al., 2010) (Figure 9k). As a reliable proxy for the Nile and the Niger/Sanaga runoffs, the planktonic foraminiferal Ba/Ca records are considered to represent a spatially integrated measure of changes in precipitation of the East- and West-African monsoon, respectively (Weldeab et al., 2007; 2014) (Figure 9l). It has been suggested that the intensified East-African monsoon during sapropel S1 was largely influenced by Indian Ocean SST variations (Tierney and deMenocal, 2013; Hennekam et al., 2014; Weldeab et al., 2014), while the West-African monsoon precipitation has an Atlantic Ocean moisture source (Schefuß et al., 2005; Weldeab et al., 2007; Niedermeyer et al., 2010; Shanahan et al., 2015). Consequently, the evolution of East- and West-African monsoon is different (Figure 9k,l). Placing our results and interpretations in this context, the paleodrainage delivery seems to be primarily controlled by the West-African monsoon, which maintained a high precipitation over the whole AHP (Figures 1b; 9f–l). This inference is supported by the Sahara/Sahel vulnerability to the Atlantic, West-African monsoon changes in the long-term (Lézine et al., 2011). Furthermore, it is in agreement with various proxy records of West-African monsoon variability, showing persistently enhanced precipitation during the late-AHP, S1b interval (e.g. deMenocal et al., 2000; Schefuß et al., 2005; Niedermeyer et al., 2010; Shanahan et al., 2015, and references therein).

In summary, the above-discussed correspondences appear to indicate a dominant control of Saharan humid surfaces on the reactivation and delivery of paleodrainage systems over North Africa, which were modulated by groundwater level, in response to insolation-driven West-African monsoon precipitation.

5 Conclusions

On the basis of provenance determination for terrigenous detrital sediments in core CP10/11, we draw the following conclusions for the central Mediterranean during the past 18 ka:

a) During the African Humid period (AHP; ~11–5 ka), largely coinciding with the formation of sapropel S1, riverine deposition to the central Mediterranean dominates, whereas for the preceding and following arid climate periods, the provenance is dust-dominated. Two aeolian and two fluvial end members can be distinguished using end-member modeling of grain-size distributions, elemental and clay mineralogical composition, with their elemental fingerprints quantitatively estimated.

b) The two aeolian end members represent the different supplies of Saharan dust that dominate before and after the AHP. Saharan dust is characterized by generally high Ti and kaolinite, and detectable palygorskite contents. The different provenance of Saharan dust is related to changes in the meridional

position of the ITCZ before and after the AHP, reflecting a large-scale atmospheric reorganization over North Africa.

c) During sapropel S1a (~10.6–8.0 ka), the NBEM (Northern Borderlands of Eastern Mediterranean) riverine inputs rise, as indicated by co-increasing illite and chlorite, and enhanced K contents.

d) During late-AHP, S1b interval (~8.0–5.5 ka), by contrast, riverine inputs appear to be predominantly derived from the North-African, Libyan-Tunisian margin. The inferred fluvial discharge should have transported considerable (Mg- and smectite-rich) detrital materials and freshwater via the paleodrainage networks towards the Gulf of Gabès (mainly via the paleo-river Irharhar). These ancient water courses were reactivated by intensified African monsoon precipitation and were most developed during the late-AHP. This period coincides with the enhanced fluvial dynamics and wettest conditions over western Libya and Tunisia/Algeria. In a wider perspective, the late-AHP, S1b phase is not only synchronous with the lowest supply of Saharan dust and the largest extension of open-water bodies in North Africa, but is also consistent with the West-African monsoon variability. Furthermore, changes in this North-African fluvial discharge correspond with a paleodrainage record offshore the Atlantic, West-African margin, which may indicate a common headwaters' region in the central Saharan mountains, with a similar climate mechanism. Taken together, we propose that the reactivation and delivery of paleodrainage discharges over North Africa were mainly controlled by Saharan humid surfaces, with modulation by groundwater level, in response to the insolation-driven West-African monsoon precipitation.

Acknowledgments

Many thanks are given to Yanli Li who performed the XRD analyses at Tongji University. We acknowledge Arnold van Dijk, Helen de Waard, as well as Dineke van de Meent-Olieman and Ton Zalm for $\delta^{18}O_{ruber}$, ICP-OES, and grain-size analyses at Utrecht University. We also thank Viviane Bout-Roumazeilles and Gert Jan Weltje for kindly providing clay-mineral data of core MD04-2797 and the End-Member Model Algorithm, respectively. We are grateful to crew and scientists on board RV *Pelagia* during CORTADO 2011 cruise for collecting cores CP10BC and CP11PC. Two anonymous reviewers are thanked for their valuable comments and suggestions. The China Scholarship Council – Utrecht University PhD Program is acknowledged for financial support (CSC No. 201206260116).

Appendix. Supplementary material

Supplementary material related to this article is attached.

Chapter 3 Appendix. Supplementary material

This **Supplementary material** provides a detailed description of age model for core CP10/11.

The chronology for core CP10/11 was developed by means of 8 radiocarbon dates on mixed planktonic foraminifers, and 9 measurements of ^{210}Pb and ^{137}Cs on sediment samples. Around 15 mg of mixed planktonic foraminifera (*G. ruber* and *G. sacculifer*) in the 150–600 μm fractions was picked for ^{14}C analyses at Poznan Radiocarbon Laboratory (Table 1). All ^{14}C dates were converted into calendar ages using the Marine13 calibration curve (Reimer et al., 2013) implemented in the program Calib 7.0 (Stuiver and Reimer, 1993), with no regional reservoir correction (i.e. ΔR=0) which is valid for the modern Mediterranean (Siani et al., 2000).

Table S1 Age tie-points of cores CP10BC and CP11PC

Core	Depth (cm)	Age ± 2σ (ka cal. BP) [a]	Analysis
CP10BC	0–3	0	^{210}Pb and ^{137}Cs on bulk sediment
CP10BC	6–6.5 [a]	1.893 ± 0.085	^{14}C on planktonic foraminifera
CP10BC	18.5–19 [a]	5.486 ± 0.099	^{14}C on planktonic foraminifera
CP10BC	25.5–26	7.422 ± 0.089	^{14}C on planktonic foraminifera
CP10BC	28–28.5 [a]	7.795 ± 0.107	^{14}C on planktonic foraminifera
CP10BC	34–34.5 [a]	9.423 ± 0.101	^{14}C on planktonic foraminifera
CP11PC	4–4.5	2.385 ± 0.085	^{14}C on planktonic foraminifera
CP11PC	12.5–13	6.1	S1-ending, based on Mn/Al
CP11PC	26–26.5	10.8	S1-onset, based on Ba/Al
CP11PC	30–30.5	12.691 ± 0.116	^{14}C on planktonic foraminifera
CP11PC	47–47.5	17.201 ± 0.253	^{14}C on planktonic foraminifera

[a] Data from Wu et al. (2016).

Inventories and activities of $^{210}Pb_{xs}$ (excess-^{210}Pb, i.e. ^{210}Pb minus ^{226}Ra activities) and ^{137}Cs on bulk sediments from core CP10BC were determined at ENEA, La Spezia (c.f. Barsanti et al., 2011). As presented in Figure S1, the profiles of $^{210}Pb_{xs}$ and ^{137}Cs activities show generally decaying shapes, with a subsurface maximum at 2 cm. Both radionuclides are below the minimum detectable activities at 4 cm. The similarity between the profiles of the two radionuclides, despite their different input functions, indicates that the difference in their input at the sediment-water interface is not important. Therefore, the main process occurring is diffusion, suggesting minor bioturbation down to 3 cm depth at most (Figure S1). This justifies taking the age of CP10BC core-top as the present-day (c.f. Wu et al., 2016). Moreover, assuming a negligible sedimentation rate compared to the decay rate, and fitting the $^{210}Pb_{xs}$ profile with an exponential decay, it is possible to estimate the bioturbation coefficient (Db): Db = 0.047±0.009 cm^2/yr. The $^{210}Pb_{xs}$ and ^{137}Cs inventories are 2740±240 and 92±14 Bq/m^2, respectively. The ^{210}Pb surface value and inventory are

in the same range as for other cores in Ionian Sea (Barsanti et al. 2011, Angelidis et al., 2011).

The correlation between CP11PC and CP10BC was carried out on the basis of absolute ^{14}C dates in the respective sections, and of well-established criteria of sapropel S1 boundaries. The residual S1 is characterized by enhanced total organic carbon (TOC) contents, while the initial full S1 period is recognized as the elevated Ba/Al zone (Figure S2a,b). The difference is due to the post-depositional oxidation that removed most of TOC but not biogenic Ba from the upper-most S1 interval; thus Ba/Al ratio is considered to reflect initial TOC accumulation rates, i.e. sapropel boundaries (De Lange et al., 1989; Van Santvoort et al., 1996; Thomson et al., 1999; Mercone et al., 2000). The two separated Mn-rich zones correspond to the upper boundaries of the residual and the initial S1, respectively. The lower Mn-rich zone is forming actively, whereas the upper one has been related to reventilation of the water column during S1 termination, signaling the conversion from anoxic to oxic sedimentary conditions (Thomson et al., 1995; 1999; Van Santvoort et al., 1996; Reitz et al., 2006) (Figure S2).

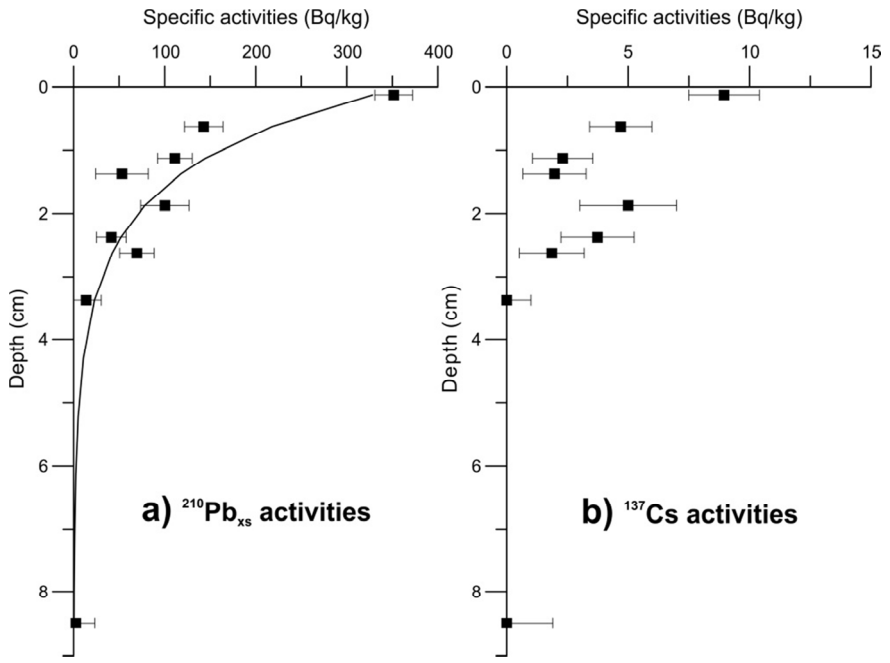

Figure S1 Specific activities of a) $^{210}Pb_{xs}$ (i. e. ^{210}Pb minus ^{226}Ra activities) and b) ^{137}Cs on bulk sediments of core CP10BC, showing very minor bioturbation going down to 3 cm depth at most. This justifies the use of CP10BC core-top as the present day in this paper. Where values reaches zero, the error bars represent the MDA instead of measurement uncertainties (1σ). The solid line indicates the exponential fitting.

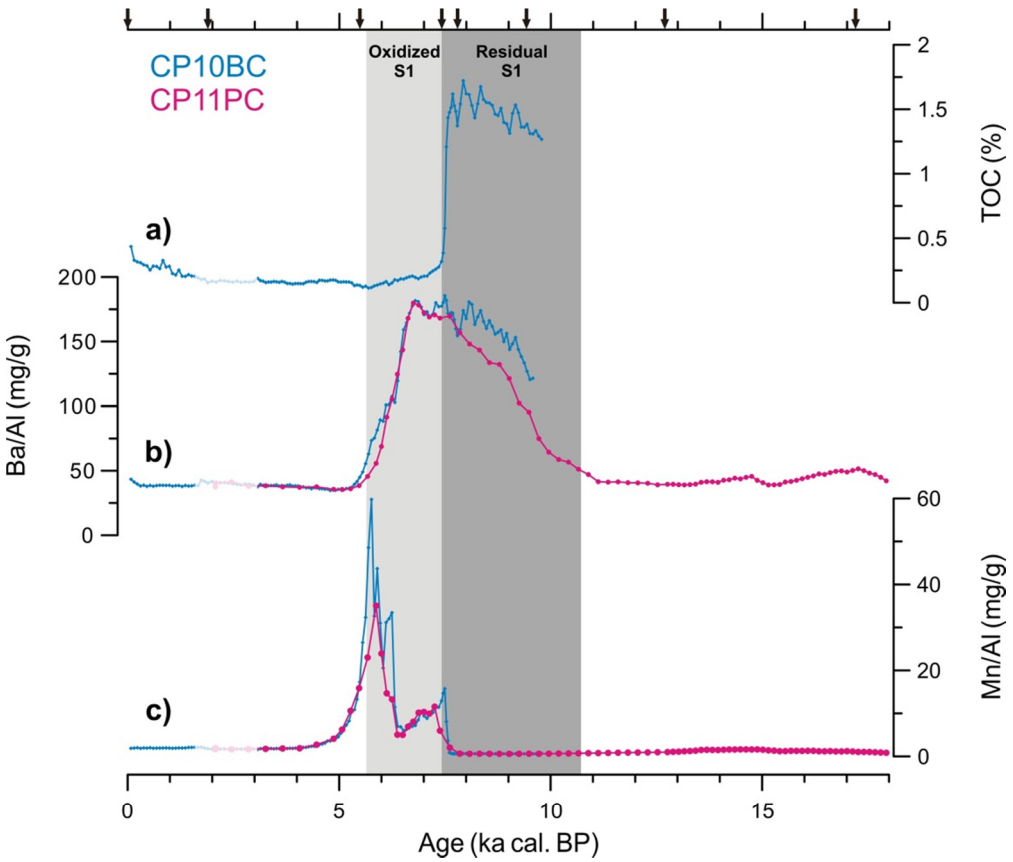

Figure S2 Sapropel S1 geochemistry of core-site CP10/11, with CP10BC (blue) (Wu et al., 2016) and CP11PC (magenta) records shown. a) TOC (total organic carbon). b) Ba/Al and c) Mn/Al on bulk samples. Dark and light bars indicate the residual and oxidized sections of sapropel S1, respectively. Age tie-points are indicated by arrows at the upper axis.

In this context, it has been systematically shown that the S1 deposition as defined on the Ba/Al and TOC criteria began basin-wide at 10.8±0.5 ka (i.e. cal. BP, unless stated otherwise), and on the Ba/Al and Mn/Al criteria finished at 6.1±0.5 ka (De Lange et al., 2008). In view of reservoir age and other uncertainties (e.g. Siani et al., 2001), the accuracy for sapropel S1 boundaries for CP10/11 may be similar to those reported for basin-wide determined boundaries. Therefore, we take the ages of "10.8 ka" and "6.1 ka" as the onset and the ending of sapropel S1, respectively (after Mercone et al., 2000; De Lange et al., 2008) (Table S1). These calibration ages are fully supported by the observed variability in water contents, color changes, and elemental ratios. By the use of these two correlation points, together with the absolute ^{14}C dates on the overlapped intervals (Table S1), a depth composite was accurately constructed, resulting in the consistent depth-age curves (Figure S3). The

sedimentation rates are between 2.8 and 4.1 cm/ka. A small interval (~7.8–7.4) with seemingly large sedimentation rate occurs in CP10BC (Figure S3a). This may be related to the uncertainties mentioned above. As this has no influence on the data discussed in this paper, we have chosen to keep the age model simple and transparent by using interpolation between ^{14}C age dates.

The reliability of the composite chronology is verified by the close correspondences for various records between CP10BC and CP11PC (Figures S2 and S4). In general, such a more oceanographically consistent policy we adopted for cores CP10BC and CP11PC, i.e. differentiating between sapropel and non-sapropel periods, are likely not only to generate compositional-, but also quantitative differences between such climatically contrasting episodes. Note that the small differences in elemental data between these two cores are mostly related to small analytical differences between ICP-OES series measured in different years. For Mn (Figure S2c), there may be an additional diagenetic component that can be different between cores even if taken at an identical site (Thomson et al, 1995).

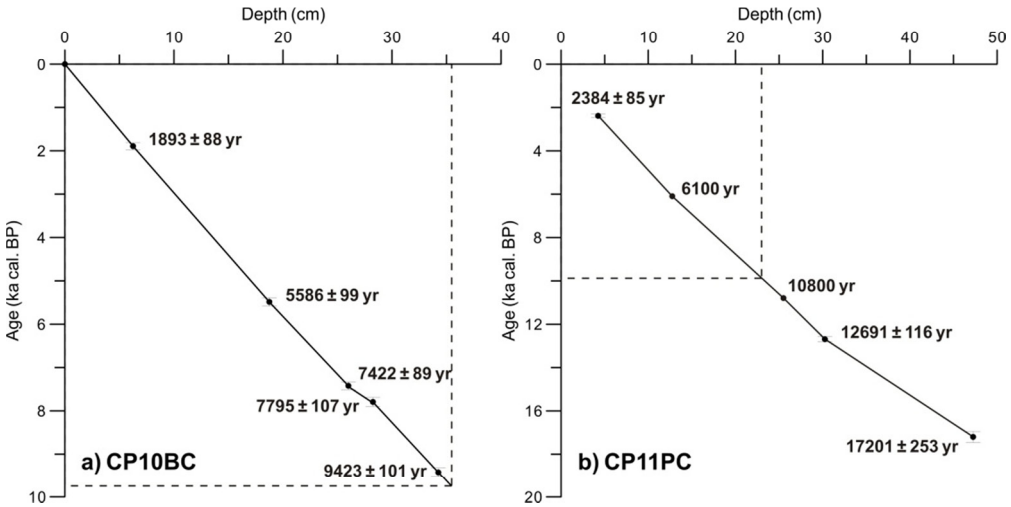

Figure S3 Age model for cores a) CP10BC and b) CP11PC. Note that the depth-age curves are consistent. The 2σ errors are specified. As commonly found, there is a slight difference between the box core (CP10BC) and piston core (CP11PC): the topmost part of CP11PC is thought to be missing. Sediments are slightly more compacted for CP11PC than for CP10BC due to difference in coring friction. Data sources refer to Tables 1 and S2.

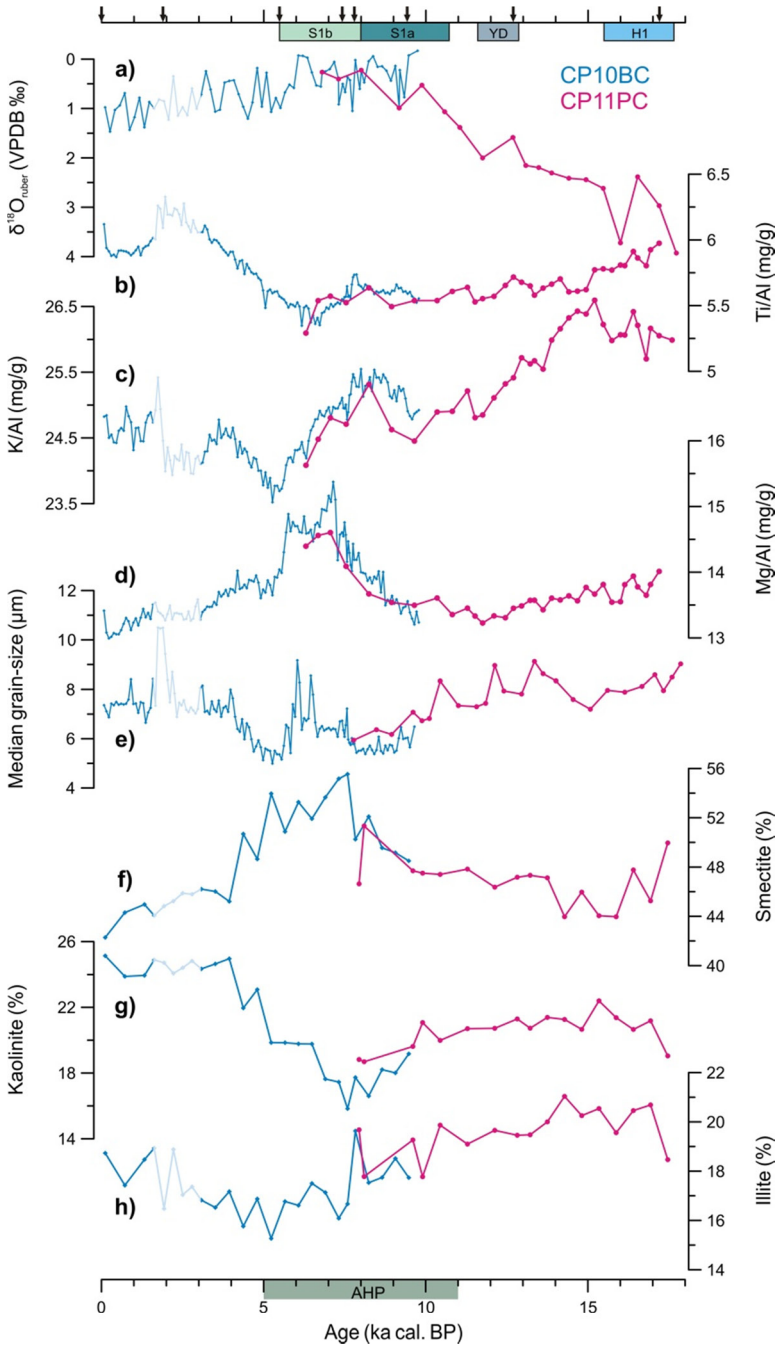

Figure S4 Comparison of various records from CP10BC (blue) and CP11PC (magenta). a) Planktonic foraminiferal G. ruber δ18O. b) Ti/Al, c) K/Al, and d) Mg/Al on detrital basis. e) Median grain-size of detrital particles. f) Smectite, g) Kaolinite, and h) Illite contents.

CHAPTER 4

Riverine supply to the eastern Mediterranean during last interglacial sapropel S5 formation: a basin-wide perspective

Jiawang Wu [a*], Amalia Filippidi [a], Gareth R. Davies [b], and Gert J. de Lange [a]

[a] Department of Earth Sciences – Geochemistry, Faculty of Geosciences, Utrecht University, Princetonplein 9, 3584 CC Utrecht, The Netherlands

[b] Department of Petrology, Faculty of Earth and Life Sciences, Vrije Universiteit (VU) Amsterdam, De Boelelaan 1085, 1081 HV Amsterdam, The Netherlands

[*] Corresponding author: j.w.wu@uu.nl (J. Wu).

(under review in Chemical Geology)

Abstract

Organic-rich sapropel sediments were repeatedly deposited in the eastern Mediterranean Sea (EMS), in response to insolation-driven freshwater forcing. However, the exact freshwater sources and causal associated paleoclimate-related processes remain unresolved. Sapropel S5, formed during the insolation maximum of the last interglacial, is one of the most intensely developed sapropels of the Late-Quaternary. Here, detrital sediments of sapropel S5 obtained from 8 cores, together with 13 EMS surface samples, are analyzed for major elements, rare earth elements, and Sr and Nd isotopes. This permits a basin-wide investigation of the source and distribution of river-borne material to the EMS for sapropel S5, and its comparison to the present-day and the Holocene sapropel S1 period. During the sapropel S5, there was minor Saharan dust input. The marked east–west geochemical gradient in S5 detrital sediments across the EMS is therefore attributed to mixing between fluvial contributions, being Nile discharge, Aegean/Adriatic riverine inputs, and Libyan-Tunisian paleodrainage fluxes. The offshore distribution of Nile sediments during sapropel S5 was comparable to those during S1 and the present. The Nile sediment contribution appears to be only dominant for the Levantine Basin, decreasing to negligible values south of Crete. This rather limited sediment delivery, despite inferred increased runoff during S5, is related to denser vegetation cover on the Ethiopian Highlands. By contrast, small rivers around the Aegean (and Adriatic) Sea brought large amounts of detrital material into the EMS. This is particularly noticeable around Crete and the northern Ionian Sea. The enhanced riverine input is probably due to strong precipitation seasonality over the northern EMS borderlands, particularly for the early phase of the last interglacial maximum. Furthermore, there are substantial fluvial contributions from the Libyan-Tunisian margin to the Ionian Sea sediments, in particular during the last part of sapropel S5. The inferred river-borne material was transported via paleodrainage systems reactivated by intensified monsoon precipitation, and derived from central-Saharan mountains. Compared to sapropel S1, these S5-related paleodrainage fluxes were not only stronger, but also had a more predominant provenance from eastern rather than western Libya.

Keywords

sapropel S5; eastern Mediterranean Sea; provenance; radiogenic isotopes; major elements; rare earth elements

1 Introduction

The eastern Mediterranean Sea (EMS) is a semi-enclosed basin surrounded by catchment areas characterized by different climate regimes (Tzedakis, 2007; Magny et al., 2013; Rohling et al., 2015) and rock compositions (Krom et al., 1999a; Weldeab et al., 2002a; Revel et al., 2010; Wu et al., 2016). Moreover, the EMS has a dynamic thermohaline circulation (Pinardi and Masetti, 2000; Rohling et al., 2015), making it particularly sensitive to changes in the hydrological cycle. This sensitivity is best documented by the rhythmic deposition of organic-rich sapropel units, which is at an astronomically controlled cyclicity throughout the last 13.5 million years (see review by Rohling et al., 2015). Sapropels occur only during the precession-forced summer insolation maxima in the northern hemisphere, coupled with increased seasonal contrast and river runoff (Rossignol-Strick, 1983; Bar-Matthews et al., 2000; Lourens, 2004; Zhao et al., 2012). The enhanced freshwater and nutrients delivered by runoff stimulated a pronounced density stratification of the water column and an increased primary productivity in the surface waters. This ultimately led to anoxic deep-water conditions and sapropel formation in the EMS (e.g. Rossignol-Strick, 1983; De Lange and Ten Haven, 1983; Rohling, 1994; Emeis et al., 2000; 2003; Marino et al., 2007; De Lange et al., 2008).

Regardless of the relative importance of deep-water stagnation versus surface-ocean productivity, sapropel deposition can be viewed as directly related to freshwater forcing and its hydrographic response (Rohling, 1994; Emeis et al., 2003; Marino et al., 2007; Grelaud et al., 2012; Rohling et al., 2015). Indeed, using numerical models, physical oceanography studies have shown that with increasing freshwater forcing the strength of the deep-water stagnation is increased, and that changes in the source of freshwater modulate this effect (Myers et al., 1998; Myers, 2002). This is in agreement with the interplay between thermohaline circulation and deep-water oxygen consumption, as revealed by ocean-biogeochemical modeling (Stratford et al., 2000; Bianchi et al., 2006; Grimm et al., 2015). However, the exact freshwater sources and the controlling paleoclimatic processes are still debated, thereby strongly urging for a spatial investigation on a basin-wide scale.

1.1 Circulation pattern and freshwater forcing

An important characteristic of the present-day Mediterranean is its anti-estuarine circulation pattern. The surface inflow of relatively fresh, low-density water flows eastward with increasing salinity and in a counter-clockwise pathway (Figure 1). Strong evaporation causes the Mediterranean to function as a concentration basin, converting the surface water into deeper outflow of salty, denser water (Pinardi and Masetti, 2000). Consequently, the aridity and, more generally speaking, the hydroclimate over the Mediterranean region, strongly influences the physical parameters of the surface waters (Rohling, 1994; Emeis et al., 2000; 2003; Marino

et al., 2007). These include precipitation/evaporation balance and changes in regional convection, all of which play a central role in the functioning of the thermohaline circulation (Myers et al., 1998; Myers, 2002; Rohling et al., 2015). In other words, there is a basin-averaged excess of evaporation (X) over total freshwater input (i.e. X = E (evaporation) – P (precipitation) – R (runoff); X > 0), in particular for the EMS (Rohling et al., 2015, and references therein).

Such pattern may have varied in the past, especially at times of sapropel formation. The spatial estimates for changes in paleo-freshwater forcing and consequent circulation pattern are mostly based on planktonic foraminiferal oxygen isotope ($\delta^{18}O$) data. Three different hypotheses exist for the Holocene sapropel S1 period suggesting that the present-day west–east surface-water salinity gradient was: 1) reversed to an estuarine-type condition (Thunell and Williams, 1989), 2) changed to a flat field, i.e. no gradient but not reversed (Kallel et al., 1997), and 3) similar to that of today but with a weaker gradient (Rohling and De Rijk, 1999). For an in-depth discussion of these hypotheses see Emeis et al. (2000). Specifically, in comparing single-species records only, Rohling and De Rijk (1999) suggested that the S1 salinity gradient reduced to ~75% of its modern magnitude. This is consistent with simulations regarding changes in Mediterranean salinity and $\delta^{18}O$, inferring that the S1 salinity gradient remained at ~80% of its current value, in response to an X that decreased to 65% (Rohling, 1999). Numerical models of Mediterranean circulation show development of deep-water stagnation with a reduction in X to less than 80% of its present-day value (Myers et al., 1998; Myers, 2002).

Although changes in freshwater balance can be reconstructed from foraminiferal $\delta^{18}O$, such spatial estimate is only done for sapropel S1. More critically, this approach is complicated by the uncertainties in the use of salinity vs. $\delta^{18}O$ relationships and different foraminiferal species (Rohling, 1999; Rohling and De Rijk, 1999), and it carries little provenance information which is crucial for the EMS. In fact, the former uncertainty is related to the runoff freshwater $\delta^{18}O$ which in turn depends on its river system and provenance (e.g. altitude, latitude).

1.2 Detrital sediment provenance and paleodrainage fluxes

The EMS sediments contain distinct terrigenous detrital components, with aeolian and riverine origin, driven by competing climatic processes. A strong east–west gradient has been reported for the EMS sediments, with three main sediment provenances proposed (Venkatarathnam and Ryan, 1971; Krom et al., 1999a; Weldeab et al., 2002a; Klaver et al., 2015). This is due to mixing between two endmembers: “young and mafic” Nile sediment is diluted towards the west by “old and felsic” Saharan dust. Such a provenance pattern can generally explain the variability of sediment composition in the eastern part of the EMS, i.e. the Levantine

Basin (e.g. Krom et al., 1999b; Wehausen and Brumsack, 2000; Ehrmann et al., 2007; Revel et al., 2010; Zhao et al., 2012). For the areas west of Crete, however, the system is much more complex. Besides the traditional two endmembers, a third component needs to be invoked, in particular for the Ionian Sea (e.g. Freydier et al., 2001; Weldeab et al., 2002b; Goudeau et al., 2013; Klaver et al., 2015; Wu et al., 2016). This has been related to fluvial contributions from the wider North-African margin, derived from reactivated paleodrainage systems during sapropel periods (Klaver et al., 2015; Wu et al., 2016; 2017), when a much diminished impact from Saharan dust could be detected (e.g. Weldeab et al., 2002b; Larrasoaña et al., 2003; Castañeda et al., 2009; Liu et al., 2012; Wu et al., 2017).

During sapropel times, intensified monsoon precipitation reactivated the fossil river/wadi systems along the wider North-African margin (Vörösmarty et al., 2000; Paillou et al., 2009; 2012; Coulthard et al., 2013). This not only provided green corridors that favored human dispersal (e.g. Castañeda et al., 2009; Drake et al., 2011; Hoffmann et al., 2016; Timmermann and Friedrich, 2016), but also transported substantial amounts of detrital material and freshwater to the EMS. Such runoff routes have been reported to function for a majority of the Quaternary sapropels, such as S1 (Krom et al., 1999b; Freydier et al., 2001; Wu et al., 2016; 2017), S5 (Rohling et al., 2002; 2004; Sangiorgi et al., 2006; Osborne et al., 2008; 2010), and S6 (Emeis et al., 2003). This scenario is supported by the reconstructed long-term dust records (Larrasoaña et al., 2003), and may also occur for the humid-climate episodes without sapropel deposition (Hoffmann et al., 2016). However, limited information is available on the origin, distribution, and intensity of this North-African paleodrainage contribution. This is partly because existing datasets do not adequately cover the Ionian Sea, and in particular lack information for the Libyan margin. This knowledge is very important as such paleodrainage fluxes and associated networks may have 1) constituted a considerable freshwater source for sapropel formation, 2) played a key role in the nonlinear feedbacks to insolation forcing, and 3) had a major influence on the human migrations out of Africa (c.f. Rohling et al., 2015; Wu et al., 2017).

1.3 Sapropel S5 and the last interglacial maximum

Previous sapropel studies mainly focused on the most-recent, radiocarbon datable sapropel S1 in the Holocene (e.g. Emeis et al. 2000; Freydier et al., 2001; Reitz et al., 2006; Box et al., 2011; Hennekam et al., 2014; Filippidi et al., 2016). Although the general principles are similar, all individual sapropels show their own specific features (Rohling et al., 2015). Sapropel S5 is one of the most intensely developed of the Late Quaternary. It has elevated organic carbon (C_{org}), commonly 7–8% compared to ~2% usually found in other sapropels, and lacks benthic fossils, which indicates persistent anoxia occurred below 300 m water-depth (e.g. Schmiedl et al.,

2003; Rohling et al., 2004; Sangiorgi et al., 2006; Marino et al., 2007; Grelaud et al., 2012).

An important aim of this work is also to provide better analogues for the present-day climate. This is needed to comprehend paleoclimate variability to distinguish between natural climatic- and human induced-changes. Sapropels S1 and S5 formed during insolation-driven monsoon maxima of the current (Holocene) and the last interglacial periods respectively. Both monsoon maxima were interrupted by a dry interlude of several centuries, with concomitant cooling over the Northern Borderlands of the Eastern Mediterranean (NBEM; i.e. Aegean and Adriatic regions) (e.g. S1: Emeis et al., 2000; Hennekam et al., 2014; Filippidi et al., 2016; S5: Rohling et al., 2002; 2004; Schmiedl et al., 2003; Scrivner et al., 2004). As a result, the period of sapropel S5 deposition in the EMS (~128 to 121 ka cal. BP; c.f. Rohling et al., 2015) – last interglacial insolation maximum – Marine Isotope sub-Stage 5e (MIS 5e), has long been regarded as a potential analogue for the present (e.g. Kukla et al., 1997; Rohling et al., 2002; Marino et al., 2007). This period had a strong boreal summer insolation maximum, driven by the coincidence of a minimum in the precessional cycle with a distinct maximum in orbital eccentricity (Berger and Loutre, 1991). This superposition causes a more intensified African monsoon and associated northward migration of the Intertropical Convergence Zone (ITCZ). As a consequence, the freshwater flooding was stronger during sapropel S5 than during S1 (e.g. Rossignol-Strick, 1983; Bar-Matthews et al., 2000; Rohling et al., 2002; 2004).

In short, detailed knowledge of riverine supply to the EMS during sapropel S5 can contribute to a better understanding of sapropel formation, paleoclimate variability, and human migration. Here, we present a comprehensive and basin-wide study for the geochemical composition of detrital sediments of sapropel S5 and of surface samples. Our approach combines the use of major-, trace-elements, as well as Sr and Nd isotopes. Integrating our results with those from published and existing datasets (Table 1; Figure 1), we investigate the influences of different riverine contributions for sapropel S5 at a basin-wide scale and make comparisons with the present-day and Holocene sapropel S1.

2 Material and methods

A total of 17 samples were obtained from sapropel S5 layers in 8 core-sites selected to give a geographical and bathymetric coverage of the EMS (Table 1; Figure 1). The stratigraphic frameworks for these cores were generally established by foraminiferal $\delta^{18}O$ and sapropel chronology (Passier et al., 1998; Lourens, 2004; Kraal et al., 2010; Boere et al., 2011; Wu et al., 2017) (Table 1). The samples were taken to represent the most typical sapropel conditions, based on C_{org}, Ba/Al criteria,

and $\delta^{18}O$ data (c.f. Bar-Matthews et al., 2000; De Lange et al., 2008; Rohling et al., 2015). Note that the foraminiferal surface-water $\delta^{18}O$ data have two distinct peaks for sapropel S5 separated by an interruption of ~1,000 years (Rohling et al., 2002; 2004). Accordingly, our S5 samples are differentiated between a lower S5a and an upper S5b interval. In addition to sapropel S5 samples, 11 surface sediments as well as 2 recent, late-Holocene samples from key-sites in the EMS were processed (Table 1; Figure 1). This provides a refined base for the comparison between sapropel and non-sapropel periods.

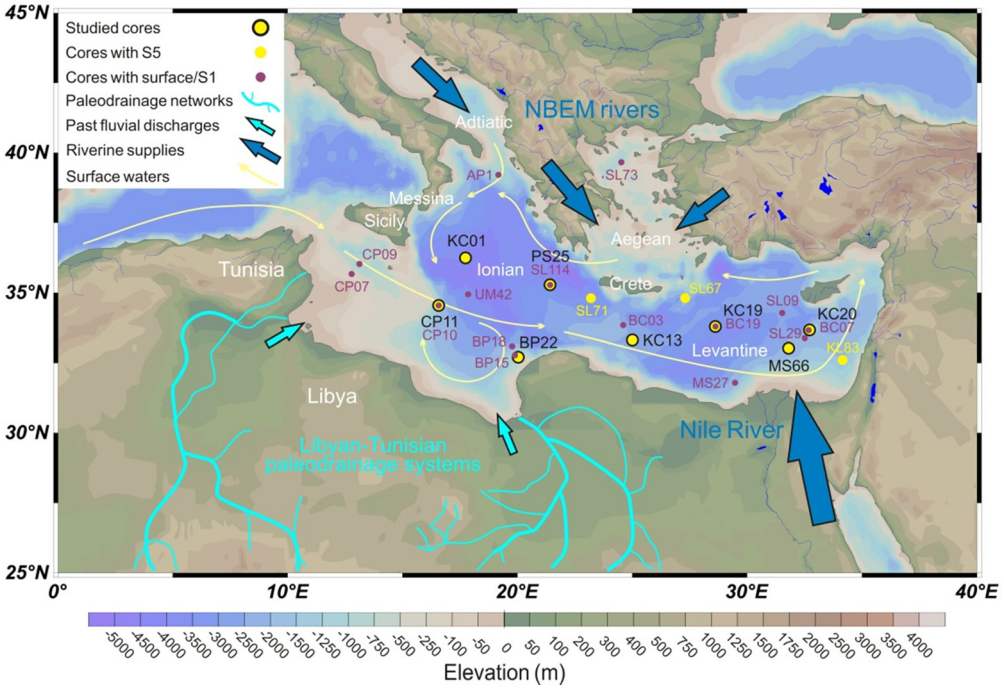

Figure 1 Map of the eastern Mediterranean Sea (EMS) and adjacent areas, showing the locations of studied cores, and the auxiliary cores with samples analyzed and/or data used (Table 1). Paleodrainage networks derived from central Saharan mountains towards the wider North-African margin are outlined (Vörösmarty et al., 2000; Rohling et al., 2002; Paillou et al., 2009; 2012; Coulthard et al., 2013). Present-day perennial riverine discharges into the EMS are also indicated. Large-scale circulation of surface waters is after Pinardi and Masetti (2000).

All geochemical analyses were performed on the detrital, i.e. non-biogenic, lithogenic sediment fraction. Following the protocol of Van Santvoort et al. (1996), freeze-dried, powdered bulk sediments were decarbonated by shaking in 1 M HCl for 4 and 12 hours. Subsequently, the residues were rinsed twice with deionized water, oven-dried at 80 °C, and finely ground for a routine three-step total digestion.

Approximately 125 mg of sample was digested in a mixture of HF-$HClO_4$-HNO_3 and heated at 90 °C in a gastight Teflon vessel for at least 12 hours. Afterward, the solution was evaporated at 160 °C to near dryness, and the residue was then dissolved in 4.5% HNO_3 at 90 °C (Reitz et al., 2006).

Major elements were measured by inductively coupled plasma optical emission spectroscopy (ICP-OES) on a Ciros Vision. The samples were further diluted to analyze trace elements including rare earth elements (REE), using an X-series II inductively coupled plasma mass spectrometry (ICP-MS). For both techniques analytical uncertainties were monitored by measuring blanks, duplicates, and international standards ISE 921 (Van Dijk and Houba, 2000) and MAG-1 (Govindaraju, 1994). For the reported data of major- and trace-elements, the accuracy is better than 6% and 8%, and the precision better than 3% and 5%, respectively.

A smaller selection of 10 samples, including one sapropel S5 sample for each core and two surface sediment samples, was used for isotopic analyses at the Vrije Universiteit (VU) Amsterdam. The Sr and Nd isotopes were separated using conventional ion exchange techniques, and measured on a Triton Plus thermal ionization mass spectrometers and a Neptune Plus multi-collector inductively coupled plasma mass spectrometry, respectively. The $^{87}Sr/^{86}Sr$ and $^{143}Nd/^{144}Nd$ ratios were corrected for mass fractionation by normalizing to $^{86}Sr/^{88}Sr = 0.1194$ and $^{146}Nd/^{144}Nd = 0.7219$, applying the exponential law. The isotopic ratios were reported relative to the standard NBS-SRM 987 ($^{87}Sr/^{86}Sr = 0.710245$; Thirlwall, 1991) and in-house Nd reference material CIGO ($^{143}Nd/^{144}Nd = 0.511342$ equivalent to a La Jolla value of 0.511852; Griselin et al. 2001), respectively. The NBS-SRM 987 gave $^{87}Sr/^{86}Sr = 0.710240 \pm 0.000016$ (2σ, n = 11), and the CIGO yielded $^{143}Nd/^{144}Nd = 0.511384 \pm 0.000014$ (2σ, n = 7). The 2σ reproducibility of Nd isotope measurements was also checked using an in-house standard CPI (8 ppm, n = 3). International reference material MAG-1 was repeatedly run through the entire analytical procedures (n = 3), yielding $^{87}Sr/^{86}Sr$ and $^{143}Nd/^{144}Nd$ ratios of 0.722653 ± 0.000016 and 0.512054 ± 0.000007, respectively. Within error these values are consistent with the average values measured at the same lab ($^{87}Sr/^{86}Sr$: 0.722657 ± 0.000028; $^{143}Nd/^{144}Nd$: 0.512070 ± 0.000012) (Meyer et al., 2011; Klaver et al., 2015; Van der Lubbe et al., 2016). Total procedural blanks were negligible in all cases. Nd isotope compositions are expressed as: $\varepsilon_{Nd} = [(^{143}Nd/^{144}Nd)_{measured} / (^{143}Nd/^{144}Nd)_{CHUR} - 1] \times 10^4$, while CHUR (chondritic uniform reservoir) is 0.512638 (Jacobson and Wasserburg, 1980).

Table 1 General information of the investigated cores over the eastern Mediterranean Sea

Core [a]	Corer/Site [b]	Location	Water-depth	Cruise	Sample analyzed & Data source [c]
CP11 [d]	PC	34°32.7'N, 16°34.0'E	1501 m	RV *Pelagia* 2011	Sapropel S5; Wu et al. (2017)
KC01	site-B	36°15.3'N, 17°44.3'E	3643 m	RV *Marion Dufresne* 1991	Sapropel S5
BP22	PC	32°42.7'N, 20°01.8'E	438 m	RV *Pelagia* 2001	Sapropel S5
PS25	PC	35°17.4'N, 21°24.8'E	3304 m	RV *Pelagia* 2000	Sapropel S5; Kraal et al. (2010)
KC13	site-B	33°19.4'N, 25°00.8'E	2181 m	RV *Marion Dufresne* 1991	Sapropel S5
KC19	site-C	33°47.9'N, 28°36.5'E	2750 m	RV *Marion Dufresne* 1991	Sapropel S5; Passier et al. (1998)
MS66	PC	33°01.9'N, 31°47.9'E	1630 m	RV *Pelagia* 2004	Sapropel S5; Boere et al. (2011)
KC20	site-A	33°40.6'N, 32°42.6'E	882 m	RV *Marion Dufresne* 1991	Sapropel S5
CP07	BC	35°40.5'N, 12°46.7'E	275 m	RV *Pelagia* 2011	Surface
CP09	BC	36°02.2'N, 13°06.6'E	524 m	RV *Pelagia* 2011	Surface
CP10 [d]	BC	34°32.7'N, 16°34.0'E	1501 m	RV *Pelagia* 2011	Surface; Wu et al. (2016; 2017)
AP1 [d]	GC	39°13.0'N, 19°06.8'E	811 m	RV *Urania* 1998	Surface; Tachikawa et al. (2004)
BP18	BC	33°06.0'N, 19°46.4'E	1850 m	RV *Pelagia* 2001	Surface
BP15	BC	32°46.7'N, 19°52.6'E	665 m	RV *Pelagia* 2001	Surface
SL114 [d]	BC	35°17.2'N, 21°24.5'E	3390 m	RV *Logachev* 1999	Surface; Wu et al. (2016)
SL73 [d]	BC	39°39.7'N, 24°30.7'E	339 m	RV *Logachev* 1999	Surface; Tachikawa et al. (2004)
SL09	BC	34°17.2'N, 31°31.4'E	2302 m	RV *Logachev* 1999	Surface
SL29	BC	33°23.4'N, 32°30.2'E	1587 m	RV *Logachev* 1999	Surface
BC07 [d]	BC	33°40.0'N, 32°40.0'E	893 m	RV *Marion Dufresne* 1995	Surface; Freydier et al. (2001)
BC03 [d]	BC	33°22.5'N, 24°46.0'E	2180 m	RV *Marion Dufresne* 1995	post-S1; Freydier et al. (2001)
BC19 [d]	BC	33°47.9'N, 28°36.5'E	2750 m	RV *Marion Dufresne* 1991	post-S1; Freydier et al. (2001)
UM42 [d]	BC	34°57.2'N, 17°51.8'E	1375 m		Freydier et al. (2001)
MS27 [d]	GC	31°47.9'N, 29°27.3'E	1389 m		Revel et al. (2010; 2014)
SL71 [e]	GC	34°48.6'N, 23°11.7'E	2827 m		Weldeab et al. (2002b)
SL67 [e]	GC	34°48.8'N, 27°17.8'E	2157 m		Weldeab et al. (2002b)
KL83 [e]	GC	32°36.9'N, 34°08.9'E	1431 m		Weldeab et al. (2002b)

[a] The appellation is referred to as core-name only (i.e. no corer/site) in the paper.

[b] BC: box core, PC: piston core, GC: gravity core.

[c] Samples analyzed in this study; S5 samples are taken based on the stratigraphy frameworks in previous studies, otherwise after G.J. de Lange (unpublished data); The post-S1, late-Holocene samples are used to represent arid-climate condition as recent period.

[d] Published data of sapropel S1 are used.

[e] Published data of sapropel S5 are used.

3 Results

The Sr and Nd isotopes on detrital sediments determined are reported in Table 2. The major element and REE (i.e. rare earth elements) data are given in Tables 3 and 4, respectively.

3.1 Sr and Nd isotopes

There is a generally inverse relationship between Sr and Nd isotope ratios and a clear east–west gradient for sapropel S5 detrital sediments (Figure 2). The lowest $^{87}Sr/^{86}Sr$ and highest ε_{Nd} values occur in the Levantine Basin (KL83, KC20, MS66, and KC19), moderate values for the areas around the Island of Crete (SL67, KC13, SL71, and PS25), and the highest $^{87}Sr/^{86}Sr$ and lowest ε_{Nd} ratios in the Ionian Sea (PS25, BP22, KC01, and CP11). Compared to the EMS surface sediments, the overall domain of sapropel S5 samples tends towards a lower $^{87}Sr/^{86}Sr$ and higher ε_{Nd} signature. Note that an updated, integrated dataset of EMS surface sediments is provided and regionally grouped to better indicate the present-day situation (Figure 2) (see Supplementary material).

Table 2 Sr and Nd isotope compositions of detrital sediments of investigated cores

Core	Depth (cm)	Sample type	Sr (ppm)	$^{87}Sr/^{86}Sr$ ($\pm 2\sigma \times 10^{-6}$) [a]	Nd (ppm)	$^{143}Nd/^{144}Nd$ ($\pm 2\sigma \times 10^{-6}$) [b]	ε_{Nd} [c]
CP11	391.25	S5a	138.0	0.715881 (10)	20.7	0.512011 (13)	-12.2
KC01	880.25	S5a	99.5	0.719321 (10)	22.2	0.512050 (10)	-11.4
BP22	222.25	S5a	117.5	0.717286 (9)	19.7	0.512002 (12)	-12.4
PS25	485.75	S5a	139.9	0.711774 (10)	10.8	0.512108 (13)	-10.3
KC13	367.75	S5a	122.7	0.713825 (10)	14.9	0.512129 (11)	-9.9
KC19	417.25	S5a	97.4	0.711629 (11)	10.0	0.512190 (10)	-8.7
MS66	554.5	S5a	74.5	0.710249 (9)	9.8	0.512372 (15)	-5.2
KC20	322.25	S5a	81.9	0.710508 (10)	10.7	0.512273 (10)	-7.1
CP07	0–0.5	Surface	127.6	0.716435 (10)	15.2	0.511992 (9)	-12.6
BP15	0–0.5	Surface	146.0	0.718807 (11)	23.8	0.512006 (17)	-12.3

[a] Normalized to the NBS-SRM 987 value of $^{87}Sr/^{86}Sr = 0.70525$ (Thirlwall, 1991).
[b] Normalized to the in-house reference material CIGO ($^{143}Nd/^{144}Nd = 0.511342$), equivalent to a La Jolla value of 0.511852 (Griselin et al. 2001).
[c] $\varepsilon_{Nd} = [(^{143}Nd/^{144}Nd)\ \text{measured} / (^{143}Nd/^{144}Nd)\ \text{CHUR} - 1] \times 10^4$, while CHUR (chondritic uniform reservoir) is 0.512638 (Jacobson and Wasserburg, 1980).

3.2 Major elements

Two distinct segments of sapropel S5 (S5a and S5b; Rohling et al., 2004) were analyzed for elemental data. Following a recent study of Wu et al (2017), a ternary diagram of Ti, K, and Mg contents is employed to distinguish detrital input. The major-element ternary diagram (Figure 3) is made as follows: 1) Al-normalized ratios are used to limit the minimum and maximum values for each component, i.e. Ti/Al (0.05 – 0.08), K/Al (0.12 – 0.30), and Mg/Al (0.11 – 0.23); 2) three relative values are then determined for each sample, and proportionally recalculated to make a sum of

100%; 3) the respective fractions are plotted accordingly. Note that the pattern is identical whether using Al-normalization or not.

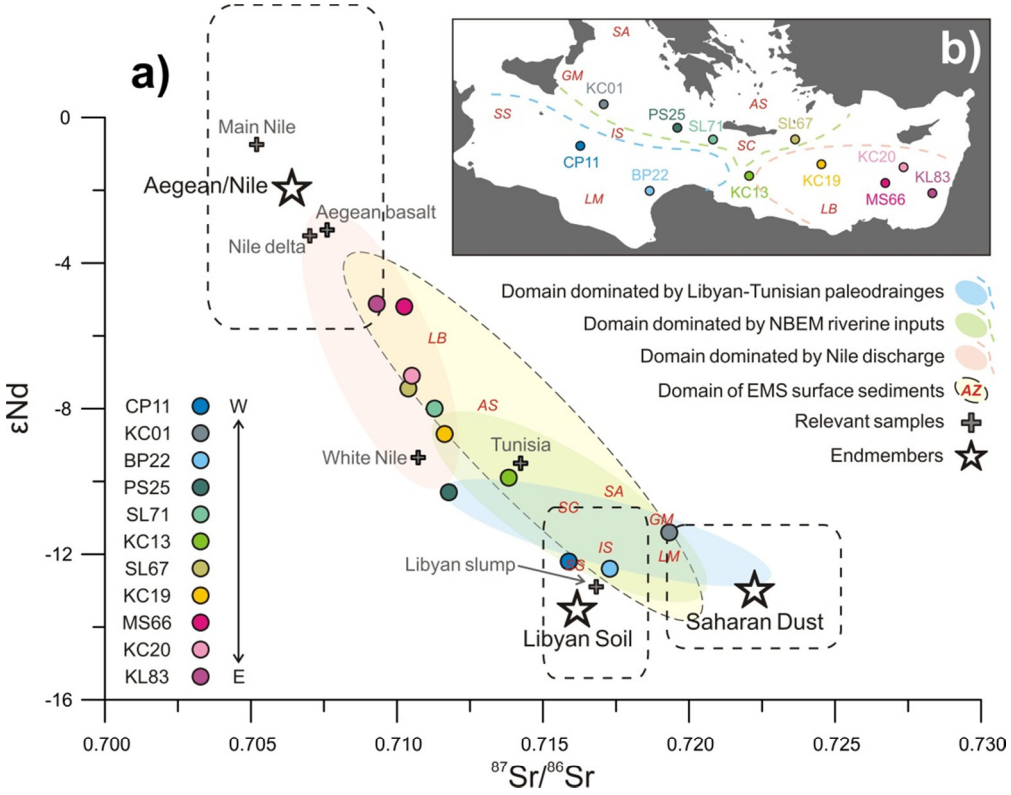

Figure 2(*) There are three data layers: 1) surface sediments (yellow-shaded ellipse in a) and red letters of locality in a) and b)); 2) sapropel S1 sediments (pink-, green-, and blue-shaded ellipses in a) and the related dashed lines indicating distribution in b)), and 3) sapropel S5 sediments (colored dots representing different cores). Sr and Nd isotope ratios of detrital sediments over the eastern Mediterranean Sea (EMS), revealing three major riverine contributions on a basin-wide scale during sapropel S5 period (Table 2). Sapropel S5 data of cores SL71, SL67, and KL83 are reported as average values (Weldeab et al., 2002b). For the Holocene S1 provenance distribution, data of representative cores per area were taken (Freydier et al., 2001; Revel et al., 2010; 2014; Wu et al., 2016) (see Supplementary material). The data of EMS surface sediments (Weldeab et al., 2002a) is compiled with other published and new data, to better characterize the present-day situation (see Supplementary material). The abbreviations of EMS localities used in the paper (red letters): *SS* = Strait of Sicily, *GM* = Gulf of Messina, *SA* = South Adriatic, *LM* = Libyan-Tunisian Margin, *IS* = Ionian Sea, *AS* = Aegean Sea, *SC* = South of Crete, *LB* = Levantine Basin. Average inputs of the endmembers and their ranges (open stars and their surrounding dashed rectangles) are taken from Wu et al. (2016). The "relevant samples" (grey crosses) regarding the endmember defining in Wu et al. (2016) are also displayed. Note that the Sr-Nd isotope signatures for Aegean and Nile rivers are similar and cannot be differentiated here (see Section 4.2).

Table 3 Major elemental ratios of detrital sediments of investigated cores

Core	Depth (cm)	Sample type	Ti/Al (mg/g)	K/Al (mg/g)	Mg/Al (mg/g)
CP11	383.75	S5b	58.2	250	168
CP11	387.25	S5a	58.6	251	151
CP11	391.25	S5a	58.2	255	151
KC01	875.75	S5b	56.0	260	158
KC01	880.25	S5a	52.9	256	147
BP22	214.75	S5b	70.1	256	187
BP22	222.25	S5a	69.7	266	155
PS25	464.25	S5b	67.1	284	228
PS25	487.75	S5a	56.2	277	213
KC13	337.25	S5b	61.3	258	212
KC13	367.75	S5a	61.6	258	213
KC19	397.75	S5b	68.2	225	220
KC19	417.25	S5a	62.3	200	210
MS66	539.50	S5b	71.6	128	120
MS66	554.50	S5a	66.4	128	127
KC20	309.25	S5b	78.4	178	159
KC20	322.25	S5a	71.3	163	153
CP07	0–0.5	Surface	69.6	275	131
CP09	0–0.5	Surface	61.9	220	126
CP10 [a]	0–0.5	Surface	61.1	248	126
AP1	0–0.5	Surface	58.2	261	161
BP18	0–0.5	Surface	72.7	268	140
BP15	0–0.5	Surface	68.9	265	152
SL114	0–0.5	Surface	66.9	250	160
SL73	0–0.5	Surface	52.6	258	170
SL09	0–0.5	Surface	76.9	187	188
SL29	0–0.5	Surface	88.5	177	143
BC07	0–0.5	Surface	86.0	169	146
BC03	5.60	post-S1	71.0	256	186
BC19	3.75	post-S1	75.2	239	163
Saharan dust [b]		Endmember	81.1	223	143
Nile sediment [b]		Endmember	155	105	175
Aegean river [c]		Endmember	60.0	300	400
Adriatic river [d]		Endmember	49.6	317	150
Libya/Tunisia [a]		Endmember	54.6	238	172
UCC [e]			37.3	349	164

[a] Data from Wu et al. (2017); Libya/Tunisia refers to the calculated endmember of Libyan-Tunisian paleodrainage fluxes therein.
[b] Data from Krom et al. (1999a; 1999b), reported as average values.
[c] Data from Wehausen and Brumsack (2000), estimated values are taken.
[d] Average values of Ti/Al and K/Al from Dolenec et al. (1998), the detrital Mg/Al ratio is estimated after Wehausen and Brumsack (2000) and Wu et al. (2017).
[e] Average upper continental crust (Taylor and McLennan, 1985).

Table 4 Rare earth element (REE) concentrations (ppm) and fractionation parameters of detrital sediments of investigated cores

Core	Depth (cm)	Sample type	La	Ce	Pr	Nd	Sm	Eu	Gd	Tb	Dy	Ho	Er	Tm	Yb	Lu	Eu/Eu^{*}_{a}	La_N/Yb_N $_{a,b}$	$L/H_{a,b}$
CP11	383.75	S5b	30.2	56.9	5.47	18.8	2.79	0.56	2.57	0.32	1.94	0.38	1.20	0.19	1.27	0.20	0.644	16.04	4.994
CP11	387.25	S5a	31.9	59.9	5.71	19.6	2.94	0.58	2.58	0.33	2.03	0.39	1.25	0.20	1.32	0.21	0.649	16.32	5.083
CP11	391.25	S5a	33.1	62.0	5.99	20.7	3.11	0.69	2.94	0.36	2.18	0.42	1.34	0.21	1.43	0.22	0.695	15.61	4.853
KC01	875.75	S5b	35.6	66.8	6.34	21.7	3.21	0.75	3.03	0.36	2.16	0.42	1.35	0.22	1.43	0.22	0.731	16.77	5.140
KC01	880.25	S5a	37.3	70.5	6.60	22.2	3.20	0.61	2.93	0.35	2.17	0.43	1.40	0.22	1.49	0.23	0.611	16.83	5.312
BP22	214.75	S5b	27.4	49.3	5.22	18.9	3.15	0.66	2.95	0.40	2.43	0.46	1.41	0.22	1.46	0.23	0.661	12.69	3.914
BP22	222.25	S5a	28.7	51.7	5.46	19.7	3.25	0.69	3.06	0.42	2.55	0.48	1.49	0.24	1.58	0.25	0.672	12.23	3.866
PS25	464.25	S5b	30.1	56.2	5.81	20.9	3.49	0.71	3.14	0.43	2.56	0.48	1.49	0.23	1.54	0.24	0.654	13.19	4.120
PS25	487.75	S5a	15.1	29.1	3.02	10.8	1.72	0.34	1.56	0.19	1.15	0.22	0.71	0.11	0.78	0.12	0.641	13.13	4.380
KC13	337.25	S5b	24.1	44.1	4.49	15.9	2.57	0.65	2.40	0.31	1.92	0.37	1.16	0.19	1.24	0.19	0.797	13.10	4.160
KC13	367.75	S5a	22.7	41.4	4.24	14.9	2.43	0.59	2.21	0.29	1.81	0.35	1.10	0.17	1.17	0.18	0.776	13.03	4.168
KC19	397.75	S5b	16.0	29.0	3.10	11.2	1.87	0.41	1.71	0.24	1.49	0.28	0.87	0.14	0.94	0.15	0.700	11.49	3.738
KC19	417.25	S5a	14.9	25.9	2.81	10.0	1.68	0.40	1.55	0.22	1.42	0.28	0.87	0.14	0.94	0.15	0.749	10.75	3.525
MS66	539.50	S5b	16.2	25.1	2.87	10.2	1.81	0.47	1.78	0.28	1.84	0.36	1.12	0.18	1.21	0.19	0.799	9.044	2.901
MS66	554.50	S5a	15.8	24.0	2.78	9.79	1.75	0.51	1.72	0.27	1.79	0.35	1.08	0.17	1.17	0.18	0.891	9.093	2.894
KC20	309.25	S5b	20.5	34.7	3.72	13.3	2.31	0.56	2.19	0.33	2.15	0.41	1.27	0.20	1.35	0.21	0.766	10.23	3.268
KC20	322.25	S5a	16.8	27.3	3.02	10.7	1.89	0.49	1.86	0.29	1.88	0.37	1.14	0.18	1.24	0.19	0.796	9.127	2.975
CP07	0–0.5	Surface	22.2	42.4	4.67	15.2	2.46	0.44	2.03	0.29	1.90	0.38	1.25	0.19	1.37	0.20	0.598	10.85	4.022
CP09	0–0.5	Surface	31.6	58.1	6.47	21.0	3.22	0.53	2.60	0.37	2.37	0.47	1.58	0.23	1.67	0.24	0.557	12.72	4.503
CP10	0–0.5	Surface	34.4	65.8	7.11	22.8	3.53	0.58	2.84	0.40	2.53	0.51	1.67	0.25	1.78	0.26	0.561	13.07	4.614
AP1	0–0.5	Surface	28.9	53.8	6.01	19.8	3.10	0.51	2.59	0.36	2.38	0.48	1.64	0.24	1.75	0.25	0.555	11.15	4.083
BP18	0–0.5	Surface	30.2	58.8	6.60	22.3	3.87	0.67	3.27	0.49	3.10	0.60	1.92	0.29	2.05	0.30	0.579	10.29	3.612
BP15	0–0.5	Surface	33.6	64.1	7.34	23.8	4.05	0.70	3.36	0.48	3.03	0.59	1.89	0.28	1.98	0.28	0.576	11.45	4.023
SL114	0–0.5	Surface	26.7	49.8	5.63	18.5	3.06	0.53	2.57	0.36	2.28	0.45	1.48	0.22	1.54	0.22	0.580	11.70	4.083
SL73	0–0.5	Surface	19.2	36.5	4.17	14.3	2.53	0.48	2.11	0.29	1.85	0.35	1.15	0.19	1.22	0.18	0.634	10.64	3.743
SL09	0–0.5	Surface	19.3	36.0	4.10	13.7	2.36	0.45	2.08	0.32	2.14	0.42	1.39	0.21	1.51	0.22	0.626	8.645	3.217
SL29	0–0.5	Surface	19.8	38.8	4.21	14.1	2.55	0.52	2.32	0.36	2.39	0.47	1.55	0.24	1.67	0.24	0.655	7.974	3.010
BC07	0–0.5	Surface	18.9	34.8	4.02	13.5	2.44	0.49	2.20	0.34	2.26	0.44	1.45	0.22	1.57	0.23	0.648	8.157	3.018
BC03	5.60	post-S1	28.9	54.6	6.27	21.1	3.64	0.61	3.11	0.45	2.91	0.57	1.85	0.28	1.97	0.29	0.555	9.880	3.581
BC19	3.75	post-S1	27.8	52.1	5.94	20.1	3.48	0.61	3.03	0.44	2.87	0.56	1.82	0.28	1.97	0.29	0.579	9.521	3.469
Saharan soil [c]			47.5	102	12.0	49.5	7.50	1.25	9.00	1.25	7.50	1.50	3.50	<0.5	4.00	<0.5	0.465	8.006	2.603
Nile mud [d]			34.4	74.1	9.80	36.8	8.21	2.18	7.65	1.34	7.13	1.37	4.20	0.64	4.09	0.60	0.841	5.667	2.186
UCC [e]			30.0	64.0	7.10	26.0	4.50	0.88	3.80	0.64	3.50	0.80	2.30	0.33	2.20	0.32	0.651	9.194	3.275

[a] With normalization to chondrite (Boynton, 1985); $Eu/Eu^{*} = Eu_N / (Sm_N \times Gd_N)^{1/2}$.

[b] Ratio of LREE (light REE, La–Sm) to HREE (heavy REE, Gd–Lu), abbreviated here as L/H, often approximated by the ratio of La_N/Yb_N.

[c] Data from Moreno et al. (2006), average values of central-Sahara desert samples (Hoggar Massif and Chad Basin).

[d] Data from Padoan et al. (2011), average values of main Nile muds are reported.

[e] Average upper continental crust (Taylor and McLennan, 1985).

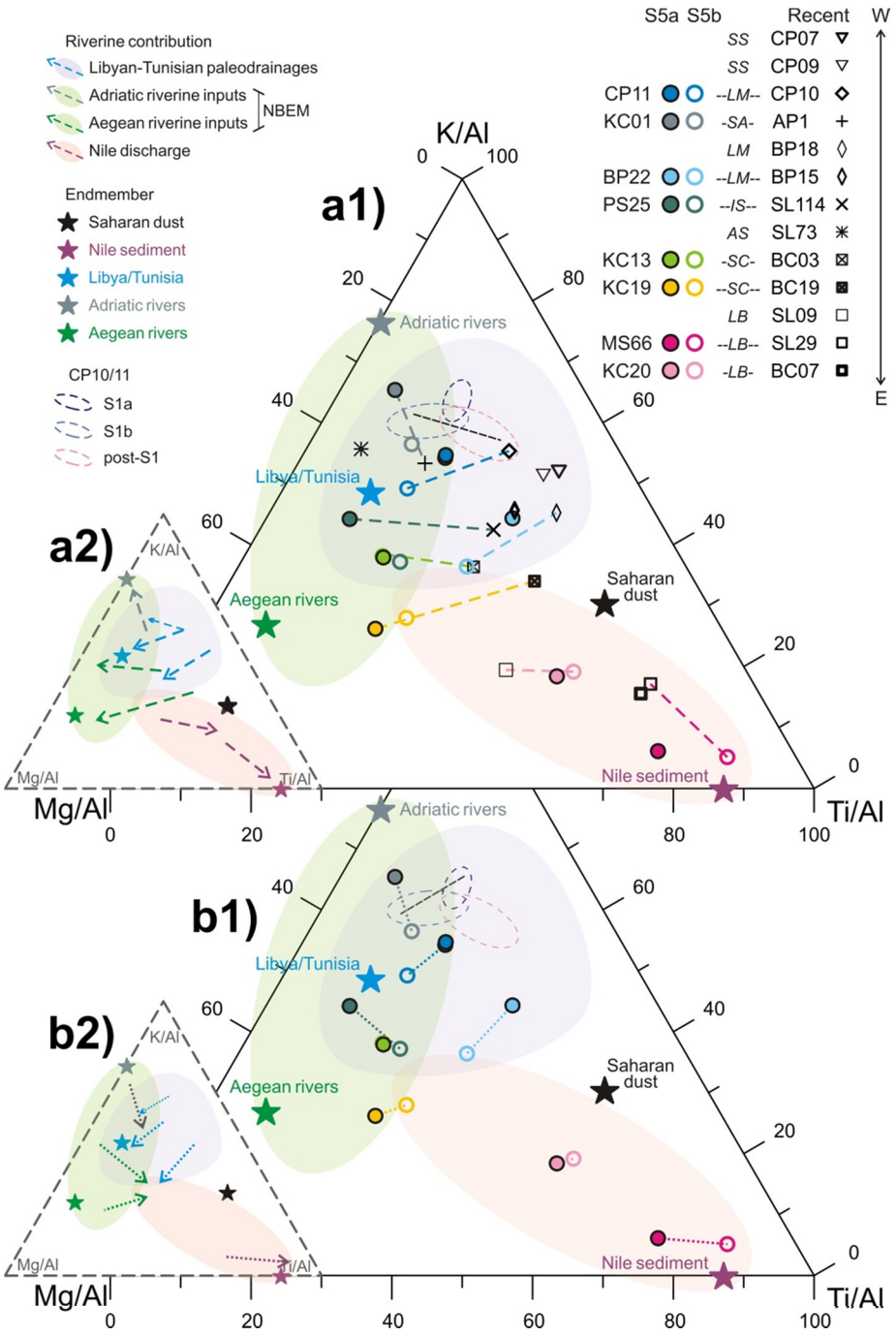

Figure 3 Ternary diagram for major elements in the detrital fraction of sapropel S5 and recent sediments (Table 3). Sapropel S5 samples are differentiated between S5a and S5b (see Section 2). a1) Colored dashed-lines between recent and S5 samples for the same sites/areas show the differences from

arid to humid climatic conditions. Note that the longest lines are used regardless of S5a or S5b sample, to represent the largest hydroclimate changes. The fields of major riverine contributions (shaded areas) are outlined, with associated endmembers (colored stars) (for sources see Table 3). In sub-plot a2), the colored arrows indicate the direction of increasing riverine contributions for each area from arid/recent to humid/S5 period, and for CP10/11 also for recent to S1. b1) Colored dotted-lines between S5a and S5b samples for each site/area show the hydroclimate changes within sapropel S5. In sub-plot b2), the colored arrows indicate the changes in riverine contributions for each area from S5a to S5b intervals, and for CP10/11 also from S1a to S1b. The S5a to S5b change points towards more enhanced riverine contributions for all southern EMS borderlands, and towards more reduced contributions for the northern borderlands. The S1a to S1b shift for core CP10/11 (Wu et al., 2017) is similar to that for S5a to S5b. For abbreviations of EMS localities see caption of Figure 2. For details of diagram methodology see Section 3.2.

Cores KC20 and MS66 (and KC19) located in the Levantine Basin have the highest Ti contents, especially for S5b samples (Figure 3). For the cores around the Island of Crete, KC19, KC13, and PS25 samples show relatively high Mg contents. The samples of the Ionian Sea (CP11, BP22, and KC01) are characterized by relatively high K contents. Notably, there is a Mg-rich trend for cores CP11 and BP22, with higher Mg/Al values for S5b than S5a samples. A similar pattern is also observed for the surface/recent sediments, such as BC07, SL29, and SL09 in the Levantine Basin, BC19, BC03 and SL73 for the areas around Crete, and SL114, AP1, BP15, BP18, CP10, CP09 and CP07 for the Ionian Sea. Compared to the sapropel S5 detrital sediments, the surface samples are characterized by relatively high Ti and, a somewhat higher K value (Figure 3).

3.3 Rare earth elements

The REE contents of the EMS samples are all depleted relative to the average upper continental crust (UCC) (Taylor and McLennan, 1985) (Figure 4). With normalization to UCC, the REE patterns of sapropel S5 samples exhibit a greater enrichment of LREE (i.e. light REE, La–Sm) from east to west. In addition to the LREE enrichment, the UCC-normalized data are characterized by relatively homogenous HREE (i.e. heavy REE, Gd–Lu) contents but more heterogeneous middle REE contents. The latter is associated with variable Eu anomalies (Figure 4a). The overall pattern of the recent sediments is similar to that of sapropel S5 samples, but with a less evident east–west change in LREE enrichment relative to HREE, and weaker Eu anomalies (Figure 4b).

Variations in the UCC-normalized REE patterns (Figure 4) are diagnostic of mafic vs. felsic source areas (Figure 5). A strong negative Eu anomaly (Eu/Eu^*) indicates felsic rocks, as does a high ratio of the light to heavy REE (e.g. LREE/HREE, La_N/Yb_N) (Taylor and McLennan, 1985). Note that the REE parameters are all

normalized to chondrite (Boynton, 1985). The good negative correlations between these two parameters are associated with by a strong east–west gradient throughout the EMS. In a plot of La_N/Yb_N vs. Eu/Eu^*, r^2 is 0.48 and 0.53 for sapropel S5 and recent sediment, respectively (Figure 5a); and in the LREE/HREE vs. Eu/Eu^*, r^2 is 0.51 and 0.56 for sapropel S5 and recent sediment, respectively (Figure 5b). The arrays of surface sediments are distinctly different from those of sapropel S5, but the provenance pattern described above is also observed for sapropel S5 and surface samples (Figure 5). It must be note that the lines connecting the S5 and recent sediments for each site/area all extrapolate to the same signature (Figure 5).

4 Discussion

Coupled Sr and Nd isotope variations in detrital sediments have been widely used as fingerprints for source areas in the EMS, as their ratio appears to be little affected by transport processes and diagenesis (e.g. Freydier et al., 2001; Weldeab et al., 2002a, 2002b; Revel et al., 2010; 2014; Wu et al., 2016). In the Levantine Basin, a simple mixing model between Nile sediment and Saharan dust is sufficient to explain the variability of detrital supplies, in terms of clay minerals, elemental ratios, and Sr-Nd isotopes (Venkatarathnam and Ryan, 1971; Krom et al., 1999b; Freydier et al., 2001; Revel et al., 2010). The Sr-Nd isotope data suggest that the Late-Quaternary sediments deposited in the areas around Crete are a mixture of Saharan dust and Aegean/Nile river-borne materials (Weldeab et al., 2002b; Ehrmann et al., 2007); while the Aegean and Nile contributions cannot be differentiated using these isotopes alone (Weldeab et al., 2002a; 2002b; Wu et al., 2016). For the Ionian Sea, a three-endmember mixing system based on Sr-Nd isotopes adequately attributes the sediment provenance to Saharan dust, NBEM/Nile riverine inputs, and fluvial/shelf-derived fluxes from the Libyan-Tunisian margin (Wu et al., 2016).

These systematics are fully corroborated by a multiproxy study using detrital elements, clay minerals, and grain size end-member modeling (Wu et al., 2017, and references therein), The study reveals that Saharan dust is characterized by high Ti and kaolinite, the NBEM riverine inputs have relatively high K, illite and chlorite, and the Libyan-Tunisian paleodrainage fluxes are characterized by high Mg and smectite.

In addition, although REE may be affected by intense chemical weathering, most studies suggest that provenance plays a dominant role in determining sediment REE composition (e.g. Yang et al., 2002; Moreno et al., 2006; Padoan et al., 2011; Révillon at al., 2011; Wu et al., 2013). Thus, the sedimentary REE pattern gives robust constraints for provenance determination (Taylor and McLennan, 1985). Unfortunately, only few relevant studies with REE data have been reported for EMS sediments (c.f. Martinez-Ruiz et al., 2015).

In this study we combine the use of Sr and Nd isotopes, major elements, and REE. The results are discussed relative to riverine contributions and the main provenance areas.

4.1 Relative aeolian and riverine contributions during sapropel S5

Today, deposition of Saharan dust is a dominant (>90%) detrital component to sediments in the Eastern Mediterranean basin (Guerzoni et al., 1999), and its distribution is approximately uniform in an east–west direction (Krom et al., 1999a; Rutten et al., 2000). Compared to EMS surface sediments, representing typical arid climate conditions, sapropel S5 samples have a distinctly lower $^{87}Sr/^{86}Sr$ and a slightly higher ε_{Nd} isotopic composition (Figures 2 and 6). This difference could be due to contributions of Saharan dust being lower or those of riverine influx being higher during the humid, sapropel S5 period compared to the present. However, it has also been suggested that decreased aeolian and increased riverine fluxes occurred simultaneously at times of sapropel deposition (e.g. Krom et al., 1999b; Wehausen and Brumsack, 2000; Freydier et al., 2001; Liu et al., 2012; Wu et al., 2016). Our data of sapropel S5 show different isotopic signals for different provenance areas (Figure 2). In addition to the uniformly reduced Saharan dust, such differences in spatial variation indicate that riverine supplies must have varied spatially and possibly with different temporal pacing.

Similar patterns are recorded by the major- and trace-element data (Figure 3). Compared to the sapropel S5 detrital sediments, the EMS surface sediments are more affected by the Saharan dust inputs, characterized by relatively high Ti, and to a lesser extent, K (e.g. compare KC20-S5 to BC07/SL29 and PS25-S5 to SL114 from the same sites, respectively, at Erathostenes Seamount and mid-Ionian). Indeed, Ti principally resides in heavy minerals and is enriched in modern Saharan aerosols, allowing the Ti/Al ratio to be widely used as a proxy for Saharan dust (e.g. Wehausen and Brumsack, 2000; Lourens et al., 2001). Illite, usually enriched in K, is one of the main clay minerals of Saharan dust (Guerzoni et al., 1999; Zhao et al., 2012; see also Wu et al., 2017). By contrast, the composition of sapropel S5 samples reflects reduced dust and enhanced riverine input, for each area with a different provenance signature. This is clearly observed in Figure 3a, where for each site/area the difference between recent and S5 composition is illustrated with an arrow (i.e. away from the Saharan endmember, and towards their respective riverine endmember). This difference between arid- and humid-climatic conditions thus corresponds with different riverine supplies.

The overall REE pattern for surface sediments is similar to that for sapropel S5 samples, but with a more restricted enrichment of LREE relative to HREE, and with weaker Eu anomalies (Figure 4). These data correspond with a much higher

contribution of Saharan dust to the present-day sediments (Weldeab et al., 2002b; Larrasoaña et al., 2003; Castañeda et al., 2009; Liu et al., 2012). A higher Saharan dust contribution to surface sediments has subdued the signals of the relatively low recent riverine inputs, causing a lower east–west LREE fractionation and a lower Eu anomaly. Moreover, REE-derived parameters (i.e. Eu/Eu^{*}, La_N/Yb_N, and LREE/HREE) are consistently different between sapropel S5 and surface samples, showing the significant impact of Saharan dust today (Moreno et al., 2006) (Figure 5). Notably, extrapolations from the S5 and recent sediments for the same sites/areas all point to the same composition, representing the similar, averaged Saharan endmember (Figure 5). Taken together, the sapropel S5 samples have more varied REE patterns than recent sediments. This reflects the contributions from different riverine sources.

The spatial pattern of different riverine contributions also occurs during sapropel S1, as shown by the different S1 arrays that deviate from the modern EMS field (Figures 2 and 6). Despite a general consensus that the Nile reached its peak discharge during sapropel S1, the mapping of surface-water $\delta^{18}O$ anomalies recorded in planktonic foraminifera failed to identify the Nile as a single point-source (Kallel et al., 1997; Rohling and De Rijk, 1999; Emeis et al., 2000). Instead, a widely distributed depletion of $\delta^{18}O$ is found throughout the Levantine Basin, causing a weakening of the west–east gradient (Rohling and De Rijk, 1999; Emeis et al., 2000). In addition to the Nile discharge, the weakened west–east salinity gradient during sapropel times may partly reflect an increase in circum-Mediterranean humidity and the consequently enhanced NBEM riverine inputs (e.g. Kallel et al., 1997; Bar-Matthews et al., 2000; Magny et al., 2013; Toucanne et al., 2015). In addition, these variations partly reflect monsoon-sourced runoff along the wider North-African margin into the central Mediterranean, at least during many, if not all, sapropels (e.g. Freydier et al., 2001; Rohling et al., 2002; 2004; Emeis et al., 2003; Larrasoaña et al., 2003; Sangiorgi et al., 2006; Osborne et al., 2008; 2010; Wu et al., 2016; 2017) (see Section 1.2 and the following discussion).

In summary, during the time of sapropel S5 deposition, the pronounced last interglacial insolation maximum led to a development of dense vegetation and extensive fluvial systems over the presently hyperarid Saharan Desert, resulting in a much diminished emission of Saharan dust and enhanced riverine inputs to all parts of the EMS (Cheddadi and Rossignol-Strick, 1995; Weldeab et al., 2002b; Larrasoaña et al., 2003; Castañeda et al., 2009; Liu et al., 2012). Therefore, the geochemical variability of the sapropel S5 detrital sediments is attributed predominantly to the amount and composition of detrital material delivered via rivers, and the subsequent distribution by currents.

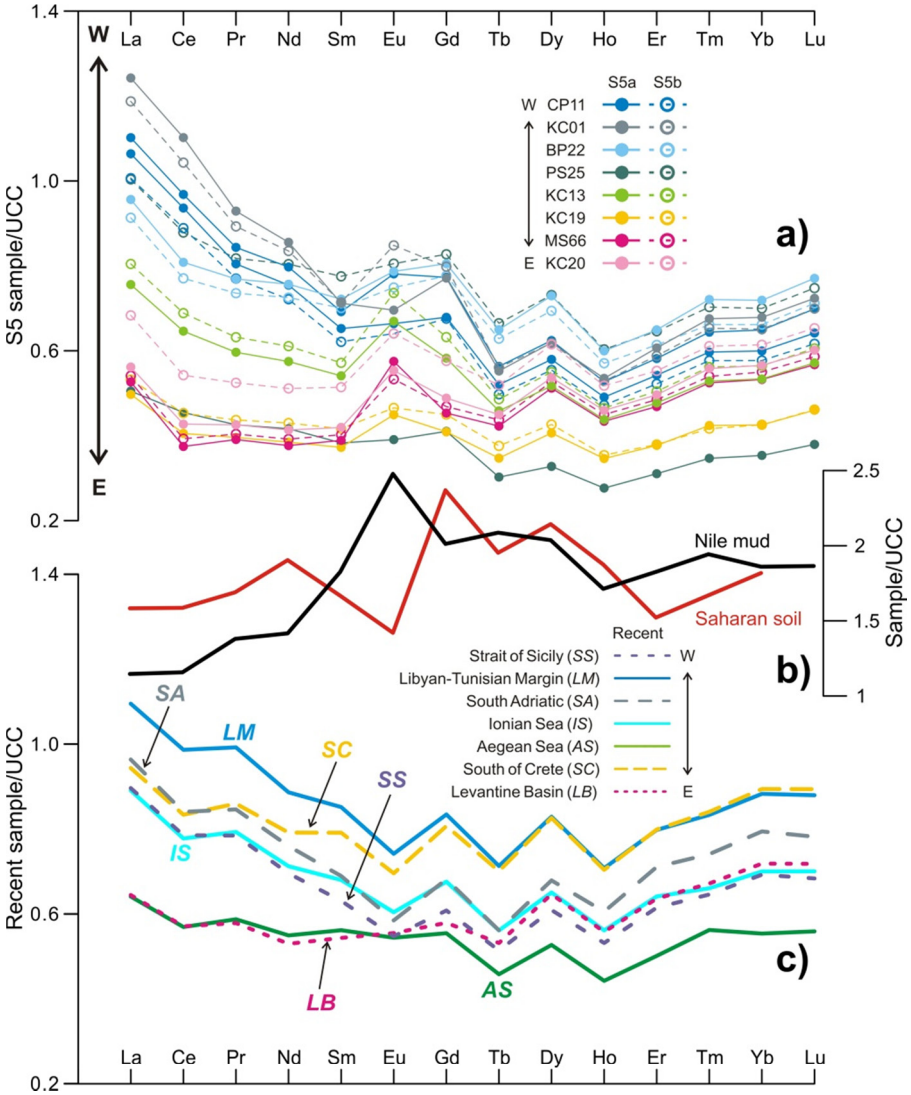

Figure 4 REE (i.e. rare earth elements) fractionation patterns with normalization to upper continental crust (UCC) (Taylor and McLennan, 1985) for a) sapropel S5 and c) recent detrital sediments over the eastern Mediterranean Sea (EMS), in comparison to b) those of Saharan soil (Moreno et al., 2006) and Nile muds (Padoan et al., 2011) (Table 4). Sapropel S5 samples are differentiated between S5a and S5b (see Section 2). Note that for the recent samples, data are averaged for the main provenance areas. For the EMS sediments, there is a strong east–west gradient of light REE (LREE, La–Sm) enrichment, with a relatively homogenous heavy REE (HREE, Gd–Lu). The UCC-normalized data are characterized by a heterogeneous pattern for the middle REE, especially with variable Eu anomalies. The observed characteristics are more pronounced for sapropel S5 than surface samples. Taken together, these indicate the control of Nile discharge for the eastern EMS, the impact of Saharan dust for the climatic arid, recent period, and that the provenance of the western EMS (Ionian Sea) is characterized by a more prominent LREE enrichment and negative Eu anomaly.

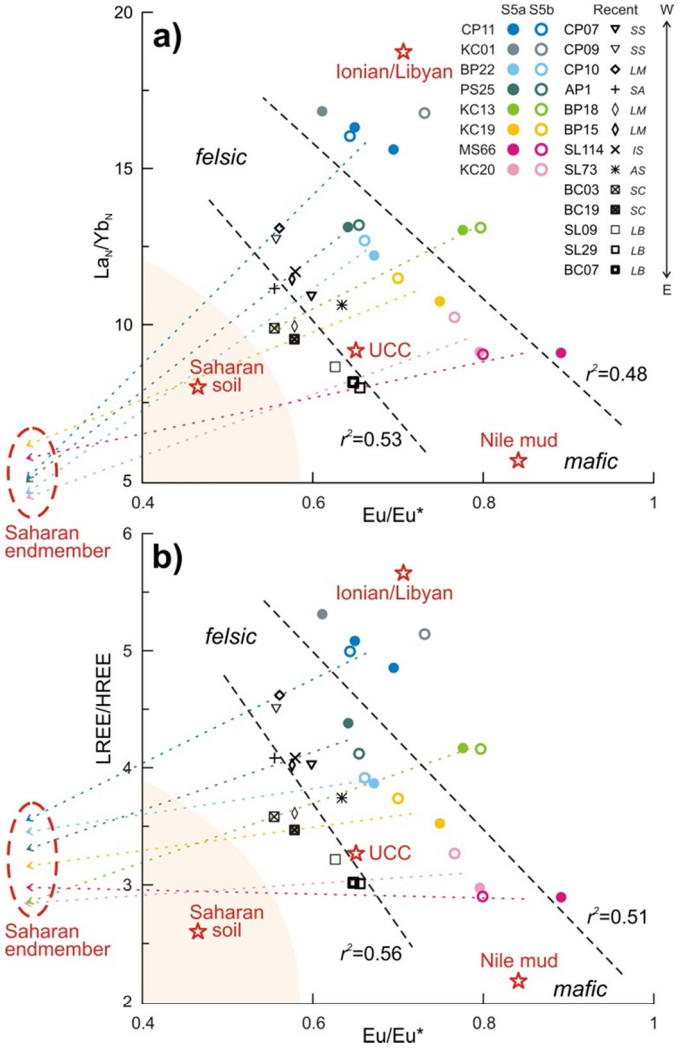

Figure 5 Plots of a) La_N/Yb_N and b) LREE/HREE vs. Eu/Eu^* for sapropel S5 and recent detrital sediments, respectively (Table 4). With normalization to chondrite (Boynton, 1983), the REE-derived parameters exhibit close negative correlations, indicating the relative contributions from felsic vs. mafic rock source areas. This is in good agreement with the Saharan soil and Nile mud (Moreno et al., 2006; Padoan et al., 2011). Sapropel S5 samples are differentiated between S5a and S5b (see Section 2). The distinct differences in the arrays between sapropel S5 and recent samples indicate the modern impact of Saharan dust. For each site/area, the colored lines go from S5 sediments through the corresponding recent sediments all point to one and the same signature of Sahara, representing the similar, averaged Saharan-dust endmember. Note that average composition of the S5 and recent sediments are taken. The Levantine Basin sediments are characterized by a relative mafic Nile signature, whereas the more felsic signature for the southwestern EMS sediments points to an Ionian/Libyan provenance, which is characterized by relatively high values for all these REE parameters. A best possible estimate for the Ionian/Libyan provenance is given. The signatures of average upper continental crust (UCC) are also shown (Taylor and McLennan, 1985). For the abbreviations of EMS localities see caption of Figure 2.

4.2 Characterization of major riverine supplies during sapropel S5

For sapropel S5 detrital sediments, the Sr and Nd isotope, major element, and REE data reveal a strong east–west gradient and the influences of different riverine contributions: namely the Nile discharge, the NBEM (i.e. Aegean and Adriatic) riverine inputs, and the Libyan-Tunisian paleodrainage fluxes (Figures 2–5).

4.2.1 Nile discharge and Aegean riverine inputs

The Nile sediment is mostly derived from the weathering products of Cenozoic basaltic rocks in the Ethiopian Highlands, thus characterized by relatively low $^{87}Sr/^{86}Sr$ and high ε_{Nd}, high Ti, low K and Mg contents, as well as high HREE and Eu concentrations (Krom et al., 1999a; 1999b; Revel et al., 2010; Box et al., 2011; Padoan et al., 2011). Such isotopic and elemental fingerprints are clearly seen in all of the Nile-influenced samples, regardless of the climatic conditions (S5: KL83, KC20, and MS66; surface: BC19, SL09, SL29, and BC07) (Figures 2–5). These data indicate the control of Nile discharge to the Levantine Basin sediments, with an approximately similar offshore spread of Nile-derived particulates for the sapropel S5 period and the present-day, i.e. roughly limited to east of 26°E.

For the cores around the Island of Crete, the influence of Aegean riverine inputs appears to only occur during humid, sapropel periods. Similar to the Nile, the S5 samples of KC19, KC13, and PS25 display relatively high HREE and positive Eu anomalies, which indicates a mafic provenance for the REE bearing host minerals (Taylor and McLennan, 1985; Padoan et al., 2011); while this pattern is not observed for the recent samples (BC19, BC03, SL73, and SL114) (Figure 4). The mafic provenance is consistent with the isotopic signature for the river-borne surface sediments in the Aegean Sea, which are derived from basalts and ultramafic rocks (Figure 2). Because of the similarity in basin lithology and the resultant REE and Sr-Nd isotope composition, however, the Nile and Aegean riverine supplies cannot be distinguished using these proxies alone (Weldeab et al., 2002a; 2002b; Ehrmann et al., 2007; Klaver et al., 2015; Wu et al., 2016).

The mixture of Nile and NBEM contributions can be unraveled, however, using elemental geochemistry. In addition to the aeolian-origin Ti, high contents of Nile-derived Ti are also shown in the Levantine Basin. The NBEM is thought to be an important contributor of illite and chlorite to the Ionian sediments, mainly via the rivers flowing into the Adriatic (Po and Apennines rivers) and Aegean Sea (southeastern European and Turkish rivers) (Venkatarathnam and Ryan, 1971; Guerzoni et al., 1999; Goudeau et al., 2013). As detrital K and Mg are usually associated with the clay minerals illite and chlorite respectively, increased NBEM riverine inputs may be documented by higher K/Al and Mg/Al in sapropel layers (e.g. Wehausen and Brumsack, 2000; Martinez-Ruiz et al., 2015, and references therein;

Wu et al., 2016). In this context, it is clear that cores KC20 and MS66 are controlled by the Ti-rich Nile discharge, while the cores around Crete such as KC19, KC13, and PS25 are more influenced by the Mg-rich riverine inputs from the Aegean Sea (Figure 3).

Furthermore, the relative distributions of the Nile and Aegean riverine supplies are revealed by the distinctly different trends in sapropel S5 samples (Figure 3). Core KC19, located at the boundary between the Levantine Basin and south of Crete suggests that the Nile sediment contribution is confined to the areas east of 26°E. This, again, indicates a limited offshore distribution of Nile sediment, even during sapropel S5. An alternative explanation is a stronger Aegean riverine input. This suggestion is consistent with previous studies concerning the Nile impact. The Sr and Nd isotope ratios on surface sediments have shown that the Nile sediment contribution rapidly decreases westward from the river-mouth to a limit south of Crete, around the Mediterranean Ridge (Krom et al., 1999a; Weldeab et al., 2002a). During sapropels, several lines of evidence argue strongly against a considerable Nile influence (i.e. dissolved and particulate) for the areas west of Crete (see in-depth discussion in Wu et al., 2016; 2017).

4.2.2 Libyan-Tunisian paleodrainage and other riverine fluxes to the Ionian

The similar mafic sources of the Nile- and Aegean -dominated areas concord with the relatively homogenous HREE distribution, whereas a more heterogeneous pattern of middle REE points to rather different felsic sources, i.e. a provenance from the areas around the Ionian Sea (Figure 4). This is in line with the surface geology of river catchments over the EMS region. Specifically, the Ionian samples are characterized by strong LREE fractionation, a negative Eu anomaly, and a flat HREE pattern (Figure 4), such as seen for the areas off Libya/Tunisia and the northern Ionian Sea (S5: KC01, CP11 and BP22; surface: AP1, CP07, CP09, CP10, BP15 and BP18). This indicates a felsic provenance. Moreover, it is clear that the REE data cannot be described by a simple mixing between Saharan dust and Nile sediment; at least one further component with a relatively high Eu/Eu^{*}, La_N/Yb_N, and LREE/HREE is required for the Ionian provenance (Figure 5).

The Ionian Sea potentially receives detrital fluxes from the Aegean Sea, Adriatic Sea, Strait of Messina, Strait of Sicily, and also from Libya and Tunisia (Venkatarathnam and Ryan, 1971; Weldeab et al., 2002a) (Figure 1). The surface samples over the Ionian area slightly deviate from the generally inverse relationship between Sr and Nd isotope ratios (Figure 2). Specifically, the signatures of Adriatic and Messina have highest $^{87}Sr/^{86}Sr$ but not the lowest ε_{Nd} values (Weldeab et al., 2002a), whereas those of Sicily and Libya are characterized by the lowest ε_{Nd} and moderate $^{87}Sr/^{86}Sr$ ratio. The latter is revealed by our surface samples CP07 and BP15

collected from the Libyan-Tunisian margin, which expand on the existing EMS datasets (see Supplementary material). Accordingly, the Sr and Nd isotope ratios for cores CP11 and BP22 being lower than those for the surface samples from the same area (i.e. CP07, CP10, and BP15) point to a significant Libyan riverine contribution during S5 time (Figure 2).

Based on the compositions summarized in Figure 3, the northwestern Ionian (core KC01) is mainly influenced by a K-rich Adriatic/Messina (NBEM) contribution, while for the southern Ionian (cores CP11 and BP22), there is an Mg-rich detrital contribution, especially for the S5b interval. Taken together, core KC01, close to the Gulf of Messina, appears to be mainly influenced by sediment outflows from the Strait of Messina and southern Adriatic Sea. By contrast, cores CP11 and BP22 are more controlled by detrital fluxes from the Libyan-Tunisian margin and Strait of Sicily.

These observations are in good agreement with previous studies (Freydier et al., 2001; Weldeab et al., 2002a; Wu et al., 2016; 2017). Riverine runoffs from the wider North-African margin have also been recorded for sapropel S5 time, using planktonic foraminiferal $\delta^{18}O$ (Rohling et al., 2002; 2004) and Nd isotope ratios (Osborne et al., 2008; 2010). In addition, North-African runoff has been documented for sapropel S1 based on the Sr and Nd isotope ratios of the detrital component (Wu et al., 2016). Aegean riverine inputs are composed of weathering products of ultramafic/mafic rocks, thus enriched in Mg (Wehausen and Brumsack, 2000; Klaver et al., 2015). In addition, a comprehensive comparison of detrital supplies between the Ionian cores has shown that the paleodrainage fluxes from the Libyan-Tunisian margin during sapropel S1 period are characterized by higher smectite and detrital Mg/Al (Wu et al., 2017). This point is clear from Figure 3, showing that for the Libyan-Tunisian margin, the sapropel S5 samples (CP11 and BP22) have systematically higher Mg contents for the surface sediments (CP07, CP09, CP10, BP15, and BP18).

4.3 Basin-wide comparison of riverine contributions between different humid periods

4.3.1 Sapropel S5 versus S1

Due to the extraordinary astronomical settings for the last interglacial insolation maximum, overall, sapropel S5 has far more runoff than the Holocene sapropel S1 (see Section 1.3). As discussed above, the Nile sediment contribution during sapropel S5 was not larger, or even slightly decreased, compared to that of sapropel S1 and the present-day. This inference is also clear from the Sr-Nd isotope data from the Levantine Basin; for a larger Nile contribution, the signatures of cores KL83, KC20, and MS66 should have a greater Nile-endmember composition, but this is not the case (Figure 2). During sapropel S5 time, the African monsoon is anticipated to

be more intensified than during S1. The higher summer precipitation may not have caused a higher Nile sediment supply, as the monsoon-generated vegetation cover is expected to be denser and consequently may have suppressed physical erosion and sediment removal for the Ethiopian highlands (e.g. Krom et al., 1999b; Weldeab et al., 2002b; Box et al., 2011; Lézine et al., 2011; Hennekam et al., 2014). This interpretation is supported by the similar major-element signature for sapropel S5 (KC20 and MS66) and surface sediments (BC07, SL29, and SL09) in the Levantine Basin (Figure 3), demonstrating that the Ti-rich detrital supply of the Nile did not increase significantly during sapropel S5 relative to the present.

By contrast, the influence of the Aegean riverine sediment input during sapropel S5 appears to have been much greater than during S1. This is indicated by the lower $^{87}Sr/^{86}Sr$ and higher ε_{Nd} ratios for the cores around Crete (KC19, SL67, KC13, SL71, and PS25), during sapropel S5 compared S1 (Figure 2). This is in line with the increased seasonality of precipitation during the last interglacial maximum proposed to explain the apparent incongruity between various records (Cheddadi and Rossignol-Strick, 1995; Tzedakis, 2007; Milner et al., 2012). Indeed, the evidence of evaporative summer conditions based on pollen studies (e.g. Tzedakis et al., 2003; Allen and Huntley, 2009) coupled with increased winter precipitation recorded by speleothem and sapropel records (e.g. Bar-Matthews et al., 2000; Drysdale et al., 2005; Toucanne et al., 2015) indicates a strong precipitation seasonality over the NBEM during sapropel S5.

Enhanced NBEM riverine inputs during sapropel times are also consistent with the results from the major-element ternary diagram (Figure 3). For the Aegean area, sapropel S5 samples (KC19, KC13, and PS25) are more towards the Mg-endmember than recent samples (BC19, BC03, SL73, and SL114). This trend is also observed for the Adriatic-related samples, showing that S5 sample of KC01 is more influenced by the K-rich Adriatic/Messina contribution than the AP1 surface sediment (Figure 3a). Thus, all these data indicate enhanced riverine input from the NBEM, including the Aegean and Adriatic Sea. We note that our results contradict the finding of Osborne et al. (2010), who concluded that there was no large influx of Aegean riverine water during sapropel S5 using planktonic foraminiferal ε_{Nd}. The explanation for these different interpretations is that the ε_{Nd} recorded in planktonic foraminifera is not related to the ambient seawater at calcification depth (i.e. surface water) but primarily reflects the bottom/pore water (Pomiés, et al., 2002; Tachikawa et al., 2014).

Relative to the Libyan-Tunisian isotopic domain of sapropel S1, the S5-samples of cores CP11 and BP22 have consistently lower ε_{Nd} values, indicating stronger North-African paleodrainage fluxes during sapropel S5 than during S1 (Figure 2). This is

further corroborated by the major-element data showing that sapropel S5 samples (CP11 and BP22) are higher in Mg than those for sapropel S1 (CP10/11, the same site as CP11) (Figure 3). The fossil river/wadi networks over eastern Libya feed towards the Gulf of Sirte and have been considered the primary source of detritus for sapropel S5 deposition (e.g. Rohling et al. 2002; 2004; Osborne et al., 2008; 2010). This more eastern pathway deviates from the runoff pathway indicated for sapropel S1, which is in western Libya and Tunisia towards the Gulf of Gabès (Wu et al., 2016; 2017) (Figure 1).

Compared to the most-humid phase of sapropel S1 (i.e. with the lowest $^{87}Sr/^{86}Sr$ and highest ε_{Nd} values in the Libyan-Tunisian domain) the relatively high $^{87}Sr/^{86}Sr$ ratios of CP11 and BP22 point to higher paleodrainage fluxes from the wider North-African margin (Figure 2). Moreover, the recent sediments offshore eastern Libya (CP07, CP09, and CP10) have systematically higher Mg contents than those offshore western Libya/Tunisia (BP15 and BP18) (Figure 3a). Thus, the derived paleodrainage fluxes with more enhanced Mg/Al for S5 than for S1, point to a more eastern Libya provenance for these fluxes during sapropel S5 time. The riverine higher Mg is related to the weathering products of ultramafic/mafic rocks over the North-African paleodrainage areas (Wu et al., 2017).

In addition to the fluvial supplies from the south, shelf-derived initially river-borne material from the east (i.e. Strait of Sicily) is likely, as anticipated for sapropel S1 (Wu et al., 2016; 2017) (Figure 2). Moreover, it seems that core KC01 is mainly controlled by the K-rich Adriatic/Messina inputs, while it is much less influenced by the inferred supplies from the Libyan-Tunisian margin (Figures 2 and 3). This core may mark a limit for the detectable distribution of North-African paleodrainage-related detrital sediments during sapropel S5.

4.3.2 Sapropel S5a versus S5b

There are considerable differences between the two distinct periods: S5a and S5b (see Section 1.3). It has been suggested that the X value for S5a and S5b was reduced to respectively 5–45% and 35–60% of the present-day value (Rohling et al., 2004). From the perspective of detrital sediments, considering a much reduced and generally constant impact of Saharan dust during sapropel S5 (Cheddadi and Rossignol-Strick, 1995; Weldeab et al., 2002b; Larrasoaña et al., 2003; Castañeda et al., 2009; Liu et al., 2012), differences observed between S5a and S5b must be attributed to changes in riverine supplies.

It is clear that riverine detrital supplies from the southern EMS borderlands, North Africa, were more enhanced during S5b than S5a; whereas the opposite is observed for the northern borderlands (i.e. NBEM) (Figure 3). Relative to S5a samples, S5b

samples in cores KC20 and MS66 are more towards the Ti-rich Nile endmember (Figure 3b), and more away from the Saharan dust endmember and from the Saharan dust dominated recent samples in cores of corresponding sites/area (SL09, SL29, and BC07) (Figure 3a). Similarly, for cores CP11 and BP22, S5b samples are more towards the Mg-rich Libya/Tunisia endmember, and distant from the Saharan dust endmember and from the corresponding recent samples (CP10, BP15, and BP18), compared to S5a samples (Figure 3). This pattern is in contrast to that for the NBEM. For the cores mainly influenced by Aegean riverine inputs (KC19, KC13, and PS25), compared to the S5b samples, S5a samples are closer to the Aegean river endmember, and more distant from the Saharan dust endmember and from the associated recent samples (BC19, BC03, and SL114) (Figure 3). Likewise, the S5a sample of core KC01 appears to receive more K-rich Adriatic river-borne material than the S5b sample, as compared to the Adriatic and Saharan endmembers, and the recent AP1 sample (Figure 3).

This south–north pattern is also generally observed in the REE data. For the cores controlled by North-African provenance areas (KC20, MS66, KC19, BP22, and CP11), there are lower Eu/Eu^{*}, and higher La_N/Lu_N and LREE/HREE ratios, thus pointing to more enhanced runoff during S5b than S5a. The opposite is the case for the NBEM-influenced cores KC01, PS25, and KC13 (Figure 5).

The higher NBEM riverine input during S5a is related to the increased seasonality of precipitation in the early part of the last interglacial maximum, coeval with boreal summer insolation maxima (Tzedakis, 2007; Milner et al., 2012) (see Section 4.3.1). Such climate effect is also evident for the analogous case of Holocene sapropel S1 (see review by Magny et al., 2013), where enhanced K-rich NBEM riverine contributions during the early phase of S1 (S1a) are associated with enhanced winter precipitation (e.g. Wu et al., 2017).

There are potentially different mechanisms for the monsoon-sourced riverine supplies from North Africa. Although an enhanced Nile discharge should have had a major contribution to the excess basin-wide freshwater input during S5a, as estimated from surface-water $\delta^{18}O$ data (Rohling et al., 2004), a higher water flow did not necessarily result in a higher sediment supply. The Nile comprises two different systems: 1) the White Nile and 2) the Blue Nile and Atbara, affected by East African monsoon (Revel et al., 2010; Hennekam et al., 2014). At present, the latter provides >50% of the water flow and >95% of the sediment load, as the Sudd swamps in Sudan filter out most of the White Nile's suspension load (Foucault and Stanley, 1989; Padoan et al., 2011). Consequently, a dense vegetation cover on the Ethiopian highlands – the source areas of the Blue Nile and Atbara, may have restricted the Nile sediment contribution (Krom et al., 1999b; Weldeab et al., 2002b;

Box et al., 2011; Hennekam et al., 2014). In this context, the stronger Nile signatures during S5b than S5a could be related to the deterioration of the vegetation cover on the Ethiopian highlands.

The potential fluvial contributions from the wider North-African margin have been linked to the reactivation and delivery of paleodrainage systems derived from central Saharan mountains (Rohling et al., 2002; 2004; Osborne et al., 2008; 2010; Wu et al., 2016; 2017). It has recently been suggested that such paleodrainage fluxes were controlled by the Saharan humid surface, i.e. the area of interlinked fluvial systems, modulated by groundwater level, in response to the insolation-driven West African monsoon precipitation (see in-depth discussion in Wu et al., 2017). Specifically, the paleodrainage systems and associated networks were only fully developed, when the persistently high precipitation had replenished the groundwater to a sufficient level during the late part of S1 (S1b) (Lézine et al., 2011). It is therefore inferred that the resulting runoff developed to the greatest extent during the S1b interval (Wu et al., 2017). This scenario is thought to have occurred also for sapropel S5, with the highest paleodrainage fluxes during the S5b interval.

This is distinct from the Nile discharge that is controlled by East African monsoon precipitation and associated vegetation cover on the Ethiopian highlands. These differences may partly account for the different responses between the Libyan-Tunisian and Nile riverine contributions to the same insolation forcing.

4.4 Integrating and quantifying detrital contributions for the eastern Mediterranean during sapropel S5

To summarize, the isotopic and elemental composition of EMS detrital sediments reveals three main provenance areas, and a general west–east gradient (Figure 6). Based on Sr and Nd isotopes, an overall stronger riverine contribution occurred during sapropel S5 than during S1, as reflected by the generally higher (lower) $^{87}Sr/^{86}Sr$ (ε_{Nd}) ratios in the west, and the lower (higher) $^{87}Sr/^{86}Sr$ (ε_{Nd}) ratios in the eastern section of the EMS (Figure 6a,b). The Eu/Eu^{*} ratios record the impact of Saharan dust that is much more enhanced in surface samples than sapropel S5 sediments (Figure 6c).

Considering the complex provenance pattern and the inadequate information for the source endmembers, a quantitative calculation for the whole EMS basin is difficult. Despite that, semi-quantitative estimates can be made for the major provenance areas, based on qualified assumptions regarding the distribution of detrital supplies (for details see Supplementary material).

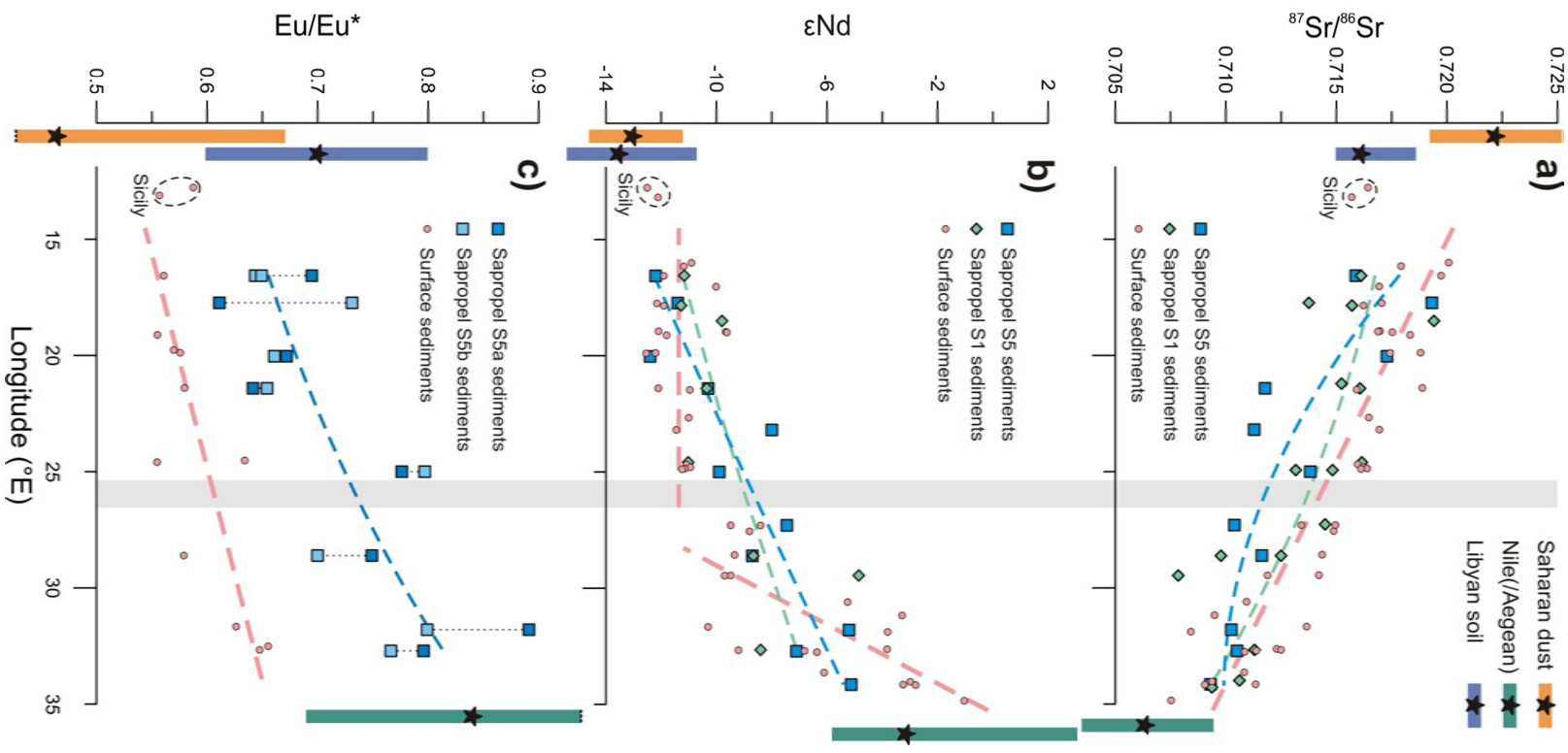

Figure 6 Geochemical provenance proxies a) $^{87}Sr/^{86}Sr$, b) ε_{Nd}, and c) Eu/Eu^{*} versus longitude throughout the eastern Mediterranean Sea. The data for sapropel S5, S1, and surface detrital sediments distinctly indicate the relative riverine contributions during these different periods. Curves of nonlinear fit are shown for S5 and S1 data, while for surface sediments linear lines are used (excluding two data-points from the Strait of Sicily). The step-wise change in the recent ε_{Nd} data emphasizes that the Nile distribution is limited to the area south of Crete around 26°E, as indicated by the vertical grey bar. The Sr and Nd isotopes data are compiled from previous studies (Frost et al., 1986; Krom et al., 1999b; Freydier et al., 2001; Weldeab et al., 2002a; 2002b; Tachikawa et al., 2004; Ehrmann et al., 2007; Revel et al., 2010; 2014; Box et al., 2011; Wu et al., 2016) and updated here (for details see Supplementary material). Anticipated endmembers and their ranges are given on the left and right. For Sr and Nd isotopes: after Wu et al. (2016). For Eu/Eu^{*}: after Moreno et al. (2006) and Padoan et al. (2011) using Saharan desert soils and main Nile muds, respectively and it estimated from observations in Figure 5 for Libyan soil.

For the Levantine Basin, the mixing hyperbola constructed from Sr and Nd isotopes and concentrations of the complete Nile-delta sediments (Revel et al., 2010) is adopted to estimate the Nile vs. Saharan contributions (see Supplementary material). The Nile accounts for ~65% and ~55% of the detrital materials in cores MS66 and KC20 during sapropel S5 (Figure 2), in good agreement with the Blue Nile contribution ranging between 40–70% for humid sapropel periods (Revel et al., 2010). For the present-day, a Nile contribution of 60–80% and 40–60% is reported for the sites of MS66 and KC20, respectively, as estimated from surface sediment Sr isotopes (Krom et al., 1999a).

For the western parts of the EMS, at least a ternary mixing system is required. For the areas around Crete, where the Nile contribution was largely reduced, a rough estimate can be made from the major-element ternary diagram using the Saharan, Aegean/Nile, and Libyan endmembers (Figure 3; see Supplementary material). The estimated detrital contributions for the cores between ~25 and 30°E are as follows (KC19; KC13): Nile (~10%; <5%), Aegean (50–60%; 30–40%), Libyan (<5%; 40–50%), and Saharan (~25%; ~20%). Note that KC19 appears to mark a distribution limit of the Libyan-Tunisian paleodrainage fluxes, and has a similar Nile contribution as presently (~5–10%), while KC13 has a negligible Nile influence throughout (see Section 4.2).

It is clear that enhanced NBEM riverine inputs dominate the northern Ionian Sea during sapropel S5 (i.e. PS25 and KC01), but the Adriatic and Aegean contributions cannot be clearly differentiated. Moreover, this area may be affected by the detrital supplies from Sicily and Messina, which makes the provenance even more complex. It appears, however, that the inferred Libyan-Tunisian paleodrainage systems contributed only a small amount of detrital materials to core KC01, but considerably more to PS25 (Figures 2 and 3).

In general, the paleodrainage contribution from the Libyan-Tunisian margin must have been larger during sapropel S5 than during S1 (Figures 2 and 3). The S1 paleodrainage fluxes account for 40–70% of the detrital sediment variability in core CP10/11, as calculated from a multiproxy approach (Wu et al., 2017). This is also supported by the Sr-Nd isotope data of sapropel S1 samples in core CP10 (~60%) (Wu et al., 2016); applying a similar approach for S5 samples of CP11 and BP22, this gives a paleodrainage-related contribution of 60–75%. Consequently, despite variable detrital components from riverine NBEM, Sicily shelf-derived materials, and Saharan dust, the predominant contribution to the southern Ionian Sea is from reactivated Libyan paleodrainage fluxes.

5 Conclusions

Based on a basin-wide geochemical characterization of Eastern Mediterranean sediments, we evaluate the riverine supplies at the times of sapropel S5 deposition and make comparisons with the present-day and the Holocene sapropel S1 period. The following conclusions are drawn:

a) During the humid-phase MIS 5e, coinciding with sapropel S5 deposition, there was minor Saharan dust over the EMS. Therefore the geochemical variability of sapropel S5 detrital sediments is mostly due to a mixing between three riverine contributions: Nile discharge, Northern Borderlands of Eastern Mediterranean (i.e. NBEM) riverine inputs, and Libyan-Tunisian paleodrainage fluxes.
b) The intensified African monsoon during MIS 5e and the associated denser vegetation cover has resulted in reduced erosion for the Blue Nile catchment areas. Consequently, despite substantially enhanced runoff, the offshore spatial distribution of Nile sediments during sapropel S5 was not larger than during sapropel S1 or today. The Nile sediment contribution is only dominant for the Levantine Basin, decreasing to undetectable levels south of Crete in sapropel S5, S1, and recent sediments.
c) An increase in the Aegean riverine inputs is observed around Crete in sapropel S5 time. This enhanced distribution is associated with the strong precipitation seasonality over the NBEM, especially for the early part of the last interglacial maximum (i.e. S5a).
d) Considerable fluvial contributions from the wider North-African margin are found in Ionian Sea sediments. Such sediment supplies must be transported via the paleodrainage systems derived from central Saharan mountains, which were reactivated by intensified monsoon precipitation. These sediment supplies were more prominent for the S5b than for the S5a phase. Moreover, the paleodrainage fluxes during sapropel S5 were stronger and appear to be preferentially derived from eastern Libya, in contrast to those during sapropel S1 which were mainly derived from western Libya/Tunisia.

Our approach demonstrates the effectiveness of a combination of major elements, REE, and Sr-Nd isotopes in determining provenance. In particular, the elemental fingerprints of detrital sediment have shown to be very practical for EMS provenance studies, not only due to their ease-of-analysis compared to isotope data, but also supplying essential complementary information.

Acknowledgements

We thank the captain & crew, scientists, and technicians on board the cruises of MD69-MARFLUX 1991, MD81-PALEOFLUX 1995 with RV *Marion Dufresne*, SIN-SAP 1998 with RV *Urania*, SMILABLE 1999 with RV *Logachev*, as well as of PASAP 2000, BIOPASS 2001, PALEOPASS & MIMES 2004, and CORTADO 2011 with RV

Pelagia, for their contributions to sample collection. We are grateful to Coen Mulder and Helen de Waard for ICP-OES and -MS analyses at Utrecht University. Many thanks are given to Richard J. Smeets who helped with chromatography, to Mathijs van de Ven and Bas van der Wagt for Sr and Nd isotope measurements at VU Amsterdam. We acknowledge financial supports from EU-projects MARFLUX, PALEOFLUX & SAP, and from CNR and NWO for shiptime and logistic support. This study is sponsored by the China Scholarship Council – Utrecht University PhD Program (CSC No. 201206260116).

Appendix. Supplementary material

Supplementary material related to this article is attached.

Note (*) *The potential barite-associated Sr remaining in the decarbonated sediments may have affected the Sr isotope data reported in this contribution (Chapter 5). In particular, the relatively low, seemingly deviating 87Sr/86Sr value of core PS25 is very likely because of the inferred remaining barite-Sr (Figure 2). Despite that, the barite-Sr impact is considered limited for the other cores. This is because of the constraint of Nd isotopes that have been proven as a conservative provenance proxy (Chapter 5).*

Chapter 4 Appendix. Supplementary material

This **Supplementary material** provides 1) a compiled dataset of Sr and Nd isotopes for surface sediments in the eastern Mediterranean Sea (EMS) and detailed data sources of Sr and Nd isotopes for sapropel S1, as well as 2) a description of the semi-quantitate estimates for the major provenance areas over the EMS.

1 Data sources

In Table S1, an updated Sr-Nd isotope dataset of EMS surface sediments is given, including published data and the data from this study. The data are regionally grouped to better indicate the present-day situation (Figures 2 and 6 in manuscript).

For the Sr and Nd isotopes data of sapropel S1, averaged values are reported for each core/site (Table S2), as shown in Figures 2 and 6 of the manuscript. The interval of sapropel S1 is based on the well-established age boundaries (10.8–6.1 ± 0.5 cal. ka; De Lange et al., 2008). Specifically, in Figure 2 of the manuscript, data of representative cores taken from the main provenance are shown for the Holocene. This is indicative of the influences of different riverine contributions over sapropel S1, i.e. the domain of Libyan-Tunisian paleodrainage fluxes (after core CP10; Wu et al., 2016), NBEM riverine inputs (after cores SL114 and BC03; Freydier et al., 2001; Wu et al., 2016), and Nile discharge (after cores BC19, MS27, and BC07; Freydier et al., 2001; Revel et al., 2010; 2014).

2 Semi-quantitative estimates

As discussed in Section 4 of the manuscript, for the three provenance areas the major detrital contributions are different, which makes a quantitative calculation for the whole EMS basin challenging. This is particularly true in view of the overlapping isotopic signatures between the Nile and Aegean riverine contributions, the complex provenance pattern of the Ionian Sea, as well as the inadequate information for the source endmembers (e.g. detrital Mg for Adriatic and Aegean). Despite these limitations, semi-quantitative estimates can be made for the different major provenance areas. This is done on the basis of some qualified assumptions concerning the distribution of detrital river-borne materials (see Section 4 of the manuscript).

For the Levantine Basin, the mixing hyperbola constructed on the basis of Sr and Nd isotopes and concentrations (after Revel et al., 2010), allows us to quantify the Nile vs. Saharan contributions (Figure S1). This is adopted because the study of Revel et al. (2010) compiled various Nile-associated samples over the past 100 ka, which provides a comprehensive and direct comparison for the detrital Sr-Nd isotope data.

The comparison is based on the assumption of a simple mixing between Nile sediment and Saharan dust in the Levantine Basin. The Nile contribution ranges between 40–70% during humid sapropel periods (i.e. Holocene sapropel S1, MIS 3, and last-interglacial sapropels S3 and S4). By contrast, the Nile contribution could fall to ~15% at least and the Saharan dust contribution could reach ~85% to the greatest extent during arid periods (Revel et al., 2010). Our sapropel S5 results are consistent with those for S1: cores MS66 and KC20 report a Nile contribution of ~65% and ~55%, respectively, for the detrital sediments (Figure S1). Similar results are obtained while using major elements (Figure S2). Assuming a mixing between Saharan dust and Nile/Aegean contributions for the Levantine Basin, the estimated Nile contribution for these cores are: MS66 (~75%), KC20 (~45%), and KC19 (~5%) (Figure S2).

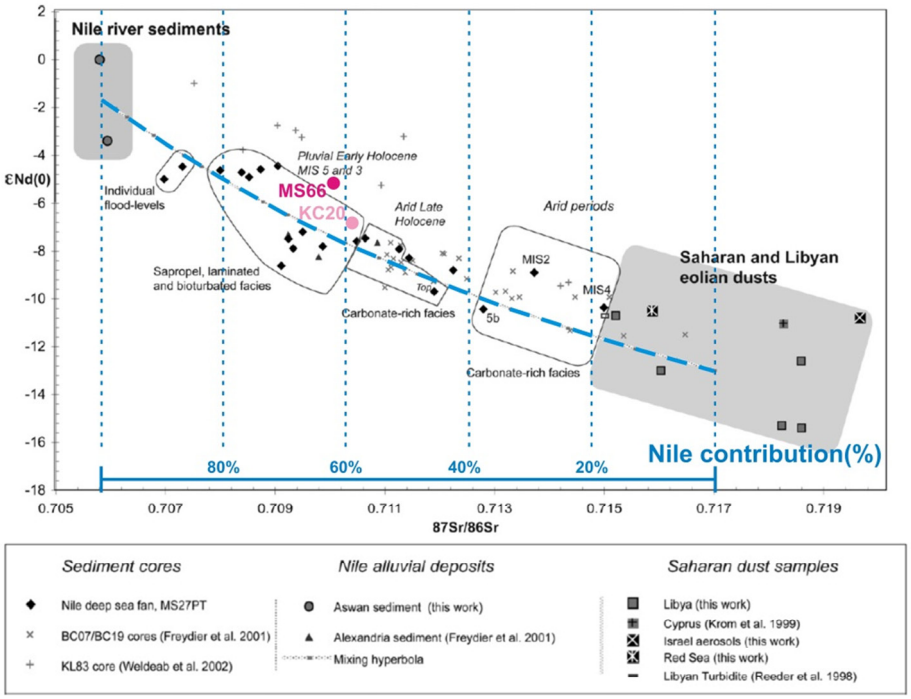

Figure S1 The plot of Sr vs. Nd isotope composition, showing a mixing hyperbola between Nile sediment and Saharan dust for the Levantine Basin (after Revel et al., 2010). This is constructed based on both Sr and Nd isotopes and concentrations, compiled from the various, completed Nile and Saharan samples. Our sapropel S5 samples of cores MS66 and KC20 show a Nile contribution of ~65% and ~55%, respectively, for the detrital sediments.

Table S1 Sr and Nd isotope composition of detrital sediments for eastern Mediterranean surface samples

Locality [a]	Core	Latitude, Longitude	Water-depth	$^{87}Sr/^{86}Sr$ ± 2σ × 10^{-6}	$^{143}Nd/144Nd$ ± 2σ × 10^{-6}	ε_{Nd}	Source [b]
SS	CP07	36°02.2'N, 13°06.6'E	524 m	0.716435 ± 10	0.511992 ± 9	-12.5	1
SS	KL60	37°20.2'N, 13°11.3'E	470 m	0.715700 ± 10	0.512017 ± 7	-12.1	2
SS				**0.716068**		**-12.3**	
GM	MC536	37°23.7'N, 16°00.4'E	2850 m	0.720086 ± 10	0.512079 ± 10	-10.9	2
GM	MC533	37°00.2'N, 16°09.4'E	2718 m	0.717931 ± 10	0.512065 ± 9	-11.2	2
GM				**0.719009**		**-11.0**	
SA	MC10	40°08.3'N, 17°01.8'E	1100 m	0.716945 ± 10	0.512123 ± 7	-10.0	2
SA	MC531	39°31.7'N, 18°58.3'E	832 m	0.716887 ± 10	0.512143 ± 9	-9.7	2
SA	MC532	39°56.8'N, 18°60.0'E	910 m	0.717533 ± 10	0.512145 ± 10	-9.6	2
SA	AP1	39°13.0'N, 19°06.8'E	811 m	0.718342 ± 15	0.512033 ± 10	-11.8	3
SA				**0.717427**		**-10.3**	
LM	CP10BC	34°32.7'N, 16°34.0'E	1501 m	0.719740 ± 15	0.512027 ± 16	-11.9	4
LM	BP15	32°46.7'N, 19°52.6'E	665 m	0.718807 ± 11	0.512006 ± 17	-12.2	1
LM				**0.719274**		**-12.0**	
IS	964A	36°15.6'N, 17°45.0'E	3657 m	0.717057 ± 10	0.512015 ± 8	-12.2	2
IS	973A	35°46.8'N, 18°56.9'E	3695 m	0.716977 ± 10	0.512018 ± 8	-12.1	2
IS	KL55	34°18.2'N, 19°53.9'E	3129 m	0.717430 ± 10	0.511995 ± 8	-12.5	2
IS	MC534	35°13.8'N, 21°28.3'E	3515 m	0.715924 ± 10	0.512076 ± 9	-11.0	2
IS	KL59	35°48.6'N, 22°40.2'E	1012 m	0.716473 ± 10	0.512074 ± 8	-11.0	2
IS	SL114	35°17.2'N, 21°24.5'E	3390 m	0.718895 ± 15	0.512019 ± 10	-12.1	3
IS				**0.717126**		**-11.8**	
AS	MC515	39°16.5'N, 23°43.0'E	1250 m	0.713245 ± 10	0.512247 ± 8	-7.6	2
AS	MC521	35°49.0'N, 25°16.0'E	1839 m	0.713724 ± 10	0.512217 ± 9	-8.2	2
AS	MC522	35°50.5'N, 25°26.0'E	1840 m	0.713734 ± 10	0.512206 ± 7	-8.4	2
AS	KL49	36°08.8'N, 25°33.8'E	828 m	0.713831 ± 10	0.512209 ± 10	-8.4	2
AS	KL50	35°36.0'N, 25°54.3'E	560 m	0.710914 ± 10	0.512341 ± 9	-5.8	2
AS	SL123	35°45.3'N, 27°33.3'E	728 m	0.714882 ± 10	0.512186 ± 9	-8.8	5
AS	SL73	39°39.7'N, 24°30.7'E	339 m	0.710380 ± 15	0.512208 ± 10	-8.4	3
AS	MST1	36°10.0'N, 25°12.0'E	1600 m	0.714010 ± 15	0.512248 ± 10	-7.6	3
AS				**0.713090**		**-7.9**	
SC	SL71	34°48.6'N, 23°11.7'E	2827 m	0.716950 ± 10	0.512051 ± 10	-11.5	2
SC	971A	33°43.6'N, 24°40.8'E	2037 m	0.715968 ± 10	0.512070 ± 10	-11.1	2

SC	970A	33°44.2'N, 24°48.1'E	2087 m	0.716211 ± 10	0.512077 ± 10	-10.9	2
SC	KL53	33°51.6'N, 24°51.5'E	2165 m	0.716395 ± 10	0.512067 ± 10	-11.1	2
SC	969A	33°50.5'N, 24°53.0'E	2200 m	0.716119 ± 10	0.512062 ± 7	-11.2	2
SC	RC9-179	34°24.0'N, 27°18.0'E		0.713428 ± 46	0.512172 ± 22	-8.4	6
SC				**0.715845**		**-10.7**	
LB	SL67	34°48.8'N, 27°17.8'E	2157 m	0.714959 ± 10	0.512152 ± 9	-9.5	2
LB	MC21	33°36.3'N, 28°34.3'E	3039 m	0.714361 ± 10	0.512157 ± 8	-9.3	2
LB	MC22	33°14.7'N, 29°27.3'E	2948 m	0.714213 ± 10	0.512150 ± 10	-9.5	2
LB	MC23	32°40.8'N, 30°35.8'E	1940 m	0.710944 ± 10	0.512367 ± 10	-5.3	2
LB	MC24	32°19.5'N, 31°10.5'E	1007 m	0.709495 ± 10	0.512468 ± 9	-3.3	2
LB	MC25	32°00.5'N, 31°53.3'E	199 m	0.708426 ± 10	0.512441 ± 8	-3.8	2
LB	MC38	34°26.1'N, 32°37.6'E	2473 m	0.712306 ± 10	0.512440 ± 10	-3.8	2
LB	966A	33°47.8'N, 32°42.1'E	926 m	0.711386 ± 10	0.512289 ± 8	-6.8	2
LB	968A	34°19.9'N, 32°45.1'E	1961 m	0.710862 ± 10	0.512312 ± 11	-6.4	2
LB	KL85	32°36.8'N, 34°01.6'E	1450 m	0.709381 ± 10	0.512485 ± 10	-3.0	2
LB	KL83	32°36.9'N, 34°08.9'E	1431 m	0.711353 ± 10	0.512472 ± 8	-3.2	2
LB	KL82	32°19.3'N, 34°09.9'E	1284 m	0.709053 ± 10	0.512495 ± 8	-2.8	2
LB	MC35	33°01.6'N, 34°50.6'E	1028 m	0.707531 ± 10	0.512583 ± 10	-1.0	2
LB	MS27PT	31°47.9'N, 29°27.7'E	1389 m	0.711896 ± 10	0.512141 ± 7	-9.7	7
LB	BC07	33°49.4'N, 32°40.0'E	893 m	0.712503 ± 15	0.512167 ± 10	-9.2	8
LB	SL09	34°17.2'N, 31°31.4'E	2302 m	0.713660 ± 15	0.512109 ± 10	-10.3	2
LB	MD84-641	33°02.0'N, 33°38.0'E	1375 m	0.710837 ± 15	0.512325 ± 10	-6.1	3
LB				**0.711363**		**-6.1**	

[a] The locality abbreviations: *SS* = Strait of Sicily, *GM* = Gulf of Messina, *SA* = South Adriatic, *LM* = Libyan-Tunisian Margin, *IS* = Ionian Sea, *AS* = Aegean Sea, *SC* = South of Crete, *LB* = Levantine Basin. Averaged values of $^{87}Sr/^{86}Sr$ and ε_{Nd} are in bold and reported in the paper.

[b] Data sources: 1= this study, 2= Weldeab et al. (2002a), 3= Tachikawa et al. (2004), 4= Wu et al. (2016), 5= Ehrmann et al. (2007), 6= Frost et al. (1986), 7= Revel et al. (2010), 8= Freydier et al. (2001).

Table S2 Sr and Nd isotope compositions of detrital sediments of sapropel S1 over the eastern Mediterranean Sea

Core	Location	Water-depth	$^{87}Sr/^{86}Sr$	ε_{Nd}	Sample number	Source [a]
CP10BC	34°32.7'N, 16°34.0'E	1501 m	0.716120	-11.2	17	1
KC01	36°15.3'N, 17°44.3'E	3643 m	0.713757		3	2
UM42	34°57.2'N, 17°51.8'E	1375 m	0.715710	-11.3	5	3
MP50	39°29.0'N, 18°31.0'E	775 m	0.719415	-9.8	4	4
UM35	35°11.0'N, 21°12.5'E	2670 m	0.715235		4	2
SL114	35°17.2'N, 21°24.5'E	3390 m	0.716071	-10.4	4	1
BC03	33°22.5'N, 24°46.0'E	2180 m	0.716150	-11.0	8	3
ABC26	33°21.3'N, 24°55.7'E	2150 m	0.714827		3	2
MC12 [b]	*~ 33.4°N, 24.9°E*	~2000 m	0.713165		2	2
Stn20 [b]	*~ 34.0°N, 27.5°E*	~2000 m	0.714077		3	2
BC19	33°47.9'N, 28°36.5'E	2750 m	0.712497	-8.7	8	3
MS27PT	31°47.9'N, 29°27.3'E	1389 m	0.707848	-4.9	14	5
BC07	33°40.0'N, 32°40.0'E	893 m	0.711300	-8.4	5	3
9501	34°32.0'N, 33°59.0'E	980 m	0.710616		14	6
9509	32°02.0'N, 34°17.0'E	884 m	0.709375		11	6

[a] Data sources: 1= Wu et al. (2016), 2= Krom et al. (1999b), 3= Freydier et al. (2001), 4= J. Wu (unpublished), 5= Revel et al. (2010; 2014), 6= Box et al. (2011).
[b] Estimated locations and water-depths.

For the northern Ionian Sea (i.e. PS25 and KC01) that is dominated by enhanced NBEM riverine inputs, however, the Adriatic and Aegean contributions cannot be clearly differentiated. In addition, this area may be affected by detrital supplies from Libya, Sicily, and Messina, which makes the Ionian provenance very complex. It seems that the inferred Libyan-Tunisian paleodrainage contributed a small amount of detrital materials to core KC01, but considerably to PS25 (Figures 2 and 3 of the manuscript).

A higher paleodrainage contribution from the Libyan-Tunisian margin must have occurred during sapropel S5 than during S1. This is evidently seen from the Sr-Nd isotopes and major elements (Figures 2 and 3 of the manuscript). Based on a multiproxy approach, the S1 paleodrainage fluxes have been reported to account for 40–70% of the detrital sediments in core CP10/11 (the same site as CP11) (Wu et al., 2017). This is also supported by the estimate (~60%) according to the Sr and Nd isotopes data of sapropel S1 in core CP10 (Wu et al., 2016); for sapropel S5 samples (CP11 and BP22), a similar three-endmember estimate gives the proportions of 60–75%. Taken together, regardless of other minor detrital contributions and the associated dilution effects, such as the NBEM riverine inputs, shelf-derived fluxes from Sicily, and reduced Saharan dust, a predominant contribution of the S5 paleodrainage flux for the southern Ionian Sea is demonstrated (i.e. ~60–75% contributions for CP11 and BP22 during sapropel S5 time) (Figure S2).

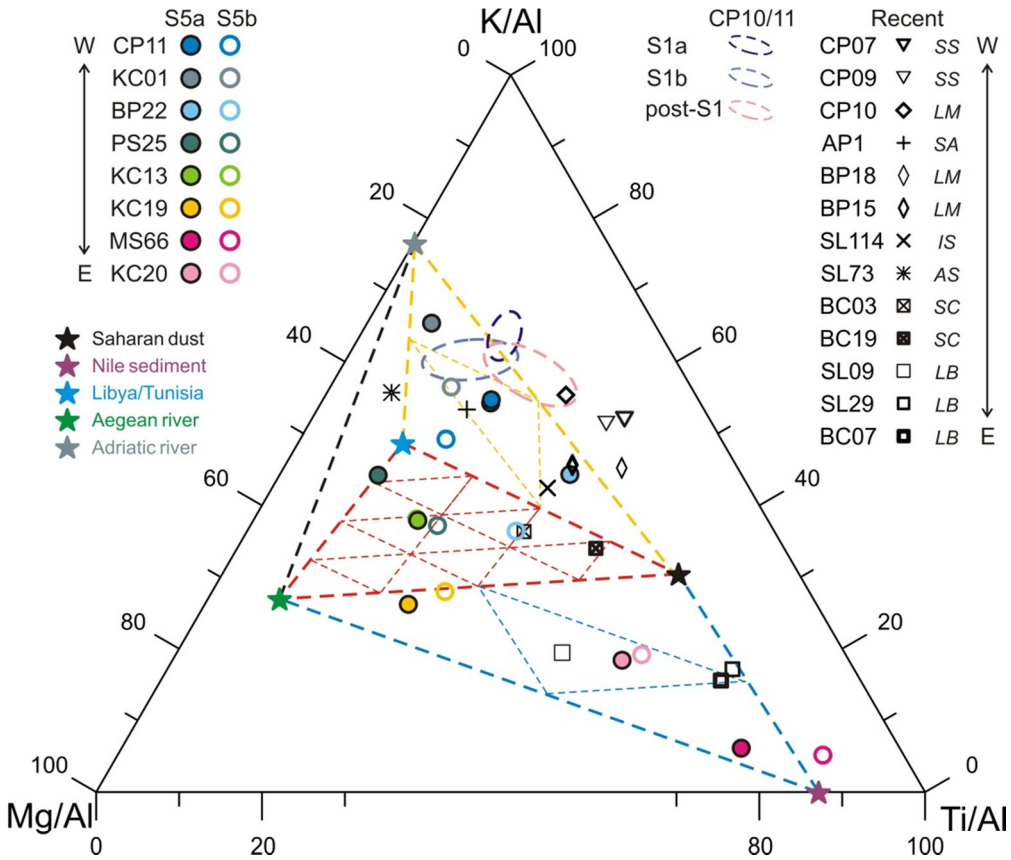

Figure S2 A ternary diagram of major elements in the detrital fraction is used to estimate the detrital contributions during sapropel S5 period (also see Figure 3 of the manuscript). For the Levantine Basin, a mixing between Saharan dust and Nile/Aegean contributions can be assumed (MS66, KC20, and KC19) (blue-triangle area). For the area south of Crete, a mixing between Saharan, Nile/Aegean, and Libyan contributions can be assumed (KC19 and KC13) (red-triangle area). For the northern Ionian Sea (PS25 and KC01), riverine inputs from the Aegean and Adriatic areas must have dominated. For the Libyan-Tunisian margin (CP11 and BP22), paleodrainage fluxes are substantially higher during S5 (60–75%) than during sapropel S1 (40–70%) (yellow-triangle area).

CHAPTER 5

The effect of marine barite associated Sr on provenance studies using Sr concentration and isotopes: with pertinent examples from Mediterranean sediments

Jiawang Wu * and Gert J. de Lange

Department of Earth Sciences – Geochemistry, Faculty of Geosciences, Utrecht University, Princetonplein 9, 3584 CC Utrecht, The Netherlands

* Corresponding author: j.w.wu@uu.nl (J. Wu).

(in preparation)

Abstract

Strontium (Sr) concentration and isotopes ($^{87}Sr/^{86}Sr$) of the carbonate-free component of marine sediments have been widely used for provenance studies. The authigenic Sr associated with marine barite, however, may still remain in the decarbonated sediments. This may substantially affect the detrital Sr signature, in particular for sediments with enhanced barite content. Accordingly, this hitherto unreported deviation is expected to be prominent in regions with high biological productivity. The Mediterranean is a suitable area to examine this problem, because not only successful provenance studies have been done based on Sr concentration and isotopes; but also enhanced levels of barite occur in distinct sediment intervals. Here, we use samples from the organic-rich sapropel S1 interval to demonstrate the effect of barite-Sr remaining after traditional carbonate removal. A total of 130 samples from 11 Mediterranean cores are used. After the routine decarbonation using twice a 1 M HCl solution, the remaining sediment was subject to a 2 M NH_4Cl (pH = 7) extraction, known to selectively dissolve barite. Our results show that considerable barite-associated Sr remains in the decarbonated sediments. The amount remaining is proportional to the barite content in the sediment. For the samples with a relatively low barite content, the remaining barite-Sr is negligible; whereas for samples with >400 ppm total barite, this remaining, barite-associated Sr is substantial. Naturally this effect is even more enhanced if detrital sediments have high $^{87}Sr/^{86}Sr$ (>0.713) and low Sr/Al ratio (<0.0010). Consequently, potential barite-associated Sr needs to be taken into account for provenance studies using detrital Sr composition. This is strongly recommended for sediments characterized by a relatively high barite content (>400 ppm). A direct correction for the barite-Sr remaining in decarbonated sediment is suggested for all provenance studies using detrital $^{87}Sr/^{86}Sr$ and Sr concentration as diagnostic tools.

Keywords

barite; barium (Ba); strontium (Sr); Sr isotopes; sapropel S1; provenance; marine sediment; Mediterranean Sea

1 Introduction

1.1 Sr isotopes and concentration for provenance studies

Strontium (Sr) concentration and isotopes in terrigenous, fine-grained sediment accumulating in the deep sea are determined by detrital minerals, which can be treated as mixtures of two endmembers: the weathering products of predominantly young volcanic rocks vs. those derived from old continental, unradiogenic rocks from the crust (Dasch, 1969; Faure, 1986). As a fingerprint of source rocks, Sr isotopic composition ($^{87}Sr/^{86}Sr$) and Sr concentration have therefore been widely employed as tracers for the provenance of silicate detritus in marine sediments (e.g. Grousset et al., 1992; 1998; Biscaye et al., 1997; Krom et al., 1999a; 1999b; 2002; Grousset and Biscaye, 2005; Stein et al., 2007; Box et al., 2011; Palchan et al., 2013). Nevertheless, Sr isotopes of detrital sediments seem to be fractionated between mineralogically different grain-size fractions during erosion and transport processes (e.g. Dasch, 1969; Goldstein et al., 1984; Biscaye et al., 1997; Walter et al., 2000; Tütken et al., 2002; Meyer et al., 2011). In fact, variations in the detrital $^{87}Sr/^{86}Sr$ of marine sediments cores have been used to reflect changes in the weathering regimes, as Sr is relatively mobile during chemical weathering (e.g. Blum and Erel, 1997; Jung et al., 2004; Colin et al., 2006; Meyer et al., 2011). These demerits can be offset by the joint use of Sr isotopes with, for instance, Nd isotopes that have been demonstrated as a conservative provenance proxy (e.g. Freydier et al., 2001; Weldeab et al., 2002a; 2002b; Cole et al., 2009; Revel et al., 2010; 2015; Wu et al., 2016).

However, there is a potential problem associated with the application of $^{87}Sr/^{86}Sr$ and Sr concentration, not only in provenance studies, but also in paleoenvironmental reconstructions. This is related to the barite-associated Sr.

1.2 Marine barite and its associated Sr phase

For the marine sediments deposited above the carbonate compensation depth, the Sr composition is primarily controlled by carbonates, whose $^{87}Sr/^{86}Sr$ is identical to that of the seawater from which they formed (Elderfield, 1986; e.g. Klaver et al., 2015). Indeed, the $^{87}Sr/^{86}Sr$ ratios preserved in carbonates have been widely used to indicate seawater evolution in the geological past (Miller et al., 1987; Raymo et al., 1988; Paytan et al., 1993). Thus, various acid leaching techniques (e.g. acetic acid and hydrochloric acid) are employed to separate the seawater- and detrital-derived Sr phases in marine sediments (e.g. Krom et al., 1999a; 1999b; Freydier et al., 2001; Weldeab et al., 2002a; 2002b; Tachikawa et al., 2004; Stein et al., 2007; Revel et al., 2010; Wu et al., 2016). However, such decarbonation alone is not adequate to fully extract the seawater-Sr recorded in authigenic minerals, such as barites and sulphides (Lyle et al., 1984; Tribovillard et al., 1996; Des Combes et al.,

1999; Rutten and De Lange, 2002).

Marine barite, a ubiquitous minor phase of pelagic sediments, has been demonstrated as a reliable monitor of seawater $^{87}Sr/^{86}Sr$ (Paytan et al., 1993; Martin et al., 1995; Paytan and Griffith, 2007, and references therein). The exact mechanism of barite formation is unclear, while a correlation has been found between the vertical fluxes of organic carbon (C_{org}) and particulate barite in sediment traps (Dymond et al., 1992; Paytan et al., 1993; Paytan and Griffith, 2007). Although seawater is usually undersaturated with barite, this mineral is thought to precipitate within sulphate-rich microenvironments associated with decaying organic matter or as the result of the dissolution of Ba-rich celestite tests of acantharia, both causing localized supersaturation with respect to barite (e.g. Dehairs et al., 1980; Bishop, 1988; Dymond et al., 1992; Paytan et al., 1993; Dymond and Collier, 1996; Paytan and Griffith, 2007). Whatever exact formation mode, marine barite $^{87}Sr/^{86}Sr$ reflects the seawater composition at its formation (Paytan et al., 1993; 2002; Martin et al., 1995).

Marine barite ($BaSO_4$) usually occurs in the form of microcrystals or aggregates of 0.5–5 µm size, and is a rather insoluble mineral, even in acids (Dehairs et al., 1980; Bishop, 1988; Dymond et al., 1992; Paytan et al., 1993). As a result, traditional methods to remove the carbonate prior to determining the detrital sediment composition may not quantitatively remove the barite and its associated Sr. Hitherto, provenance-related studies using Sr concentration and isotopes have ignored this potential “contamination”. The potential effect, obviously, is largest for areas with high biological productivity, i.e. high barite content.

1.3 Mediterranean sediments and sapropel formation

The eastern Mediterranean Sea (EMS) is probably the most suitable area to examine the impact of barite-Sr on the detrital-Sr signature and provenance. This is because, on the one hand, there are numerous studies using the detrital Sr system to track sediment provenance changes over the circum-Mediterranean regions (e.g. Grousset et al., 1992; 1998; Krom et al., 1999a; 1999b; 2002; Freydier et al., 2001; Weldeab et al., 2002a; 2002b; Grousset and Biscaye, 2005; Stein et al., 2007; Cole et al., 2009; Revel et al., 2010; 2015; Box et al., 2011; Palchan et al., 2013; Wu et al., 2016). On the other hand, the EMS is characterized by the cyclic deposition of organic-rich units called sapropels, with enhanced barite contents. Sapropel formation has been attributed to stagnating deep-water condition and enhanced biological production, which is thought to be induced by increased river runoff and nutrients (Rossignol-Strick et al., 1982; Cramp and O'Sullivan, 1999; Emeis et al., 2000; De Lange et al., 2008; Rohling et al., 2015; Tachikawa et al., 2015).

The full extent of sapropels is usually recognized by the elevated zone of Ba/Al in bulk sediments (De Lange et al., 1989; 2008; Thomson et al., 1995; 1999; Van Santvoort et al, 1996; Reitz et al., 2006). Microscopic and geochemical studies have demonstrated that barite is present in the Ba-enriched but not in the Ba-lean intervals of EMS sediments (Thomson et al., 1995; Martinez-Ruiz et al., 2000; Rutten and De Lange, 2002). Sedimentary Ba commonly consists of two main components: Al-silicate related Ba, and barite-Ba (Dymond et al., 1992; Klump et al., 2000; Reitz et al., 2004). Silicate-bound Ba (i.e. detrital Ba) constitutes the major fraction of sedimentary bulk Ba in the Ba-lean intervals, whereas barite is the dominant fraction in sapropels.

1.4 Determination of barite content in marine sediments

Several attempts have been made to directly analyze the barite content in marine sediments, such as by X-ray diffraction (Gingele and Dahmke, 1994) and microscopic evaluation (Martinez-Ruiz et al., 2000). An adequate method to reconstruct changes in the seawater $^{87}Sr/^{86}Sr$, $^{143}Nd/^{144}Nd$, and $\delta^{34}S$ signatures from barite has been developed (e.g. Paytan et al., 1993; 2002; Martin et al., 1995). In this method all phases except barite are dissolved. Unfortunately, also part of the barite dissolves in this procedure thus it cannot be used to quantitatively assess the barite content. Alternative methods, distinctly dissolving the barite phase, have been developed and applied to sediments from Indian Ocean and Mediterranean (Schenau et al., 2001; Rutten and De Lange, 2002).

Here, we remove the remaining barite-Sr from decarbonated sediments using a barite-specific chemical extraction method after Rutten and De Lange, 2002. Subsequently, we make a preliminary evaluation of the effect of this barite-Sr phase on the detrital Sr composition. In particular, the factors controlling such barite-Sr effect, as well as the associated thresholds are illustrated, not only in terms of the exemplary Mediterranean sediments, but also with relevance to global implications for marine-sediment provenance studies.

2 Material and methods

The study is performed on Holocene sapropel S1 layers characterized by elevated C_{org} and Ba contents, and on the adjacent sediments with organic- and Ba-lean intervals. The samples are taken from 10 cores on a basin-wide EMS scale, to give a geographical and bathymetric coverage. A diagnostic core from the western Mediterranean Sea (WMS) is also included to provide a comparison between sapropel and non-sapropel contemporaneous sediments deposited in the EMS and WMS (Table 1; Figure 1).

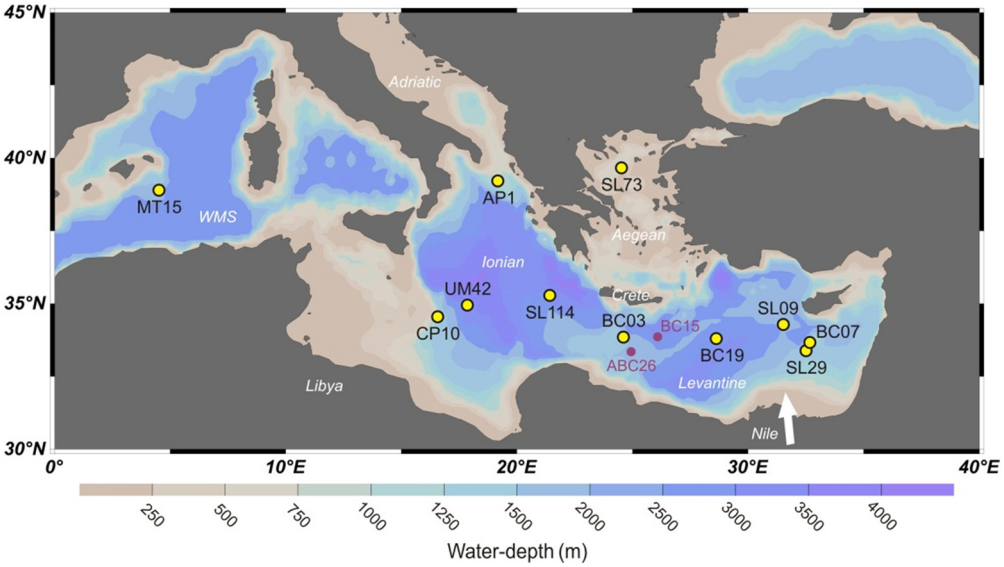

Figure 1 Bathymetric map of the Mediterranean showing the locations of studied cores (yellow circles; Table 1), and the cores (purple circles) mentioned in text. This includes the eastern Mediterranean Sea (EMS) and the western Mediterranean Sea (WMS).

Table 1 General information of the Mediterranean cores investigated

Core	Type [a]	Water-depth	Location	Cruise
SL73	BC	339 m	39°39.7'N, 24°30.7'E	RV *Logachev* 1999
AP1	GC	811 m	39°13.0'N, 19°06.8'E	RV *Urania* 1998
BC07	BC	893 m	33°40.0'N, 32°40.0'E	RV *Marion Dufresne* 1994
UM42	BC	1375 m	34°57.2'N, 17°51.8'E	RV *Urania* 1994
CP10	BC	1501 m	34°32.7'N, 16°34.0'E	RV *Pelagia* 2011
SL29	BC	1587 m	33°23.4'N, 32°30.2'E	RV *Logachev* 1999
BC03	BC	2180 m	33°22.5'N, 24°46.0'E	RV *Marion Dufresne* 1994
SL09	BC	2302 m	34°17.2'N, 31°31.4'E	RV *Logachev* 1999
BC19	BC	2750 m	33°47.9'N, 28°36.5'E	RV *Marion Dufresne* 1991
SL114	BC	3390 m	35°17.2'N, 21°24.5'E	RV *Logachev* 1999
MT15 [b]	PC	2373 m	38°53.8'N, 04°30.6'E	RV *Tyro* 1993

[a] Corer type: box core (BC), gravity core (GC), and piston core (PC).
[b] Collected from the western Mediterranean Sea (WMS).

For these cores, age models were based on conventional radiocarbon dates and the well-established boundaries of sapropel S1 (~9.8–5.7 ^{14}C ka), as defined by the C_{org} (i.e. organic carbon), Ba/Al, and Mn/Al criteria (Thomson et al., 1995; 1999; Van Santvoort et al, 1996; Reitz et al., 2006; De Lange et al., 2008). Note that sapropel S1 is the only sapropel within the range of precise radiocarbon dating, allowing its depth- and process-related compositional variations to be determined as a function of time. To avoid the complications encountered in previous radiocarbon investigations in the Mediterranean, such as reservoir age and local reservoir

correction (ΔR), and also to maintain the comparability with other published records using various calibration curves, the uncorrected ^{14}C ages are used here (c.f. De Lange et al., 2008). Generally, ^{14}C dates were determined on planktonic foraminifera sampled from in and around the zones with high bulk Ba/Al values, then the core-depths were converted to ^{14}C time from the regression of these radiocarbon ages versus depth.

A total of 130 samples from these 11 Mediterranean cores were freeze-dried and ground. To separate different fractions, the bulk sediment samples were leached with HCl to remove carbonate, and the residues subsequently were treated with NH_4Cl to remove the potentially remaining barite (Table 2). The latter extraction was repeated 6 times to ensure a full removal of barite. Subsequently, geochemical analyses were done on bulk sediments, the HCl-leached residues (i.e. carbonate-free sediments), and the NH_4Cl-leaching fluids (i.e. the fluids containing the extracted barite) (Table 3). For a set of selected samples, the analyses are also performed on HCl-leaching fluids and NH_4Cl-leached residues to verify the recovery for the various steps (Table 4). An overview of the sequential extraction procedures is given in Table 2, and is described in more detail below.

Taken together, this sample assembly and set-up permit our study on the Mediterranean sediments can be taken as a standard exemplification, with implications for all provenance studies using Sr concentration and isotopes worldwide.

2.1 HCl leaching (decarbonation)

Following the protocol by Van Santvoort et al. (1996), ~0.3 gram of freeze-dried, powdered samples were decarbonated by shaking in 7.5 ml of 1 M HCl for 4 hours firstly, and for 12 hours again after centrifuging and removing the acids. This ensures the complete dissolution of carbonate. Subsequently, the samples were rinsed and centrifuged twice with 10 ml deionized water, oven-dried at 80 °C, and finely ground. For each step, the samples were weighed, and the leaching fluids including the rinsing fluids were collected. After decarbonation, the weight loss is determined: Weight loss (%) = {[bulk sediment (wt.) – HCl-leached residue (wt.)] / bulk sediment (wt.)} * 100%.

2.2 NH4Cl leaching (barite extraction)

An aliquot of 40–80 mg decarbonated sediments (i.e. HCl-leached residue) was weighed to extract the remaining barite, using a simplified approach from a sequential barite extraction method (BASEX; Rutten and De Lange, 2002). We performed the extraction using 6 ml of a 2 M NH_4Cl (pH = 7) solution during 24 hours. This was repeated 6 times so as to be sure to have complete dissolution of

barite. The fluids of the last step have been randomly checked to confirm that there is no detectable Ba and Sr. Subsequently, the samples were washed with deionized-water, dried, weighed, and powdered.

Table 2 Sequential extraction procedure and the potential phase extracted in terms of Ba and Sr

Step	Sample used	Processed	Fraction collected	Phase extracted [a]	Total digestion [b]	ICP-OES
1	Bulk sediment (>1 g)	Freeze-dried, ground		carbonate, barite, clay, Fe-Mn oxides	Before digestion an aliquot for Step 2 is taken	All samples
2	Bulk sediment (~0.3 g)	Leached with 7.5 ml HCl (1 M) for 4+12 hours, and rinse with 10 ml deionized water 2 times	HCl-leaching fluid, carbonate-rich	carbonate (all), barite (part), clay (few), Fe-Mn oxides (part)		Selected samples
			HCl-leached residue, carbonate-free	barite (part), clay (most), Fe-Mn oxides (part)	Dried, ground, before digestion an aliquot for Step 3 is taken	All samples
3	HCl residue (40–80 mg)	Leached with 6 ml NH_4Cl (2 M; pH = 7) for 24 hours, repeated 6 times	NH_4Cl-leaching fluid, barite-rich	barite (rest), clay (few), Fe-Mn oxides (few)		All samples
			NH_4Cl-leached residue, carbonate- and barite-free	clay (most), Fe-Mn oxides (few)	Dried, ground, digestion	Selected samples

[a] Potential phases containing Ba and Sr; note that Fe-Mn oxides, i.e. Fe,Mn-OOH, contains negligible Sr (only minor amounts of Ba); "clay" is used here to include all detrital minerals, most of which are clay minerals.
[b] Using an acid mixture of HF-HClO4-HNO3 (see Section 2.3).

2.3 Total digestion

For the sediment samples, a routine three-step total destruction was applied (Reitz et al., 2006). Powdered samples was digested in a mixture of 2.5 ml concentrated HF and 2.5 ml pre-mixed acid (3:2 concentrated $HClO_4$ and HNO_3), and heated at 90 °C in a gastight Teflon vessel for at least 12 hours. Afterwards, the solution was evaporated at 150 °C to near dryness, and then the residue was dissolved in 4.5% HNO_3 at 90 °C for 6 hours. For the samples with very high Mn concentrations, the protocol was modified to a smaller amount of sample with additional peroxide steps (Reitz et al., 2006; Wu et al., 2016).

Table 3 The Ba and Sr concentrations of different leaching fractions (*) of the Mediterranean sediments used in this study; these include biogenic/authigenic and detrital components, as well as reported and corrected detrital $^{87}Sr/^{86}Sr$ data

Depth (cm)	Sample type	Age (^{14}C ka)	Bulk sediment (ppm)		Weight loss (%) [a]	HCl leaching (ppm)				NH_4Cl leaching (ppm)				Component (%) [d]				Sr $_{det/decarb}$ (%) [e]	Reported $^{87}Sr/^{86}Sr$ [f]		Corrected $^{87}Sr/^{86}Sr$ [g]
						Fluid [b]		Residue		Fluid [c]		Residue [b]		Biogenic		Detrital					
			Ba	Sr		Ba	Sr	Ba	Sr	Ba	Sr	Ba	Sr	Ba	Sr	Ba	Sr				
SL73																					
0.45	non-S1	1.7	243	834	61.5	72.6	767	171	66.6	5.1	0.0	165	66.6	32.0	92.0	68.0	8.0	100	0.710380	1	0.710380
4.65	non-S1	3.1	262	753	55.1	64.3	681	198	71.3	6.9	0.0	191	71.3	27.2	90.5	72.8	9.5	99.9	0.710558	2	0.710559
6.65	non-S1	4.1	288	780	53.0	37.4	690	251	90.3	7.2	0.0	244	90.3	15.4	88.4	84.6	11.6	100			
12.15	S1b	5.8	354	652	43.4	63.5	552	290	99.8	7.6	0.1	283	99.7	20.1	84.7	79.9	15.3	99.9	0.710483	2	0.710484
17.65	S1b	7.3	416	632	41.8	101	527	315	106	8.0	0.0	307	106	26.3	83.3	73.7	16.7	100			
19.15	S1a	7.8	401	618	42.3	141	528	259	90.7	7.1	0.2	252	90.5	37.0	85.4	63.0	14.6	99.8	0.710469	2	0.710472
22.15	S1a	8.7	385	660	42.6	75.2	551	310	108	8.4	0.0	302	108	21.7	83.6	78.3	16.4	100	0.710432	2	0.710432
26.75	non-S1	9.9	369	579	39.1	99.2	482	270	96.9	6.8	0.2	263	96.7	28.7	83.3	71.3	16.7	99.8	0.710770	2	0.710773
30.25	non-S1	10.8	396	511	34.8	44.4	391	352	120	7.9	0.1	344	120	13.2	76.6	86.8	23.4	99.9	0.711145	2	0.711146
AP1																					
21.25	S1b	6.2	264	740	58.5	128	702	136	38.0	7.4	0.3	129	37.7	51.2	94.9	48.8	5.1	99.1	0.717860	1	0.717938
26.25	S1b	7.5	465	672	51.2	294	623	172	48.4	13.0	0.0	159	48.4	65.9	92.8	34.1	7.2	99.9	0.717600	2	0.717608
29.25	S1a	8.3	434	688	55.4	296	649	138	39.4	8.4	0.1	130	39.3	70.1	94.3	29.9	5.7	99.7	0.717218	2	0.717240
31.75	S1a	8.8	453	678	54.0	310	637	143	41.0	9.4	0.6	133	40.4	70.5	94.0	29.5	6.0	98.6	0.716110	2	0.716207
33.75	S1a	9.5	425	663	53.6	279	622	145	40.5	8.3	0.1	137	40.4	67.7	93.9	32.3	6.1	99.8	0.717658	2	0.717672
38.75	non-S1	10.8	239	716	54.4	82.5	670	157	45.6	7.5	0.2	149	45.4	37.6	93.7	62.4	6.3	99.6	0.718359	2	0.718395
39.75	non-S1	11.1	214	661	56.9	71.9	620	142	41.0	5.8	0.3	136	40.8	36.3	93.8	63.7	6.2	99.3	0.717593	2	0.717649
49.75	non-S1	13.7	201	583	58.6	71.6	546	129	36.7	4.5	0.2	125	36.5	37.9	93.7	62.1	6.3	99.6	0.718348	2	0.718386
70.00	non-S1	19.0	185	550	61.9	46.2	510	139	39.8	5.0	0.0	134	39.8	27.7	92.8	72.3	7.2	99.9	0.716888	2	0.716894
BC07																					
0.25	non-S1	1.3	81.8	869	74.6	27.1	846	54.8	23.1	4.2	0.5	50.6	22.6	38.2	97.4	61.8	2.6	97.9	0.712503	3	0.712576
5.25	non-S1	2.8	87.9	909	71.4	24.9	882	63.0	26.4	4.2	0.7	58.7	25.7	33.1	97.2	66.9	2.8	97.2	0.713327	3	0.713447
10.25	non-S1	4.3	83.0	968	73.0	15.0	940	67.9	28.7	6.0	0.0	61.9	28.7	25.4	97.0	74.6	3.0	100.0	0.713028	3	0.713028
15.25	S1b	5.8	333	939	64.6	251	907	81.9	32.7	11.4	2.9	70.5	29.9	78.9	96.8	21.1	3.2	91.3	0.711297	3	0.711500
20.25	S1b	7.3	335	865	59.7	241	826	94.0	39.1	10.8	0.0	83.2	39.1	75.2	95.5	24.8	4.5	100	0.711521	3	0.711521
22.25	S1a	7.9	294	842	61.5	219	810	75.3	31.8	11.1	0.0	64.2	31.8	78.2	96.2	21.8	3.8	100	0.711385	3	0.711385
24.25	S1a	8.5	264	741	55.0	167	699	96.7	42.1	9.4	0.0	87.2	42.1	66.9	94.3	33.1	5.7	100	0.711169	3	0.711169
26.25	S1a	9.1	206	780	56.9	127	744	79.7	35.7	6.2	0.0	73.5	35.7	64.4	95.4	35.6	4.6	100	0.711130	3	0.711130
29.75	S1a	10.2	276	833	58.7	192	796	84.2	36.2	9.5	1.3	74.7	34.9	72.9	95.8	27.1	4.2	96.5	0.711071	3	0.711140
31.75	non-S1	10.8	241	784	58.3	146	741	95.5	42.5	8.8	1.3	86.8	41.3	64.0	94.7	36.0	5.3	97.0	0.711049	3	0.711107
36.25	non-S1	12.1	144	756	60.2	60.3	717	83.5	38.9	5.0	1.1	78.6	37.8	45.4	95.0	54.6	5.0	97.2	0.711125	3	0.711180
40.25	non-S1	13.3	113	839	71.1	49.6	809	63.1	30.5	4.2	0.5	58.9	30.1	47.7	96.4	52.3	3.6	98.5	0.711012	3	0.711040
48.25	non-S1	15.7	124	602	67.5	41.7	566	82.5	35.6	4.6	0.9	78.0	34.7	37.2	94.2	62.8	5.8	97.5	0.711899	3	0.711969
UM42																					
4.65	non-S1	1.8	148	768	66.0	26.8	719	121	49.1	4.9	0.6	116	48.5	21.5	93.7	78.5	6.3	98.8	0.716230	3	0.716314

9.15	non-S1	3.3	133	747	67.7	30.5	707	103	39.7	4.2	0.5	98.7	39.2	26.0	94.7	74.0	5.3	98.7	0.717569	3	0.717681
19.15	S1b	6.6	307	923	64.8	195	882	112	41.0	7.1	0.5	105	40.5	65.8	95.6	34.2	4.4	98.7	0.716462	3	0.716560
22.15	S1b	7.6	742	1011	65.1	453	962	289	49.2	150	3.8	139	45.4	81.2	95.5	18.8	4.5	92.4	0.715084	3	0.715574
23.15	S1a	7.9	814	985	65.4	639	940	175	44.7	64.8	0.0	110	44.7	86.5	95.5	13.5	4.5	100	0.715169	3	0.715169
26.15	S1a	8.9	776	974	60.7	530	924	246	50.1	110	3.9	136	46.2	82.5	95.3	17.5	4.7	92.2	0.715624	3	0.716173
27.15	S1a	9.2	600	945	59.5	386	901	214	44.4	91	3.5	123	40.9	79.5	95.7	20.5	4.3	92.1	0.716385	3	0.717004
28.65	S1a	9.7	263	907	63.3	143	862	120	44.8	9.1	0.0	111	44.8	57.8	95.1	42.2	4.9	100	0.715800	3	0.715800
32.15	non-S1	10.9	180	674	61.4	48.6	624	132	50.0	6.1	1.0	126	49.1	30.3	92.7	69.7	7.3	98.1	0.716435	3	0.716577
34.65	non-S1	11.7	152	590	65.3	34.5	540	118	50.0	4.9	0.8	113	49.3	25.9	91.7	74.1	8.3	98.5	0.716461	3	0.716576
CP10																					
0.25	non-S1	1.0	150	611	62.4	14.9	562	136	49.1	6.7	2.9	129	46.2	14.4	92.4	85.6	7.6	94.1	0.719740	4	0.720408
3.25	non-S1	1.7	172	643	57.7	27.9	590	145	52.5	7.2	4.0	137	48.6	20.3	92.4	79.7	7.6	92.5	0.719847	4	0.720718
12.25	non-S1	3.7	187	665	57.7	36.6	605	151	59.3	6.9	3.4	144	55.9	23.3	91.6	76.7	8.4	94.3	0.718365	4	0.718920
15.25	non-S1	4.4	158	719	57.8	21.3	668	137	50.7	7.5	4.0	130	46.7	18.2	93.5	81.8	6.5	92.0	0.719703	4	0.720615
17.75	non-S1	5.0	157	728	56.8	25.3	678	132	49.2	8.0	4.0	124	45.3	21.1	93.8	78.9	6.2	92.0	0.718582	4	0.719405
19.25	non-S1	5.3	254	782	52.6	101	729	153	52.3	8.0	3.9	145	48.4	42.8	93.8	57.2	6.2	92.5	0.717853	4	0.718554
21.50	S1b	5.8	509	920	53.3	294	865	214	55.1	21.0	5.1	193	50.1	62.0	94.6	38.0	5.4	90.8	0.716946	4	0.717735
23.00	S1b	6.2	822	1034	57.0	466	977	356	57.6	276	10.8	79.6	46.8	90.3	95.5	9.7	4.5	81.3	0.716065	4	0.717650
24.75	S1b	6.6	833	951	52.8	326	884	507	67.0	383	14.0	125	53.0	85.1	94.4	14.9	5.6	79.1	0.715471	4	0.717135
26.25	S1b	6.9	871	930	52.8	422	863	449	67.0	280	11.6	169	55.5	80.6	94.0	19.4	6.0	82.8	0.714622	4	0.715758
27.75	S1b	7.3	842	901	50.9	502	835	340	66.3	178	7.4	162	58.8	80.8	93.5	19.2	6.5	88.8	0.714916	4	0.715643
28.75	S1b	7.5	840	898	50.2	516	835	323	63.5	133	6.1	190	57.4	77.3	93.6	22.7	6.4	90.4	0.715166	4	0.715807
29.50	S1b	7.6	824	931	52.5	437	865	387	65.8	221	8.5	166	57.3	79.8	93.8	20.2	6.2	87.0	0.714822	4	0.715665
30.25	S1a	7.8	813	839	49.1	525	777	288	62.6	127	6.0	160	56.6	80.3	93.3	19.7	6.7	90.5	0.716075	4	0.716803
31.00	S1a	8.0	827	939	48.7	480	877	347	62.0	100	5.3	247	56.6	70.2	94.0	29.8	6.0	91.4	0.716393	4	0.717072
32.50	S1a	8.3	798	855	48.6	499	792	299	63.1	126	6.0	173	57.1	78.3	93.3	21.7	6.7	90.5	0.716694	4	0.717482
33.75	S1a	8.6	667	837	50.2	416	777	251	59.3	95.6	5.7	156	53.6	76.6	93.6	23.4	6.4	90.4	0.716986	4	0.717820
34.75	S1a	8.8	637	903	49.8	393	843	244	59.2	98.6	5.7	146	53.5	77.1	94.1	22.9	5.9	90.3	0.718064	4	0.719016
SL29																					
5.25	non-S1	3.2	88.9	861	66.5	15.2	830	73.7	30.8	4.2	0.0	69.5	30.8	21.8	96.4	78.2	3.6	100	0.713470	2	0.713470
10.25	non-S1	4.4	89.8	915	65.0	0.7	877	89.1	37.5	5.1	2.5	84.1	35.1	6.4	96.2	93.6	3.8	93.5	0.712907	2	0.713169
17.75	S1b	6.2	467	869	56.4	360	830	108	39.1	23.1	3.2	84.6	36.0	81.9	95.9	18.1	4.1	91.9	0.711056	2	0.711222
23.25	S1b	7.5	730	758	51.6	526	717	205	41.3	108	3.7	97.0	37.5	86.7	95.1	13.3	4.9	90.9	0.711081	2	0.711272
27.25	S1a	8.4	646	774	48.1	484	731	162	42.9	65.4	0.0	96.8	42.9	85.0	94.5	15.0	5.5	100			
32.25	S1a	9.6	254	762	49.5	156	719	98.7	43.1	9.3	0.0	89.4	43.1	64.8	94.3	35.2	5.7	100	0.710975	2	0.710975
35.25	non-S1	10.3	239	749	47.9	125	699	114	49.4	6.8	0.0	107	49.4	55.2	93.4	44.8	6.6	100	0.710674	2	0.710674
39.25	non-S1	11.2	108	657	47.7	0	608	108	49.3	6.2	0.0	102	49.3	5.6	92.5	94.4	7.5	100	0.710772	2	0.710772
BC03																					
5.60	non-S1	4.8	131	875	67.8	14.3	835	117	40.2	5.0	0.6	112	39.6	14.7	95.5	85.3	4.5	98.6	0.718206	3	0.718333
7.40	non-S1	5.2	122	885	71.7	36.1	856	86.1	29.3	5.2	0.0	80.9	29.2	33.8	96.7	66.2	3.3	99.9	0.718082	3	0.718091
12.80	S1b	6.6	394	1147	72.9	320	1124	74.2	23.2	6.6	0.2	67.6	23.0	82.9	98.0	17.1	2.0	99.1	0.716159	3	0.716224
14.00	S1b	6.9	631	1201	71.9	531	1178	100	23.1	32.8	0.5	67.0	22.5	89.4	98.1	10.6	1.9	97.6	0.716140	3	0.716309
15.80	S1b	7.3	920	1237	69.8	549	1204	371	32.7	253	5.2	118	27.5	87.2	97.8	12.8	2.2	84.0	0.715043	3	0.716159

17.00	S1a	7.7	997	1248	65.4	619	1216	378	31.9	328	6.0	49.4	25.9	95.0	97.9	5.0	2.1	81.2	0.717099	3	0.718937
18.20	S1a	8.1	724	1444	64.2	386	1412	338	31.8	270	4.5	68.1	27.3	90.6	98.1	9.4	1.9	85.7	0.716155	3	0.717322
21.20	S1a	8.7	480	1456	63.6	341	1419	139	37.2	35.7	1.6	103	35.6	78.6	97.6	21.4	2.4	95.8	0.715738	3	0.716029
21.80	S1a	8.9	222	1258	64.2	123	1227	98.5	30.7	15.1	0.3	83.4	30.4	62.4	97.6	37.6	2.4	99.0	0.716134	3	0.716203
24.80	S1a	9.6	169	1071	64.4	76.8	1039	92.5	32.4	4.8	0.1	87.6	32.3	48.2	97.0	51.8	3.0	99.8	0.716730	3	0.716744
28.40	non-S1	10.4	125	961	68.0	28.6	928	96.2	33.6	4.9	0.3	91.2	33.3	26.9	96.5	73.1	3.5	99.1	0.717995	5	0.718077
35.00	non-S1	12.1	147	627	61.4	28.3	585	119	42.2	4.9	0.6	114	41.6	22.5	93.4	77.5	6.6	98.6	0.716255	3	0.716359
40.40	non-S1	13.4	118	584	68.7	30.2	553	87.8	31.1	3.8	0.3	84.0	30.8	28.8	94.7	71.2	5.3	99.2	0.716589	3	0.716650
50.00	non-S1	15.8	118	556	68.7	24.4	526	93.3	29.8	4.1	0.3	89.2	29.5	24.2	94.7	75.8	5.3	99.0	0.717461	3	0.717543
60.20	non-S1	18.2	147	510	59.7	26.8	471	120	39.1	5.1	0.4	115	38.7	21.7	92.4	78.3	7.6	99.1	0.716255	3	0.716322
SL09																					
0.35	non-S1	0.3	101	780	60.6	23.3	748	77.6	31.8	4.5	0.0	73.1	31.8	27.6	95.9	72.4	4.1	100	0.713660	1	0.713660
9.95	non-S1	2.4	99.0	763	59.2	19.4	730	79.7	32.5	4.7	0.0	75.0	32.5	24.3	95.7	75.7	4.3	100	0.714630	2	0.714630
18.95	non-S1	4.3	83.2	802	62.3	1.4	768	81.8	34.0	5.0	0.0	76.8	34.0	7.7	95.8	92.3	4.2	100	0.713951	2	0.713951
24.95	S1b	5.6	242	871	54.6	137	830	105	40.8	7.2	0.0	98.1	40.8	59.5	95.3	40.5	4.7	100	0.712873	2	0.712873
29.95	S1b	6.7	789	847	56.2	600	817	189	30.9	120	3.5	68.7	27.4	91.3	96.8	8.7	3.2	88.7	0.713675	2	0.714248
32.45	S1b	7.3	947	737	53.9	479	698	468	38.8	338	8.2	130	30.6	86.3	95.8	13.7	4.2	78.9	0.713334	2	0.714449
34.95	S1a	7.8	885	666	47.0	597	629	289	36.4	207	4.0	82.0	32.3	90.7	95.1	9.3	4.9	88.9	0.713656	2	0.714218
37.45	S1a	8.4	848	714	49.4	514	676	334	38.2	218	4.1	116	34.1	86.4	95.2	13.6	4.8	89.2	0.713390	2	0.713901
40.45	S1a	9.0	556	869	51.2	421	836	135	32.2	66.7	0.0	68.0	32.2	87.8	96.3	12.2	3.7	100	0.713068	2	0.713068
44.95	non-S1	10.0	165	679	48.3	48.5	627	117	51.7	9.9	0.0	107	51.7	35.3	92.4	64.7	7.6	100	0.712796	2	0.712796
BC19																					
3.75	non-S1	2.1	130	1044	69.2	39.9	1011	90.0	32.8	5.9	0.0	84.1	32.8	35.3	96.9	64.7	3.1	100			
5.75	non-S1	2.7	136	1021	67.8	44.2	988	91.5	33.8	6.4	0.0	85.2	33.8	37.2	96.7	62.8	3.3	100	0.716484	3	0.716484
7.25	non-S1	3.2	129	1046	68.0	39.6	1013	89.8	33.3	5.2	0.0	84.6	33.3	34.6	96.8	65.4	3.2	100	0.715635	3	0.715635
10.50	non-S1	4.3	343	439	33.7	34.6	381	308	57.7	4.8	1.2	303	56.6	11.5	87.1	88.5	12.9	98.0			
12.75	non-S1	4.9	112	1097	71.9	36.4	1068	75.4	28.2	6.0	0.0	69.4	28.2	37.9	97.4	62.1	2.6	100	0.715030	3	0.715030
15.75	non-S1	5.9	110	1135	69.4	25.3	1102	84.2	32.8	5.9	0.0	78.4	32.8	28.4	97.1	71.6	2.9	100	0.714476	3	0.714476
19.25	S1b	6.9	1086	1116	68.7	595	1085	491	31.3	457	8.8	34.0	22.5	96.9	98.0	3.1	2.0	71.9	0.713208	3	0.714786
20.75	S1b	7.4	963	795	56.6	764	755	199	40.8	78.8	0.0	120	40.8	87.5	94.9	12.5	5.1	100	0.713343	3	0.713343
23.25	S1a	8.0	1322	831	58.0	954	801	368	29.4	325	4.0	42.7	25.4	96.8	96.9	3.2	3.1	86.3	0.712096	3	0.712559
25.75	S1a	8.6	1022	829	56.7	725	794	297	35.2	189	3.9	108	31.2	89.4	96.2	10.6	3.8	88.8	0.711117	3	0.711363
27.25	S1a	9.0	710	1163	57.0	622	1132	88.5	30.9	19.3	0.0	69.2	30.9	90.3	97.3	9.7	2.7	100	0.711309	3	0.711309
29.25	S1a	9.5	275	986	53.6	175	946	100	40.0	8.6	1.4	91.1	38.6	66.9	96.1	33.1	3.9	96.5	0.712362	3	0.712476
30.25	non-S1	9.8	248	999	52.0	150	959	97.7	39.9	8.8	1.3	88.9	38.6	64.2	96.1	35.8	3.9	96.8	0.712066	3	0.712161
32.25	non-S1	10.4	160	971	53.2	41.6	924	119	46.9	5.7	1.9	113	45.0	29.5	95.4	70.5	4.6	96.0	0.713460	3	0.713640
34.95	non-S1	11.2	151	935	60.1	42.5	893	108	42.2	5.1	1.4	103	40.8	31.6	95.6	68.4	4.4	96.8	0.714383	3	0.714557
SL114																					
15.55	non-S1	4.1	144	938	61.5	2.2	897	142	41.2	5.8	0.5	136	40.7	5.6	95.7	94.4	4.3	98.8	0.718905	1	0.719019
22.05	non-S1	5.9	169	1196	65.4	51.3	1165	118	31.1	4.2	0.3	114	30.8	32.7	97.4	67.3	2.6	98.9	0.717818	5	0.717911
24.05	S1b	6.4	721	1172	68.4	536	1146	186	25.7	96.6	2.7	89.3	23.0	87.6	98.0	12.4	2.0	89.5	0.716694	4	0.717573
26.55	S1b	7.1	928	874	56.0	486	829	442	45.0	245	4.0	197	41.0	78.7	95.3	21.3	4.7	91.1	0.716365	5	0.717070
28.05	S1b	7.6	1066	913	58.3	629	881	437	32.6	369	6.4	67.7	26.2	93.6	97.1	6.4	2.9	80.4	0.715441	4	0.716966

32.05	S1a	8.7	991	1078	62.8	506	1044	485	34.4	391	6.3	94.5	28.1	90.5	97.4	9.5	2.6	81.6	0.715743	4	0.717223
34.05	S1a	9.2	833	1156	62.3	740	1135	93.2	20.5	20.6	0.4	72.6	20.1	91.3	98.3	8.7	1.7	98.0	0.716405	4	0.716550
39.05	non-S1	10.6	159	746	56.3	12	697	146	48.3	6.1	0.4	140	47.9	11.5	93.6	88.5	6.4	99.2	0.716243	4	0.716299
49.20	non-S1	13.5	146	530	52.2	8.6	488	138	42.8	6.2	0.4	131	42.4	10.1	92.0	89.9	8.0	99.1	0.718041	4	0.718124
MT15																					
0.25	non-S1	1.5	219	787	54.9	30.1	734	189	52.9	4.7	0.2	184	52.7	15.9	93.3	84.1	6.7	99.6	0.719894	1	0.719941
20.25	non-S1	3.3	189	805	66.6	45.3	764	144	40.5	4.4	0.3	139	40.3	26.3	95.0	73.7	5.0	99.4	0.719355	2	0.719419
50.25	non-S1	6.0	191	799	59.7	4.8	750	186	48.8	5.3	0.0	181	48.8	5.2	93.9	94.8	6.1	100	0.718863	2	0.718863
80.25	non-S1	8.7	268	778	57.8	86.5	726	182	52.4	5.1	0.3	176	52.1	34.2	93.3	65.8	6.7	99.5	0.718140	2	0.718188
90.25	non-S1	9.7	319	796	57.3	136	745	183	51.2	6.5	0.0	177	51.2	44.5	93.6	55.5	6.4	100	0.718830	2	0.718830
100.3	non-S1	10.6	316	458	46.7	62.9	393	253	64.6	5.5	0.2	247	64.4	21.7	85.9	78.3	14.1	99.6	0.722311	2	0.722358
104.0	non-S1	10.9	331	407	45.2	68.3	341	263	66.2	5.5	0.3	258	65.9	22.2	83.8	77.8	16.2	99.6	0.722736	2	0.722791
108.0	non-S1	11.3	307	512	48.4	73.2	451	234	61.1	5.9	0.0	228	61.1	25.7	88.1	74.3	11.9	99.9	0.721350	2	0.721357
114.0	non-S1	11.8	351	648	51.0	135	590	216	57.6	6.7	0.1	209	57.5	40.4	91.1	59.6	8.9	99.8	0.719385	2	0.719405
118.0	non-S1	12.2	316	677	54.5	125	627	191	50.4	6.6	0.0	184	50.4	41.6	92.6	58.4	7.4	100	0.718800	2	0.718800
120.3	non-S1	12.4	285	704	57.8	94.2	654	191	50.4	6.1	0.1	185	50.3	35.1	92.9	64.9	7.1	99.8	0.719500	2	0.719522
140.0	non-S1	14.2	348	564	49.3	121	507	227	57.1	7.0	0.4	220	56.6	36.8	90.0	63.2	10.0	99.2	0.720160	2	0.720244

(*) All results were calculated so as to give concentrations relative to the initial total sample.

[a] Weight loss of bulk sediment after decarbonation, roughly proportional to $CaCO_3$ (%).

[b] Calculated data: HCl-fluid = bulk-sediment – HCl-residue; NH_4Cl-residue = HCl-residue – NH_4Cl-fluid. The calculation is justified by measurements on selected samples (Table 4; Figure 2).

[c] Some of the data (*italic*) have larger uncertainties (~10–15%) because of the very low concentrations.

[d] Taking the NH4Cl-residue as pure detrital component: biogenic/authigenic component = bulk-sediment – detrital-component; note the use of percentage.

[e] $Sr_{det/decarb}$ = det-Sr / decarb-Sr, i.e. the ratio of the Sr in detrital component to the Sr in decarbonated sediment (i.e. HCl-residue).

[f] Data source: 1= Tachikawa et al. (2004), 2= A. Michard (unpublished), 3= Freydier et al. (2001); 4= Wu et al. (2016); 5= J. Wu (unpublished).

[g] Detrital $^{87}Sr/^{86}Sr$ composition in the carbonate- and barite-free sediments is corrected using the equation: $^{87}Sr/^{86}Sr_{corrected} = (^{87}Sr/^{86}Sr_{original} - ^{87}Sr/^{86}Sr_{barite} \times (1 - Sr_{det/decarb})) / Sr_{det/decarb}$, where $^{87}Sr/^{86}Sr_{barite}$ refers to the $^{87}Sr/^{86}Sr$ value (0.709165) of deep Mediterranean barite (De Lange et al., 1990) and $Sr_{det/decarb}$ is the percentage of the Sr in detrital component to the Sr in decarbonated sediment (i.e. $Sr_{det/decarb}$ = NH_4Cl-residue (Sr) / HCl-residue (Sr)).

Table 4 The calculated and measured Ba and Sr data for a selected set of samples
a) Upper part: for the NH_4Cl-residue with resulting detrital Ba/Al and Sr/Al ratios
b) Lower part: for the HCl-fluid

Core	Depth (cm)	Calculated		Measured		Measured [a]	
		Ba	Sr	Ba	Sr	Ba/Al	Sr/Al
		(ppm)	(ppm)	(ppm)	(ppm)	(mg/g)	(mg/g)
a) NH_4Cl-leached residue							
SL73	4.65	191	71.3	194	70.1	5.31	1.92
SL73	19.15	252	90.5	241	80.4	5.84	1.95
AP1	26.25	159	48.4	143	45.0	3.48	1.10
AP1	38.75	149	45.4	142	44.3	3.38	1.06
BC07	5.25	58.7	25.7	53.5	22.7	2.35	1.00
BC07	22.25	64.2	31.8	62.2	28.5	1.82	0.84
UM42	22.15	139	45.4	128	39.4	4.47	1.38
UM42	27.15	123	40.9	107	35.1	3.37	1.11
CP10	3.25	137	48.6	114	44.2	3.14	1.22
CP10	19.25	145	48.4	129	46.5	3.05	1.10
CP10	24.75	125	53.0	108	48.4	2.45	1.09
CP10	30.25	160	56.6	157	50.0	3.80	1.21
SL29	10.25	84.1	35.1	75.7	31.7	2.40	1.01
SL29	32.25	89.4	43.1	89.8	41.1	2.40	1.10
BC03	7.40	80.9	29.2	76.0	29.0	3.48	1.33
BC03	21.80	83.4	30.4	76.3	29.0	3.11	1.18
SL09	9.95	75.0	32.5	73.1	31.2	2.35	1.00
SL09	40.45	68.0	32.2	64.2	31.5	1.97	0.97
BC19	15.75	78.4	32.8	73.9	31.7	2.84	1.22
BC19	23.25	42.7	25.4	38.7	21.6	1.47	0.82
BC19	32.25	113	45.0	108	39.6	2.75	1.01
SL114	22.05	114	30.8	112	27.8	3.87	0.96
SL114	32.05	94.5	28.1	83.7	24.5	3.46	1.01
MT15	20.25	139	40.3	151	40.0	4.31	1.14
MT15	114.0	209	57.5	190	50.5	4.27	1.14
b) HCl-leaching fluid							
CP10	0.25	30.0	568	22.3	587		
CP10	3.25	45.1	597	18.4	567		
CP10	12.25	55.3	612	16.3	580		
CP10	15.25	37.1	675	16.9	629		
CP10	17.75	41.0	686	27.5	695		
CP10	19.25	126	737	112	742		
CP10	21.50	345	874	303	836		
CP10	23.00	549	987	432	952		
CP10	24.75	409	894	305	838		
CP10	26.25	510	872	438	846		
CP10	27.75	586	844	468	796		
CP10	28.75	600	844	490	811		
CP10	29.50	520	875	431	836		
CP10	30.25	606	785	555	775		
CP10	31.00	563	886	478	846		
CP10	32.50	579	801	459	776		
CP10	33.75	482	786	428	781		
CP10	34.75	457	852	389	795		

[a] The average values of Ba/Al (0.0032 ± 0.0011) and Sr/Al (0.0012 ± 0.0003) in the residue after HCl- and NH_4Cl-leaching (i.e. NH_4Cl-residue), are considered as pure detrital signatures.

2.4 ICP-OES analysis

The elemental composition was determined by Inductively Coupled Plasma – Optical Emission Spectroscopy (ICP-OES) on a Perkin-Elmer Optima 3000 and a Spectro Arcos at Utrecht University. Different ICP-OES calibration programs were used for water samples and total digested sediment samples. In addition, the data for sediments from different cores were measured at different times and using different procedures (c.f. Reitz et al., 2006; De Lange et al., 2008; Wu et al., 2016). International standards, duplicate samples and blanks were included to monitor the analytical uncertainty. For the extraction-related data the soil standard ISE 921 (Van Dijk and Houba, 2000) was used. Relative deviations are <6% for the reported data, unless stated otherwise in Table 3.

3 Results and discussion

The general information of the studied cores is given in Table 1, with their locations and water-depths shown in Figure 1. The detailed extraction procedure is described in Table 2, with the potential phases containing Ba and Sr indicated. The Ba and Sr concentrations in the different fractions of the samples, including bulk sediments, HCl-fluids and -residue, and NH_4Cl-fluids and -residues, are compiled in Table 3. Finally, a correction of the detrital $^{87}Sr/^{86}Sr$ data for the barite-Sr that remained undissolved in the decarbonated sediment is reported (Table 3).

For our preliminary assessment, we calculate the biogenic/authigenic and detrital components from the extraction results (Table 3). Most extractions do not leach a single phase alone (Table 2). Therefore, we have done all analyses of extracts and remaining sediment for a set of selected samples (Table 4; Figure 2). In this way we can verify the general validity of these calculations for the full set of samples.

First, we assess the extraction methods that are used to separate different fractions of the Mediterranean sediments (Section 3.1). Then we estimate the net barite phase by using different calculations, and the barite Sr/Ba ratio (Section 3.2). Next, the existence of barite-associated Ba and Sr that remained undissolved in the decarbonated sediments is discussed (Section 3.3). After that, the effect of remaining barite-Sr after traditional carbonate removal is evaluated, and illustrated by a correction of the reported detrital $^{87}Sr/^{86}Sr$ data (Section 3.4).

3.1 Evaluation of extraction approaches

A sequential extraction method (BASEX) has been developed to determine different Ba fractions in sediments (Rutten and De Lange, 2002). The complete barite extraction with this method was evaluated using pure barite in a mixed mineral standard and Mediterranean sapropel S1 samples (Rutten and De Lange, 2002).

Based on this pioneering work, we adopted the barite-dissolving extraction step using a NH_4Cl solution and apply it to the sediment remaining after the decarbonation step, which is commonly used to remove non-detrital phases for provenance studies. As summarized in Table 2, there are two extractions: HCl-leaching (i.e. carbonate extracted) and NH_4Cl-leaching (i.e. barite extracted), resulting in four fractions: HCl-fluid, HCl-residue, NH_4Cl-fluid, and NH_4Cl-residue.

It is clear that the HCl-leaching removed all of the carbonate, and may have dissolved some Ba, Sr, and Al from clay and barite (Table 3). Some studies used acetic acid for decarbonation (e.g. Grousset et al., 1998; Weldeab et al., 2002a; 2002b; Colin et al., 2006; Cole et al., 2009; Revel et al., 2010). In general, acetic acid is relatively gentle and is thought to dissolve less Al from aluminosilicates. In addition, a limited amount of barite (4–15%) dissolved with an acetic acid pH = 5 leaching for Pacific Ocean sediments (Lyle et al., 1984).

The difference between the use of HCl and acetic acid for decarbonation was stated to be minor for Nd isotope analyses of the leachate phase (Tachikawa et al., 2004). However, this is not the case for detrital Sr composition. For instance, there are distinct differences in Sr isotopes and concentration between the data from Krom et al. (1999b) and from Freydier et al. (2001), for the same areas (e.g. south of Crete: cores ABC26 vs. BC03) or even for the same sites (e.g. BC19) in the EMS (Figure 1). Both using HCl-decarbonation, the former data show systematically lower $^{87}Sr/^{86}Sr$ values and higher Sr concentrations in the decarbonated sediment phase than the latter. This suggests that a marine-derived phase may not be fully dissolved during decarbonation, and thus its associated-Sr may remain in the decarbonated sediments in various degrees. Indeed, for HCl-decarbonation alone, there are various, different procedures (e.g. ignition, temperature, leaching time, repetition, etc.) and acid strengths (e.g. 1 M or 1.25 M) involved in the previous studies (e.g. Krom et al., 1999a; 1999b; Freydier et al., 2001; Jung et al., 2004; Box et al., 2011; Wu et al., 2016). Considering that using HCl removes carbonates quantitatively, the inferred marine-derived phase must be related to barite. Such remaining barite-Sr fraction is considered to be even more important if acetate leaching is used for decarbonation.

It has been demonstrated that repeated leaching of NH_4Cl is adequate to extract the biogenic/authigenic Ba usually found in organic-rich sediments (Schenau et al., 2001; Rutten and De Lange, 2002). Indeed, the complete dissolution of barite using NH_4Cl-leaching can be seen from the detrital Ba/Al ratio of Mediterranean sediments in our study (Table 4). The results give an average Ba/Al value of 0.0032 ± 0.0011 for the NH4Cl-residue, which is in good agreement with the reported values for the EMS sediments (0.0027–0.0039) (Rutten and De Lange, 2002; Reitz et al., 2004).

The detrital Sr/Al signature for the Mediterranean sediments (0.0012 ± 0.0003) is also provided here (Table 4). Moreover, considering the very low Ba content in the NH4Cl-residue, there is negligible – if any – Ba left related with Fe-Mn oxides that may have remained undissolved in some samples.

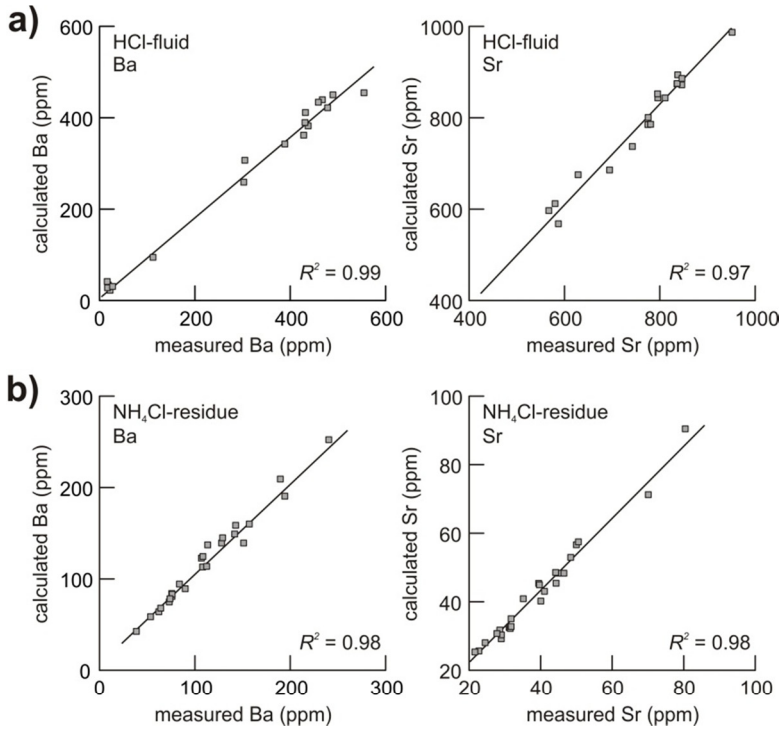

Figure 2 Correlations between the measured and calculated data in terms of Ba and Sr concentrations for the a) HCl-fluid and b) NH_4Cl-residue samples, respectively (Table 4). The strong correlations on selected samples justify the calculations and thus the applicability of the calculated data.

These observations are consistent with the results from the more comprehensive and detailed BASEX method on the EMS sediments (Rutten and De Lange, 2002). It was demonstrated that excess Ba (i.e. the Ba fraction not associated with aluminosilicates) can be attributed to barite, and that other Ba fractions, e.g. associated to carbonate or to Fe-Mn oxides are negligible (Schenau et al., 2001; Rutten and De Lange, 2002).

Applying the HCl- and NH_4Cl extractions sequentially therefore results in the complete removal of carbonate and barite. Consequently, the NH_4Cl-residue contains only detrital minerals and associated Sr. Although the direct ICP-OES analyses have not been done for all NH_4Cl-residue samples, the detrital Ba and Sr data for this fraction can be estimated from the extraction results using Equation 1

(Tables 2 and 3). The validity of this calculation is confirmed by the good correlation between calculated and measured data for selected samples for which also the NH_4Cl-residue has been analyzed (Table 4; Figure 2b).

NH_4Cl-residue (det-Ba, det-Sr) = HCl-residue (decarb-Ba, decarb-Sr) – NH_4Cl-fluid (NH_4Cl-Ba, NH_4Cl-Sr)

Equation 1

In addition, the leaching efficiency of HCl and NH_4Cl is checked by the ICP-OES measurements for the selected samples (Table 4). For the HCl-fluid and NH_4Cl-residue fractions, the strong correlation (R^2 >0.97) between the calculated- and measured-data for Ba and Sr concentrations (Figure 2) confirms that our sequential extraction approach is adequate (Tables 2 and 3).

3.2 Estimates and records of different Ba and Sr phases

3.2.1 Biogenic Ba (barite) content

Determination of barite content in marine sediments is an important issue. A simple way is to analyze bulk Ba (hereafter referred to as “bulk-Ba”), assuming that barite is the major Ba contributor in the sediment. However, detrital Ba (hereafter referred to as “det-Ba”) also constitutes a considerable fraction of the bulk Ba in many cases. Moreover, usually minor amounts of Ba may be present in Fe-Mn oxides (i.e. Fe,Mn-OOH), or be associated with organic matter, opal, or carbonates (Gingele et al., 1994; Schenau et al., 2001; Rutten and De Lange, 2002). The often used method to estimate the biogenic Ba (hereafter referred to as “bio-Ba”, mostly barite), is to correct the total Ba for the detrital Ba concentration using a constant or regional Ba/Al ratio for detrital material (e.g. Dymond et al., 1992; Klump et al., 2000; Reitz et al., 2004; 2006). Following this method, the barite content is then calculated using Equation 2, where bulk-Ba and bulk-Al are the Ba and Al concentration in bulk sediments; and the values of detrital Ba/Al are those derived from our extractions.

*Barite (bio-Ba) = bulk-sediment (bulk-Ba) – bulk-sediment (bulk-Al) * detrital-Ba/Al*

Equation 2

Alternatively, the Ba content in the biogenic/authigenic component can be estimated using Equation 3, where det-Ba refers to the Ba in NH_4Cl-residue. The NH_4Cl-residue contains no carbonate, no barite, negligible – if any – Fe-Mn oxides, thus represents the detrital sedimentary component alone (Table 2), as discussed in Section 3.1.

Barite (bio-Ba) = bulk-sediment (bulk-Ba) – NH_4Cl-residue (det-Ba)

Equation 3

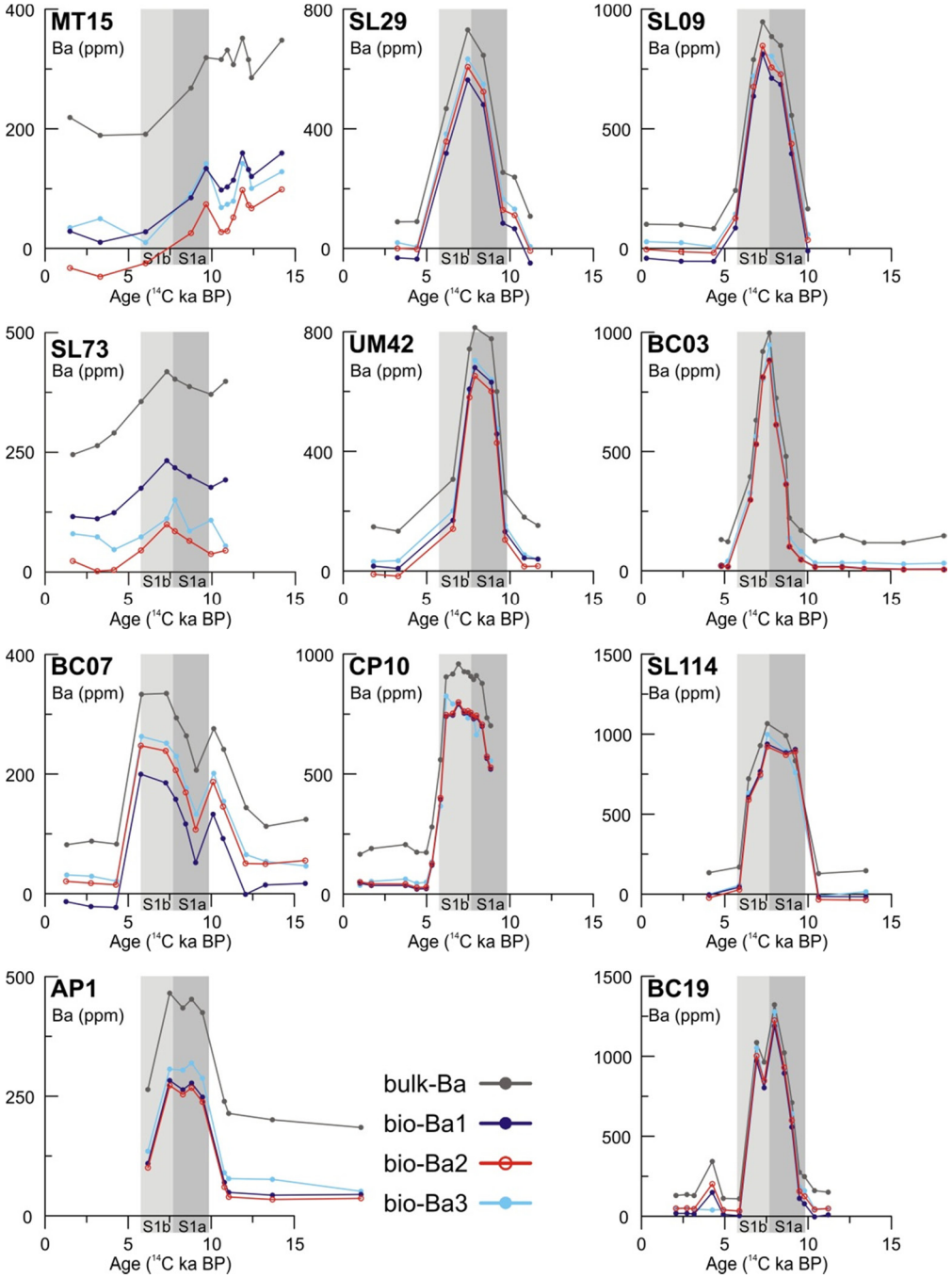

Figure 3 The Ba concentrations in the biogenic/authigenic components (bio-Ba, i.e. barite) and bulk sediments (bulk-Ba). The differences between the bio-Ba profiles are large for the cores with barite content <400 ppm during sapropel S1 period (the 1st column: MT15, SL73, BC07, and AP1). Smaller

differences occur for the cores characterized by a S1 elevated zone of barite between 200 and 800 ppm (the 2nd column: SL29, UM42, and CP10). Minor differences are observed for the cores with highest barite content between 400 and 1200 ppm during sapropel S1 (the 3rd column: SL09, BC03, SL114, and BC19). The sequence and array of cores according to barite content are also used for the following figures (if applicable). The comparison shows that the estimate used for bio-Ba3 is most appropriate method to derive barite content for the Mediterranean sediments. The different methods for the bio-Ba profiles refer to Section 3.2.1.

Here, we compare and evaluate the bio-Ba profiles estimated by these different methods (Figure 3). Using Equation 2, there are two options for the detrital Ba/Al value: either using a basin-averaged value (0.0032) for all Mediterranean cores (i.e. bio-Ba1), or using core-averaged values for each core (i.e. bio-Ba2). The bio-Ba3 is calculated using Equation 3.

The differences between the different bio-Ba profiles are negligible for the cores with abundant barite, but are considerable for the cores with a relatively low barite content (i.e. SL73, AP1, BC07, and MT15) (Figure 3). Although the general patterns are similar, the profiles of bio-Ba1 and bio-Ba2 display large differences in some cores (e.g. BC07, SL09, and MT15) (Figure 3). Indeed, applying a constant detrital Ba/Al ratio to different cores may introduce major errors for sedimentary environments, depending on the source-rock Ba/Al composition (e.g. Dehairs et al., 1980; Dymond et al., 1992; Fagel et al., 1999; Klump et al., 2000; Reitz et al., 2004). This is particularly true for the EMS that receives significant quantities of detrital inputs from different distinct source-rocks (e.g. Krom et al., 1999b; Weldeab et al., 2002a; 2002b; Klaver et al., 2015; Wu et al., 2016).

Therefore, the bio-Ba3 estimate appears to be the most appropriate method to derive the biogenic/authigenic Ba content for Mediterranean sediments. Accordingly, this approach will be used in the following discussion.

3.2.2 Barite-associated Sr content

Although variable amounts of barite (and thus of associated Sr) may be dissolved during decarbonation, depending on solvent used and sediment composition of the sample, it is clear that most of the barite is leached with the NH_4Cl extraction. As a result, the Sr/Ba ratio in the NH_4Cl-fluid can be taken to represent the Sr/Ba signature in barite. Theoretically, as barite forms and picks up the Ba and Sr from the water column, the Sr/Ba ratio in barite should be constant reflecting the water-column Sr/Ba but each with its own fractionation factor.

The downcore changes of the Sr/Ba ratio in the NH_4Cl-fluid fraction show much lower values during the sapropel S1 period (Figure 4), which is characterized by

elevated barite content (De Lange et al., 1989; 2008; Van Santvoort et al, 1996; Thomson et al., 1999; Reitz et al., 2006) (Figure 3). For the non-sapropel intervals where there is no barite, some Ba and Sr is still extracted. This must be related to partly dissolving (clay) minerals or analytical artifacts. Taking the appropriate selection, a pure-barite Sr/Ba is deduced, but with a large potential uncertainty (0.031 ± 0.013) (Figure 4). Applying this barite Sr/Ba value to the calculated barite content (see Section 3.2.1), we derive the amounts of Sr associated with barite (Figure 5).

Taken together, the derived barite content (bio-Ba) constitutes the major component (>70%) of the total Ba in bulk sediments, in particular for the elevated Ba zone during sapropel S1, with a minor contribution of detrital Ba (det-Ba) (Figures 3 and 5). By contrast, the sediments in cores MT15 and SL73 have relatively low barite contents (bio-Ba <200 ppm), and large contributions from detrital materials (det-Ba and det-Sr) (Figures 3 and 5a). Although the detrital contributions display no discernable pattern (Figure 5), for each core, the det-Ba and det-Sr profiles show similar variability, pointing to the same aluminosilicate, detrital sources (Figure 5). These observations are supported by the BASEX extracted results from EMS cores ABC26 and BC15 located south of Crete (i.e. close to cores BC03 and BC19, respectively; Figure 1) (Rutten and De Lange, 2002). The biogenic Ba (>80%) constitutes the major component of the total Ba, with minor detrital Ba (10–15%), and negligible amount of other Ba (<5%).

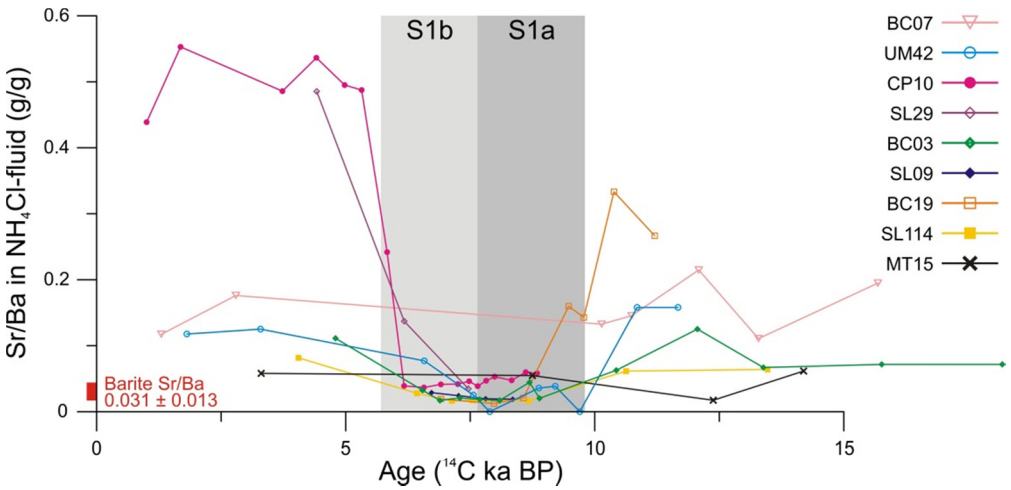

Figure 4 The Sr/Ba ratio in the NH_4Cl-fluid fraction versus time, showing much lower values during sapropel S1 period that is characterized by elevated barite content. These low values for sapropel S1 can be therefore taken to generally represent the Sr/Ba signature in pure barite alone. The average value of Sr/Ba in barite is reported as 0.031 ± 0.013 here; but note that there may be large potential uncertainty due to analytical limitations.

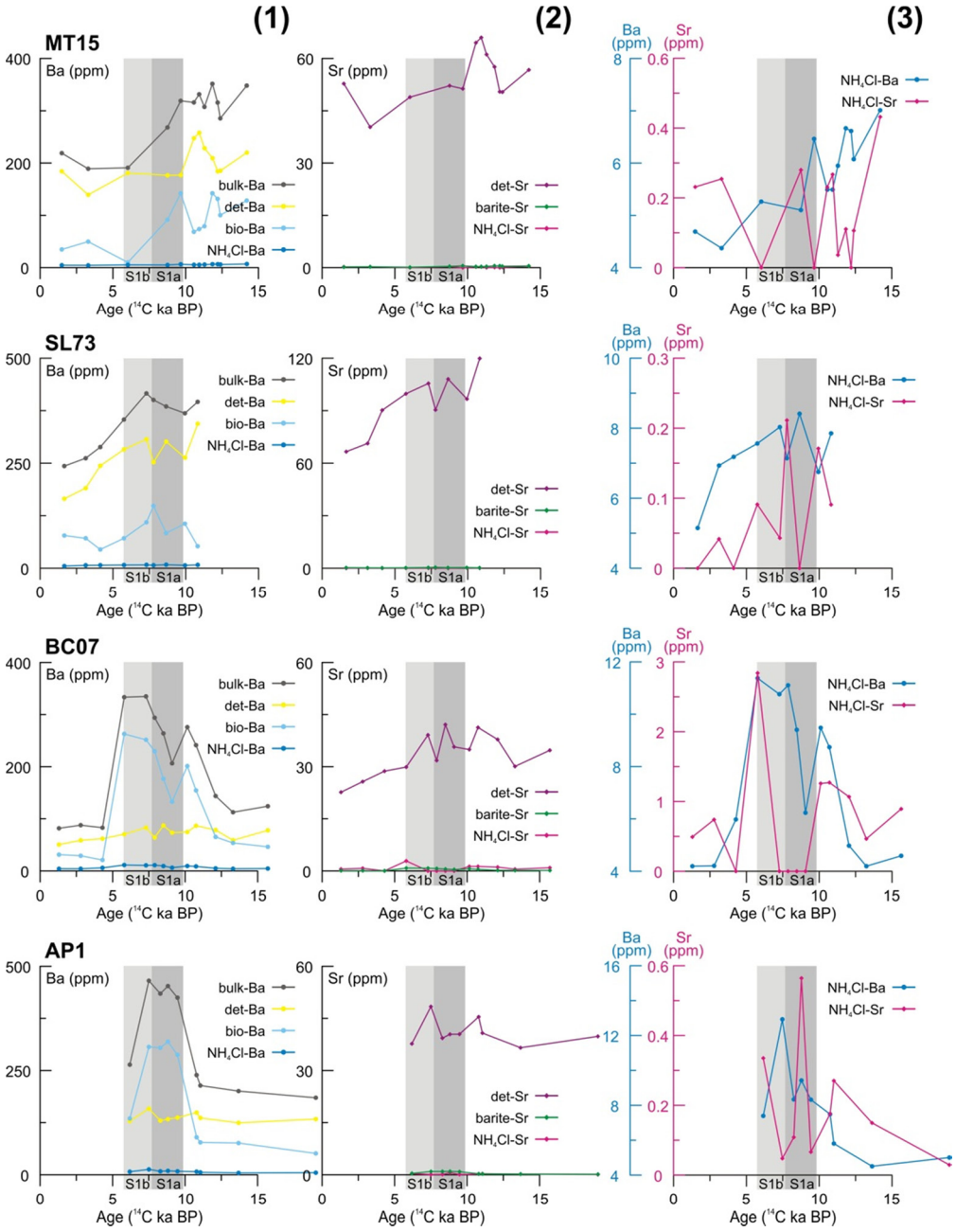
(1)
(2)
(3)
MT15
SL73
BC07
AP1
Ba (ppm)
Sr (ppm)
bulk-Ba
det-Ba
bio-Ba
NH4Cl-Ba
det-Sr
barite-Sr
NH4Cl-Sr
S1b S1a
Age (14C ka BP)

Figure 5a

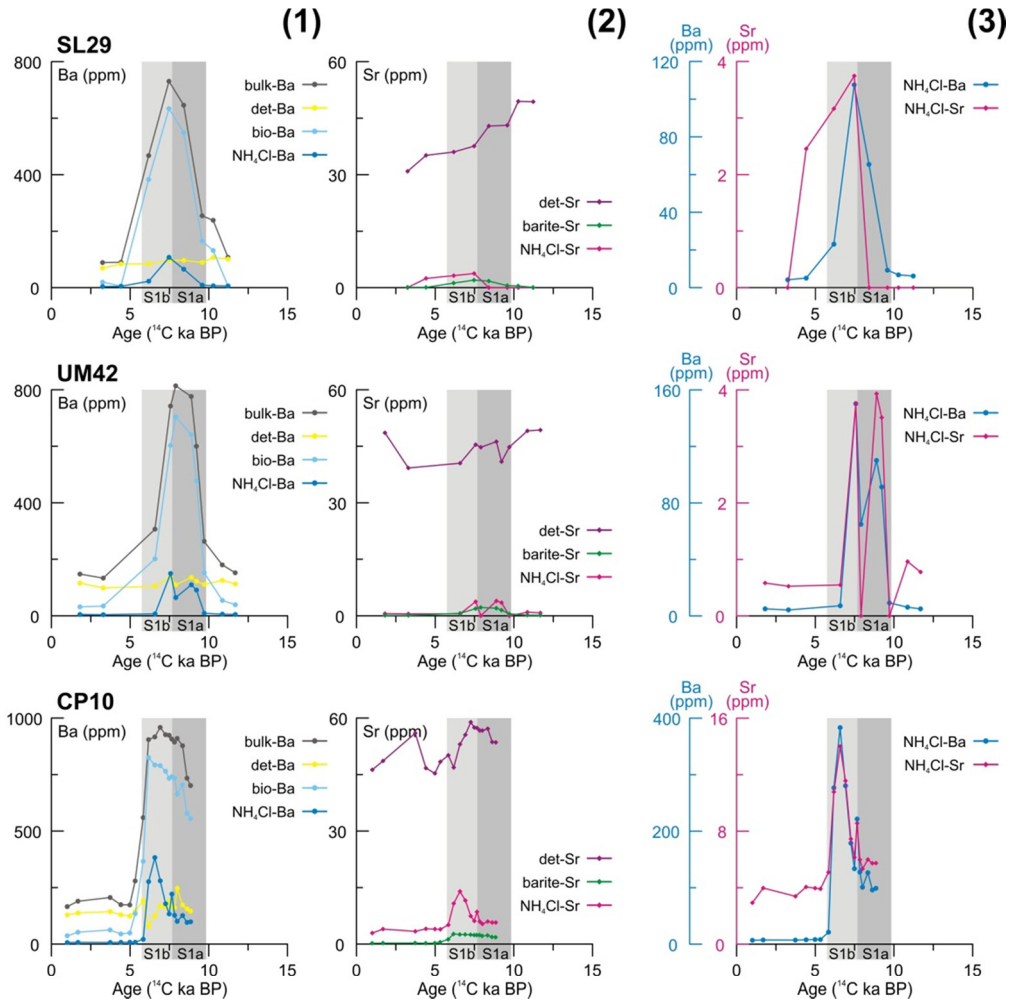

Figure 5b

Figure 5 Temporal profiles of Ba and Sr concentrations in different fractions. Column (1): Ba concentrations in the bulk sediment (bulk-Ba), detrital component (det-Ba), biogenic barite phase (bio-Ba), and NH_4Cl fluid (NH_4Cl-Ba). Column (2): Sr concentrations in the detrital component (det-Sr), barite phase (barite-Sr), and NH_4Cl fluid (NH_4Cl-Sr). Column (3): Ba and Sr concentrations of the NH_4Cl leaching fluid. Note that the horizontal axis is in uncorrected ^{14}C ages, and the scales of the vertical axis vary. The sapropel S1 period (~9.8–5.7 ^{14}C ka; De Lange et al., 2008) and its sub-segments S1a and S1b are indicated. The sequence and group of cores are according to barite content (see caption of Figure 3).

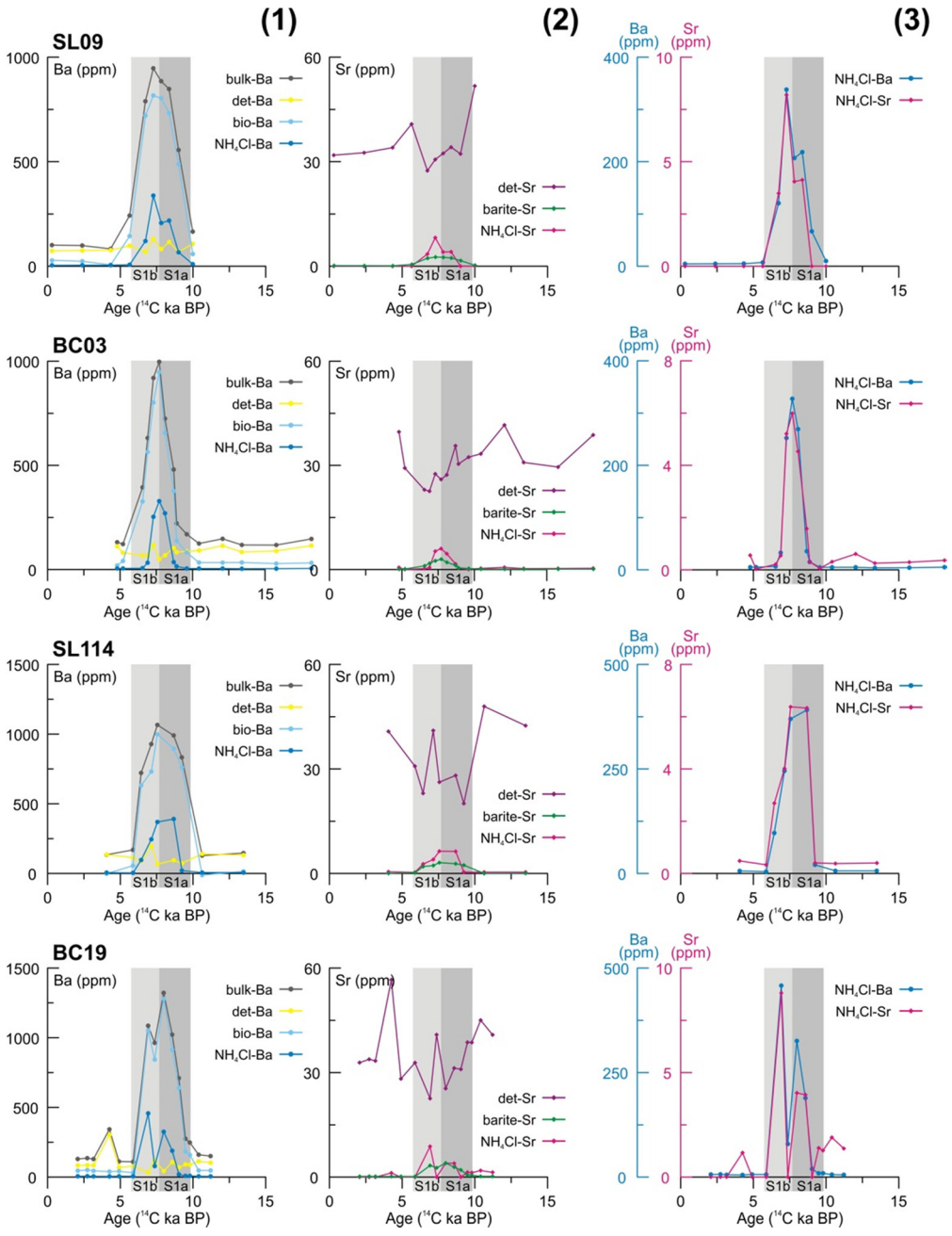
(1)
(2)
(3)
SL09
BC03
SL114
BC19
Ba (ppm)
Sr (ppm)
bulk-Ba
det-Ba
bio-Ba
NH4Cl-Ba
det-Sr
barite-Sr
NH4Cl-Sr
S1b
S1a
Age (14C ka BP)

Figure 5c

3.3 Remaining barite and associated Sr in decarbonated sediment

Our results reveal the existence of barite and associated Sr remaining in the decarbonated sediments. This can be clearly observed from the leaching fractions: HCl-residue, NH_4Cl-fluid, and the resultant NH_4Cl-residue (Table 2). In the HCl-residue, the high amount of Ba that is subsequently leached in the NH_4Cl-fluid, clearly points to a substantial, remaining barite fraction after HCl-decarbonation. In the NH_4Cl-residue, there is a good correlation for all the cores, between Ba and Sr concentrations. As this residue contains no barite, but mostly clay minerals and little Fe-Mn oxides, it consists merely of a single phase, the detrital component. Between the various cores, main differences can be observed for the HCl-residue and NH_4Cl-fluid, which seem to be mostly related to the initial barite contents. However, within cores grouped by barite content, there is a consistent pattern.

3.3.1 Low-barite content cores (MT15, SL73, BC07, and AP1)

Complete barite extraction is obtained using repeated NH_4Cl-leaching, but there is very limited – if any – Ba and Sr in the NH_4Cl-fluids of cores MT15, SL73, BC07, and AP1. The data show scattered, irrelevant distributions as some of them are below the detection limit because of the very low concentrations (Table 3; Figure 7). This indicates not only that no biogenic barite is extracted from the decarbonated sediments, but also that the HCl-leaching removed all barite.

The small amounts of barite and its associated Sr in the decarbonated sediments of cores MT15, SL73, BC07, and AP1, are consistent with the core characteristics. Regardless of the locations, these cores have relatively low barite contents (bio-Ba: 0–400 ppm), even for the elevated Ba zone during sapropel S1-equivalent period (Figure 3); whereas detrital material accounts for relatively large contributions (det-Ba: ~100–300 ppm; det-Sr: ~30–120 ppm) (Figures 3 and 5a).

Strong correlations between Ba and Sr concentrations for cores MT15, SL73, BC07, and AP1, are observed in the HCl- and NH_4Cl-residues (Figure 6). This points to a rather constant composition of the detrital phase. For these cores, the values of detrital Ba/Al and Sr/Al as determined from NH_4Cl-residues are rather high, in particular for cores MT15 (Ba/Al: 0.0043; Sr/Al: 0.0012) and SL73 (Ba/Al: 0.0056; Sr/Al: 0.0019) with a dominant detrital contribution (Table 4).

3.3.2 Intermediate-barite content cores (SL29, UM42, and CP10)

For the cores SL29, UM42, and CP10 in contrast to the good correlations in the NH_4Cl-residues, the poor linear relationships between Ba and Sr concentrations observed for the HCl-residues suggest that, apart from detrital phases, at least minor amounts of biogenic constituents remain in the decarbonated sediments (Figure 6).

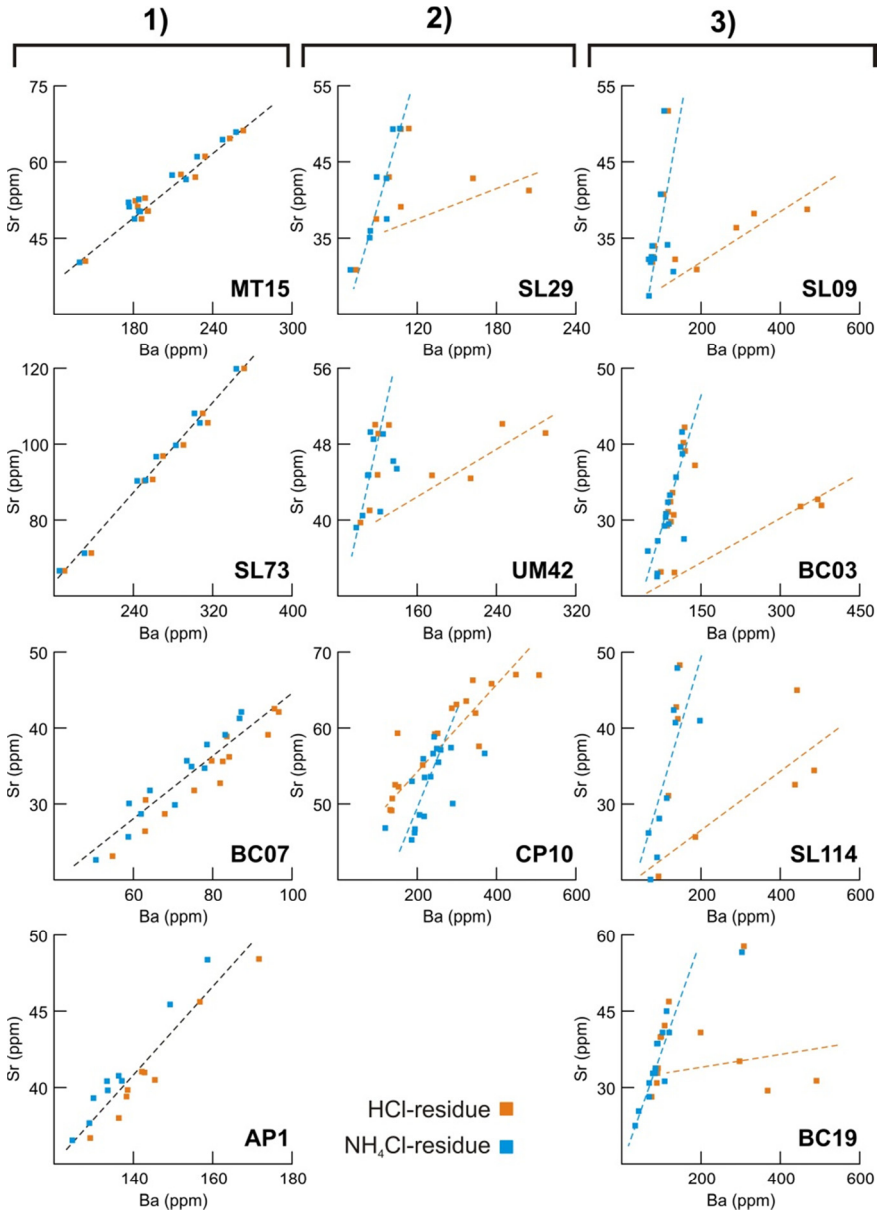

Figure 6 Plots of Ba vs. Sr concentrations in the HCl-leached residues (HCl-residue, i.e. carbonate-free sediment) and in the residues after HCl- and NH_4Cl-leaching (NH_4Cl-residue, i.e. carbonate- and barite-free sediment) (Tables 2 and 3). The data relationship for HCl-residue and NH_4Cl-residue fractions are illustrated by dashed lines. The cores are grouped according to barite content, shown in the panels 1–3) respectively (see caption of Figure 3).

On the other hand, the linear relationships are seen in the plots of Ba vs. Sr data

(Figure 7), indicating large amounts of barite and barite-Sr leached in the NH_4Cl-fluids. Accordingly, close correspondences between the NH_4Cl-Ba and NH_4Cl-Sr records (i.e. in the barite-extracted fluids) are displayed for cores SL29, UM42, and CP10 (Figure 5b). Note that some samples from the non-S1 sections have large uncertainties in the data, due to the very low Ba and Sr concentrations and associated large error (Table 3).

These together indicate that considerable amounts of barite and its associated Sr remain in the decarbonated sediments of cores SL29, UM42, and CP10. These cores are all characterized by barite contents ranging between ~200–800 ppm during sapropel S1 time (Figure 3), with intermediate contents of detrital Ba and Sr (det-Ba: ~100–250 ppm; det-Sr: 30–60 ppm) (Figure 3 and 5b). Moderate detrital Ba/Al (0.0024–0.0039) and Sr/Al (0.0011–0.0012) values are reported for these cores (Table 4).

3.3.3 High-barite content cores (SL09, BC03, SL114, and BC19)

For the cores with elevated zones of barite (bio-Ba >400 ppm) during sapropel S1 intervals (i.e. SL09, BC03, SL114, and BC19) (Figure 3), there is a rather bifurcated distribution of Ba vs. Sr data in the HCl-residues (Figure 6). This indicates the presence of two Ba, Sr-containing components in the decarbonated sediments. By contrast, the improved correlations occurring in the NH_4Cl-residues (Figure 6) suggests that all of the biogenic, barite-associated Ba and Sr have been removed from the decarbonated sediments using NH_4Cl leaching, leaving the detrital phase only. This can also be seen from the NH_4Cl-fluid data. The high Ba and Sr concentrations and the good linear relationships between them suggest that significant amounts of barite-associated Sr are leached in the NH_4Cl-fluids (Figure 7).

The core group of SL09, BC03, SL114, and BC19 is characterized by the most enhanced barite content, between 400 and 1200 ppm for the sapropel S1 (Figure 3), with relatively low detrital Ba, Sr contributed (det-Ba: ~100–200 ppm; det-Sr: ~30–50 ppm) (Figures 3 and 5c). For these cores, values of the detrital Ba/Al (0.0023–0.0037) and Sr/Al (0.0009–0.0013) are relatively low (Table 4).

To sum up, although our HCl-decarbonation has removed some barite from bulk sediments, as revealed by the differences between bio-Ba and NH_4Cl-Ba profiles (Figure 5), there is considerable barite-associated Sr remaining in the carbonate-free sediments of sapropel S1 samples. This is particularly the case for samples with high barite content. To be specific, for the cores that have <400 ppm barite contents (i.e. MT15, SL73, BC07, and AP1), negligible amounts of barite-Sr could be detected, even during the sapropel S1 interval with enhanced bulk Ba contents. For

the other cores characterized by higher barite contents (i.e. >400 ppm), by contrast, significant barite-Sr remains in the decarbonated, sapropel S1 sediments. Therefore, for an initial barite content exceeding 400 ppm, such remaining barite-associated Sr becomes prominent, and is likely to affect the detrital Sr composition if applying decarbonation alone.

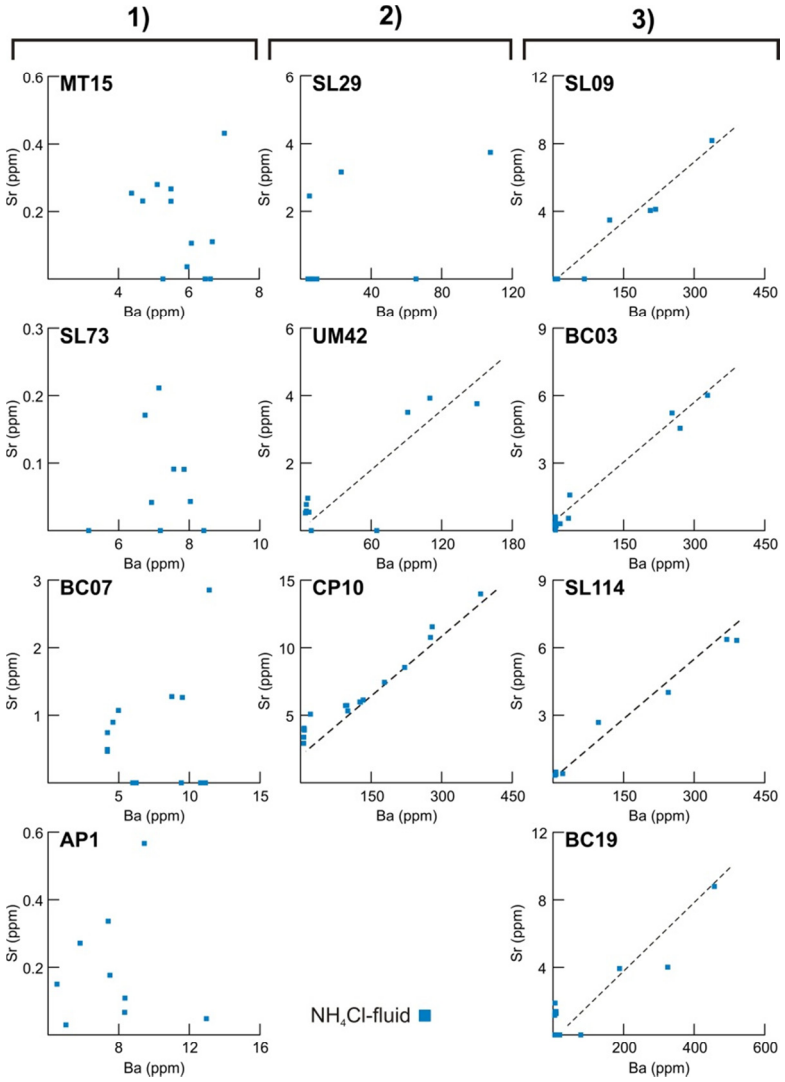

Figure 7 Plots of Ba vs. Sr concentrations in the NH_4Cl-leaching fluids, considered to extract barite (Tables 2 and 3). Despite that some data are close to detection limit and have a large uncertainty due to the very low concentrations, most results show a barite-related pattern. Dashed lines depict a linear data relationship for the cores with relatively high barite content. The cores are grouped according to barite content, shown in the panels 1–3), respectively (see caption of Figure 3).

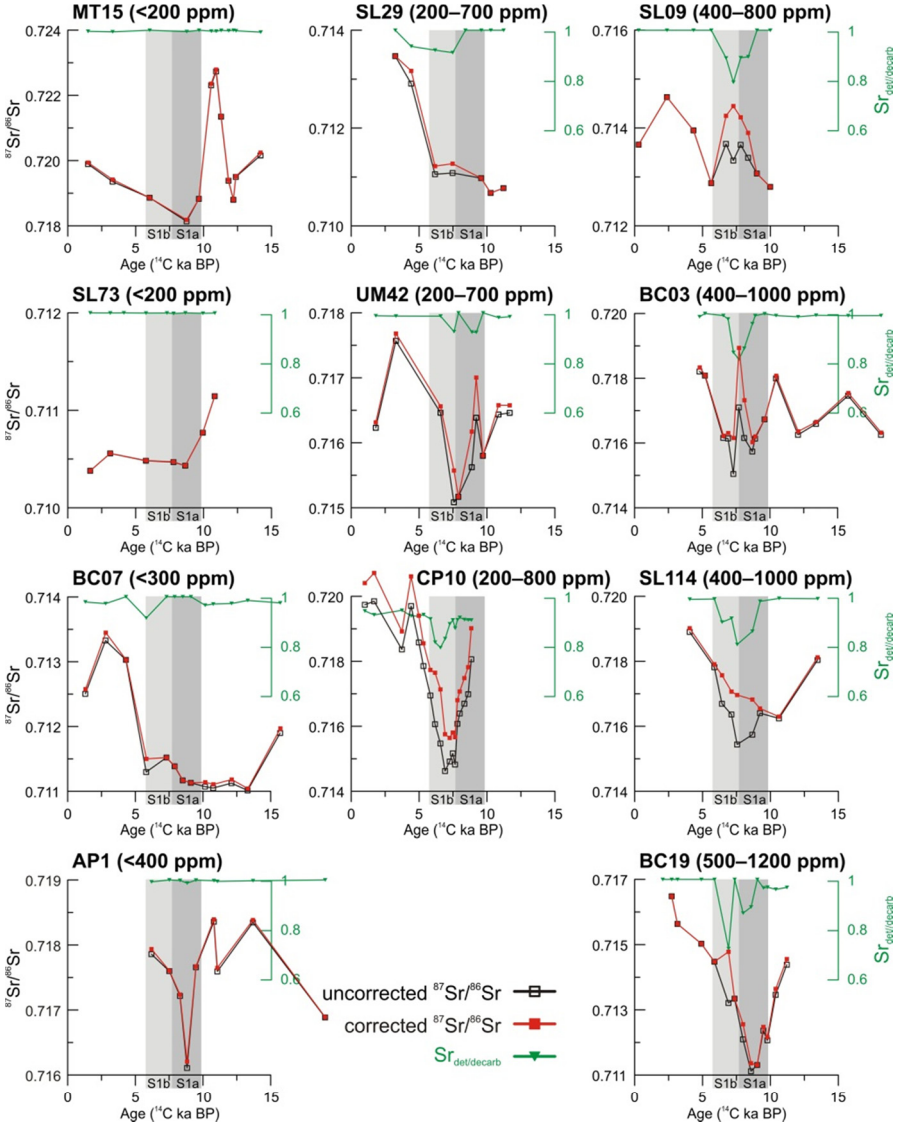

Figure 8 Comparison of detrital $^{87}Sr/^{86}Sr$ records between the original data (Freydier et al., 2001; Tachikawa et al., 2004; Wu et al., 2016; A. Michard, unpublished; J. Wu, unpublished) and our corrected results. Based on the separation and evaluation of the Sr with different origins (Table 3), the detrital Sr isotopic ratio is corrected by the equation: $^{87}Sr/^{86}Sr_{corrected} = (^{87}Sr/^{86}Sr_{original} - ^{87}Sr/^{86}Sr_{barite} \times (1 - Sr_{det/decarb})) / Sr_{det/decarb}$, where the $^{87}Sr/^{86}Sr$ value of 0.709165 of marine-barite reported for deep Mediterranean Sea is used (De Lange et al., 1990), and $Sr_{det/decarb}$ refers to the percentage of the corrected Sr to the uncorrected Sr (i.e. $Sr_{det/decarb}$ = det-Sr / decarb-Sr = NH_4Cl-residue (Sr) / HCl-residue (Sr)). For each core, the barite content during sapropel S1 period is indicated. The sequence and array of cores are according to barite content (see caption of Figure 3). Distinctive differences are observed for the samples characterized by high barite content in bulk sediments (>400 ppm) and 2) high $^{87}Sr/^{86}Sr$ ratio for detrital sediments (>0.713) (see Section 3.4).

3.4 Effect of remaining barite-Sr on detrital Sr composition and global implications

3.4.1 Correction of reported detrital Sr and $^{87}Sr/^{86}Sr$ data

After the separation and evaluation of the Ba and Sr with different origins, we are now able to correct for the barite-related Sr remaining in the decarbonated sediments. The correction is performed on the detrital $^{87}Sr/^{86}Sr$ data reported or produced previously (Table 3), and is based on the assumption that for each sample the decarbonated sediment composition i.e. the extraction efficiency for these reported studies, is the same as that evaluated in this study.

Accordingly, the Sr isotopic ratio of the detrital phase is corrected using Equation 4. Therein, $^{87}Sr/^{86}Sr_{barite}$ is the marine-barite $^{87}Sr/^{86}Sr$ value reported for the deep Mediterranean Sea (0.709165; De Lange et al., 1990), which is close to the reported $^{87}Sr/^{86}Sr$ value of modern oceanic marine-barite (0.709175; Paytan et al., 1993). The $Sr_{det/decarb}$ is the percentage of the corrected Sr (in detrital component, NH_4Cl-residue) to the uncorrected Sr (in the decarbonated sediments, HCl-residue), i.e. $Sr_{det/decarb}$ = det-Sr / decarb-Sr = NH_4Cl-residue (Sr) / HCl-residue (Sr) (Table 3).

$$^{87}Sr/^{86}Sr_{corrected} = (^{87}Sr/^{86}Sr_{original} - {}^{87}Sr/^{86}Sr_{barite} \times (1 - Sr_{det/decarb})) / Sr_{det/decarb}$$

Equation 4

The comparisons between the corrected and uncorrected data of the Mediterranean sediments are exhibited in the form of temporal $^{87}Sr/^{86}Sr$ records (Figure 8), the Sr-Nd isotopic plot (Figure 9), and the $^{87}Sr/^{86}Sr$–1000/Sr diagram (Figure 10). These comparisons allow us to exemplify the impacts of correction on previous provenance studies (Section 3.4.2) and to further discuss the factors influencing the barite-Sr effect (Section 3.4.3). After exemplifying the various factors involved in terms of the Mediterranean, globally important implications for marine-sediment provenance studies are given (Section 3.4.4).

3.4.2 Impacts of detrital Sr correction on provenance studies

In terms of the temporal variability, the correction does not change the overall pattern but rather the absolute values of $^{87}Sr/^{86}Sr$ (Figure 8). Between the uncorrected and the corrected $^{87}Sr/^{86}Sr$ records, considerable differences appear to occur only within the sapropel S1 intervals, indicating the dominant influences of barite-associated Sr (Figure 8).

However, the correction for detrital $^{87}Sr/^{86}Sr$ and in particular, Sr concentration could have substantially changed the data arrays and associated interpretations. Coupled Sr and Nd isotope variations have been shown to be a powerful tool for the study of provenance of detrital materials in marine sediment cores (e.g. Freydier et al., 2001;

Weldeab et al., 2002a; Jung et al., 2004; Revel et al., 2010; Cole et al., 2009; Meyer et al., 2011; Wu et al., 2016). As shown in Figure 9, even with the constraint of Nd isotopes that have been proven as a conservative provenance proxy, the correction for detrital $^{87}Sr/^{86}Sr$ data have changed the data distribution to a certain extent, for cores CP10, BC03, and SL114 in particular.

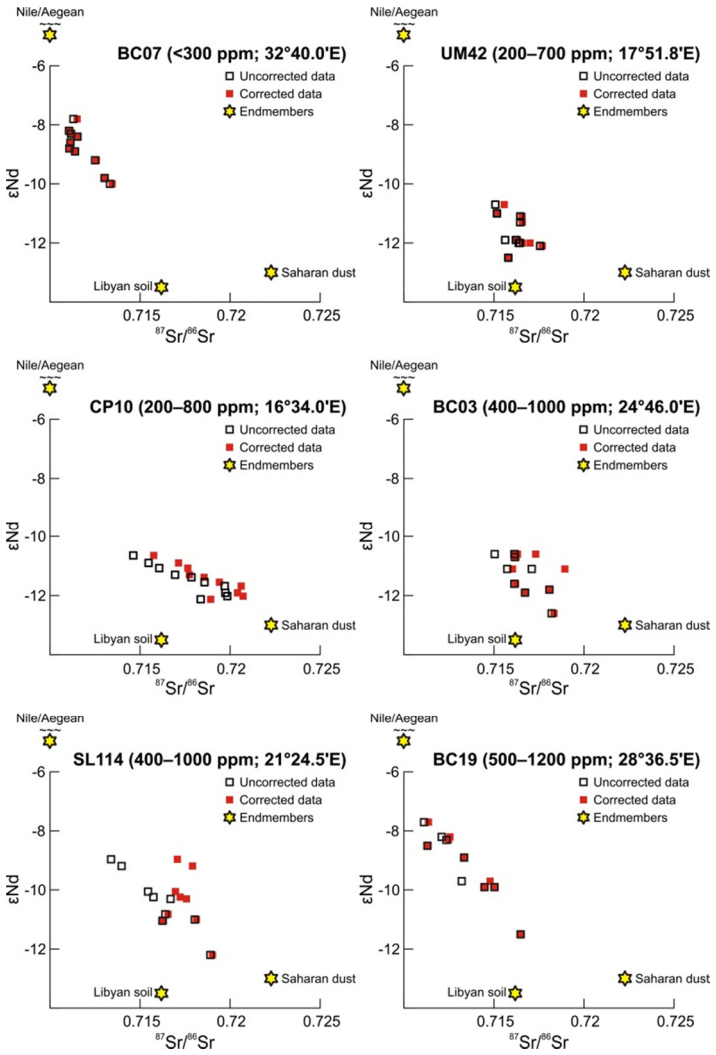

Figure 9 Comparison of detrital $^{87}Sr/^{86}Sr$ data between the reported data (Freydier et al., 2001; Wu et al., 2016) and our corrected results, in terms of the Sr vs. Nd isotopic composition. The mixing system for the whole EMS basin is used, with the endmembers shown after Wu et al. (2016). For each core the initial barite content during sapropel S1 period and its longitude are indicated. It appears that with higher barite contents and a more western location (i.e. generally higher $^{87}Sr/^{86}Sr$ of regional background in the EMS), a larger difference occurs (see Section 3.4).

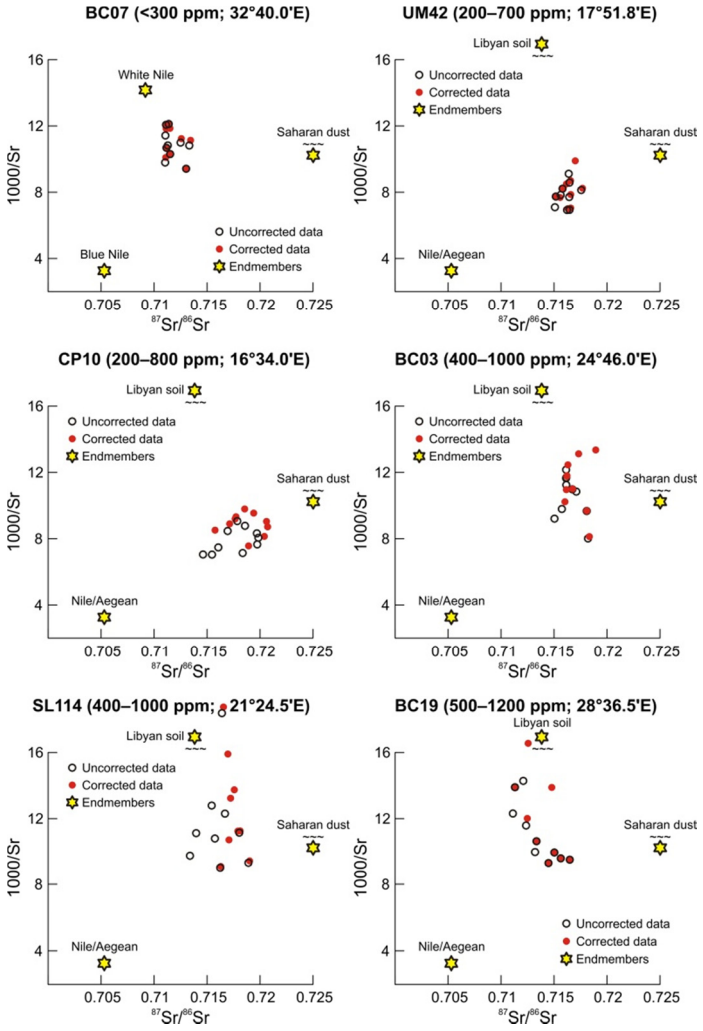

Figure 10 Comparison of detrital Sr isotopes and concentrations between the reported data (Freydier et al., 2001; Wu et al., 2016) and our corrected results. This is performed on the $^{87}Sr/^{86}Sr$–1000/Sr diagram, which has been widely used for provenance studies. The mixing system for the whole EMS basin is used, with the endmembers shown after Wu et al. (2016); except for core BC07 located in the Levantine Basin (i.e. area dominated by Nile-sediments) that is following Box et al. (2011). The correction has largely changed the absolute values and variation patterns, which could have caused different associated interpretations. For each core the initial barite content during sapropel S1 period and its longitude are indicated. It is clear that with higher barite contents and a more western location (i.e. generally higher $^{87}Sr/^{86}Sr$ of regional background in the EMS), a larger difference occurs (see Section 3.4).

This is particular true when considering the detrital Sr composition alone. The $^{87}Sr/^{86}Sr$–1000/Sr diagram has been widely used for provenance study (e.g.

Grousset et al., 1992; 1998; Krom et al., 1999a; 1999b; 2002; Box et al., 2011; Wu et al., 2016). This is because, in considering the Sr isotope data, inverting the concentration can constrain the mixtures between two endmembers to lie upon straight lines instead of hyperbola, making the identification of binary mixing straight forward (Faure, 1986). Clearly, the correction for Sr isotopes and concentration not only alters the absolute values, but also substantially affect the variation patterns, which could have resulted in different interpretations (Figure 10).

Using $^{87}Sr/^{86}Sr$ and Sr concentration, changes in the Levantine sediments have been described by a three endmember mixing model comprising Blue Nile, White Nile, and Sahara Dust (Box et al., 2011). In order to quantitatively assess the impact from the barite-Sr correction on provenance studies, we apply the same equations to cores BC07 and SL29, using the corrected and uncorrected data of $^{87}Sr/^{86}Sr$ and Sr concentration. Although cores BC07 and SL29 show relatively small differences in Sr isotopes and concentration data with and without the barite-Sr correction, these two cores are situated in the Levantine Basin which is thought to be dominated by Nile sediments (Figure 1), thereby having a similar sedimentation setting as the cores investigated in Box et al. (2011). Our recalculations show, taking a sapropel S1 sample from core SL29 as an example, the relative concentrations of White Nile, Blue Nile, and Saharan Dust: 64:20:16% vs. 74:5:22%, before and after correction, respectively. Therefore, considering the model uncertainties, a barite-Sr correction could cause a more than 30% difference in the White Nile contribution and about 5–20% associated shift in the contributions from the Blue Nile and Saharan Dust endmembers (Figure 10).

3.4.3 Controlling factors for the potential barite-Sr effect

Furthermore, in contrast to the correction for detrital Sr concentration, the corrected $^{87}Sr/^{86}Sr$ values are higher than the uncorrected ones (Figures 8–10). This is because the Sr isotopic signature of marine barite (Mediterranean: 0.709165, De Lange et al., 1990; oceanic: 0.709175, Paytan et al., 1993) is relatively low compared to that of most detrital sources over the Mediterranean Sea ($^{87}Sr/^{86}Sr$: ~0.707–0.725) (Figure 9 and 10). Specifically, a strong east–west geochemical gradient has been reported for the EMS sediments due to a mixing between: the “young and mafic” Nile sediment ($^{87}Sr/^{86}Sr$: ~0.707–0.712; Sr: ~120–200 ppm) is diluted towards the west by the “old and felsic” Saharan dust ($^{87}Sr/^{86}Sr$: ~0.717–0.725; Sr: ~90–120 ppm) (Krom et al., 1999a; 1999b; Freydier et al., 2001; Weldeab et al., 2002a; Box et al., 2011; Scheuvens et al., 2013; Wu et al., 2016). Note that these values of published Sr isotopes and concentration refer to those detected in decarbonated sediments.

In fact, the detrital Ba/Al and Sr/Al signatures derived from our extractions also

exhibit a clear east–west pattern throughout the Mediterranean Sea, showing that generally higher values for the more western part (Figure 11a). This gradient is particular pronounced when excluding core SL73 which is located in the northern Aegean Sea and thus receives substantial amounts of detrital material from different sources (Figures 1 and 11). Moreover, there appear to be increases in the detrital Ba/Al and Sr/Al ratios from south to north across the Mediterranean Sea (Figure 11b). This may reflect the differences in the catchment areas characterized by different climate regimes and rock composition, between the northern borderlands of the Mediterranean and North Africa (Weldeab et al., 2002a; Tzedakis, 2007; Magny et al., 2013; Rohling et al., 2015; Wu et al., 2016).

Taken together, the differences between the uncorrected and corrected Sr isotope and concentration data depend on 1) the amount of barite-associated Sr remaining in decarbonated sediment, and 2) the $^{87}Sr/^{86}Sr$ and Sr concentration (i.e. Sr/Al) of detrital sediment itself. The former is primarily related to the initial barite content in bulk sediments (see Section 3.3), and the latter is influenced by regional terrigenous detrital inputs. In other words, distinct differences between full and partly removed barite content are expected to occur in the samples characterized by 1) high initial barite content in bulk sediments and 2) high $^{87}Sr/^{86}Sr$ ratio for detrital sediments. In addition, the effect is more enhanced if detrital sediments have low Sr/Al ratio.

We exemplify these factors using Mediterranean sediments. The largest differences are observed for cores SL114 and CP10, which have both high barite contents (S1: 400–1200 ppm) and high $^{87}Sr/^{86}Sr$ values (background: >0.716) (Figures 8–10). Core UM42 has a relatively low barite and detrital Sr/Al (0.0013), thus the difference is relatively small (Figures 8–11). Cores SL29, SL09, BC03, and BC19 show considerable differences due to the abundant barite. Nevertheless, detrital sediments in these cores are dominated by enhanced Nile/Aegean contributions during S1 period (i.e. low $^{87}Sr/^{86}Sr$ and high Sr), which makes the differences between the corrected and uncorrected records not very prominent (Figures 8–10). Cores BC07, AP1, SL73, and MT15 have limited impacts from the remaining barite-Sr, because of the low barite content (<400 ppm) (Figures 8–10).

3.4.4 Important implications for marine-sediment provenance studies

Our findings have important implications for provenance studies using Sr concentration and $^{87}Sr/^{86}Sr$ as diagnostic tools. For sediments containing a significant barite fraction, decarbonation alone jeopardizes the use of Sr isotopes and concentration as provenance proxies.

In the Mediterranean Sea, the barite content is up to ~1200 ppm even during the most-recent sapropel S1. However, the barite content could be much higher in

oceanic high-productivity areas. For example, a benthic Ba flux of ~4–7.5 mg/cm^2/ka has been suggested for the present-day Equatorial Pacific (Paytan and Kastner, 1996), compared to the biogenic Ba flux of ~0.5–2 mg/cm^2/ka for the EMS during sapropel S1 period (De Lange et al, 2008). Moreover, during glacial periods, the benthic Ba flux was two times of its current value in the Equatorial divergence high-productivity zones (Paytan et al., 1996). High barite content is also seen in continental settings in the tropical Pacific Ocean and the commonly used decarbonation cannot adequately remove all barite and associated Sr (Lyle et al., 1984).

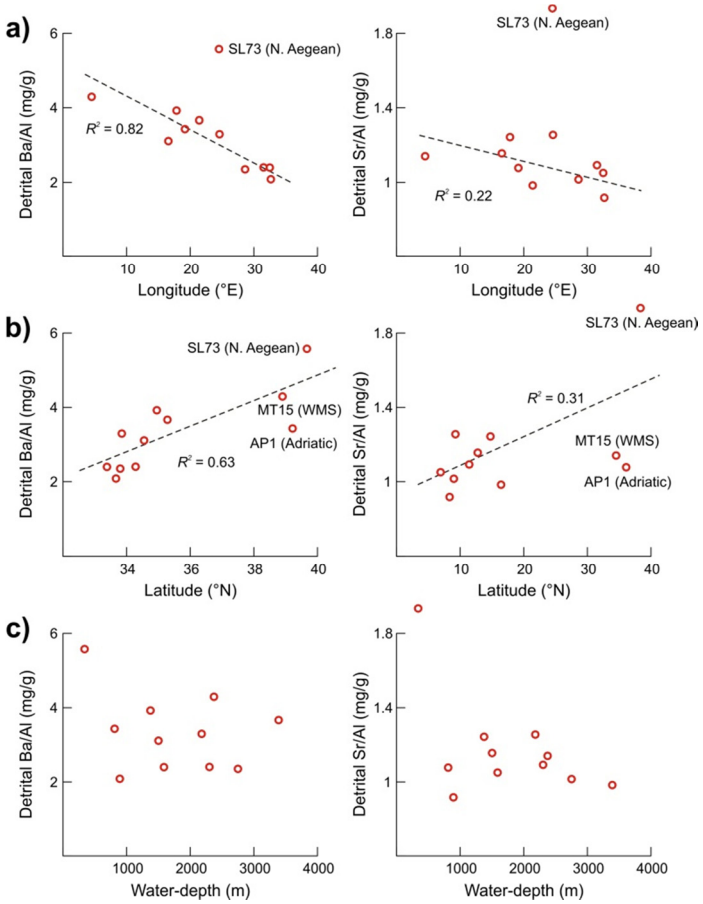

Figure 11 Detrital Ba/Al and Sr/Al values derived from our extractions (Table 4) versus 1) longitude, 2) latitude, and 3) water-depth. Average value for each core is used. There are gradients in both detrital signatures from east to west and from south to north, resulting in a SE–NW increase in Ba/Al and Sr/Al values. There is no/poor relation between the detrital ratios and water-depth. Note that cores SL73, AP1, and MT15 are located in/close to the northern Aegean, the Adriatic, and the WMS, respectively, and thus receive detrital materials from distinctly different sources.

Consequently, for provenance studies using Sr isotopes and concentration as diagnostic parameters, the barite-associated Sr must be considered. Not fully removing of the barite-Sr during commonly applied decarbonation alone, may largely affect the assumed detrital Sr composition in the remaining sediment fraction. Therefore, a careful evaluation and potential correction are indispensable. Based on our results using Mediterranean sediments, we strongly recommend a correction for barite-associated Sr for marine sediments with >400 ppm barite content. This is particularly needed if there is also a detrital $^{87}Sr/^{86}Sr$ signature >0.713 for the regional detrital input. Obviously, this correction is even more required if detrital sediments have a low Sr/Al ratio (e.g. <0.0010).

The simplest, only direct way is applying an additional leaching with NH_4Cl (1 M, pH = 7) to fully remove barite and associated Sr after decarbonation. Alternatively, such additional leaching could be done on a few representative samples, so as to assess the amounts of barite-Sr remaining in decarbonated sediments. The derived signatures of Ba/Al and Sr/Al ratios in “pure” detrital phase, and/or the barite Sr/Ba ratio, can then be applied to the full sample set.

It must be noted that this is an estimate of necessary conditions for a barite-associated Sr correction based on Mediterranean sediments and using a rigorous decarbonation method. Commonly, less aggressive methods are used, e.g. acetate pH = 5, or less acidic, lower sample/acid ratio, shorter reaction times. All of these result in a much lower barite removal during this process and a consequently higher remaining barite fraction in the leached sediment used for detrital provenance studies.

4 Conclusions

Mediterranean sediments are used to demonstrate that potential barite-associated Sr remaining in decarbonated sediment must be taken into account for provenance studies using Sr-concentration and -isotopes. Our results show that considerable barite-associated Sr remains in the decarbonated sediments. The amount of such remaining barite-Sr appears to increase with increasing initial barite content in the sediments. A direct correction of the potentially remaining barite-Sr is suggested. Using Mediterranean samples as illustration, we estimate that such a correction is required for marine sediments with >400 ppm barite content. The correction is strongly needed if there is also a $^{87}Sr/^{86}Sr$ signature >0.713 and low Sr/Al ratio (e.g. <0.0010) for the detrital sediments. We stress that decarbonation alone may jeopardize detrital provenance studies using Sr concentration and $^{87}Sr/^{86}Sr$ as proxies. Applying additional leaching with 1 M NH_4Cl removes all remaining barite in decarbonated sediments and makes samples suitable for provenance studies using the detrital Sr elemental and isotopic composition.

Acknowledgements

Many thanks are given to the captain & crew, scientists, and technicians on board the following cruises for the core collections: MD81-PALEOFLUX 1994 with RV *Marion Dufresne*, MT93 1993 with RV *Tyro*, SIN-SAP 1998 with RV *Urania*, SMILABLE 1999 with RV *Logachev*, as well as PASAP 2000, BIOPASS 2001, PALEOPASS & MIMES 2004, and CORTADO 2011 with RV *Pelagia*. We are grateful to David Gallego-Torres, Sanela Gusic, Rinske Knoop, Enno Schefuss, and Patrick van Santvoort for sediment processing and data analyses. We thank Coen Mulder and Helen de Waard for ICP-OES measurements. We acknowledge financial supports from EU-projects MARFLUX, PALEOFLUX & SAP, and from CNR and NOW for shiptime and logistic supports. This study is sponsored by the China Scholarship Council – Utrecht University PhD Program (CSC No. 201206260116).

CHAPTER 6

Mediterranean seawater circulation for the Holocene sapropel S1 period – reconstructed using Nd isotopes in fish debris and foraminifera

Jiawang Wu [a*], Katharina Pahnke [b], Philipp Böning [b], Annie Michard [c], and Gert J. de Lange [a]

[a] Department of Earth Sciences – Geochemistry, Faculty of Geosciences, Utrecht University, Princetonplein 9, 3584 CC Utrecht, The Netherlands
[b] Max Planck Research Group for Marine Isotope Geochemistry, Institute for Chemistry and Biology of the Marine Environment (ICBM), University of Oldenburg, Carl-von-Ossietzky-Strasse 9-11, 26129 Oldenburg, Germany
[c] CEREGE, Aix-Marseille Université, CNRS, IRD, Collège de France, CEREGE UM34, 13545 Aix en Provence, France

[*] Corresponding author: j.w.wu@uu.nl (J. Wu).

(to submit)

Abstract

Organic-rich layers called sapropels formed repeatedly in the eastern Mediterranean Sea (EMS). Sapropel formation has been attributed to deep-water stagnation and enhanced biological production, but the complex interactions between climatic and paleoceanographic processes are still debated. For the first time, we present a basin-wide reconstruction of seawater Nd isotopic ratios (εNd) at the time of Holocene sapropel S1 deposition (~10.8–6.1 ka cal. BP). The εNd signal from fish debris and foraminiferal tests is considered to be a reliable archive for the composition of the deep-water during their deposition. Using these data from nine cores in a geographical and bathymetric coverage of the EMS permits us to constrain circulation and sources of water masses. In addition, HCl-leached εNd data of Holocene Mediterranean sediments in two cores are used.

The obtained εNd values of -4.9 ± 0.4 for the EMS seawater below ~800 m water-depth during the S1 period, are not only more homogenous but also much more radiogenic than those at present. The homogenous εNd distribution in the deep water points to a much enhanced residence time for Nd, and in view of its rather conservative behavior, also to an enhanced residence time for the deep-water masses. This is consistent with the generally accepted deep-water stagnation during sapropel S1 formation. From a more detailed εNd profile in one core, as well as the consistent changes in sediment-leachate data in another core, it is clear that such stagnation persisted over the whole S1 period, but with decreasing importance at the end of this period. The leachate εNd-data also suggest that the EMS deep-water stagnation might have been preconditioned two thousand years earlier than S1 formation started, whereas it terminated synchronously with the S1 ending.

The more radiogenic εNd value during S1 in the EMS is attributed to a reduced inflow of the Modified Atlantic Water (MAW) combined with an enhanced riverine contribution. The latter may mainly come from the Nile River as it is the only known important radiogenic Nd source. The latter relates to enhanced riverine dissolved and to release from particulate loads and is consistent with a slight – if any – east–west gradient. Using a simple mass/isotope balance for Nd, we assess the most realistic scenario: a 2-fold (1.5–3x) flux of pre-Aswan Nile discharge and a MAW inflow across the Strait of Sicily that is half (45–65%) of its recent value. In addition, enhanced contributions from other riverine systems (e.g. northern EMS borderlands), and from other mechanisms due to suboxic conditions (e.g. boundary exchange) is possible.

During the S1 period, a much stronger longitudinal gradient in seawater-εNd exists for the western Mediterranean Sea (WMS), than for the EMS. This difference between the western and the eastern basins is in contrast to the continuous west–

east gradient throughout the Mediterranean today. Combining this evidence with the less radiogenic and more heterogeneous εNd signatures for the WMS indicates not only an enhanced Nile runoff, but also a reduced hydrological exchange between EMS and WMS during S1 formation. Consequently, a reduced and shallower outflow of intermediate water across the Strait of Sicily occurred during the S1 period, while the WMS water circulation must have persistently functioned. This EMS–WMS difference supports the vision that deep-water stagnation is a prerequisite for sapropel formation.

Keywords

Nd isotopes; sapropel S1; eastern Mediterranean Sea; Mediterranean thermohaline circulation; fish debris

1 Introduction

The Mediterranean Sea is a semi-enclosed basin, with an anti-estuarine thermohaline circulation. The circulation is driven by excess evaporation over freshwater inputs, which transforms the surface inflow of relatively low-density Atlantic waters into saltier intermediate waters. The dense intermediate waters also reach several sites at the northern borderlands of the Mediterranean; where they precondition the water column for the formation of deep-water masses in both the eastern and the western basins (Roether et al., 1996; Pinardi and Masetti, 2000; Pinardi et al., 2015). This pattern may have varied in the past, as documented by the periodical occurrence of organic-rich sedimentary units called sapropels (see reviews by Cramp and O'Sullivan, 1999; Rohling et al., 2015). Sapropel deposition has been attributed to deep-water stagnation, enhanced biological production, or both, as a result of enhanced river runoff and associated nutrient input during precession-forced insolation maxima (e.g. Rossignol-Strick et al., 1982; Rohling, 1994; Emeis et al., 2000; De Lange et al., 2008; Schmiedl et al., 2010; Tachikawa et al., 2015). However, many aspects for the complex interactions between climatic and paleoceanographic processes are still unclear.

The knowledge of sapropel formation mechanisms is mostly based on the latest, Holocene sapropel S1 deposited in the eastern Mediterranean Sea (EMS) between ~10.8 and 6.1 ka cal. BP (hereafter referred to as “ka”) (c.f. De Lange et al., 2008). This is the only sapropel within the range of precise radiocarbon dating. It is hypothesized that a reduction of intermediate and deep-water formation as a consequence of surface hydrological changes acted as a precondition for S1 formation (Rohling, 1994; De Lange et al., 2008; Rohling et al., 2015; Tachikawa et al., 2015). Faunal- and stable- isotope records of benthic foraminifera suggest a collapse of the intermediate waters synchronous with the sapropel S1 deposition, in contrast to the well-ventilated conditions before the S1 (e.g. Jorissen et al., 1999; Kuhnt et al., 2008; Schmiedl et al., 2010). Yet, the use of this approach for deep-sea sapropels is hampered by the paucity of epibenthic species under low-oxygen conditions. Numerical physical oceanographical models show that with increasing strength of the freshwater forcing, the strength of the deep-water stagnation increases (Myers et al., 1998; Myers, 2002). Several studies have also used planktonic foraminiferal oxygen isotopes to spatially estimate the surface hydrological changes during sapropel S1, but yielding different hypotheses (Thunell and Williams, 1989; Kallel et al., 1997; Rohling and De Rijk, 1999). This is mainly because of the uncertainties in the use of salinity:$\delta^{18}O$ relationships (Rohling, 1999). Bulk sediment geochemistry, in particular redox-sensitive elements, can be used to indicate the re-ventilation of the water column, but only if post-depositional processes are carefully considered (Van Santvoort et al. 1996; Thomson et al., 1999; Reitz et al., 2006). Ocean-biogeochemical modeling studies, addressing the

interplay between physical circulation and deep-water oxygen consumption, have concluded that stagnating deep-water circulation, combined with a large external nutrient input, is a prerequisite for S1 formation (Stratford et al., 2000; Bianchi et al., 2006; Grimm et al., 2015). This is consistent with a compilation study, revealing the presence of an anoxic boundary at a depth of ~1800 m (De Lange et al., 2008). However, proxy reconstructions that can be compared with simulations are still scarce for the Holocene sapropel S1. In particular, a direct, systematic reconstruction of the Mediterranean thermohaline circulation for that period is hitherto lacking.

1.1 Seawater εNd as a quasi-conservative water-mass tracer

The neodymium (Nd) isotopes have proven to be an adequate tracer for modern ocean circulation and have great potential to trace past circulation of water masses (see reviews by Frank, 2002; Goldstein and Hemming, 2003). Its composition is conventionally expressed as: $\varepsilon Nd = [(^{143}Nd/^{144}Nd)_{sample} / (^{143}Nd/^{144}Nd)_{CHUR} - 1] \times 10^4$ where CHUR (chondritic uniform reservoir) is 0.512638 (Jacobsen and Wasserburg, 1980).

The application of Nd isotopes seems particularly appropriate to study paleoceanographic deep-water processes, provided that a suitable archive can be identified (see review by Tachikawa et al., 2014). Sedimentary dispersive Fe-Mn oxyhydroxides extracted with various leaching techniques have been widely used to investigate bottom-water circulation (e.g. Bayon et al.; 2004; Piotrowski et al., 2005; Pahnke et al., 2008; Chen et al., 2012). Yet, this archive may be complicated by the possible contamination from a labile terrigenous fraction (e.g. volcanogenic matter and preformed continental Fe-Mn coatings). To minimize the risk, sedimentary oxyhydroxides attached on foraminiferal tests have been used to reconstruct bottom-water εNd (e.g. Roberts et al., 2010; Elmore et al., 2011; Piotrowski et al., 2012; Wu et al., 2015).

Several studies were done using planktonic foraminifera to extract surface-seawater εNd signals for sapropels S1 and S5 in the EMS, using various oxidative-reductive cleaning methods (Scrivner et al., 2004; Vance et al., 2004; Osborne et al., 2008; 2010). However, it has been suggested that the εNd composition of fossil planktonic foraminifera is not related to the ambient seawater at calcification depth but primarily reflects the bottom and/or pore water (Tachikawa et al., 2013; 2014).

The use of deep-sea corals as a seawater properties recorder is relatively recent (Colin et al., 2010; van de Flierdt et al., 2010; Dubois-Dauphin et al., 2017), but certain time intervals are bare for this archive because of environmental conditions that are hostile for this organism (Frank et al., 2011). In carbonate-rich sediments,

the bulk carbonate fraction has also been used (Freydier et al., 2001; Gourlan et al., 2008; 2010). However, it has been shown that leaching performance may vary with the mineralogy and accumulation conditions of marine sediments (Tachikawa et al., 2004). This performance may be different for the episodes of sapropel formation, which is characterized by anoxic depositional environments (Van Santvoort et al. 1996; Thomson et al., 1999; Reitz et al., 2006).

By contrast, fossil fish debris has been recognized as the most reliable recorder of the seawater εNd signature, although the occurrence of this archive is not constant and barren samples are not uncommon (Martin and Haley, 2000; Martin and Scher, 2004; Martin et al., 2010; Horikawa et al., 2011). Due to the anoxic bottom-water conditions in the EMS during sapropel formation, biogenic apatite that may make up the bulk phosphorus inventory including fish debris is better preserved (e.g. Schenau and De Lange, 2000; Slomp et al., 2002; Schenau et al., 2005; Kraal et al., 2010). This allows a sufficient amount of fish fragments and teeth to be preserved in sapropel S1 sections of some EMS cores.

1.2 Seawater εNd in the present-day Mediterranean Sea

For the recent Mediterranean, seawater εNd has been systematically investigated (Frost et al., 1986; Spivack and Wasserburg, 1988; Henry et al., 1994; Tachikawa et al., 2004; Vance et al., 2004). The dissolved εNd appears to behave conservatively in line with salinity (Tachikawa et al., 2004).

The Mediterranean Sea communicates with the Atlantic Ocean through the Strait of Gibraltar, and is separated between the eastern basin (EMS) and western basin (WMS) by the Strait of Sicily (Figure 1). At the surface (<200 m depth), the Atlantic inflow characterized by εNd values of -10.8 to -9.4, enters the Mediterranean Sea. Below it, at ~200 to 800 m, the Mediterranean outflow has εNd values of -9.2 to -8.9 (Spivack and Wasserburg, 1988; Henry et al., 1994; Tachikawa et al., 2004). During its eastward flow, the Atlantic waters mix with Mediterranean intermediate Water forming the Modified Atlantic Water (MAW) that spreads within the basins (Pinardi and Masetti, 2000; Rolison et al., 2015). This eastward-flowing surface water in the EMS becomes denser due to its mixing and evaporation, and eventually sinks, leading to the formation of the Levantine Intermediate Water (LIW) (Pinardi and Masetti, 2000; Pinardi et al., 2015). The LIW spreads throughout the entire Mediterranean Sea at depths between ~200 and 800 m and is characterized by εNd values ranging from -7.9 to -4.8 in the EMS and from -10.4 to -7.6 in the WMS (Henry et al., 1994; Tachikawa et al., 2004; Vance et al., 2004). The LIW is thought to acquire its εNd signature mainly from the partial dissolution of Nile River particles, which have an average isotopic composition of -3.3 (Frost et al., 1986; Freydier et al., 2001; Weldeab et al., 2002; Revel et al., 2010). The LIW finally enters the

Atlantic Ocean at intermediate depths with an average εNd value of -9.2 (Henry et al., 1994; Tachikawa et al., 2004).

Overall, the present-day LIW/deep-water dissolved εNd values become less radiogenic from east to west: its average εNd value is -7.0 in the EMS and -9.5 in the WMS (Tachikawa et al., 2004). This east–west gradient has been attributed to a mixing between two distinct sources: “less radiogenic” Atlantic inflowing surface water is diluted towards the east by “more radiogenic” Nile contributions by mixing with the underlying LIW (e.g. Frost et al., 1986; Spivack and Wasserburg, 1988; Greaves et al., 1991; Henry et al., 1994; Tachikawa et al., 2004; Ayache et al., 2016). In addition, there is a rather uniform impact of Saharan dust (εNd: about -10; Frost et al., 1986) over the Mediterranean Sea.

Although the general pattern of the recent Nd distribution in the Mediterranean is clear, there seems to be an imbalance in the concentration and isotopic distributions of Nd on a Mediterranean basin-wide scale. The Nd influx brought by the Atlantic inflow is smaller than the Nd flux exiting with the Mediterranean outflow (Greaves et al., 1991; Henry et al., 1994; Tachikawa et al., 2004). Moreover, the εNd value of the Mediterranean outflow is higher than that of the Atlantic inflow (Spivack and Wasserburg, 1988; Henry et al., 1994)). The additional Nd source might be partially dissolved river particles, aeolian particles (Frost et al., 1986; Spivack and Wasserburg, 1988), or could be from marine or Black Sea origin (Greaves et al. 1991; Schijf et al. 1991). Using a two-box model, Henry et al. (1994) calculated the Nd inventory in the WMS, and suggested that the EMS is a source of radiogenic Nd for the WMS. More recently, Tachikawa et al. (2004) proposed that the missing source could originate from the partial dissolution of Nile River particles being the only known significant source of radiogenic Nd. High-resolution modeling also highlighted the exchange between the sediments deposited on the oceanic margins and the waters flowing along these margins, called the “boundary exchange”, but it simulated a somewhat too radiogenic value for the Mediterranean waters (Ayache et al., 2016). In other words, the Nd cycle of the Mediterranean Sea is still insufficiently constrained.

To date, only a few Nd-related paleoceanography studies exist for the Mediterranean Sea (Jiménez-Espejo et al., 2015; Dubois-Dauphin et al., 2017), and all of them are focused on the western Mediterranean Sea (WMS). For a better understanding of the Mediterranean thermohaline circulation during sapropel formation, we present, for the first time, a basin-wide reconstruction of seawater εNd signatures for the Holocene sapropel S1 period (Table 1; Figure 1). The reconstruction of a more extreme case of Mediterranean circulation may also shed light on the knowledge gap for the present-day Nd balance. The selected cores

represent a geographical and bathymetric coverage of the EMS. Our results will be discussed and compared with existing εNd data of seawater and sediment, for both the present-day and sapropel S1 period, on a Mediterranean basin-wide scale.

2 Material and methods

A total of 15 samples obtained from sapropel S1 layers in 9 cores were selected to give a basin-wide geographical and bathymetric coverage of the EMS (Tables 1 and 2; Figure 1). The chronologies for these cores were mainly based on radiocarbon dating on planktonic foraminifera, and the well-established boundaries of sapropel S1 (~10.8–6.1 ± 0.5 ka) (De Lange et al., 2008).

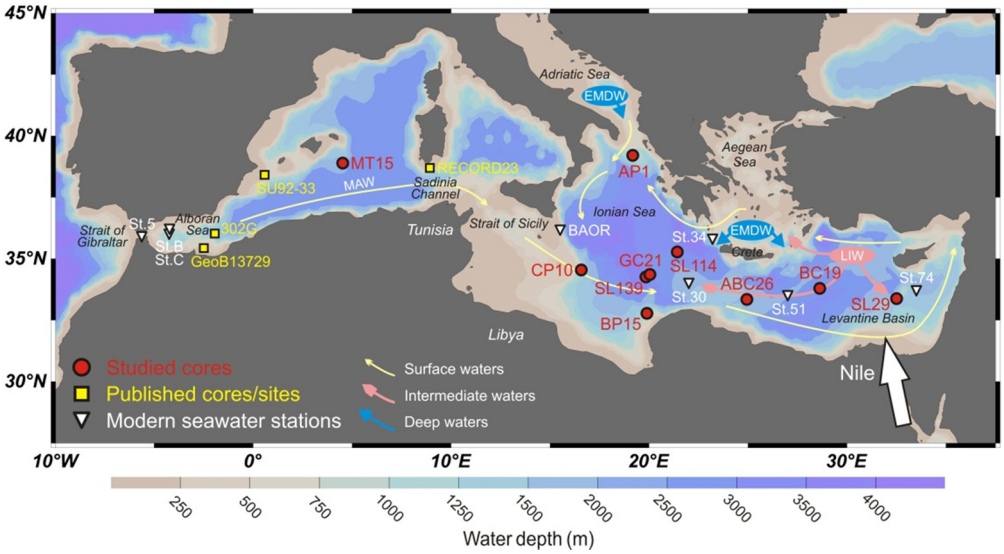

Figure 1 Bathymetric map of the Mediterranean Sea showing the locations of cores investigated (red circles; Table 1) and the published cores/sites discussed in the text (yellow squares; Jiménez-Espejo et al., 2015; Dubois-Dauphin et al., 2017). Modern seawater stations over the Mediterranean are also indicated (white triangles; Henry et al., 1994; Tachikawa et al., 2004). Large-scale oceanography after Pinardi and Masetti (2000), depicting the general surface-water circulation: Modified Atlantic Water (MAW), formation sites and pathways of Levantine Intermediate Water (LIW), as well as Eastern Mediterranean Deep Water (EMDW).

All of the fish and foraminiferal samples were handpicked from the >150 µm size fraction of wet-sieved sediments. Fish debris (~0.2–2 mg), including teeth, bones, and fragments, were processed after Martin et al. (2010) using ultraclean reagents. Samples were ultrasonicated in methanol for 10 seconds, before pipetting the fluids to waste. This step was subsequently applied in deionized water and repeated until the water remained clear and free of clay. All samples were checked for contaminant

detrital material under a microscope and any remaining detrital particles were removed. Thereafter, the fish debris was leached in a closed Teflon beaker with 30% H_2O_2 at 80 °C for 2 minutes, dried down at 90 °C, followed by the digestion in a mixture of concentrated HNO_3 and HCl (1:1) at 140 °C for 4 minutes in open Teflon beakers.

Table 1 General information of the investigated cores over the Mediterranean Sea

Core	Corer	Location	Water depth	Cruise
CP10	Box	34°32.7'N, 16°34.0'E	1501 m	RV *Pelagia* 2011
BP15	Box	32°46.7'N, 19°52.6'E	665 m	RV *Pelagia* 2001
AP1	Gravity	39°13.0'N, 19°06.8'E	811 m	RV *Urania* 1998
GC21 [a]	Gravity	34°21.9'N, 20°02.1'E	3250 m	RV *Bannock* 1988
SL139	Box	34°16.1'N, 19°49.8'E	3293 m	RV *Logachev* 1999
SL114	Box	35°17.2'N, 21°24.5'E	3390 m	RV *Logachev* 1999
ABC26	Box	33°21.3'N, 24°55.7'E	2150 m	RV *Tyro* 1987
BC19	Box	33°47.9'N, 28°36.5'E	2750 m	RV *Marion Dufresne* 1991
SL29	Box	33°23.4'N, 32°30.2'E	1587 m	RV *Logachev* 1999
MT15 [b]	Piston	38°53.8'N, 04°30.6'E	2573 m	RV *Tyro* 1993

[a] Collected from a permanent anoxic, brine basin.
[b] Collected from the western Mediterranean Sea.

For the cores where no fish debris was found in the sapropel S1, approximately 30 mg of mixed planktonic foraminifera (dominated by *G. ruber*) were picked. The shells were crushed between glass plates, ensuring that all chambers were opened. They were then ultrasonicated in a glass beaker for 2 minutes before pipetting off the fluids. This step was repeated until the water remained clear and free of clay. The cleanliness of samples was checked under a microscope and detrital particles were removed, Foraminifera were then dissolved in ultraclean 1 M acetic acid. This is after the general protocol described in previous studies (Roberts et al., 2010; Tachikawa et al., 2014).

All samples were purified by column chromatography before isotopic analysis. The rare earth elements (REE) were isolated using Eichrom TRU-Spec® resin, collected in 1 M HCl. Neodymium was then separated from other REE using Eichrom Ln-Spec® resin on volumetrically calibrated columns, with 0.25 M HCl as eluent (Wu et al., 2016).

The Nd isotope composition was analyzed using a Thermo Scientific® Neptune Plus multi-collector inductively coupled plasma mass spectrometry (MC-ICP-MS) at ICBM, Oldenburg. Instrumental mass bias was corrected by normalizing $^{146}Nd/^{144}Nd$ to 0.7219 using an exponential law. Measured $^{143}Nd/^{144}Nd$ ratios were normalized to the certified JNdi-1 value of 0.512115 (Tanaka et al., 2000). The 2σ external reproducibility monitored by repeated analyses of JNdi-1 (n = 17) was better than

0.3 εNd. An in-house standard solution (Merck; Basak et al., 2015) also gave a similar 2σ uncertainty (±0.2 εNd; n = 3). Blank levels were negligible in all cases.

To reconstruct temporal changes over the S1-equivalent period for the eastern and western basin of the Mediterranean, the Nd isotope data of two additional cores are used (Tables 1 and 3; Figure 1). The data were analyzed on the 1 M HCl leachate fraction of bulk sediments, done at CEREGE. The analytical procedures were given in detail by Freydier et al. (2001). All BC19 data and the most recent sample in MT15 have been published (Freydier et al., 2001; Tachikawa et al., 2004), whereas all sub-recent MT15 samples are reported here (Table 3).

Table 2 Neodymium isotope compositions of fish debris and mixed planktonic foraminifera over the eastern Mediterranean Sea

Core	Depth (cm)	Age (cal. ka BP)	Material	$^{143}Nd/^{144}Nd$ [a]	εNd ± 2σ [b]
CP10	20.5–21.5 [c]	6.1	Fish	0.512367 (15)	-5.3 ± 0.3
CP10	24.5–25.0 [c]	7.2	Fish	0.512382 (22)	-5.0 ± 0.4
CP10	26.0–26.5	7.5	Fish	0.512380 (12)	-5.0 ± 0.3
CP10	28.0–28.5	7.8	Fish	0.512380 (12)	-5.0 ± 0.3
CP10	30.0–30.5	8.3	Fish	0.512393 (10)	-4.8 ± 0.3
CP10	34.5–35.0	9.6	Fish	0.512399 (15)	-4.7 ± 0.3
BP15	32.5–33.0 [d]	8.8	Foraminifera	0.512324 (27)	-6.1 ± 0.5
AP1	31.0–32.0	9.6	Fish	0.512389 (06)	-4.9 ± 0.3
GC21	40.8	~9 ka / S1a	Fish	0.512375 (15)	-5.1 ± 0.3
SL139	27.5–28.5	9.3	Foraminifera	0.512374 (05)	-5.2 ± 0.3
SL114	32.75–34.25	9.6	Fish	0.512384 (19)	-5.0 ± 0.4
ABC26	15.95–16.25 [c]	7.1	Fish	0.512384 (04)	-5.0 ± 0.3
ABC26	20.45–20.75	8.9	Fish	0.512395 (10)	-4.8 ± 0.3
BC19	24.5–27.5	9.3	Foraminifera	0.512406 (13)	-4.5 ± 0.3
SL29	28.5–29.5	9.5	Fish	0.512398 (10)	-4.7 ± 0.3

[a] Normalized to the JNdi-1 value of $^{143}Nd/^{144}Nd = 0.512115$ (Tanaka et al., 2000), with 2σ standard errors indicated.
[b] Propagated errors are reported.
[c] Samples taken from oxidized sapropel intervals.
[d] The larger error is due to the small amount of Nd that was analyzed, caused by its low concentration in foraminiferal calcite (Roberts et al., 2012).

3 Results

The information on investigated cores is given in Table 1, and the isotopic results are reported in Tables 2 and 3, plotted in Figure 2, and compared with other Mediterranean records in Figure 3.

During the sapropel S1 period, the εNd (fish debris) of core CP10 varies within the analytical uncertainty (from -5.3 to -4.7 ± 0.3) (Figure 3). These values are slightly more radiogenic in the earlier S1a interval than in the subsequent S1b interval. At the end of sapropel S1 formation (~6.1 ka), core CP10 reports a less radiogenic εNd value of -5.3 ± 0.3. Core ABC26 also registers more radiogenic εNd (-4.8 ± 0.2) for

the S1a, and less (-5.0 ± 0.2) for S1b (Figure 3). Moreover, this S1a–S1b difference is also clearly observed in the HCl-leachate data of core BC19 (Figure 3). Therefore, although this trend is within error for each core, it appears to be systematic for all cores. Note that the S1b samples are often taken from the post-depositionally oxidized sapropel section (Van Santvoort et al., 1996; Thomson et al., 1999) (Table 2), but this is unlikely to affect the εNd signature (Roberts et al., 2012; Tachikawa et al., 2014).

Table 3 Neodymium isotope composition of 1 M HCl leaching fluid of Mediterranean sediments

Depth (cm)	Age (cal. ka BP)	$^{143}Nd/^{144}Nd$	εNd [a]	Source [b]
EMS core BC19				
0.25	1.4	0.512315	-6.3	1
3.75	2.5	0.512264	-7.3	1
5.75	3.2	0.512252	-7.5	2
7.25 [c]	3.7	0.512373	-5.2	2
12.75	5.4	0.512240	-7.8	2
15.75	6.3	0.512380	-5.0	2
19.25	7.3	0.512379	-5.0	2
20.75	7.7	0.512361	-5.4	2
23.25	8.3	0.512429	-4.1	2
25.75	9.1	0.512426	-4.1	2
27.25	9.6	0.512409	-4.5	2
29.25	10.0	0.512418	-4.3	2
30.25	10.4	0.512419	-4.3	2
32.25	11.0	0.512393	-4.8	2
34.95	11.8	0.512356	-5.5	2
WMS core MT15				
0.25	0.9	0.512159	-9.3	1
20.25	3.1	0.512185	-8.8	3
50.25	6.4	0.512160	-9.3	3
80.25	9.6	0.512164	-9.2	3
90.25	10.7	0.512170	-9.1	3
100.25	11.8	0.512149	-9.5	3
108.00	12.7	0.512134	-9.8	3
114.00	13.3	0.512180	-8.9	3
118.00	13.8	0.512146	-9.6	3
120.25	14.0	0.512170	-9.1	3
140.00	16.1	0.512162	-9.3	3

[a] 2σ uncertainty is ~10 ppm, i.e. ± 0.2 εNd; for analytical details refer to Freydier et al. (2001).
[b] 1= Tachikawa et al. (2004), 2= Freydier et al. (2001), 3= this study,
[c] The sample is possibly affected by Santorini tephra, and thus not shown in Figure 3.

In addition, the BC19 εNd record shows very distinct differences between sapropel and pre-/post sapropel sediments. These values are more radiogenic during sapropel S1 formation (-5.0 to -4.1) than during the periods before and after (-7.8 to -5.5) (Figure 3). Note that these BC19 HCl-leachate data are consistent (within error)

with the more reliable fish- and foraminiferal-derived data from the same site/area in the EMS (i.e. CP10, ABC26, and BC19). For the WMS, core MT15 displays relatively invariant changes with no discernible pattern for the whole Holocene period (HCl-leachate εNd: -9.6 to -8.8) (Figure 3).

The εNd values from all EMS cores below 800 m water-depth are characterized by very homogeneous bottom-water signatures for the S1 period: -5.2 to -4.5 ± 0.3 (Figure 2). In particular, these data show a small (within error) but systematic increase in bottom-water εNd from west to east (Figure 2c). By contrast, the sample from core BP15, located at a water-depth of 665 m, has a much less radiogenic value (-6.1 ± 0.5) (Table 2; Figure 2).

4 Discussion

4.1 Seawater εNd in the Mediterranean during sapropel S1 formation

In contrast to the much less radiogenic values and rather heterogeneous seawater εNd values in the present-day EMS deep-water (even for 1–3 km water-depth: -7.8 to -6.5), the homogenous and more radiogenic deep-water εNd values for sapropel S1 samples (for 1–3 km water-depth: -4.7 to -5.3) covering a large geographical and bathymetric range are remarkable (Figure 2). This not only indicates that the ratio of riverine, more radiogenic relative to Atlantic-origin less radiogenic Nd fluxes has increased, but also that the residence time of the deep-water has augmented. These two features are concordant with reduced circulation and known stagnant and anoxic deep-water conditions during S1 formation (e.g. Rossignol-Strick et al., 1982; Rohling, 1994; Emeis et al., 2000; De Lange et al., 2008; Schmiedl et al., 2010; Tachikawa et al., 2015) (see Section 1).

The basin-wide homogeneous εNd signature for samples below 800 m depth and the much less radiogenic sample at 661 m depth (core BP15) (Figure 2) indicate a boundary between more permanently stagnating waters below and waters with more frequent renewal above ~800 m water-depth. Such boundary is consistent with a shallower interface between the inflowing surface waters from the Atlantic and the outflowing intermediate waters during S1 time (Rohling, 1994; Myers et al., 1998; Rohling et al., 2015). Apart from supporting evidence from physical oceanographical models, this inference is in good agreement with other proxy reconstructions. The consistent variability of ventilation-related, benthic-foraminiferal proxies in EMS cores have been reported to indicate reduced, depth-dependent ventilation conditions for a water column between about 700–2300 m depth (Schmiedl et al., 2010; Tachikawa et al., 2015). Moreover, on the basis of geochemical evidence in particular, an anoxic boundary at ~1800 m or even above 1155 m water-depth has

been suggested to occur during the sapropel S1 period (De Lange et al., 2008; Bayon et al., 2013).

Alternatively, the deviating εNd value for the shallow offshore Libya core BP15 (-6.1 ± 0.5) (Figure 2) may reflect considerable paleodrainage runoffs from the wider North-African margin. During sapropel times, intensified monsoon precipitation has reactivated fossil river/wadi systems over the Libyan-Tunisian region (Vörösmarty et al., 2000; Paillou et al., 2009; 2012; Coulthard et al., 2013), transporting substantial amounts of detrital material and freshwater to the EMS (Rohling et al., 2002; Osborne et al., 2008; 2010; Wu et al., 2016; 2017). However, if the deviating εNd would be related to this, then a similar impact would have occurred to CP10-sediments located on the Libyan-Tunisian margin (Wu et al., 2016; 2017), but this is not the case for this site at 1501 m water-depth. Thus, although this effect cannot be fully excluded, it is unlikely to be a dominant factor.

The Nile discharge is thought to have caused deep-water stagnation during sapropel S1 formation (i.e. freshwater forcing), as suggested by numerical models of Mediterranean thermohaline circulation (Myers et al., 1998; Myers, 2002). As far as we know, Nile discharge is the only source that can deliver accountably radiogenic Nd to the Mediterranean Sea (Frost et al., 1986; Spivack and Wasserburg, 1988; Henry et al., 1994; Tachikawa et al., 2004; Vance et al., 2004). Therefore, if the more radiogenic Nd signal for the deep-water samples is related to enhanced Nile riverine input, then this εNd signal is also a measure for the degree of deep-water stagnation.

As a result, we argue for a marked deep-water stagnation below ~800 m depth during the S1 time (Figure 2b). On the basis of the temporal records, the fish-debris-derived εNd record of core CP10 suggests that such a deep-water stagnation may have persisted over the whole period of sapropel S1 formation (Figure 3). The record shows less radiogenic values during the latter interval S1b and more radiogenic values during the S1a (Figure 3). These inferences are also supported by the ABC26 data, and the BC19 sediment leachate data discussed below (Figure 3). Although within reported analytical uncertainty, this consistent difference may imply a higher degree of deep-water stagnation during S1a than during S1b. In other words, the degree of stratification of the water column appears to be most intense during the early phase of sapropel S1. This is in line with benthic foraminiferal and geochemical studies, suggesting more frequent ventilations at least in some intermediate-depth areas of the EMS after 8.2 ka and even more so after 7.5 ka (e.g. Jorissen et al., 1999; Kuhnt et al., 2008; Schmiedl et al., 2010; Tachikawa et al., 2015; Filippidi et al., 2016).

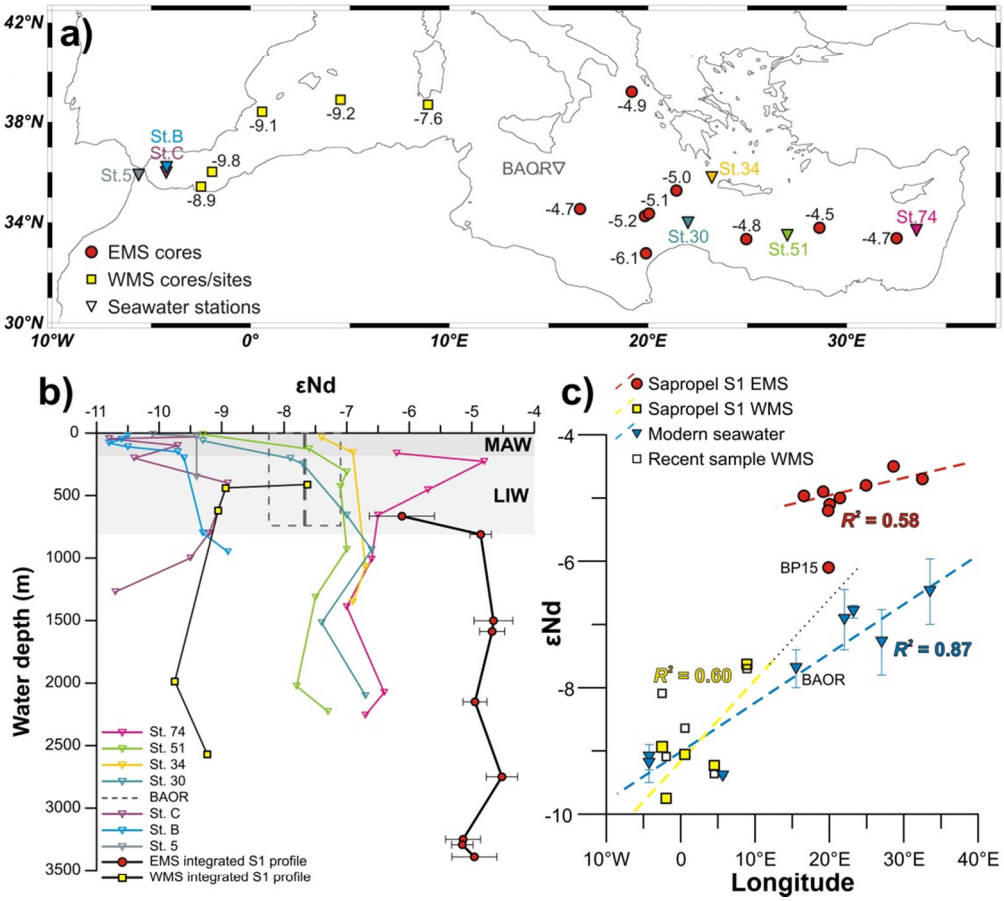

Figure 2 Mediterranean derived seawater-εNd values for the sapropel S1 period (6–10 ka), compared to recent seawater *in-situ* data. a) For the S1 period, average εNd values are reported for the eastern Mediterranean Sea (EMS; red-circles: Table 2) and western Mediterranean Sea (WMS; yellow-squares: Jiménez-Espejo et al., 2015; Dubois-Dauphin et al., 2017; Table 3). For the WMS sapropel S1 is absent, thus data refer to S1-equivalent age. Note that MT15 data are from HCl-leachate fraction of the sediment (this study, Table 3). In the map, the colored triangles indicate modern seawater stations (Tachikawa et al., 2004), corresponding to the colored vertical-profiles displayed in b). b) Regardless of their geographical location, the seawater-εNd signatures of sapropel S1 time are plotted against water-depth for the EMS and the WMS, respectively. The resulting integrated S1 paleo-seawater profiles are compared to the present-day seawater-εNd depth-profile. Note that the seawater samples of site BAOR are combined for the depths of 100, 200, 400, and 800 m, which represents the eastern flowing Levantine Intermediate Water (LIW) through the Strait of Sicily (Henry et al., 1994). c) The S1 and recent seawater-εNd values are plotted for the west–east transect. For the modern seawater stations, average εNd values and their ranges for >300 m water-depth are shown. For each WMS core/site, εNd values of the surface samples are also displayed, representing the recent bottom-water signature (Tachikawa et al., 2004; Jiménez-Espejo et al., 2015; Dubois-Dauphin et al., 2017). In the EMS, the seawater-εNd values are distinctly more radiogenic, and the west–east gradient is much weaker for the

sapropel S1 period than for the recent. By contrast, there is negligible difference for the WMS. Note that the WMS trend-line would continue towards the EMS shallow core BP15 (665 m water-depth) for the S1 period.

This consistent S1a versus S1b difference is clearly observed in the HCl-leachate εNd data of core BC19. These data are coherent (within error) with the more reliable fish- and foraminiferal-derived data from the same sites/areas (i.e. CP10, ABC26, and BC19) (Figure 3). Despite the reported potential difficulty in extracting seawater-εNd from sediments (Tachikawa et al., 2004; 2013), the tight correspondence between different archive data allows us to use the BC19 HCl-leachate data to indicate the general trends of seawater εNd versus time. The more radiogenic εNd values in core BC19 during the sapropel S1 period indicate stagnant deep-water conditions, as demonstrated above. Such reduced deep-water circulation appears to begin ~2,000 years before S1 formation started, to subsequently maintain over the whole S1 period (~10.8–6.1 ± 0.5 ka; De Lange et al., 2008), and to end synchronously with the S1 termination (Figure 3). The much earlier start of deep-water stagnation seems to be in harmony with a recent study of biogeochemical models, which suggests a long prelude of deep-water stagnation prior to S1 (i.e. ~6,000 years since deglaciation) (Grimm et al., 2015).

4.2 Sources of radiogenic Nd for the eastern Mediterranean Sea

One of the critical questions is related to the potential sources of the rather radiogenic Nd in the EMS deep-water during S1 time. Even for the present-day, the available data suggest an imbalance with respect to Nd flux and εNd signature between the inflowing and the outflowing waters across the Straits of Gibraltar and of Sicily, and a substantial source of radiogenic Nd is required (e.g. Frost et al., 1986; Spivack and Wasserburg, 1988; Greaves et al., 1991; Schijf et al. 1991; Henry et al., 1994; Tachikawa et al., 2004; Ayache et al., 2016) (see Section 1.2).

In general, volcanic material has been suggested as the most significant contributor for radiogenic Nd, either via direct aeolian fluxes or via the weathering of volcanic rocks (Frank, 2002). Saharan dust is a dominant detrital component to the recent Mediterranean sediments (Guerzoni et al., 1997; Rutten et al., 2000), but its εNd is quite unradiogenic (about -10 to -13; Frost et al., 1986; Grousset and Biscaye, 2005). Due to its relatively low Nd-content and -fractional solubility, dust for recent fluxes is thought to contribute minor amounts of dissolved Nd (Greaves et al., 1991; 1994; Tachikawa et al., 2004). Moreover, dust contribution has been reported to be largely decreased during the S1-humid climatic phase (e.g. Emeis et al. 2000; Freydier et al., 2001; Revel et al., 2010; Wu et al., 2016; 2017). Consequently, for the S1 period,

an aeolian Nd contribution can be considered negligible (see also Supplementary material).

By contrast, the contribution from riverine fluxes during such humid climate phase must have contributed to the much more radiogenic εNd signature in the EMS. The Nile is the only known riverine source with a rather radiogenic εNd. Accordingly, the highest, i.e. most-radiogenic recent seawater εNd value of -4.8 was found at ~200 m depth, in the easternmost Levantine Basin (Tachikawa et al., 2004), which is mainly obtaining Nile-discharged materials derived from basaltic rocks in the Ethiopian Highlands (Weldeab et al., 2002; Padoan et al., 2011). It has been suggested that it is the partially dissolved Nile River particles, rather than the river water itself, which could provide quantitatively significant amounts of radiogenic Nd (Tachikawa et al., 2004). However, even when considering optimal quantities of both Nile river-water and river-particles derived dissolved Nd, the calculated EMS seawater-εNd is still less radiogenic than the observed field data. Therefore, apart from these known aeolian and riverine contributions, there must be other important Nd fluxes in the Mediterranean, potentially including 1) volcanic debris, 2) “boundary exchange”, and 3) “reversible scavenging”.

During the Holocene several volcanic eruptions have distributed material but were mainly confined to the western Ionian (Italian origin) or Aegean. Moreover, any impact from volcanic eruptions will be short-lasting due to the rather short residence time of the Mediterranean water. Thus, substantial release from such volcanic debris would occur only from bottom sediment or via boundary exchange (e.g. the major Etna edifice). However, the water-column investigations do not indicate a clear radiogenic source from these distinct volcanic regions, but rather suggest a major radiogenic source from the most eastern Mediterranean, i.e. the Nile-dominated area (Tachikawa et al., 2004).

The “boundary exchange” that is defined as interactions between continental margin sediments and water masses by co-occurring sediment dissolution and desorption (Lacan and Jeandel, 2005) has been widely invoked to explain the missing Nd source in the oceans. For this purpose, a dense compilation of Nd concentrations and isotopic compositions of the different materials at the Mediterranean margins, expected to interact with the water masses, is used for a high-resolution modeling study (Ayache et al., 2016).
However, the modeling simulated too radiogenic εNd values (~1.5–3.0 εNd higher than *in-situ* data) for all water-depths, in both the eastern and western Mediterranean basins (Ayache et al., 2016). This bias points to insufficiently constrained boundary conditions, i.e. to unknown source(s) and sink(s) for Nd in the Mediterranean.

As one of the rare earth elements (REE), Nd concentration versus depth-profiles in the ocean suggest that not only continental input and partial dissolution of shelf sediment influence its vertical distribution, but also that particle scavenging occurs (Elderfield and Greaves, 1982; Frank, 2002). The so-called reversible scavenging, a process of coupled adsorption and desorption between dissolved Nd in the water column and the marine particulate phase, has been proposed to explain the decoupling of Nd concentrations and isotopes (Siddall et al., 2008; Arsouze et al., 2009; Rempfer et al., 2011). This process is thought to be also sensitive to the oxidation state of seawater, because the scavenging and release of Nd and other REE is generally believed to be coupled to the redox cycling of Fe and Mn. This makes the reversible scavenging important for the EMS, particularly during sapropel S1 formation (e.g. Schijf et al., 1991; 1995; Slomp et al., 2002). However, if we imply that such marine-mechanism releases substantial amounts of Nd into the Mediterranean seawater, then an isotopic fractionation upon adsorption/desorption is also needed to obtain the observed radiogenic Nd values. Such fractionation has not been reported thus far; hence we cannot rely on this potential mechanism but will rather explore relative contributions and changes required for the other mechanisms.

In the traditional sense a change in seawater εNd can be interpreted as a change in radiogenic, riverine contribution relative to the unradiogenic, Atlantic-origin contribution, as these two are the most important known sources. Regardless of the phase (dissolved or particulate), the Nile discharge is the most important known radiogenic source (Frost et al., 1986; Scrivner et al., 2004; Tachikawa et al., 2004). Other sources may be from rivers draining the mafic/ultramafic rocks over the northern EMS borderlands (e.g. Aegean basalts and Italian volcanic province) (Weldeab et al., 2002; Ayache et al., 2016; Wu et al., 2016)., or from reactivated North-African paleodrainage runoff derived from volcanic provinces in Libya (Scrivner et al., 2004; Osborne et al., 2008; 2010; Wu et al., 2016). Moreover, the “boundary exchange” may well have played a more important role during sapropel S1 time. This is on the one hand, because of the more shallow circulation system (see Section 4.3) and on the other due to different environmental conditions. The “boundary exchange” for the oxygen-depleted waters during S1 formation should have released more radiogenic Nd from sediments, including Nile-derived sediments, because of the dissolution of Fe-Mn oxyhydroxides. This process may also have released more radiogenic Etna-derived Nd from the Sicily margin.

However, enhanced riverine-related fluxes alone cannot account for the observed change in EMS εNd values, as the inflowing MAW is dominant (Frost et al., 1986; Tachikawa et al., 2004). This point is evidently shown by our model calculations. A

simplified one-box EMS model is provided to semi-quantitatively investigate the relative Nile vs. MAW contributions for the radiogenic signature found in the EMS deep-water during sapropel S1 time (see Supplementary material). The Nd-budget model for the S1 EMS is constructed so as to be directly comparable with the present-day, *in-situ* data of Tachikawa et al. (2004). In the calculation, uncertainties in the Nd concentration of the water masses appear to be mainly responsible for the Nd imbalance, which is larger for S1 time than for the present. This may imply an enhanced effect from the unknown sources/sinks during S1 formation.

For the S1 period, our calculations suggest that, with a two- or even three-fold pre-Aswan Nile discharge, a 50% (35–55%) reduction in the hydrological exchange across the Strait of Sicily, i.e. of inflowing MAW and outflowing LIW is required to obtain the observed basin-wide EMS deep-water εNd value of about -5. If taking the 1% partial dissolution of Nile particle into account (i.e. the potentially maximum Nile-related Nd flux anticipated for the present-day situation; Tachikawa et al., 2004), a 2-fold increased Nile contribution would still correspond with a 35–40% reduction in the MAW contribution. For the anticipated most extreme case, during S1, assuming 5% fractional Nd dissolution from Nile particles in anoxic seawater, a 2-fold Nile discharge requires a 20% reduction in the MAW inflow (for details see Supplementary material).

It must be noted that for the Nile runoff during S1 time, an enhanced flux of water is evident but not for its sediment delivery. This is because the monsoon-generated vegetation cover is denser and consequently suppresses physical erosion and sediment removal in the catchment areas (Ethiopian highlands) of the Blue Nile, which provides >95% of the total present-day Nile particulates (William et al., 2000; Padoan et al., 2011; Hennekam et al., 2014). In fact, on the basis of Sr and Nd isotopes and major elements, a rather limited Nile sediment delivery and its offshore distribution during sapropel periods have been suggested (Krom et al., 1999b; Weldeab et al., 2002b; Wu et al., 2016; 2017).

The other main branch, the White Nile has been reported to provide a larger relative sediment contribution during humid S1-phases, but its sediments are very unradiogenic (Box et al., 2011; Padoan et al., 2011). In view of the more radiogenic εNd during S1, it seems unlikely that the White Nile Nd contribution can have contributed substantially. Instead, the flux of less radiogenic dissolved Nd may partly be compensated by an enhanced release from previously deposited Blue Nile sediments, due to suboxic conditions during sapropel S1. Thus, a ~5% release taken relative to recent sediment fluxes also compensates for different hinterlands during S1 time, and can be considered as a maximum value for Nile sediment-derived Nd.

Another important parameter to consider is the Atlantic inflow. The derived stagnation of deep-water and the more radiogenic EMS εNd values during S1 time correspond with a much reduced but continued MAW inflow, and also fit well with paleoceanographical modeling and proxy observations (see Section 1). Moreover, the predominance of the MAW is in agreement with the conservative mixing between inflowing Atlantic surface-water and the underlying intermediate-water, as demonstrated also for dissolved Al (Rolison et al., 2015).

Taken together, the relatively radiogenic εNd signature found in the EMS deep-water during the S1 period can be attributed to a combination of factors: an increased Nile water discharge, enhanced boundary exchange for anoxic sediments, and a decreased MAW inflow to the EMS. In addition, a consequently long residence time for the deep-water is required. The most realistic scenario (i.e. potential best fit) is the combination of a 2-fold Nile contribution (1.5–3x) and a 50% reduced MAW contribution (45–65%), relative to the present-day fluxes (see Supplementary material). If the Nd cycle can be considered fully conservative, then this results in an estimated residence time for the EMS deep-water of ~110 ± 20 years.

4.3 Comparison between the eastern and western Mediterranean basins

To sum up, the west–east increase in our εNd data for the EMS during the sapropel S1 period is in line with a radiogenic source of the Nile in the east, and less radiogenic Atlantic waters flowing from west to east (Figure 2c). In turn, the minor west–east gradient for the S1 deep-water compared to the present-day indicates a longer residence time and a more reduced EMS circulation during the sapropel S1 period. This is consistent with the decoupling between the deep-water and intermediate waters at ~800 m depth, which points to a more shallow circulation in the EMS during the S1 formation. In a wider perspective, we further compare our results for EMS and WMS with published data of the WMS to shed light on the Mediterranean circulation during sapropel S1 time.

Recent studies have reconstructed the εNd variation of the intermediate waters for the WMS over the sapropel S1 equivalent period, by using coral and foraminiferal archives (Jiménez-Espejo et al., 2015; Dubois-Dauphin et al., 2017) (Figure 1). The S1-seawater εNd values are reported to be between about -10 and -8 for most areas in the WMS (except for the more eastern, shallow site RECORD23). The latter site seems to have slightly more radiogenic εNd values during the S1 period compared to the present-day, but these values are still much less radiogenic than those in the EMS (Figures 2 and 3). Moreover, the water column during the S1 period has a more heterogeneous εNd signature in the WMS than in the EMS (Figures 2 and 3).

In addition, during the S1 period the seawater εNd also shows a much stronger west–east gradient for the WMS than for the EMS (Figure 2c). This Mediterranean S1-gradient is distinctly different from the recent-gradient that seems rather continuous across both basins (Figure 2c). Together, these observed differences indicate an uncoupling of the EMS and WMS deep-water during the S1 time.

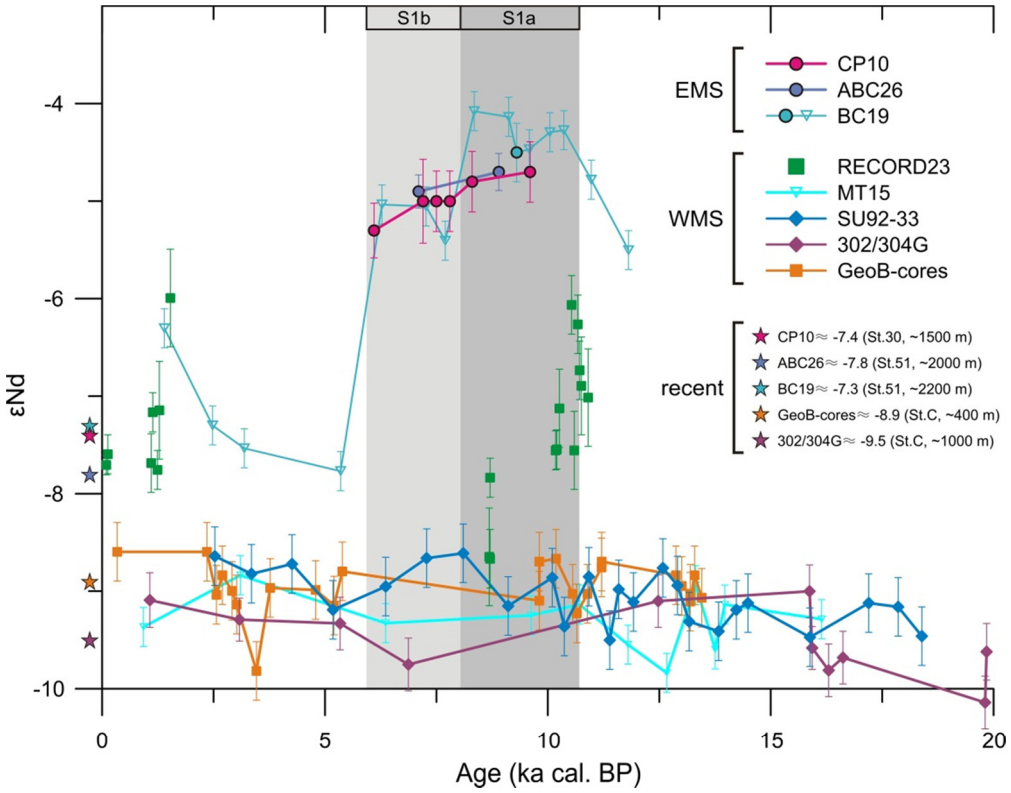

Figure 3 Reconstructed seawater εNd evolution of the eastern Mediterranean Sea (EMS; CP10, ABC26, and BC19) compared to the western Mediterranean Sea (WMS; all other records) over the Holocene sapropel S1 period. The data analyzed on fish debris/foraminifera in this study are marked as circles (CP10, ABC26, and BC19; Table 2); the data of sediment HCl-leachate fraction for cores BC19 and MT15 are marked as triangles (Freydier et al., 2001; Tachikawa et al., 2004; Table 3); and the WMS data from cold-water coral calcite and mixed planktonic foraminifera are marked as squares (RECORD23 and GeoB-cores; Dubois-Dauphin et al., 2017) and diamonds (SU92-33, Dubois-Dauphin et al., 2017; 302/304G, Jiménez-Espejo et al., 2015), respectively. The 2σ error bars are indicated. The stars approximately represent the recent bottom-water εNd values for the cores/sites, taken from the modern seawater data (Tachikawa et al., 2004) with a nearby location and a similar water-depth. Note that the HCl-leachate data are consistent with the more reliable fish-, foraminiferal, and coral-derived data from the same sites/areas (within error), therefore can be used to indicate the general trends of seawater εNd.

However, there may have been a coupling for shallower waters between the EMS and WMS, as suggested by the potential interaction between the EMS core BP15 (665 m depth) and the WMS coral-site RECORD23 located at the Sardinia Channel (414 m depth, close to the Strait of Sicily) (Figure 1). This hydrological interaction is revealed by the continuous WMS dashed-line through the data-point of RECORD23 towards that of BP15 (Figure 2c).

Moreover, this inference is supported by the seawater-εNd changes at RECORD23 site, which are thought to monitor the influence of LIW flowing from the EMS to the WMS (Dubois-Dauphin et al., 2017). Different from other WMS records that show invariant changes and no discernable pattern, the RECORD23 displays εNd values of about -8.5 to -7.5 for the S1 time-slice, and more radiogenic values between -7.5 and -6.0 for the arid intervals before and after S1 (Figure 3). This is also distinctly different from the pattern observed for the EMS (Figure 3). The changes recorded in site RECORD23 have been suggested to reflect a replacement of intermediate waters (Dubois-Dauphin et al., 2017), or an increased inflow of Atlantic waters (Grimm et al., 2015). Instead, this can be explained by a reduced LIW flow characterized by a more radiogenic εNd signature, as deduced in this study. A reduced LIW could have resulted in a less radiogenic Nd signature for the WMS intermediate water even without a dramatic change in the Atlantic inflow. This influence may be limited to a rather shallow depth, due to the enhanced riverine input and consequently less saline EMS seawater. The latter results in the LIW flowing into the WMS to be less dense, thus shallower during S1 compared to the present-day. In fact, the lack of changes in the εNd signature during S1 for all other WMS records is in line with a smaller LIW, a smaller Atlantic inflow, and relatively similar WMS circulation conditions as today. Further studies are required to verify these hypotheses, and in particular to evaluate budgets and balances for EMS and WMS.

In short, the differences in the seawater εNd data suggest a drastic reduction of the hydrological exchanges through the Strait of Sicily between the EMS and WMS during S1 formation. This is also explicitly shown by our model calculations, indicating an approximate 50% decrease in the exchanges across the Strait of Sicily during S1 (see Section 4.2 and Supplementary material for details). The more radiogenic deep-water was isolated in the EMS, with only limited exchange in the upper waters (above ~800 m depth) with the WMS. For the S1 period in the EMS, this reflects a decrease in the inflowing MAW surface-water characterized by an unradiogenic εNd signature, as well as a decrease in outflowing intermediate-water with a radiogenic εNd, and flowing at shallower depths than at present.

For the sapropel S1 period and on a basin-wide scale, these observations imply diminished production of intermediate waters and reduced or even ceased formation of deep water in the EMS, whereas the WMS water circulation may have continued to function similarly as today. This difference between the EMS and WMS suggests that stagnating deep-water condition is a prerequisite for sapropel formation.

5 Conclusions

For the first time, the seawater εNd signature is reported for the sapropel S1 period on a basin-wide EMS scale. This is done using the reliable seawater archives of fish debris and foraminiferal shells taken from 9 cores, and additional εNd data of Mediterranean sediment leachates from 2 cores. All together these represent a bathymetrical and geographical coverage. The derived deep-water signature is used to reconstruct water circulation and to constrain mixing and sources of water masses.

Our results exhibit very homogeneous εNd signatures (-5.3 to -4.5) of the EMS seawater below ~800 m depth, indicating severe deep-water stagnation during the S1 period. This stagnation persisted during the whole S1 period, with slightly less stagnant conditions, i.e. less radiogenic εNd values, during the latter interval, especially at the termination of S1 formation. The preconditioning of deep-water stagnation begun a few thousand years earlier than S1 formation started, whereas it terminated synchronously with the end of sapropel S1.

A relatively unradiogenic εNd value (-6.1) recorded at the shallow-water location is thought to reflect a boundary between stagnating waters below and waters with frequent renewal above ~800 m depth. This uncoupling of the EMS deep-water is supported by the longitudinal gradient in seawater-εNd data below ~800 m depth during the S1 period, which is much weaker than that during the present-day. Such a decreased gradient further indicates a longer residence time and not only a more reduced but also shallower EMS circulation during S1 time. Accordingly, the much more radiogenic εNd values of the S1-seawater compared to modern-seawater can be mainly explained by a combination of intensified, 2-fold Nile discharge (1.5–3x) delivering radiogenic Nd, and a 50% reduced MAW inflow (45–65%) bringing unradiogenic Nd to the EMS. Potential Nd fluxes from other riverine systems (e.g. northern borderlands) and from other mechanisms (e.g. boundary exchange) may have increased and also contributed to the observed EMS deep-water εNd value.

A stronger west–east gradient in seawater-εNd occurs for the WMS than for the EMS during the sapropel S1 period, which is distinctly different from the continuous west–east gradient throughout the Mediterranean Sea in the present-day. In addition to the less radiogenic and more heterogeneous S1-εNd signatures for the WMS, this suggests a drastic reduction of the hydrological exchange across the Strait of Sicily

during S1 period. This exchange appears to have been shallower, as suggested by a coupling between shallow EMS circulation and the WMS. A decreased outflow of intermediate water from the EMS is also deduced. These observations together correspond with diminished production of intermediate water and ceased formation of deep water in the EMS, whereas the WMS water circulation continued to function similarly.

Acknowledgements

Many thanks are given to Martina Schulz for sample preparation and column extraction at ICBM. We thank the captain & crew, scientists, and technicians on board the cruises of RV *Tyro* 1987 & 1993, RV *Bannock* 1988, RV *Marion Dufresne* 1991, RV *Urania* 1998, RV *Logachev* 1999, and RV *Pelagia* 2001 & 2011 for core collection. We acknowledge financial supports from EU-projects MARFLUX, PALEOFLUX & SAP, and from CNR and NWO for shiptime and logistic support. This study is sponsored by the China Scholarship Council – Utrecht University PhD Program (CSC No. 201206260116).

Appendix. Supplementary material

Supplementary material related to this article is attached.

Chapter 6 Appendix. Supplementary material

This **Supplementary material** provides a detailed description of a simplified one-box model, which aims to investigate aspects of the Nd balance for the eastern Mediterranean Sea (EMS) during sapropel S1 period. This approach is a semi-quantitative test, i.e. we do not aim to constrain precisely the Nd budget and derived hydrological changes in the EMS. This is because on the one hand, the available data do not allow us to carry out such a calculation; and on the other hand, the Nd oceanic cycle of the Mediterranean Sea, including its sources and sinks for the present-day, is still insufficiently known (see Sections 1.2 and 4.2 in the manuscript).

In fact, because of the uncertainties in the potential sources and sinks for Nd in the EMS, we decided to run our model calculation for the S1 period and to compare the results with those in Tachikawa et al. (2004) for the present-day. The more extreme boundary conditions for the S1 period compared to the present-day may help to further constrain sources and sinks for Nd. In addition, it will increase our understanding of water-mass circulation and difference therein between the present-day and the sapropel S1 period.

This EMS model evaluates the relative contributions between Nile and MAW (i.e. Modified Atlantic Water), respectively, representing the riverine contribution into the EMS (freshwater forcing), and the hydrological exchange between the EMS and WMS across the Strait of Sicily (circulation effect). The calculation is based on three balances, i.e. for water-masses, Nd-fluxes, and Nd-isotopes. Accordingly, three equations may be written as below, with the following assumptions made:

1) The EMS volume and surface area for today is the same as during sapropel S1 period (in fact, due to lower sea level, its volume was 1% less; thus a negligible difference).
2) The EMS-inflow + Nile water-discharge = EMS-outflow + Excess-evaporation (in analogy to Tachikawa et al. (2004); for constraining maximal Nile effect, we ignore other rivers).
3) Excess-evaporation = evaporation – precipitation – runoff (i.e. the basin-averaged excess of evaporation over total freshwater input). Here, a 65% of the current value is used. In general, 50–80% of the present-day value is suggested for sapropel periods (Rohling et al., 2015).
4) A fractional 2% dissolution of Nd from aeolian dust in seawater (after Tachikawa et al., 2004), and the dust flux for sapropel S1 is taken to be ~20% of that for the present-day (see the manuscript).

EMS-inflow + Nile-discharge = EMS-outflow + Excess-evaporation,

Equation 1) water-mass balance

EMS-inflow × [Nd] EMS-inflow + Nile-discharge × [Nd] Nile-discharge + aeolian Nd-flux = EMS-outflow × [Nd] EMS-outflow

Equation 2) Nd-flux balance

EMS-inflow × [Nd] EMS-inflow × [εNd] EMS-inflow + Nile-discharge × [Nd] Nile-water × [εNd] Nile-water + Nile-discharge × [Nd] Nile-particle × [εNd] Nile-particle + aeolian Nd-flux × [εNd] dust = EMS-outflow × [Nd] EMS-outflow × [εNd] EMS-outflow

Equation 3) Nd-isotope balance

The parameters used in the model are listed in Table S1; the three remaining variables are: Nile-discharge (x), EMS-inflow (y), [Nd] EMS-S1 (z). The description and explanation justifying the values used in the calculation are given in Table S1.

In order to test the relative contributions between the Nile discharge and the inflowing MAW to reach the radiogenic Nd signature in the EMS during sapropel S1 formation, four scenarios have been tested. The scenarios are set by changing the Nile contribution, which is the most important (known) radiogenic Nd source for the Mediterranean Sea. The partial dissolution of Nile River particles (i.e. boundary exchange) is considered. The tests are described as follows:

1) All of the dissolved Nd from Nile River water enters the EMS (100%), with no dissolution of river particles.
2) All of the dissolved Nd from Nile River waters enters the EMS (100%), with partial dissolution of river particles (1%). The sedimentary Nd flux is set as equal to the pre-Aswan Nile sediment flux.
3) All of the dissolved Nd from Nile River waters enters the EMS (100%), with partial dissolution of river particles (1%). The sedimentary Nd flux is set as proportional to the Nile water discharge.
4) All of the dissolved Nd from Nile River waters enters the EMS (100%), with partial dissolution of river particles (5%). The sedimentary Nd flux is set as constant equal to the pre-Aswan Nile sediment flux.

It must be noted that for all the four scenarios, a pre-Aswan Nile runoff is used as the present-day flux (i.e. base-line) to give optimal quantities of Nile river-water and river-particles derived dissolved-Nd. This setting is to be in analogy to and to make our results comparable to those by Tachikawa et al., 2004). The modern Nile particle flux is at most similar to recent pre-Aswan flux or possibly even smaller (Frost et al., 1986; Scrivner et al., 2004; see also the manuscript). Using a 1% partial dissolution of Nile particle, it represents the potentially maximum Nile-related Nd flux anticipated for the present-day situation (after Tachikawa et al., 2004). For the anticipated most extreme case, during sapropel S1, we assume 5% fractional Nd dissolution from

Nile particles. The motivation for this is that, during S1 anoxic conditions, in the EMS deep-water, enhanced release of Nd is likely in association with the dissolution of Fe-Mn hydroxides (Reitz et al., 2006; De Lange et al., 2008; Roberts et al., 2012; Tachikawa et al., 2013). The fourth scenario takes this possibility into account, thus representing the potentially maximum Nd-flux during sapropel periods, not only related to the Nile discharge itself and but also to “boundary exchange” processes.

As presented in Figure S1, Scenario-1 shows a gradual increase in the Nile and MAW contributions, until reaching the values of MAW (>0.8x) and Nile (>4x). The Scenario-2 displays a similar curve as that of Scenario-1, but with generally higher MAW values corresponding to the same Nile fluxes. The Scenario-3 shows a relatively rapid increase in the MAW contribution with the increasing Nile discharge from 1-fold to 3-fold. The Scenario-4 exhibits the highest MAW corresponding to the same Nile contribution, and a very steep gradient.

In all scenarios/calculations, the main uncertainties appear to come from the Nd concentration taken for the water-masses across the Strait of Sicily, for which limited Nd-information is available even for the present. As a result, the observed imbalance in terms of Nd concentrations and isotopes for the recent setting (Tachikawa et al., 2004) also exists and is even larger for our S1-period calculation for all scenarios. This may imply an enhanced effect from unknown sources/sinks during S1 time, or may be related to assumptions we made in the model. The simulated results show that the Nd concentrations of the EMS during sapropel S1 time are between 36–38 pmol/kg, compared to the 29.5 pmol/kg today (Tachikawa et al., 2004). The dust impact is minor. Even if assuming a 5-fold increase in the S1 Nd-dust-flux, the calculated results for the EMS εNd signature are similar (not shown). However, in that case a larger dust Nd-flux would cause a larger Nd concentration and larger isotope imbalance in the model calculation.

It is clear that the partial dissolution of Nile river-particle must be much more important as a radiogenic Nd source than the river-water. For the most extreme case (Scenario-4), we assume 5% particles of pre-Aswan Nile discharge dissolving in seawater. In that scenario, a two-fold Nile discharge would call for an 18–20% reduction in the MAW inflow (Figure S1). Taking the 1% partial dissolution of Nile particles into account (i.e. the highest Nile Nd-flux in a realistic sense), a 2-fold increased Nile discharge would correspond with a 35–40% reduction in the MAW contribution (Scenario-2 and -3) (Figure S1). If we consider the Nile water alone (Scenario-1), then a 2-fold Nile contribution is related to a 55% reduction in the EMS–WMS hydrological exchange across the Strait of Sicily (Figure S1).

Therefore, our results suggest that a combination of an enhanced Nile discharge and a decreased MAW inflow is needed to obtain the observed radiogenic signature found in the EMS deep-water during S1 time. As indicated by best fit, the most realistic scenario is: a 2-fold Nile contribution (1.5–3 times) and an MAW contribution that is 50% (45–65%), relative to their present-day fluxes. In addition, if the Nd oceanic cycle can be considered fully conservative, then this will yield an estimated residence time for the EMS deep-water of ~110 ± 20 years.

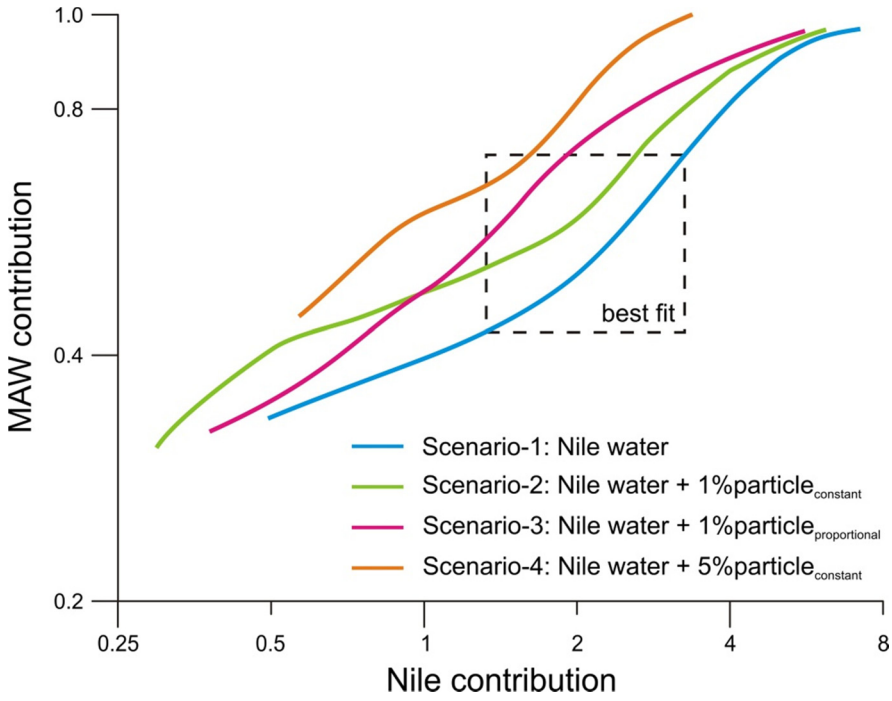

Figure S1 The simulated curves between Nile and MAW (i.e. Modified Atlantic Water, across the Strait of Sicily) contribution, relative to their present-day fluxes respectively. This EMS model is set to evaluate the possible routes (i.e. relative contributions between riverine and circulation effects) to reach the observed radiogenic Nd signature for the EMS deep-water during sapropel S1 time. Four scenarios with different Nd contributions from the Nile River are tested: 1) with 100% water only; 2) 100% water and 1% of Nd in river particles, and the sedimentary Nd flux is set as constant present-day value; 3) 100% water and 1% of Nd in river particles, and the sedimentary flux is assumed to be proportional to the Nile discharge; and 4) 100% water and 5% of Nd in river particles, and the sedimentary Nd flux is set as constant present-day value. The most realistic scenario is a combination of enhanced Nile flux (150–300%) and reduced MAW flux (45–65%), as suggested by the potential "best fit".

Table S1 Parameters of model calculation for Nd balance in the eastern Mediterranean Sea (EMS) during sapropel S1 period

Parameters [a]	Description	Water flux (10^{12} m^3/yr)		Dissolved Nd (pmol/kg)		εNd		Dissolved Nd flux (10^3 mol/yr)		Source [h]
		recent	S1	recent	S1	recent	S1	recent	S1	
Nile discharge [b]	Water	0.08	x	277	277	-1	-1			F86, S04
	Particle (1–5% dissolution)					-2	-2	270		F86, SW88, W02
Aeolian dust [c]	2% dissolution					-10		100	20	G94, T94, W17
EMS [d]				29.5	z	-7.3	-5.5			B80, T04, this study
EMS-inflow [e]	WMS surface water (MAW)	39.8	y	22	22	-10.5				T04
EMS-outflow [f]	EMS intermediate water (LIW)	38.0	x+y-1.2	26.4	f(z)	-7.7	-6.6			H94, T04
Excess evaporation [g]		1.8	1.2							R99

[a] With the same present-day EMS volume (2200×10^{12} m^3) assumed for the S1 time, a mass balance can be applied: EMS-outflow = Nile-water flux (variable: x) + EMS-inflow (variable: y) – Excess-evaporation.

[b] The set-up for the modern (pre-Aswan) Nile discharge after Tachikawa et al., (2004). For S1 period, the Nd-associated signatures are assumed to be the same as today. The 1% of the recent Nile particle is thought to be dissolved in seawater. During sapropel S1 time, a 5% partial dissolution may occur in the most extreme case during sapropel S1 anoxic seawater.

[c] Assuming 2% of aeolian particle is dissolved in seawater; and dust flux is assumed for the humid sapropel S1 time to be 20% of its present-day value(Wu et al., 2017).

[d] Dissolved Nd in S1-EMS is set as one of the three variables (z). The εNd value for S1-seawaters below and above ~800 m depth is -4.9 and -6.5, respectively (this study), and the volume weighed average is taken (-5.5).

[e] The Nd signature for the inflowing water during S1 time is assumed to be the same as that of the modern Atlantic-origin, WMS surface-water (i.e. Modified Atlantic Water) (Tachikawa et al., 2004).

[f] Assuming a simple linear mixing, assumptions can be made. Dissolved Nd in S1 EMS-outflow: f(z) = (recent [Nd] of EMS-outflow + simulated [Nd] of S1-EMS) / 2; seawater-εNd in S1 EMS-outflow: (recent [εNd] of EMS-outflow + reported [εNd] of S1-EMS) / 2 = (-7.7) + (-5.5) = -6.6. Data after Henry et al. (1994) and Tachikawa et al. (2004). See also Subscript [a].

[g] The basin-averaged excess evaporation over total freshwater input has been suggested to reduce to ~50-80% of the present-day value during sapropel S1 (Rohling, 1999), A 65% of present-day value is used here.

[h] B80= Bethoux (1980); F86= Frost et al. (1986); SW88= Spivack and Wasserburg (1988); G94= Greaves et al. (1994); H94 = Henry et al. (1994); T94= Thomas et al. (1994); R99= Rohling (1999); S04= Scrivner et al. (2004); T04= Tachikawa et al. (2004); W17= Wu et al. (2017).

References

Al-Hafdh, N.M., Gafeer, A.S., 2015. The petrology and geochemistry of Gharyan volcanic province of NW Libya. Journal of African Earth Sciences 104, 71–102.

Allègre, C. J., Dupré, B., Lambret, B., Richard, P., 1981. The subcontinental versus suboceanic debate, I Lead-neodymium-strontium isotopes in primary alkali basalts from a shield area the Ahaggar volcanic suite. Earth and Planetary Science Letters 52, 85–92.

Allen, J.R.M., Huntley, B., 2009. Last Interglacial palaeovegetation, palaeoenvironments and chronology: a new record from Lago Grande di Monticchio, southern Italy. Quaternary Science Reviews 28, 1521–1538.

Almogi-Labin, A., Bar-Matthews, M., Shriki, D., Kolosovsky, E., Paterne, M., Schilman, B., Ayalon, A., Aizenshtat, Z., Matthews, A., 2009. Climatic variability during the last similar to 90 ka of the southern and northern Levantine Basin as evident from marine records and speleothems. Quaternary Science Reviews 28, 2882–2896.

Angelidis, M.O., Radakovitch, O., Veron, A., Aloupi, M., Heussner, S., Price, B., 2011. Anthropogenic metal contamination and sapropel imprints in deep Mediterranean sediments. Marine Pollution Bulletin 62, 1041–1052.

Antobreh, A.A., Krastel, S., 2006. Morphology, seismic characteristics and development of Cap Timiris Canyon, offshore Mauritania: A newly discovered canyon preserved-off a major and climatic region. Marine and Petroleum Geology 23, 37–59.

Armitage, S.J., Bristow, C.S., Drake, N.A., 2015. West African monsoon dynamics inferred from abrupt fluctuations of Lake Mega-Chad. Proceedings of the National Academy of Sciences of the United States of America 112, 8543–8548.

Arsouze, T., Dutay, J.C., Lacan, F., Jeandel, C., 2009. Reconstructing the Nd oceanic cycle using a coupled dynamical - biogeochemical model. Biogeosciences 6, 2829–2846.

Augé, T., Joubert, M., Bailly, L., 2012. Typology of mafic-ultramafic complexes in Hoggar, Algeria: Implications for PGE, chromite and base-metal sulphide mineralisation. Journal of African Earth Sciences 63, 32–47.

Ayache, M., Dutay, J.-C., Arsouze, T., Révillon, S., Beuvier, J., Jeandel, J., 2016. High resolution neodymium characterization along the Mediterranean margins and modeling of εNd distribution in the Mediterranean basins. Biogeosciences 13, 5259–5276.

Bar-Matthews, M., Ayalon, A., Kaufman, A., 2000. Timing and hydrological conditions of Sapropel events in the Eastern Mediterranean, as evident from speleothems, Soreq cave, Israel. Chemical Geology 169, 145–156.

Bar-Matthews, M., Ayalon, A., Gilmour, M., Matthews, A., Hawkesworth, C.J., 2003. Sea-land oxygen isotopic relationships from planktonic foraminifera and speleothems in the Eastern Mediterranean region and their implication for paleorainfall during interglacial intervals. Geochimica et Cosmochimica Acta 67, 3181–3199.

Bard, E., Delaygue, G., Rostek, F., Antonioli, F., Silenzi, S., Schrag, D.P., 2002. Hydrological conditions over the western Mediterranean basin during the deposition of the cold Sapropel 6 (ca. 175 kyr BP). Earth and Planetary Science Letters 202, 481–494.

Bard, E., 2013. Out of the African Humid Period. Science 342, 808–809.

Barich, B.E., 2014. Northwest Libya from the early to late Holocene: New data on environment and subsistence from the Jebel Gharbi. Quaternary International 320, 15–27.

Barsanti, M., Delbono, I., Schirone, A., Langone, L., Miserocchi, S., Salvi, S., Delfanti, R., 2011. Sediment reworking rates in deep sediments of the Mediterranean Sea. Science of the Total Environment 409, 2959–2970.

Basak, C., Pahnke, K., Frank, M., Lamy, F., Gersonde, R., 2015. Neodymium isotopic characterization of Ross Sea Bottom Water and its advection through the southern South Pacific. Earth and Planetary Science Letters 419, 211–221.

Bayon, G., German, C.R., Burton, K.W., Nesbitt, R.W., Rogers, N., 2004. Sedimentary Fe-Mn oxyhydroxides as paleoceanographic archives and the role of aeolian flux in regulating oceanic dissolved REE. Earth and Planetary Science Letters 224, 477–492.

Bayon G., Dupré S., Ponzevera E., Etoubleau J., Chéron S., Pierre C., Mascle J., Boetius A., De Lange G.J., 2013. Formation of carbonate chimneys in the Mediterranean Sea linked to deep-water oxygen depletion. Nature Geoscience 6, 755–760.

Béranger, K., Mortier, L., Crepon, M., 2005. Seasonal variability of water transport through the Straits of Gibraltar, Sicily and Corsica, derived from a high-resolution model of the Mediterranean circulation. Progress in Oceanography 66, 341–364.

Berger, A., Loutre, M.F., 1991. Insolation values for the climate of the last 10 million years. Quaternary Science Reviews 10, 297–317.

Bethoux, J.-P., 1980. Mean water fluxes across sections in the Mediterranean Sea, evaluated on the basis of water and salt budgets and of observed salinities. Oceanologica Acta 3, 79–88.

Bianchi, D., Zavatarelli, M., Pinardi, N., Capozzi, R., Capotondi, L., Corselli, C., Masina, S., 2006. Simulations of ecosystem response during the sapropel S1 deposition event. Palaeogeography Palaeoclimatology Palaeoecology 235, 265–287.

Biscaye, P.E., 1965. Mineralogy and sedimentation of recent deep-sea clay in Atlantic Ocean and adjacent seas and oceans. Geological Society of America Bulletin 76, 803–832.

Bishop, J.K.B., 1988. The barite-opal-organic carbon association in oceanic particulate matter. Nature 332, 341–343.

Blum, J.D., Erel, Y., 1997. Rb-Sr isotope systematics of a granitic soil chronosequence: The importance of biotite weathering. Geochimica et Cosmochimica Acta 61, 3193–3204.

Boere, A.C., Rijpstra, W.I.C., de Lange, G.J., Malinverno, E., Damste, J.S.S., Coolen, M.J.L., 2011. Exploring preserved fossil dinoflagellate and haptophyte DNA signatures to infer ecological and environmental changes during deposition of sapropel S1 in the eastern Mediterranean. Paleoceanography 26, PA2204. Doi:10.1029/2010PA001948.

Böttcher, M.E., Rinna, J., Warning, B., Wehausen, R., Howell, M.W., Schnetger, B., Stein, R., Brumsack, H.J., Rullkotter, J., 2003. Geochemistry of sediments from the connection between the western and the eastern Mediterranean Sea (Strait of Sicily, ODP Site 963). Palaeogeography Palaeoclimatology Palaeoecology 190, 165–194.

Bout-Roumazeilles, V., Nebout, N.C., Peyron, O., Cortijo, E., Landais, A., Masson-Delmotte, V., 2007. Connection between South Mediterranean climate and North African atmospheric circulation during the last 50,000 yr BP North Atlantic cold events. Quaternary Science Reviews 26, 3197–3215.

Bout-Roumazeilles, V., Combourieu-Nebout, N., Desprat, S., Siani, G., Turon, J.L., Essallami, L., 2013. Tracking atmospheric and riverine terrigenous supplies variability during the last glacial and the Holocene in central Mediterranean. Climate of the Past 9, 1065–1087.

Box, M.R., Krom, M.D., Cliff, R.A., Bar-Matthews, M., Almogi-Labin, A., Ayalon, A., Paterne, M., 2011. Response of the Nile and its catchment to millennial-scale climatic change since the LGM from Sr isotopes and major elements of East Mediterranean sediments. Quaternary Science Reviews 30, 431–442.

Boynton, W.V. 1985. Cosmochemistry of the rare earth elements: Meteorite studies, In: Henderson, P. (Ed.), Rare Earth Element Geochemistry, Elservier, Amsterdam, p.115–1522.

Caquineau, S., Gaudichet, A., Gomes, L., Magonthier, M.C., Chatenet, B., 1998. Saharan dust: Clay ratio as a relevant tracer to assess the origin of soil-derived aerosols. Geophysical Research Letters 25, 983–986. Doi:10.1029/2000JD000247.

Calvert, S.E., Fontugne, M.R., 2001. On the late Pleistocene-Holocene sapropel record of climatic and oceanographic variability in the eastern Mediterranean. Paleoceanography 16, 78–94.

Castañeda, I.S., Mulitza, S., Schefuss, E., dos Santos, R.A.L., Damste, J.S.S., Schouten, S., 2009. Wet phases in the Sahara/Sahel region and human migration patterns in North Africa. Proceedings of the National Academy of Sciences of the United States of America 106, 20159–20163.

Castañeda, I.S., Schouten, S., Patzold, J., Lucassen, F., Kasemann, S., Kuhlmann, H., Schefuss, E., 2016. Hydroclimate variability in the Nile River Basin during the past 28,000 years. Earth and Planetary Science Letters 438, 47–56.

Chamley, H., 1989. Clay Sedimentology. Springer, Berlin, p.623.

Cheddadi, R., Rossignol-strick, M., 1995. Eastern Mediterranean quaternary paleoclimates from pollen and isotope records of marine cores in the Nile cone area. Paleoceanography 10, 291–300.

Chen, T.Y., Frank, M., Haley, B.A., Gutjahr, M., Spielhagen, R.F., 2012. Variations of North Atlantic inflow to the central Arctic Ocean over the last 14 million years inferred from hafnium and neodymium isotopes. Earth and Planetary Science Letters 353, 82–92.

Claude, J., Francillon, G., Loyer, J. Y., 1977. Les alluvions déposées par l'Oued Medjerda lors de la crue exceptionnelle de mars 1973. Cahiers de l'Orstom, sér. Hydrologie 14, 37–109.

Claussen, M., Kubatzki, C., Brovkin, V., Ganopolski, A., Hoelzmann, P., Pachur, H.J., 1999. Simulation of an abrupt change in Saharan vegetation in the mid-Holocene. Geophysical Research Letters 26, 2037–2040.

Clemens, S.C., 1998. Dust response to seasonal atmospheric forcing: Proxy evaluation and calibration. Paleoceanography 13, 471–490.

Cockerton, H.E., Holmes, J.A., Street-Perrott, F.A., Ficken, K.J., 2014. Holocene dust records from the West African Sahel and their implications for changes in climate and land surface conditions. Journal of Geophysical Research-Atmospheres 119, 8684–8694.

Cole, J.M., Goldstein, S.L., Demenocal, P.B., Hemming, S.R., Grousset, F.E., 2009. Contrasting compositions of Saharan dust in the eastern Atlantic Ocean during the last deglaciation and African Humid Period. Earth and Planetary Science Letters 278, 257–266.

Colin, C., Turpin, L., Blamart, D., Frank, N., Kissel, C., Duchamp, S., 2006. Evolution of weathering patterns in the Indo-Burman Ranges over the last 280 kyr: Effects of sediment provenance on 87Sr/86Sr ratios tracer. Geochemistry Geophysics Geosystems 7, Q03007. Doi:10.1029/2005GC000962.

Colin, C., Frank, N., Copard, K., Douville, E., 2010. Neodymium isotopic composition of deep-sea corals from the NE Atlantic: implications for past hydrological changes during the Holocene. Quaternary Science Reviews 29, 2509–2517.

Coulthard, T. J., Ramirez, J. A., Barton, N., Rogerson, M., Brücher, T., 2013. Were rivers flowing across the Sahara during the last Interglacial? Implications for human migration through Africa. PloS ONE 8, e74834. Doi:10.1371/journal.pone.0074834.

Cramp, A., O'Sullivan, G., 1999. Neogene sapropels in the Mediterranean: a review. Marine Geology 153, 11–28.

Cremaschi, M., Zerboni, A., 2009. Early to Middle Holocene landscape exploitation in a drying environment: Two case studies compared from the central Sahara (SW Fezzan, Libya). Comptes Rendus Geoscience 341, 689–702.

Dasch, E.J., 1969. Strontium isotopes in weathering profiles, deep-sea sediments, and sedimentary rocks. Geochimica et Cosmochimica Acta 33, 1521–1552.

De Lange, G.J., Ten Haven, H.L., 1983. Recent sapropel formation in the Eastern Mediterranean. Nature 305, 797–798.

De Lange, G.J., Middelburg, J.J., Pruysers, P.A., 1989. Middle and Late Quaternary depositional sequences and cycles in the eastern Mediterranean - Discussion. Sedimentology 36, 151–156.

De Lange, G.J., Boelrijk, N.A.I.M., Catalano, G., Corselli, C., Klinkhammer, G.P., Middelburg, J.J., Müller, D.W., Ullman, W.J., Van Gaans, P., Woittiez, J.R.W., 1990. Sulphate related equilibria in the hypersaline brines of the Tyro and Bannock basins, eastern Mediterranean. Marine Chemistry 31, 89–112.

De Lange, G.J., Thomson, J., Reitz, A., Slomp, C.P., Principato, M.S., Erba, E., Corselli, C., 2008. Synchronous basin-wide formation and redox-controlled preservation of a Mediterranean sapropel. Nature Geoscience 1, 606–610.

Dehairs, F., Chesselet, R., Jedwab, J., 1980. Discrete suspended particles of barite and the barium cycle in the open ocean. Earth and Planetary Science Letters 49, 528–550.

deMenocal, P., Ortiz, J., Guilderson, T., Adkins, J., Sarnthein, M., Baker, L., Yarusinsky, M., 2000. Abrupt onset and termination of the African Humid Period: rapid climate responses to gradual insolation forcing. Quaternary Science Reviews 19, 347–361.

deMenocal, P., Tierney, J., 2012. Green Sahara: African Humid Periods paces by Earth's orbital changes. Nature Education Knowledge 3, 10.

Des Combes, H.J., Caulet, J.P., Tribovillard, N.P., 1999. Pelagic productivity changes in the equatorial area of the northwest Indian Ocean during the last 400,000 years. Marine Geology 158, 27–55.

Dolenec, T., Faganeli, J., Pirc, S., 1998. Major, minor and trace elements in surficial sediments from the open Adriatic Sea: a regional geochemical study. Geologia Croatica 51, 59–73.

Drake, N.A., Blench, R.M., Armitage, S.J., Bristow, C.S., White, K.H., 2011. Ancient watercourses and biogeography of the Sahara explain the peopling of the desert. Proceedings of the National Academy of Sciences of the United States of America 108, 458–462.

Drysdale, R.N., Zanchetta, G., Hellstrom, J.C., Fallick, A.E., Zhao, J.X., 2005. Stalagmite evidence for the onset of the Last Interglacial in southern Europe at 129 ± 1 ka. Geophysical Research Letters 32, L24708. Doi:10.1029/2005GL024658.

Dubois-Dauphin, Q., Montagna, P., Siani, G., Douville, E., Wienberg, C., Hebbeln, D., Liu, Z., Kallel, N., Dapoigny, A., Revel, M., Pons-Branchu, E., Taviani, M., Colin, C., 2017. Hydrological variations of the intermediate water masses of the western Mediterranean Sea during the past 20 ka inferred from neodymium isotopic composition in foraminifera and cold-water corals. Climate of the Past 13, 17–37.

Dymond, J., Suess, E., Lyle, M., 1992. Barium in deep-sea sediment: A geochemical proxy for paleoproductivity. Paleoceanography 7, 163–181.

Dymond, J., Collier, R., 1996. Particulate barium fluxes and their relationships to biological productivity. Deep-Sea Research Part II – Topical Studies in Oceanography 43, 1283–1308.

Egerer, S., Claussen, M., Reick, C., Stanelle, T., 2016. The link between marine sediment records and changes in Holocene Saharan landscape: simulating the dust cycle. Climate of the Past 12, 1009–1027.

Ehrmann, W., Schmiedl, G., Hamann, Y., Kuhnt, T., 2007a. Distribution of clay minerals in surface sediments of the Aegean Sea: a compilation. International Journal of Earth Sciences 96, 769–780.

Ehrmann, W., Schmiedl, G., Hamann, Y., Kuhnt, T., Hemleben, C., Siebel, W., 2007b. Clay minerals in late glacial and Holocene sediments of the northern and southern Aegean Sea. Palaeogeography Palaeoclimatology Palaeoecology 249, 36–57.

Elderfield, H., Greaves, M.J., 1982. The rare earth elements in seawater. Nature 296, 214–219.

Elderfield, H., 1986. Strontium isotope stratigraphy. Palaeogeography, Palaeoclimatology, Palaeoecology 57, 71–90.

Elmore, A.C., Piotrowski, A.M., Wright, J.D., Scrivner, A.E., 2011. Testing the extraction of past seawater Nd isotopic composition from North Atlantic deep sea sediments and foraminifera. Geochemistry Geophysics Geosystems 12, Q09008. Doi:10.1029/2011GC00374.

Elmouden, A., Bouchaou, L., Snoussi, M., 2005. Constraints on alluvial clay mineral assemblages in semiarid regions. The Souss Wadi Basin (Morocco, Northwestern Africa). Geologica Acta 3, 3–13.

Emeis, K.C., Schulz, H., Struck, U., Rossignol-Strick, M., Erlenkeuser, H., Howell, M.W., Kroon, D., Mackensen, A., Ishizuka, S., Oba, T., Sakamoto, T., Koizumi, I., 2003. Eastern Mediterranean surface water temperatures and δ18O composition during deposition of sapropels in the late Quaternary. Paleoceanography 18, 1005. Doi:10.1029/2000PA000617.

Essallami, L., Sicre, M.A., Kallel, N., Labeyrie, L., Siani, G., 2007. Hydrological changes in the Mediterranean Sea over the last 30,000 years. Geochemistry Geophysics Geosystems 8, Q07002. Doi:10.1029/2007GC001587.

Faure, G., 1986. Principles of isotope geology. Wiley, New York, p.589.

Filippidi, A., Triantaphyllou, M.V., De Lange, G.J., 2016. Eastern-Mediterranean ventilation variability during sapropel S1 formation, evaluated at two sites influenced by deep-water formation from Adriatic and Aegean Seas. Quaternary Science Reviews 144, 95–106.

Fontugne, M., Arnold, M., Labeyrie, L., Paterne, M., Calvert, S., Duplessy, J., 1994. Paleoenvironment, sapropel chronology, and Nile river discharge during the last 20,000 years as indicated by deep-sea sediment records in the eastern Mediterranean. Radiocarbon 34, 75–88.

Foucault, A., Stanley, D.J., 1989. Late Quaternary paleoclimatic oscillations in East Africa recorded by heavy minerals in the Nile delta. Nature 339, 44–46.

Foucault, A., Mélière, F., 2000. Palaeoclimatic cyclicity in central Mediterranean Pliocene sediments: the mineralogical signal. Palaeogeography Palaeoclimatology Palaeoecology 158, 311–323.

Francois, R., Honjo, S., Manganini, S.J., Ravizza, G.E., 1995. Biogenic barium fluxes to the deep-sea - Implications for paleoproductivity reconstruction. Global Biogeochemical Cycles 9, 289–303.

Frank, M., 2002. Radiogenic isotopes: Tracers of past ocean circulation and erosional input. Reviews of Geophysics 40, 1. Doi: 10.1029/2000RG000094

Frank, N., Freiwald, A., Correa, M.L., Wienberg, C., Eisele, M., Hebbeln, D., Van Rooij, D., Henriet, J.-P., Colin, C., van Weering, T., de Haas, H., Buhl-Mortensen, P., Roberts, J.M., De Mol, B., Douville, E., Blamart, D., Hatté, C., 2011. Northeastern Atlantic cold-water coral reefs and climate. Geology 39, 743–746.

Freydier, R., Michard, A., de Lange, G.J., Thomson, J., 2001. Nd isotopic compositions of Eastern Mediterranean sediments: tracers of the Nile influence during sapropel S1 formation? Marine Geology 177, 45–62.

Frost, C., O'Nions, R., Goldstein, S., 1986. Mass balance for Nd in the Mediterranean Sea. Chemical Geology 55, 45–50.

Gingele, F., Dahmke, A., 1994. Discrete barite particles and barium as tracers of paleoproductivity in South Atlantic sediments. Paleoceanography 9, 151–168.

Giraudi, C., Mercuri, A.M., Esu, D., 2013. Holocene palaeoclimate in the northern Sahara margin (Jefara Plain, northwestern Libya). Holocene 23, 339–352.

Goldstein, S.L., Onions, R.K., Hamilton, P.J., 1984. A Sm-Nd isotopic study of atmospheric dusts and particulates from major river systems. Earth and Planetary Science Letters 70, 221–236.

Goldstein, S., Hemming, S., 2003. Long-lived isotopic tracers in oceanography, paleoceanography, and ice-sheet dynamics. Treatise on Geochemistry.

Goudeau, M.L.S., Grauel, A.L., Bernasconi, S.M., de Lange, G.J., 2013. Provenance of surface sediments along the southeastern Adriatic coast off Italy: An overview. Estuarine Coastal and Shelf Science 134, 45–56.

Goudeau, M.L.S., Grauel, A.L., Tessarolo, C., Leider, A., Chen, L., Bernasconi, S.M., Versteegh, G.J.M., Zonneveld, K.A.F., Boer, W., Alonso-Hernandez, C.M., de Lange, G.J., 2014. The Glacial–Interglacial transition and Holocene environmental changes in sediments from the Gulf of Taranto, central Mediterranean. Marine Geology 348, 88–102.

Goudeau, M.L.S., Reichart, G.J., Wit, J.C., de Nooijer, L.J., Grauel, A.L., Bernasconi, S.M., de Lange, G.J., 2015. Seasonality variations in the Central Mediterranean during climate change events in the Late Holocene. Palaeogeography Palaeoclimatology Palaeoecology 418, 304–318.

Goudie, A.S., Middleton, N.J., 2001. Saharan dust storms: nature and consequences. Earth-Science Reviews 56, 179–204.

Gourlan, A.T., Meynadier, L., Allegre, C.J., 2008. Tectonically driven changes in the Indian Ocean circulation over the last 25 Ma: Neodymium isotope evidence. Earth and Planetary Science Letters 267, 353–364.

Gourlan, A.T., Meynadier, L., Allegre, C.J., Tapponnier, P., Birck, J.L., Joron, J.L., 2010. Northern Hemisphere climate control of the Bengali rivers discharge during the past 4 Ma. Quaternary Science Reviews 29, 2484–2498.

Govindaraju, K., 1994. 1994 compilation of working values and sample description for 383 geostandards. Geostandards and Geoanalytical Research 18, 1–158.

Greaves, M.J., Rudnicki, M., Elderfield, H., 1991. Rare earth elements in the Mediterranean Sea and mixing in the Mediterranean outflow. . Earth and Planetary Science Letters 103, 169–181.

Greaves, M.J., Statham, P.J., Elderfield, H., 1994. Rare earth element mobilization from marine atmospheric dust into seawater. Marine Chemistry 46, 255–260.

Grelaud, M., Marino, G., Ziveri, P., Rohling, E.J., 2012. Abrupt shoaling of the nutricline in response to massive freshwater flooding at the onset of the last interglacial sapropel event. Paleoceanography 27, PA3208. Doi:10.1029/2012PA002288.

Grimm, R., Maier-Reimer, E., Mikolajewicz, U., Schmiedl, G., Muller-Navarra, K., Adloff, F., Grant, K.M., Ziegler, M., Lourens, L.J., Emeis, K.C., 2015. Late glacial initiation of Holocene eastern Mediterranean sapropel formation. Nature Communications 6, 7099. Doi: 10.1038/ncomms8099.

Griselin, M., van Belle, J.C., Pomies, C., Vroon, P.Z., van Soest, M.C., Davies, G.R., 2001. An improved chromatographic separation technique of Nd with application to NdO+ isotope analysis. Chemical Geology 172, 347–359.

Grousset, F.E., Rognon, P., Coudegaussen, G., Pedemay, P., 1992. Origins of peri-Saharan dust deposits traced by their Nd and Sr isotopic composition. Palaeogeography Palaeoclimatology Palaeoecology 93, 203–212.

Grousset, F.E., Parra, M., Bory, A., Martinez, P., Bertrand, P., Shimmield, G., Ellam, R.M., 1998. Saharan wind regimes traced by the Sr-Nd isotopic composition of subtropical Atlantic sediments: Last Glacial maximum vs. today. Quaternary Science Reviews 17, 395–409.

Grousset, F.E., Biscaye, P.E., 2005. Tracing dust sources and transport patterns using Sr, Nd and Pb isotopes. Chemical Geology 222, 149–167.

Guerzoni, S., Molinaroli, E., Chester, R., 1997. Saharan dust inputs to the western Mediterranean Sea: Depositional patterns, geochemistry and sedimentological implications. Deep-Sea Research Part II-Topical Studies in Oceanography 44, 631–654.

Guerzoni, S., Chester, R., Dulac, F., Herut, B., Loye-Pilot, M.D., Measures, C., Migon, C., Molinaroli, E., Moulin, C., Rossini, P., Saydam, C., Soudine, A., Ziveri, P., 1999. The role of atmospheric deposition in the biogeochemistry of the Mediterranean Sea. Progress in Oceanography 44, 147–190.

Güleç, N., 1991. Crust-mantle interaction in Western Turkey: implications from Sr and Nd isotope geochemistry of Tertiary and Quaternary volcanics. Geological Magazine 128, 417–435.

Hamann, Y., Ehrmann, W., Schmiedl, G., Kruger, S., Stuut, J.B., Kuhnt, T., 2008. Sedimentation processes in the Eastern Mediterranean Sea during the Late Glacial and Holocene revealed by end-member - 198 -odeling of the terrigenous fraction in marine sediments. Marine Geology 248, 97–114.

Hamann, Y., Ehrmann, W., Schmiedl, G., Kuhnt, T., 2009. Modern and late Quaternary clay mineral distribution in the area of the SE Mediterranean Sea. Quaternary Research 71, 453–464.

Hennekam, R., Jilbert, T., Schnetger, B., de Lange, G.J., 2014. Solar forcing of Nile discharge and sapropel S1 formation in the early to middle Holocene eastern Mediterranean. Paleoceanography 29, 343–356.

Hennekam, R., Donders, T., Zwiep, K., de Lange, G., 2015. Integral view of Holocene precipitation and vegetation changes in the Nile catchment area as inferred from its delta sediments. Quaternary Science Reviews 130, 189–199.

Henry, F., Jeandel, C., Dupre, B., Minster, J.F., 1994. Particulate and dissolved Nd in the western Mediterranean Sea: sources, fate and budget. Marine Chemistry 45, 283–305.

Hilgen, F.J., 1991. Astronomical calibration of Gauss to Matuyama sapropels in the Mediterranean and implication for the geomagnetic Polarity Time Scale. Earth and Planetary Science Letters 104, 226–244.

Hoelzmann, P., Jolly, D., Harrison, S.P., Laarif, F., Bonnefille, R., Pachur, H.J., 1998. Mid-Holocene land-surface conditions in northern Africa and the Arabian Peninsula: A data set for the analysis of biogeophysical feedbacks in the climate system. Global Biogeochemical Cycles 12, 35–51.

Hoffmann, D.L., Rogerson, M., Spotl, C., Luetscher, M., Vance, D., Osborne, A.H., Fello, N.M., Moseley, G.E., 2016. Timing and causes of North African wet phases during the last glacial period and implications for modern human migration. Scientific Reports 6, 36367. Doi:10.1038/srep36367.

Horikawa, K., Martin, E.E., Asahara, Y., Sagawa, T., 2011. Limits on conservative behavior of Nd isotopes in seawater assessed from analysis of fish teeth from Pacific core tops. Earth and Planetary Science Letters 310, 119–130.

Israelevich, P., Ganor, E., Alpert, P., Kishcha, P., Stupp, A., 2012. Predominant transport paths of Saharan dust over the Mediterranean Sea to Europe. Journal of Geophysical Research-Atmospheres 117, D02205. Doi:10.1029/2011JD016482.

Jacobsen, S.B., Wasserburg, G.J., 1980. Sm-Nd isotopic evolution of chondrites. Earth and Planetary Science Letters 50, 139–155.

Jebari, S., Berndtsson, R., Lebdi, F., Bahri, A., 2012. Historical aspects of soil erosion in the Mejerda catchment, Tunisia. Hydrological Sciences Journal 57, 901–912.

Jilbert, T., Reichart, G.J., Aeschlimann, B., Gunther, D., Boer, W., de Lange, G.J., 2010. Climate-controlled multidecadal variability in North African dust transport to the Mediterranean. Geology 38, 19–22.

Jiménez-Espejo, F.J., Pardosgene, M., Martinezruiz, F., Garciaalix, A., van de Flierdt, T., Toyofuku, T., Bahr, A., Kreissig, K., 2015. Geochemical evidence for intermediate water circulation in the westernmost Mediterranean over the last 20 kyr BP and its impact on the Mediterranean Outflow. Global and Planetary Change 135, 38–46.

Jolly, D., Harrison, S.P., Damnati, B., Bonnefille, R., 1998. Simulated climate and biomes of Africa during the late quaternary: Comparison with pollen and lake status data. Quaternary Science Reviews 17, 629–657.

Jorissen, F.J., 1999. Benthic foraminiferal successions across Late Quaternary Mediterranean sapropels. Marine Geology 153, 91–101.

Kallel, N., Paterne, M., Duplessy, J.C., VergnaudGrazzini, C., Pujol, C., Labeyrie, L., Arnold, M., Fontugne, M., Pierre, C., 1997. Enhanced rainfall in the Mediterranean region during the last sapropel event. Oceanologica Acta 20, 697–712.

Kallel, N., Duplessy, J.C., Labeyrie, L., Fontugne, M., Paterne, M., Montacer, M., 2000. Mediterranean pluvial periods and sapropel formation over the last 200 000 years. Palaeogeography Palaeoclimatology Palaeoecology 157, 45–58.

Karageorgis, A., Anagnostou, C., Sioulas, A., Chronis, G., Papathanassiou, E., 1998. Sediment geochemistry and mineralogy in Milos bay, SW Kyklades, Aegean Sea, Greece. Journal of Marine Systems 16, 269–281.

Klaver, M., Djuly, T., de Graaf, S., Sakes, A., Wijbrans, J., Davies, G., Vroon, P., 2015. Temporal and spatial variations in provenance of Eastern Mediterranean Sea sediments: Implications for Aegean and Aeolian arc volcanism. Geochimica et Cosmochimica Acta 153, 149–168.

Klump, J., Hebbeln, D., Wefer, G., 2000. The impact of sediment provenance on barium-based productivity estimates. Marine Geology 169, 259–271.

Kotthoff, U., Pross, J., Muller, U.C., Peyron, O., Schmiedl, G., Schulz, H., Bordon, A., 2008. Climate dynamics in the borderlands of the Aegean Sea during formation of sapropel S1 deduced from a marine pollen record. Quaternary Science Reviews 27, 832–845.

Kraal, P., Slomp, C.P., de Lange, G.J., 2010. Sedimentary organic carbon to phosphorus ratios as a redox proxy in Quaternary records from the Mediterranean. Chemical Geology 277, 167–177.

Krastel, S., Hanebuth, T.J.J., Antobreh, A.A., Henrich, R., Holz, C., Kölling, M., Schulz, H.D., Wien, K., Wynn, R.B., 2004. Cap Timiris Canyon: a newly discovered channel-system off Mauritania. EOS Transactions–American Geophysical Union 85, 417–432.

Krom, M.D., Cliff, R.A., Eijsink, L.M., Herut, B., Chester, R., 1999a. The characterisation of Saharan dusts and Nile particulate matter in surface sediments from the Levantine basin using Sr isotopes. Marine Geology 155, 319–330.

Krom, M.D., Michard, A., Cliff, R.A., Strohle, K., 1999b. Sources of sediment to the Ionian Sea and western Levantine basin of the Eastern Mediterranean during S-1 sapropel times. Marine Geology 160, 45–61.

Krom, M.D., Stanley, J.D., Cliff, R.A., Woodward, J.C., 2002. Nile River sediment fluctuations over the past 7000 yr and their key role in sapropel development. Geology 30, 71–74.

Kuhnt, T., Schmiedl, G., Ehrmann, W., Hamann, Y., Andersen, N., 2008. Stable isotopic composition of Holocene benthic foraminifers from the Eastern Mediterranean Sea: Past changes in productivity and deep water oxygenation. Palaeogeography Palaeoclimatology Palaeoecology 268, 106–115.

Kukla, G., McManus, J.F., Rousseau, D.D., Chuine, I., 1997. How long and how stable was the last interglacial?. Quaternary Science Reviews 16, 605–612.

Kuper, R., Kropelin, S., 2006. Climate-controlled Holocene occupation in the Sahara: Motor of Africa's evolution. Science 313, 803–807.

Kurtz, J., 1983. Geochemistry of Early Mesozoic basalts from Tunisia. Journal of African Earth Sciences 1, 113–125.

Kutzbach, J.E., 1981. Monsoon Climate of the Early Holocene - Climate Experiment with the Earths Orbital Parameters for 9000 Years Ago. Science 214, 59–61.

Larrasoaña, J.C., Roberts, A.P., Rohling, E.J., Winklhofer, M., Wehausen, R., 2003. Three million years of monsoon variability over the northern Sahara. Climate Dynamics 21, 689–698.

Larrasoaña, J.C., Roberts, A.P., Rohling, E.J., 2013. Dynamics of green Sahara periods and their role in hominin evolution. Plos One 8, e76514. doi:10.1371/journal.pone.0076514.

Lacan, F., Jeandel, C., 2005. Neodymium isotopes as a new tool for quantifying exchange fluxes at the continent-ocean interface. Earth and Planetary Science Letters 232, 245–257.

Laskar, J., Robutel, P., Joutel, F., Gastineau, M., Correia, A.C.M., Levrard, B., 2004. A long-term numerical solution for the insolation quantities of the Earth. Astronomy and Astrophysics 428, 261–285.

Lézine, A.M., Hely, C., Grenier, C., Braconnot, P., Krinner, G., 2011. Sahara and Sahel vulnerability to climate changes, lessons from Holocene hydrological data. Quaternary Science Reviews 30, 3001–3012.

Liu, Q.S., Larrasoana, J.C., Torrent, J., Roberts, A.P., Rohling, E.J., Liu, Z.F., Jiang, Z.X., 2012. New constraints on climate forcing and variability in the circum-Mediterranean region from magnetic and geochemical observations of sapropels S1, S5 and S6. Palaeogeography Palaeoclimatology Palaeoecology 333, 1–12.

Liu, Z.F., Colin, C., Trentesaux, A., Blamart, D., Bassinot, F., Siani, G., Sicre, M.A., 2004. Erosional history of the eastern Tibetan Plateau since 190 kyr ago: clay mineralogical and geochemical investigations from the southwestern South China Sea. Marine Geology 209, 1–18.

Lolis, C.J., Bartzokas, A., Katsoulis, B.D., 2002. Spatial and temporal 850 hPA air temperature and sea-surface temperature covariances in the Mediterranean region and their connection to atmospheric circulation. International Journal of Climatology 22, 663–676.

Lourens, L.J., Antonarakou, A., Hilgen, F.J., Van Hoof, A.A.M., Vergnaud-Grazzini, C., Zachariasse, W.J., 1996. Evaluation of the Plio-Pleistocene astronomical timescale. Paleoceanography 11, 391–413.

Lourens, L.J., Wehausen, R., Brumsack, H.J., 2001. Geological constraints on tidal dissipation and dynamical ellipticity of the Earth over the past three million years. Nature 409, 1029–1033.

Lourens, L.J., 2004. Revised tuning of Ocean Drilling Program Site 964 and KC01B (Mediterranean) and implications for the delta O-18, tephra, calcareous nannofossil, and geomagnetic reversal chronologies of the past 1.1 Myr. Paleoceanography 19, PA3010. Doi:10.1029/2003PA000997.

Lyle, M., Heath, G.R., Robbins, J.M., 1984. Transport and release of transition-elements during early diagenesis - sequential leaching of sediments from Manop Site-M and Site-H .1. pH 5 acetic-acid leach. Geochimica et Cosmochimica Acta 48, 1705–1715.

Magny, M., Vanniere, B., Calo, C., Millet, L., Leroux, A., Peyron, O., Zanchetta, G., La Mantia, T., Tinner, W., 2011. Holocene hydrological changes in south-western Mediterranean as recorded by lake-level fluctuations at Lago Preola, a coastal lake in southern Sicily, Italy. Quaternary Science Reviews 30, 2459–2475.

Magny, M., Combourieu-Nebout, N., de Beaulieu, J.L., Bout-Roumazeilles, V., Colombaroli, D., Desprat, S., Francke, A., Joannin, S., Ortu, E., Peyron, O., Revel, M., Sadori, L., Siani, G., Sicre, M.A., Samartin, S., Simonneau, A., Tinner, W., Vanniere, B., Wagner, B., Zanchetta, G., Anselmetti, F., Brugiapaglia, E., Chapron, E., Debret, M., Desmet, M., Didier, J., Essallami, L., Galop, D., Gilli, A., Haas, J.N., Kallel, N., Millet, L., Stock, A., Turon, J.L., Wirth, S., 2013. North-south palaeohydrological contrasts in the central Mediterranean during the Holocene: tentative synthesis and working hypotheses. Climate of the Past 9, 2043–2071.

Mandel, R.D., Simmons, A.H., 2001. Prehistoric occupation of late quaternary landscapes near Kharga Oasis, Western Desert of Egypt. Geoarchaeology: An International Journal 16, 95–117.

Manning, K., Timpson, A., 2014. The demographic response to Holocene climate change in the Sahara. Quaternary Science Reviews 101, 28–35.

Marino, G., Rohling, E.J., Rijpstra, W.I.C., Sangiorgi, F., Schouten, S., Damste, J.S.S., 2007. Aegean Sea as driver of hydrographic and ecological changes in the eastern Mediterranean. Geology 35, 675–678.

Martin, E.E., Haley, B.A., 2000. Fossil fish teeth as proxies for seawater Sr and Nd isotopes. Geochimica et Cosmochimica Acta 64, 835–847.

Martin, E.E., Scher, H.D., 2004. Preservation of seawater Sr and Nd isotopes in fossil fish teeth: bad news and good news. Earth and Planetary Science Letters 220, 25–39.

Martin, E.E., Blair, S.W., Kamenov, G.D., Scher, H.D., Bourbon, E., Basak, C., Newkirk, D.N., 2010. Extraction of Nd isotopes from bulk deep sea sediments for paleoceanographic studies on Cenozoic time scales. Chemical Geology 269, 414–431.

Martinez-Ruiz, F., Kastner, M., Gallego-Torres, D., Rodrigo-Gamiz, M., Nieto-Moreno, V., Ortega-Huertas, M., 2015. Paleoclimate and paleoceanography over the past 20,000 yr in the Mediterranean Sea Basins as indicated by sediment elemental proxies. Quaternary Science Reviews 107, 25–46.

McGee, D., deMenocal, P.B., Winckler, G., Stuut, J.B.W., Bradtmiller, L.I., 2013. The magnitude, timing and abruptness of changes in North African dust deposition over the last 20,000 yr. Earth and Planetary Science Letters 371, 163–176.

Mercone, D., Thomson, J., Croudace, I.W., Siani, G., Paterne, M., Troelstra, S., 2000. Duration of S1, the most recent sapropel in the eastern Mediterranean Sea, as indicated by accelerator mass spectrometry radiocarbon and geochemical evidence. Paleoceanography 15, 336–347.

Meyer, I., Davies, G.R., Stuut, J.B.W., 2011. Grain size control on Sr-Nd isotope provenance studies and impact on paleoclimate reconstructions: An example from deep-sea sediments offshore NW Africa. Geochemistry Geophysics Geosystems 12, Q03005. Doi:10.1029/2010GC003355.

Miller, K.G., Fairbanks, R.G., Mountain, G.S., 1987. Tertiary oxygen isotope synthesis, sea level history, and continental margin erosion. Paleoceanography 2, 1–19.

Milner, A.M., Collier, R.E.L., Roucoux, K.H., Muller, U.C., Pross, J., Kalaitzidis, S., Christanis, K., Tzedakis, P.C., 2012. Enhanced seasonality of precipitation in the Mediterranean during the early part of the Last Interglacial. Geology 40, 919–922.

Moreno, T., Querol, X., Castillo, S., Alastuey, A., Cuevas, E., Herrmann, L., Mounkaila, M., Elvira, J., Gibbons, W., 2006. Geochemical variations in aeolian mineral particles from the Sahara-Sahel Dust Corridor. Chemosphere 65, 261–270.

Myers, P.G., Haines, K., Rohling, E.J., 1998. Modeling the paleocirculation of the Mediterranean: The last glacial maximum and the Holocene with emphasis on the formation of sapropel S-1. Paleoceanography 13, 586–606.

Myers, P.G., 2002. Flux-forced simulations of the paleocirculation of the Mediterranean. Paleoceanography 17, 1009. Doi:10.1029/2000PA000613.

Niedermeyer, E. M., Schefuß, E., Sessions, A.L., Mulitza, S., Mollenhauer, G., Schulz, M., Wefer, G., 2010. Orbital- and millennial-scale changes in the hydrologic cycle and vegetation in the western African Sahel: Insights from individual plant wax δD and δ13C. Quaternary Science Reviews 29, 2996–3005.

Nijenhuis, I.A., de Lange, G.J., 2000. Geochemical constraints on Pliocene sapropel formation in the eastern Mediterranean. Marine Geology 163, 41–63.

Osborne, A.H., Vance, D., Rohling, E.J., Barton, N., Rogerson, M., Fello, N., 2008. A humid corridor across the Sahara for the migration of early modern humans out of Africa 120,000 years ago. Proceedings of the National Academy of Sciences of the United States of America 105, 16444–16447.

Osborne, A.H., Marino, G., Vance, D., Rohling, E.J., 2010. Eastern Mediterranean surface water Nd during Eemian sapropel S5: monitoring northerly (mid-latitude) versus southerly (sub-tropical) freshwater contributions. Quaternary Science Reviews 29, 2473–2483.

Padoan, M., Garzanti, E., Harlavan, Y., Villa, I.M., 2011. Tracing Nile sediment sources by Sr and Nd isotope signatures (Uganda, Ethiopia, Sudan). Geochimica et Cosmochimica Acta 75, 3627–3644.

Pahnke, K., Goldstein, S.L., Hemming, S.R., 2008. Abrupt changes in Antarctic Intermediate Water circulation over the past 25,000 years. Nature geoscience, 1: 870-874.

Paillou, P., Schuster, M., Tooth, S., Farr, T., Rosenqvist, A., Lopez, S., Malezieux, J.M., 2009. Mapping of a major paleodrainage system in eastern Libya using orbital imaging radar: The Kufrah River. Earth and Planetary Science Letters 277, 327–333.

Paillou, P., Tooth, S., Lopez, S., 2012. The Kufrah paleodrainage system in Libya: A past connection to the Mediterranean Sea?. Comptes Rendus Geoscience 344, 406–414.

Palchan, D., Stein, M., Almogi-Labin, A., Erel, Y., Goldstein, S.L., 2013. Dust transport and synoptic conditions over the Sahara-Arabia deserts during the MIS6/5 and 2/1 transitions from grain-size, chemical and isotopic properties of Red Sea cores. Earth and Planetary Science Letters 382, 125–139.

Passier, H.F., Dekkers, M.J., de Lange, G.J., 1998. Sediment chemistry and magnetic properties in an anomalously reducing core from the eastern Mediterranean Sea. Chemical Geology 152, 287–306.

Paytan, A., Kastner, M., Martin, E.E., Macdougall, J.D., Herbert, T., 1993. Marine barite as a monitor of seawater strontium isotope composition. Nature 366, 445–449.

Paytan, A., Kastner, M., 1996. Benthic Ba fluxes in the central Equatorial Pacific, implications for the oceanic Ba cycle. Earth and Planetary Science Letters 142, 439–450.

Paytan, A., Kastner, M., Chavez, F.P., 1996. Glacial to interglacial fluctuations in productivity in the equatorial Pacific as indicated by marine barite. Science 274, 1355–1357.

Paytan, A., Mearon, S., Cobb, K.M., Kastner, M., 2002. Origin of marine barite deposits: Sr and S isotope characterization. Geology 30, 747–750.

Paytan, A., Griffith, E.M., 2007. Marine barite: Recorder of variations in ocean export productivity. Deep-Sea Research Part II – Topical Studies in Oceanography 54, 687–705.

Petschick, R., Kuhn, G., Gingele, F., 1996. Clay mineral distribution in surface sediments of the South Atlantic: Sources, transport, and relation to oceanography. Marine Geology 130, 203–229.

Petschick, R., 2000. MacDiff 4.2.2.

Peyron, O., Goring, S., Dormoy, I., Kotthoff, U., Pross, J., de Beaulieu, J.L., Drescher-Schneider, R., Vanniere, B., Magny, M., 2011. Holocene seasonality changes in the central Mediterranean region reconstructed from the pollen sequences of Lake Accesa (Italy) and Tenaghi Philippon (Greece). Holocene 21, 131–146.

Peyron, O., Magny, M., Goring, S., Joannin, S., de Beaulieu, J.L., Brugiapaglia, E., Sadori, L., Garfi, G., Kouli, K., Ioakim, C., Combourieu-Nebout, N., 2013. Contrasting patterns of climatic changes during the Holocene across the Italian Peninsula reconstructed from pollen data. Climate of the Past 9, 1233–1252.

Pinardi, N., Masetti, E., 2000. Variability of the large scale general circulation of the Mediterranean Sea from observations and modelling: a review. Palaeogeography Palaeoclimatology Palaeoecology 158, 153–174.

Pinardi, N., Zavatarelli, M., Adani, M., Coppini, G., Fratianni, C., Oddo, P., Simoncelli, S., Tonani, M., Lyubartsev, V., Dobricic, S., Bonaduce, A., 2015. Mediterranean Sea large-scale low-frequency ocean variability and water mass formation rates from 1987 to 2007: A retrospective analysis. Progress in Oceanography 132, 318–332.

Piotrowski, A.M., Goldstein, S.L., Hemming, S.R., Fairbanks, R.G., 2005. Temporal relationships of carbon cycling and ocean circulation at glacial boundaries. Science 307, 1933–1938.

Piotrowski, A.M., Galy, A., Nicholl, J.A.L., Roberts, N., Wilson, D.J., Clegg, J.A., Yu, J., 2012. Reconstructing deglacial North and South Atlantic deep water sourcing using foraminiferal Nd isotopes. Earth and Planetary Science Letters 357, 289–297.

Prins, M., Postma, G., Weltje, G.J., 2000. Controls on terrigenous sediment supply to the Arabian Sea during the late Quaternary: the Makran continental slope. Marine Geology 169, 351–371.

Ratmeyer, V., Fischer, G., Wefer, G., 1999. Lithogenic particle fluxes and grain size distributions in the deep ocean off northwest Africa: Implications for seasonal changes of aeolian dust input and downward transport. Deep-Sea Research Part I-Oceanographic Research Papers 46, 1289–1337.

Raymo, M.E., Ruddiman, W.F., Froelich, P.N., 1988. Influence of Late Cenozoic mountain building on ocean geochemical cycles. Geology 16, 649–653.

Reimer, P.J., Bard, E., Bayliss, A., Beck, J.W., Blackwell, P.G., Ramsey, C.B., Buck, C.E., Cheng, H., Edwards, R.L., Friedrich, M., Grootes, P.M., Guilderson, T.P., Haflidason, H., Hajdas, I., Hatte, C.,

Heaton, T.J., Hoffmann, D.L., Hogg, A.G., Hughen, K.A., Kaiser, K.F., Kromer, B., Manning, S.W., Niu, M., Reimer, R.W., Richards, D.A., Scott, E.M., Southon, J.R., Staff, R.A., Turney, C.S.M., van der Plicht, J., 2013. Intcal13 and Marine13 radiocarbon age calibration curves, 0–50,000 years cal BP. Radiocarbon 55, 1869–1887.

Reitz, A., de Lange, G.J., 2006. Abundant Sr-rich aragonite in eastern Mediterranean sapropel S1: Diagenetic vs. detrital/biogenic origin. Palaeogeography Palaeoclimatology Palaeoecology 235, 135–148.

Reitz, A., Thomson, J., de Lange, G.J., Hensen, C., 2006. Source and development of large manganese enrichments above eastern Mediterranean sapropel S1. Paleoceanography 21, PA3007. Doi:10.1029/2005PA001169.

Rempfer, J., Stocker, T.F., Joos, F., Dutay, J.-C. Siddall, M., 2011. Modelling Nd-isotopes with a coarse resolution ocean circulation model: sensitivities to model parameters and source/sink distributions. Geochimica et Cosmochimica Acta 75, 5927–5950.

Revel, M., Ducassou, E., Grousset, F.E., Bernasconi, S.M., Migeon, S., Revillon, S., Mascle, J., Murat, A., Zaragosi, S., Bosch, D., 2010. 100,000 Years of African monsoon variability recorded in sediments of the Nile margin. Quaternary Science Reviews 29, 1342–1362.

Revel, M., Colin, C., Bernasconi, S., Combourieu-Nebout, N., Ducassou, E., Grousset, F.E., Rolland, Y., Migeon, S., Bosch, D., Brunet, P., Zhao, Y.L., Mascle, J., 2014. 21,000 Years of Ethiopian African monsoon variability recorded in sediments of the western Nile deep-sea fan. Regional Environmental Change 14, 1685–1696.

Revel, M., Ducassou, E., Skonieczny, C., Colin, C., Bastian, L., Bosch, D., Migeon, S., Mascle, J., 2015. 20,000 years of Nile River dynamics and environmental changes in the Nile catchment area as inferred from Nile upper continental slope sediments. Quaternary Science Reviews 130, 200–221.

Révillon, S., Jouet, G., Bayon, G., Rabineau, M., Dennielou, B., Hemond, C., Berne, S., 2011. The provenance of sediments in the Gulf of Lions, western Mediterranean Sea. Geochemistry Geophysics Geosystems 12, Q08006. Doi:10.1029/2011GC003523.

Roberts, N.L., Piotrowski, A.M., McManus, J.F., Keigwin, L.D., 2010. Synchronous deglacial overturning and water mass source changes. Science 327, 75–78.

Roberts, N.L., Piotrowski, A.M., Elderfield, H., Eglinton, T.I., Lomas, M.W., 2012. Rare earth element association with foraminifera. Geochimica et Cosmochimica Acta 94, 57–71.

Rodrigo-Gámiz, M., Martinez-Ruiz, F., Chiaradia, M., Jimenez-Espejo, F.J., Ariztegui, D., 2015. Radiogenic isotopes for deciphering terrigenous input provenance in the western Mediterranean. Chemical Geology 410, 237–250.

Roether, W., Manca, B.B., Klein, B., Bregant, D., Georgopoulos, D., Beitzel, V., Kovacevic, V., Luchetta, A., 1996. Recent changes in eastern Mediterranean deep waters. Science 271, 333–335.

Rohling, E.J., Hilgen, F.J., 1991. The eastern Mediterranean climate at times of sapropel formation: a review. Geologie En Mijnbouw 70, 253–264.

Rohling, E.J., 1994. Review and new aspects concerning the formation of Eastern Mediterranean sapropels. Marine Geology 122, 1–28.

Rohling, E.J., 1999. Environmental control on Mediterranean salinity and δ18O. Paleoceanography 14, 706–715.

Rohling, E.J., De Rijk, S., 1999. Holocene climate optimum and last glacial maximum in the Mediterranean: the marine oxygen isotope record. Marine Geology 161, 385–387.

Rohling, E.J., Cane, T.R., Cooke, S., Sprovieri, M., Bouloubassi, I., Emeis, K.C., Schiebel, R., Kroon, D., Jorissen, F.J., Lorre, A., Kemp, A.E.S., 2002. African monsoon variability during the previous interglacial maximum. Earth and Planetary Science Letters 202, 61–75.

Rohling, E.J., Sprovieri, M., Cane, T., Casford, J.S.L., Cooke, S., Bouloubassi, I., Emeis, K.C., Schiebel, R., Rogerson, M., Hayes, A., Jorissen, F.J., Kroon, D., 2004. Reconstructing past planktic foraminiferal habitats using stable isotope data: a case history for Mediterranean sapropel S5. Marine Micropaleontology 50, 89–123.

Rohling, E.J., Pälike, H., 2005. Centennial-scale climate cooling with a sudden cold event around 8,200 years ago. Nature 434, 975–979.

Rohling, E.J., Marino, G., Grant, K.M., 2015. Mediterranean climate and oceanography, and the periodic development of anoxic events (sapropels). Earth-Science Reviews 143, 62–97.

Rolison, J.M., Middag, R., Stirling, C.H., Rijkenberg, M.J.A., de Baar, H.J.W., 2015. Zonal distribution of dissolved aluminium in the Mediterranean Sea. Marine Chemistry 177, 87–100.

Rossignol-Strick, M., Nesteroff, W., Olive, P., Vergnaud-Grazzini, C., 1982. After the deluge: Mediterranean stagnation and sapropel formation. Nature 295, 105–110.

Rossignol-Strick, M., 1983. African monsoons, an immediate climate response to orbital insolation. Nature 304, 46–49.

Rossignol-Strick, M., 1987. Rainy periods and bottom water stagnation initiating brine accumulation and metal concentrations: 1. the Late Quaternary. Paleoceanography 2, 333–360.

Rutten, A., de Lange, G.J., Ziveri, P., Thomson, J., van Santvoort, P.J.M., Colley, S., Corselli, C., 2000. Recent terrestrial and carbonate fluxes in the pelagic eastern Mediterranean: a comparison between sediment trap and surface sediment. Palaeogeography Palaeoclimatology Palaeoecology 158, 197–213.

Rutten, A., de Lange, G.J., 2002. A novel selective extraction of barite, and its application to eastern Mediterranean sediments. Earth and Planetary Science Letters 198, 11–24.

Sarnthein, M., Tetzlaff, G., Koopmann, B., Wolter, K., Pflaumann, U., 1981. Glacial and interglacial wind regimes over the eastern subtropical Atlantic and North-West Africa. Nature 293, 193–196.

Sangiorgi, F., Dinelli, E., Maffioli, P., Capotondi, L., Giunta, S., Morigi, C., Principato, M.S., Negri, A., Emeis, K.C., Corselli, C., 2006. Geochemical and micropaleontological characterisation of a Mediterranean sapropel S5: A case study from core BAN89GCO9 (south of Crete). Palaeogeography Palaeoclimatology Palaeoecology 235, 192–207.

Schefuß, E., Schouten, S., Schneider, R.R., 2005. Climatic controls on central African hydrology during the past 20,000 years. Nature 437, 1003–1006.

Schenau, S.J., De Lange, G.J., 2000. A novel chemical method to quantify fish debris in marine sediments. Limnology and Oceanography 45, 963–971.

Schenau, S.J., Prins, M.A., De Lange, G.J., Monnin, C., 2001. Barium accumulation in the Arabian Sea: Controls on barite preservation in marine sediments. Geochimica et Cosmochimica Acta 65, 1545–1556.

Schenau, S.J., Reichart, G.J., De Lange, G.J., 2005. Phosphorus burial as a function of paleoproductivity and redox conditions in Arabian Sea sediments. Geochimica et Cosmochimica Acta 69, 919–931.

Scheuvens, D., Schutz, L., Kandler, K., Ebert, M., Weinbruch, S., 2013. Bulk composition of northern African dust and its source sediments–A compilation. Earth-Science Reviews 116, 170–194.

Schijf, J., De Baar, H.J.W., Wilbrans, J., Landing, W.M., 1991. Dissolved rare earth elements in the Black Sea. Deep-Sea Research Part-II 38, 805–823.

Schijf, J., De Baar, H.J.W., Millero, F.J., 1995. Vertical distributions and speciation of dissolved rare earth elements in the anoxic brines of Bannock Basin, eastern Mediterranean Sea. Geochimica et Cosmochimica Acta 59, 3285–3299.

Schmiedl, G., Mitschele, A., Beck, S., Emeis, K.C., Hemleben, C., Schulz, H., Sperling, M., Weldeab, S., 2003. Benthic foraminiferal record of ecosystem variability in the eastern Mediterranean Sea during times of sapropel S-5 and S-6 deposition. Palaeogeography Palaeoclimatology Palaeoecology 190, 139–164.

Schroeder, A., Wiesner, M.G., Liu, Z.F., 2015. Fluxes of clay minerals in the South China Sea. Earth and Planetary Science Letters 430, 30–42.

Scrivner, A.E., Vance, D., Rohling, E.J., 2004. New neodymium isotope data quantify Nile involvement in Mediterranean anoxic episodes. Geology 32, 565–568.

Shanahan, T.M., McKay, N.P., Hughen, K.A., Overpeck, J.T., Otto-Bliesner, B., Heil, C.W., King, J., Scholz, C.A., Peck, J., 2015. The time-transgressive termination of the African Humid Period. Nature Geoscience 8, 140–144.

Siani, G., Paterne, M., Arnold, M., Bard, E., Metivier, B., Tisnerat, N., Bassinot, F., 2000. Radiocarbon reservoir ages in the Mediterranean Sea and Black Sea. Radiocarbon 42, 271–280.

Siani, G., Paterne, M., Michel, E., Sulpizio, R., Sbrana, A., Arnold, M., Haddad, G., 2001. Mediterranean Sea surface radiocarbon reservoir age changes since the last glacial maximum. Science 294, 1917–1920.

Siddall, M., Khatiwala, S., van de Flierdt, T., Jones, K., Goldstein, S.L., Hemming, S., Anderson, R.F., 2008. Towards explaining the Nd paradox using reversible scavenging in an ocean general circulation model. Earth and Planetary Science Letters 274, 448–461.

Sirocko, F., Sarnthein, M., Lange, H., Erlenkeuser, H., 1991. Atmospheric Summer Circulation and Coastal Upwelling in the Arabian Sea during the Holocene and the Last Glaciation. Quaternary Research 36, 72–93.

Skinner, C.B., Poulsen, C.J., 2016. The role of fall season tropical plumes in enhancing Saharan rainfall during the African Humid Period. Geophysical Research Letters 43, 349–358.

Skonieczny, C., Bory, A., Bout-Roumazeilles, V., Abouchami, W., Galer, S.J.G., Crosta, X., Diallo, A., Ndiaye, T., 2013. A three-year time series of mineral dust deposits on the West African margin: Sedimentological and geochemical signatures and implications for interpretation of marine paleo-dust records. Earth and Planetary Science Letters 364, 145–156.

Skonieczny, C., Paillou, P., Bory, A., Bayon, G., Biscara, L., Crosta, X., Eynaud, F., Malaize, B., Revel, M., Aleman, N., Barusseau, J.P., Vernet, R., Lopez, S., Grousset, F., 2015. African humid periods triggered the reactivation of a large river system in Western Sahara. Nature Communications 6, 8751. doi: 10.1038/ncomms9751.

Slomp, C.P., Thomson, J., de Lange, G.J., 2002. Enhanced regeneration of phosphorus during formation of the most recent eastern Mediterranean sapropel (S1). Geochimica et Cosmochimica Acta 66, 1171–1184.

Slomp, C.P., Thomson, J., de Lange, G.J., 2004. Controls on phosphorus regeneration and burial during formation of eastern Mediterranean sapropels. Marine Geology 203, 141–159.

Sperling, M., Schmiedl, G., Hemleben, C., Emeis, K.C., Erlenkeuser, H., Grootes, P.M., 2003. Black Sea impact on the formation of eastern Mediterranean sapropel S1? Evidence from the Marmara Sea. Palaeogeography Palaeoclimatology Palaeoecology 190, 9–21.

Spivack, A.J., Wasserburg, G., 1988. Neodymium isotopic composition of the Mediterranean outflow and the eastern North Atlantic. Geochimica et Cosmochimica Acta 52, 2767–2773.

Spötl, C., Nicolussi, K., Patzelt, G., Boch, R., Team, D., 2010. Humid climate during deposition of sapropel 1 in the Mediterranean Sea: Assessing the influence on the Alps. Global and Planetary Change 71, 242–248.

Stein, M., Almogi-Labin, A., Goldstein, S.L., Hemleben, C., Starinsky, A., 2007. Late Quaternary changes in desert dust inputs to the Red Sea and Gulf of Aden from Sr-87/Sr-86 ratios in deep-sea cores. Earth and Planetary Science Letters 261, 104–119.

Stratford, K., Williams, R.G., Myers, P.G., 2000. Impact of the circulation on sapropel formation in the eastern Mediterranean. Global Biogeochemical Cycles 14, 683–695.

Stuiver, M., Reimer, P.J., 1993. Extended 14C data-base and revised Calib 3.0 14C age calibration program. Radiocarbon 35, 215–230.

Stuiver, M., Reimer,P.J., Reimer,R., 2005. Calib5.0.

Stumpf, R., Frank, M., Schonfeld, J., Haley, B.A., 2011. Climatically driven changes in sediment supply on the SW Iberian shelf since the Last Glacial Maximum. Earth and Planetary Science Letters 312, 80–90.

Stuut, J.-B.W., Prins, M.A., Schneider, R.R., Weltje, G.J., Jansen, J.H.F., Postma, G., 2002. A 300-kyr record of aridity and wind strength in southwestern Africa: inferences from grain-size distributions of sediments on Walvis Ridge, SE Atlantic. Marine Geology 180, 221–233.

Stuut, J.-B.W., Zabel, M., Ratmeyer, V., Helmke, P., Schefuß, E., Lavik, G.,Schneider, R.R., 2005. Provenance of present-day eolian dust collected off NW Africa. Journal of Geophysical Research-Atmospheres 110, D04202. Doi:10.1029/2004JD005161.

Stuut, J.B., Smalley, I., O'Hara-Dhand, K., 2009. Aeolian dust in Europe: African sources and European deposits. Quaternary International 198, 234–245.

Tachikawa, K., Roy-Barman, M., Michard, A., Thouron, D., Yeghicheyan, D., Jeandel, C., 2004. Neodymium isotopes in the Mediterranean Sea: Comparison between seawater and sediment signals. Geochimica et Cosmochimica Acta 68, 3095–3106.

Tachikawa, K., Toyofuku, T., Basile-Doelsch, I., Delhaye, T., 2013. Microscale neodymium distribution in sedimentary planktonic foraminiferal tests and associated mineral phases. Geochimica et Cosmochimica Acta 100, 11–23.

Tachikawa, K., Piotrowski, A., Bayon, G., 2014. Neodymium associated with foraminiferal carbonate as a recorder of seawater isotopic signatures. Quaternary Science Reviews 88, 1–13.

Tachikawa, K., Vidal, L., Cornuault, M., Garcia, M., Pothin, A., Sonzogni, C., Bard, E., Menot, G., Revel, M., 2015. Eastern Mediterranean Sea circulation inferred from the conditions of S1 sapropel deposition. Climate of the Past 11, 855–867.

Tachikawa, K., Arsouze, T., Bayon, G., Bory, A., Colin, C., Dutay, J., Frank, N., Giraud, X., Gourlan, A.T., Jeandel, C., Lacan, F., Meynadier, L., Montagna, P., Piotrowski, A.M., Plancherel, Y., Pucéat, E., Roy-Barman, M., Waelbroeck, C., 2017. The large-scale evolution of neodymium isotopic composition in the global modern and Holocene ocean revealed from seawater and archive data. Chemical Geology 457, 131–148.

Tanaka, T., Togashi, S., Kamioka, H., Amakawa, H., Kagami, H., Hamamoto, T., Yuhara, M., Orihashi, Y., Yoneda, S., Shimizu, H., Kunimaru, T., Takahashi, K., Yanagi, T., Nakano, T., Fujimaki, H., Shinjo, R., Asahara, Y., Tanimizu, M., Dragusanu, C., 2000. JNdi-1: a neodymium isotopic reference in consistency with LaJolla neodymium. Chemical Geology 168, 279–281.

Taylor, S.R., McLennan, S.M., 1985. The continental crust: its composition and evolution. Blackwell, Malden, p.312.

Tesi, T., Asioli, A., Minisini, D., Maselli, V., Valle, G.D., Gamberi, F., Langone, L., Cattaneo, A., Montagna, P., Trincardi, F., 2017. Large-scale response of the Eastern Mediterranean thermohaline circulation to African monsoon intensification during sapropel S1 formation. Quaternary Science Reviews 159, 139–154.

Thirlwall, M.F., 1991. Long-term reproducibility of multicollector Sr and Nd isotope analysis. Chemical Geology 94, 85–104.

Thomas, A.J., Guieu, C., Martin, J.M., 1994. Comment on “Rare earth elements in the Mediterranean Sea and mixing in the Mediterranean outflow” by M. J. Greaves, M. Rudnicki, and H. Elderfield. Earth and Planetary Science Letters 121, 655–662.

Thomson, J., Higgs, N.C., Wilson, T.R.S., Croudace, I.W., De Lange, G.J., Van Santvoort, P.J.M., 1995. Redistribution and Geochemical Behavior of Redox-Sensitive Elements around S1, the Most Recent Eastern Mediterranean Sapropel. Geochimica et Cosmochimica Acta 59, 3487–3501.

Thomson, J., Mercone, D., de Lange, G.J., van Santvoort, P.J.M., 1999. Review of recent advances in the interpretation of eastern Mediterranean sapropel S1 from geochemical evidence. Marine Geology 153, 77–89.

Thunell, R.C., Williams, D.F., 1989. Glacial-Holocene salinity changes in the Mediterranean Sea - hydrographic and depositional effects. Nature 338, 493–496.

Tierney, J. E., deMenocal, P. B. 2013. Abrupt shifts in Horn of Africa hydroclimate since the Last Glacial Maximum. Science 342, 843–846.

Timmermann, A., Friedrich, T., 2016. Late Pleistocene climate drivers of early human migration. Nature 538, 92–95.

Tjallingii, R., Claussen, M., Stuut, J.B.W., Fohlmeister, J., Jahn, A., Bickert, T., Lamy, F., Rohl, U., 2008. Coherent high- and low-latitude control of the northwest African hydrological balance. Nature Geoscience 1, 670–675.

Toucanne, S., Mintoo, C.M.A., Fontanier, C., Bassetti, M.A., Jorry, S.J., Jouet, G., 2015. Tracking rainfall in the northern Mediterranean borderlands during sapropel deposition. Quaternary Science Reviews 129, 178–195.

Tribovillard, N.P., Caulet, J.P., VergnaudGrazzini, C., Moureau, N., Tremblay, P., 1996. Lack of organic matter accumulation on the upwelling-influenced Somalia margin in a glacial–interglacial transition. Marine Geology 133, 157–182.

Tuenter, E., Weber, S.L., Hilgen, F.J., Lourens, L.J., 2003. The response of the African summer monsoon to remote and local forcing due to precession and obliquity. Global and Planetary Change 36, 219–235.

Tütken, T., Eisenhauer, A., Wiegand, B., Hansen, B.T., 2002. Glacial-interglacial cycles in Sr and Nd isotopic composition of Arctic marine sediments triggered by the Svalbard/Barents Sea ice sheet. Marine Geology 182, 351–372.

Tzedakis, P.C., Frogley, M.R., Heaton, T.H.E., 2003. Last Interglacial conditions in southern Europe: evidence from Ioannina, northwest Greece. Global and Planetary Change 36, 157–170.

Tzedakis, P.C., 2007. Seven ambiguities in the Mediterranean palaeoenvironmental narrative. Quaternary Science Reviews 26, 2042–2066.

van de Flierdt, T., Robinson, L.F., Adkins, J.F., 2010. Deep-sea coral aragonite as a recorder for the neodymium isotopic composition of seawater. Geochimica et Cosmochimica Acta 74, 6014–6032.

Van der Lubbe, H.J.L., Frank, M., Tjallingii, R., Schneider, R.R., 2016. Neodymium isotope constraints on provenance, dispersal, and climate-driven supply of Zambezi sediments along the Mozambique Margin during the past similar to 45,000 years. Geochemistry Geophysics Geosystems 17, 181–198.

Van der Weijden, C.H., 2002. Pitfalls of normalization of marine geochemical data using a common divisor. Marine Geology 184, 167–187.

Van Dijk, D., Houba, V.J.G., 2000. Homogeneity and stability of materials distributed within the wageningen evaluating programmes for analytical laboratories. Communications in Soil Science and Plant Analysis 31, 1745–1756.

Van Helmond, N., Hennekam, R., Donders, T., Bunnik, F., De Lange, G., Brinkhuis, H., Sangiorgi, F., 2015. Marine productivity leads organic matter preservation in sapropel S1: palynological evidence from a core east of the Nile River outflow. Quaternary Science Reviews 108, 130–138.

Van Santvoort, P.J.M., de Lange, G.J., Thomson, J., Cussen, H., Wilson, T.R.S., Krom, M.D., Ströhle, K., 1996. Active post-depositional oxidation of the most recent sapropel (S1) in sediments of the eastern Mediterranean Sea. Geochimica et Cosmochimica Acta 60, 4007–4024.

Vance, D., Scrivner, A.E., Beney, P., Staubwasser, M., Henderson, G.M., Slowey, N.C., 2004. The use of foraminifera as a record of the past neodymium isotope composition of seawater. Paleoceanography 19, PA2009. Doi:10.1029/2003PA000957.

Venkatarathnam, K., Ryan, W.B.F., 1971. Dispersal patterns of clay minerals in sediments of the eastern Mediterranean Sea. Marine Geology 11, 261–282.

Vörösmarty, C.J., Fekete, B.M., Meybeck, M., Lammers, R.B., 2000. Global system of rivers: Its role in organizing continental land mass and defining land-to-ocean linkages. Global Biogeochemical Cycles 14, 599–621.

Walter, H.J., Hegner, E., Diekmann, B., Kuhn, G., van der Loeff, M.M.R., 2000. Provenance and transport of terrigenous sediment in the South Atlantic Ocean and their relations to glacial and interglacial cycles: Nd and Sr isotopic evidence. Geochimica et Cosmochimica Acta 64, 3813–3827.

Wehausen, R., Brumsack, H.J., 1999. Cyclic variations in the chemical composition of eastern Mediterranean Pliocene sediments: a key for understanding sapropel formation. Marine Geology 153, 161–176.

Wehausen, R., Brumsack, H.J., 2000. Chemical cycles in Pliocene sapropel-bearing and sapropel-barren eastern Mediterranean sediments. Palaeogeography Palaeoclimatology Palaeoecology 158, 325–352.

Weldeab, S., Emeis, K.C., Hemleben, C., Siebel, W., 2002a. Provenance of lithogenic surface sediments and pathways of riverine suspended matter in the Eastern Mediterranean Sea: evidence from $^{143}Nd/^{144}Nd$ and $^{87}Sr/^{86}Sr$ ratios. Chemical Geology 186, 139–149.

Weldeab, S., Emeis, K.C., Hemleben, C., Vennemann, T.W., Schulz, H., 2002b. Sr and Nd isotope composition of Late Pleistocene sapropels and nonsapropelic sediments from the Eastern Mediterranean Sea: Implications for detrital influx and climatic conditions in the source areas. Geochimica et Cosmochimica Acta 66, 3585–3598.

Weldeab, S., Lea, D.W., Schneider, R.R., Andersen, N., 2007. 155,000 years of West African monsoon and ocean thermal evolution. Science 316, 1303–1307.

Weldeab, S., Menke, V., Schmiedl, G., 2014. The pace of East African monsoon evolution during the Holocene. Geophysical Research Letters 41, 1724–1731.

Weltje, G.J., 1997. End-member modeling of compositional data: Numerical-statistical algorithms for solving the explicit mixing problem. Mathematical Geology 29, 503–549.

Williams, M.A.J., Adamson, D., Cock, B., McEvedy, R., 2000. Late Quaternary environments in the White Nile region, Sudan. Global and Planetary Change 26, 305–316.

Wu, J, Liu, Z, Zhou, C., 2012. Late quaternary glacial cycle and precessional period of clay mineral assemblages in the western pacific warm pool. Chinese Science Bulletin 57, 3748–3760.

Wu, J., Liu, Z.F., Zhou, C., 2013. Provenance and supply of Fe-enriched terrigenous sediments in the western equatorial Pacific and their relation to precipitation variations during the late Quaternary. Global and Planetary Change 108, 56–71.

Wu, J., Böning, P., Pahnke, K., Tachikawa, K., De Lange, G.J., 2016. Unraveling North-African riverine and eolian contributions to central Mediterranean sediments during Holocene sapropel S1 formation. Quaternary Science Reviews 152, 31–48.

Wu, J., Liu, Z., Stuut, J.-B.W, Zhao, Y., Schirone, A., de Lange, G.J., 2017. North-African paleodrainage discharges to the central Mediterranean during the last 18,000 years: a multiproxy characterization. Quaternary Science Reviews 163, 95–113.

Wu, Q., Colin, C., Liu, Z.F., Thil, F., Dubois-Dauphin, Q., Frank, N., Tachikawa, K., Bordier, L., Douville, E., 2015. Neodymium isotopic composition in foraminifera and authigenic phases of the South China Sea sediments: Implications for the hydrology of the North Pacific Ocean over the past 25 kyr. Geochemistry Geophysics Geosystems 16, 3883–3904.

Zahar, Y., Ghorbel, A., Albergel, J., 2008. Impacts of large dams on downstream flow conditions of rivers: Aggradation and reduction of the Medjerda channel capacity downstream of the Sidi Salem dam (Tunisia). Journal of Hydrology 351, 318–330.

Zanchetta, G., Drysdale, R.N., Hellstrom, J.C., Fallick, A.E., Isola, I., Gagan, M.K., Pareschi, M.T., 2007. Enhanced rainfall in the Western Mediterranean during deposition of sapropel S1: stalagmite evidence from Corchia cave (Central Italy). Quaternary Science Reviews 26, 279–286.

Zerboni, A., Perego, A., Cremaschi, M., 2015. Geomorphological Map of the Tadrart Acacus Massif and the Erg Uan Kasa (Libyan Central Sahara). Journal of Maps 11, 772–787.

Zhao, Y.L., Colin, C., Liu, Z.F., Paterne, M., Siani, G., Xie, X., 2012. Reconstructing precipitation changes in northeastern Africa during the Quaternary by clay mineralogical and geochemical investigations of Nile deep-sea fan sediments. Quaternary Science Reviews 57, 58–70.

Zhao, Y.L., Colin, C., Liu, Z.F., Bonneau, L., Siani, G., 2016. Climate forcing of terrigenous sediment input to the central Mediterranean Sea since the early Pleistocene. Palaeogeography Palaeoclimatology Palaeoecology 442, 23–35.

Zhornyak, L.V., Zanchetta, G., Drysdale, R.N., Hellstrom, J.C., Isola, I., Regattieri, E., Piccini, L., Baneschi, I., Couchoud, I., 2011. Stratigraphic evidence for a "pluvial phase" between ca 8200–7100 ka from Renella cave (Central Italy). Quaternary Science Reviews 30, 409–417.

Ziegler, M., Tuenter, E., Lourens, L.J., 2010. The precession phase of the boreal summer monsoon as viewed from the eastern Mediterranean (ODP Site 968). Quaternary Science Reviews 29, 1481–1490.

Zielhofer, C., Faust, D., Escudero, R.B., del Olmo, F.D., Kadereit, A., Moldenhauer, K.M., Porras, A., 2004. Centennial-scale late-Pleistocene to mid-Holocene synthetic profile of the Medjerda Valley, northern Tunisia. Holocene 14, 851–861.

Zielhofer, C., Faust, D., Linstadter, J., 2008. Late Pleistocene and Holocene alluvial archives in the Southwestern Mediterranean: Changes in fluvial dynamics and past human response. Quaternary International 181, 39–54.

Zühlsdorff, C., Wien, K., Stuut, J.B.W., Henrich, R., 2007. Late Quaternary sedimentation within a submarine channel-levee system offshore Cap Timiris, Mauritania. Marine Geology 240, 217–234.

Samenvatting in het Nederlands

De Middellandse Zee is vrijwel ingesloten door land en is omringd door rivierbekkens die gekenmerkt worden door verschillende klimaatregimes, liggend tussen de Afrikaanse tropische en de Europese gematigde klimaatszone. Bovendien heeft het Middellandse-Zee gebied een dynamische thermohaline circulatie, waardoor het bijzonder gevoelig is voor veranderingen in de hydrologische cyclus. Deze gevoeligheid komt het beste tot uiting middels de vorming van sapropelen – dit zijn organisch rijke sedimentaire lagen, die in een astronomisch bepaalde cycliciteit gedurende de laatste 13.5 miljoen jaar zijn afgezet in de Middellandse Zee. Sapropelen komen vaker voor in de oostelijke Middellandse Zee (oMZ) en dan nog alleen tijdens precessie-gerelateerde zomer-instralings maxima op het Noordelijk Halfrond. Dit hangt samen met een hoger seizoenscontrast en afwatering. De verhoogde rivier afvoer van water en voedingsstoffen, stimuleren een uitgesproken dichtheidsstratificatie van de waterkolom en / of een verhoogde primaire productiviteit in het oppervlaktewater, wat uiteindelijk leidt tot stilstaand diepwater en sapropelvorming.

Ongeacht het relatieve belang van diepwaterstagnatie ten opzichte van primaire productiviteit in het oppervlakte-water van de oceaan, kan sapropelafzetting dus gezien worden als direct gerelateerd aan rivierwater-afvoer en de hydrografische reactie hierop. Verder is aangetoond dat bij hogere rivierwater afvoer de mate van diepwater-stagnatie toeneemt. Veranderingen in de rivierwaterafvoer zullen dit effect moduleren. Dit komt overeen met de interactie tussen oceanografische circulatie en diepwater-zuurstofverbruik, zoals volgt uit oceaan-biogeochemische modellering.

In dit proefschrift worden deze uitdagingen via drie routes onderzoekt (zie Algemene Introductie en Omschrijving: **hoofdstuk 1**). Allereerst richt ik me op *de zoetwaterbronnen en bijbehorende hydroklimaatveranderingen* om de riviertoevoer in de oMZ te reconstrueren (**hoofdstukken 2-4**). Hierbij wordt gecombineerd gebruik gemaakt van hoofd- en spoorelementen, Sr- en Nd-isotopen, kleimineralogie, korrelgrootte en de mathematische modellering hiervan, enz., welke worden toegepast op het terrigene, ‘detritische’ bestanddeel van mijn monsters (vanaf hier: DCM: detritische, dwz niet-biologische, component in mariene sedimenten). Deze monsters representeren de grootst mogelijk geografische en bathymetrische verspreiding in de oMZ, en bevatten ook monsters van de Holocene sapropel S1 en van de laatste interglaciale sapropel S5. Meer specifiek, mijn studie is gestart met de Sapropel S1 periode,

met name gericht op een goed gedateerde sediment kern in het centrale Middellandse Zeegebied (**hoofdstuk 2**). Vervolgens is dit uitgebreid naar de laatste 18.000 jaar en vergeleken met bestaande Noord-Afrikaanse hydroklimaat-reeksen op een subcontinentale schaal (**hoofdstuk 3**). Daarna wordt deze kennis toegepast op de laatste interglaciale sapropel S5 om de oorsprong en de verdeling van rivier-gerelateerde materialen op een oMZ-schaal te begrijpen (**hoofdstuk 4**).

Tijdens deze studie bleek het nodig om de toepasbaarheid van verschillende DCM proxies te evalueren en te onderzoeken. Met name het bariet-geassocieerde Sr dat achterblijft na ontkalking, kan een probleem zijn voor de DCM Sr-isotoop samenstelling. Dit probleem werd echter tot dusverre over het hoofd gezien in eerdere studies. De bedoeling en opzet van **hoofdstuk 5** is dus om voor herkomststudies met behulp van Sr isotopen en concentratie te evalueren of het belangrijk is rekening te houden met de bariet-geassocieerde Sr.

Naast de studies over DCM en proxies hiervoor, gebruik ik proxies voor de oorspronkelijke zeewater-samenstelling. Dit doe ik met name om de veranderingen in de thermohaline circulatie en waterkolom van de Middellandse Zee tijdens de vorming van een sapropel te onderzoeken. Met het oog op een beter begrip van het complexe samenspel tussen de paleoceanografische en paleoclimatische processen, wordt voor het eerst een oMZ-reconstructie van de zeewater Nd-isotoop samenstelling tijdens sapropel S1-afzetting gegeven (**hoofdstuk 6**).

Om meer specifiek te zijn, worden de hoogtepunten en inhoud van elk hoofdstuk als volgt geschetst:

In **hoofdstuk 2** worden Sr- en Nd-isotoop en element samenstelling van het sediment in hoge resolutie gebruikt om verschillende rivier- en eolische fluxen naar het centrale Middellandse-Zeegebied te bepalen voor de Holocene Sapropel S1 periode. Voor de eerste keer worden robuuste en consistente bewijzen gegeven voor belangrijke DCM bijdrages uit fossiele rivier / wadi systemen van de Libische-Tunesische regio. Deze werden geactiveerd door de intensivering van de Afrikaanse moessonprecipitatie. Deze zoetwaterroutes hadden een grote invloed op nederzettingen van neolithische gemeenschappen en zouden kunnen hebben bijgedragen aan hun migratie uit Afrika. Voorts is de

specifieke bron en verspreiding van rivier-gerelateeerde DCM geëvalueerd door middel van een west-oost transect in de oMZ.

In **hoofdstuk 3** wordt in een multiproxie-studie, met behulp van elementaire geochemie, kleimineralogie, korrelgrootte en zuurstofisotopen van planktonische foraminiferen, de variabiliteit en verspreiding van DCM naar de oMZ bepaald. Bovendien worden hiermee (paleo-) rivier fluxen vanaf de Noord-Afrikaanse regio aangetoond en gekarakteriseerd. Op een subcontinentale schaal vinden we een opvallende gelijkenis tussen verschillende paleodrainagesystemen met rivierwater-afvoer naar de Noord-Afrikaanse en de Atlantische, West-Afrikaanse kust. Dit wijst niet alleen op een gemeenschappelijk hoofdwatergebied in de bergen van de Midden-Sahara, maar ook op een vergelijkbaar klimaatmechanisme. Er blijkt een dominante invloed te zijn van oppervlakte water in de Sahara op de levering van paleodrainage rivierwater naar de Noord-Afrikaanse kust. Dit wordt gemoduleerd door het grondwaterniveau, in reactie op de instralings-gedreven West-Afrikaanse moesson regens.

In **hoofdstuk 4** wordt het bestudeerde toepassingsgebied uitgebreid naar oMZ-schaal en gericht op een andere maar vergelijkbare sapropel, S5, die tijdens het laatste interglaciale maximum is afgezet. Een geochemische inzicht van rivier aanvoer naar de oMZ wordt niet alleen voor de Sapropel S5-periode verstrekt, maar wordt ook vergeleken met die van de Holocene Sapropel S1 en met recente afzettingen. Deze gedetailleerde kennis van hydroklimaatveranderingen en bijbehorende rivier aanvoer naar de oMZ draagt bij tot een beter begrip van de vorming van sapropelen, paleoclimaatvariabiliteit en migratie. Anderzijds wijst deze aanpak op het voordeel en de mogelijkheden van een gecombineerd gebruik van belangrijke elementen, zeldzame aardelementen en Sr- en Nd-isotopen. In het bijzonder zijn de elementaire vingerafdrukken van DCM zeer doelmatig voor oMZ herkomst-studies.

Het mogelijke probleem van resterend bariet-Sr in ontkalkt sediment werd over het hoofd gezien in voorgaande studies waarbij Sr-concentratie en isotopen gebruikt werden om de herkomst van DCM te bepalen. Met behulp van mediterraan sediment als onderzoeksmateriaal, wordt in **hoofdstuk 5** aangetoond, dat er na de traditionele carbonaatverwijdering bariet-Sr achterblijft. Dit is belangrijk voor herkomststudies met behulp van DCM Sr-samenstelling. Een correctie voor deze bijdrage zal nodig zijn voor mariene sedimenten met> 400 ppm barietgehalte. Een dergelijke correctie is nog meer nodig als de ^{87}Sr / ^{86}Sr van DCM >0.713 is en een lage Sr / Al verhouding heeft (<0.0010). Voor

mariene sedimenten met een hoog barietgehalte (>1500 ppm), is na de traditionale ontkalking een extra NH4Cl-extractie stap nodig.

In **hoofdstuk 6** wordt voor het eerst de zeewater Nd isotoopsamenstelling getoond tijdens de Holocene Sapropel S1-afzetting. Als betrouwbare archieven voor het diepwater-εNd-signaal worden visresten en foraminiferen van negen kernen gebruikt. Deze kernen representeren de grootst mogelijke geografische en bathymetrische verspreiding in de oMZ. Verder worden aanvullende εNd-data van twee cores uit de Middellandse Zee gebruikt welke via HCl-extractie verkregen werden. Met deze totale dataset kan oorsprong en menging van watermassa's worden bepaaald en kan de thermohaline circulatie van de Middellandse Zee worden geevalueerd. Mijn resultaten suggereren een diepwater stagnatie in de oMZ voor dieptes groter dan 800 meter, welke gedurende de gehele S1-periode voortduurde. Deze diepwater stagnatie zou al enkele duizenden jaren eerder dan de S1-vorming zelf kunnen hebben aangevangen, terwijl het wel synchroon met het einde van de S1-vorming is beëindigd. Bovendien blijkt er tijdens de S1 een sterke vermindering van de hydrologische uitwisseling tussen de oMZ en de Westelijke Middellandse Zeee (wMZ) via de Straat van Sicilië te zijn geweest. Het lijkt erop dat er in de oMZ tijdens de S1-periode een significante vermindering van de vorming van water op 300-700 m diepte (LIW) en het stopzetten van diepwatervorming plaatsvond. Tegelijkertijd bleef de wMZ-watercirculatie gewoon functioneren. Dit oMZ-wMZ verschil ondersteunt de visie dat diepwater stagnatie een vereiste is voor de vorming van sapropelen.

中文摘要

地中海位于非洲亚热带和欧洲温带之间的交界处，其作为一个半封闭的海盆，周围环绕着以不同气候条件为特征的流域地区。此外，现代地中海具有一个活跃的温盐环流，使其对水文循环的变化特别敏感。这种敏感性尤其表现在呈天文韵律反复出现、富含有机质的腐泥层沉积。腐泥层沉积最早可以追溯到 1350 万年前，更频繁地出现在东地中海，并且只出现在岁差周期的极低值，对应于北半球夏季太阳辐射量的最大值。在这个时期，由于辐射量的季节差异以及河流径流量的增加，经河流输入的大量淡水和营养物质会造成地中海水体结构的密度分层和表层水体中初级生产力的提高，最终导致深层水体逐渐停滞以及腐泥层的形成。

无论停滞的深水条件与勃发的表层生产力的相对重要性如何，腐泥层的形成被认为与淡水输入的驱动及其水文条件的变化直接相关。物理海洋的模拟研究表明，随着淡水输入的增加，深水停滞的程度会增强，而且水源的变化将会调节这种效应。这与通过海洋地球化学模拟得出的洋流循环和水体含氧量之间的平衡是一致的。然而，关于淡水的确切来源以及相关水文气候变化，包括降水/蒸发平衡以及区域对流情况仍然不清楚。并且，在形成腐泥层的过程中，淡水输入的驱动响应于日照辐射量的变化，但古气候和古海洋过程之间的复杂相互作用仍然极具争议。

相应地，这项博士研究通过三条研究路线尝试解决上述问题，参见**第一章**《绪论与提纲》。

首先，我们针对“***淡水的来源以及相关的水文气候变化***”这个问题，主要通过在海洋沉积物的陆源碎屑组分上的研究分析，重建东地中海的河流输入（第二、三、四章）。研究方法包括：主量和微量元素、Sr 和 Nd 同位素、粘土矿物学、以及粒度端元模拟等手段。我们的研究样品在广度和深度上都覆盖了整个东地中海，集中在全新世腐泥层 S1 和上次间冰期腐泥层 S5。依次而言，我们的研究首先针对腐泥层 S1，主要利用一个高分辨率、定年良好的中地中海沉积物钻孔（**第二章**）。然后把时间记录扩展到过去的 18000 年，并且在更大的空间尺度上与非洲的各种水文气候记录进行对比（**第三章**）。之后，我们将这些认识应用于腐泥层 S5，在一个盆地尺度上研究该时期河流物质的来源与分布（**第四章**）。

当进行物源研究时，我们发现有必要“***评估和检查各种陆源碎屑指标的应用***”。其中一个突出的问题是重晶石相关的 Sr 很有可能残留在除钙的沉积物组分中，而这些未完全去除的生源 Sr 会在很大程度上影响陆源碎屑 Sr 的组成。然而，

这个潜在问题在以前的研究中都被忽略了。因此，我们针对这个问题进行了评估和分析（**第五章**）。

除了针对陆源碎屑沉积物的研究外，我们还使用海水自生组分来探索腐泥层形成过程时期地中海的温盐环流和水体结构。迄今首次，我们重建了东地中海海水的 Nd 同位素在腐泥层 S1 时期的情况以及相关变化（**第六章**）。这样一个盆地尺度上的洋流研究可以帮助我们更好地理解“***古海洋与古气候过程之间的复杂相互作用***”。

更具体而言，每章的内容和重点概述如下：

在**第二章**中，我们利用 Sr 和 Nd 同位素以及高分辨率的元素数据来区分并且揭示地中海沉积中不同的河流和风成输入在全新世腐泥层 S1 时期的变化。这些相互一致的证据第一次强有力的证实了，有重要的陆源碎屑物质通过古河道沿着利比亚-突尼斯地区的大陆边缘输入到地中海。在湿润的 S1 时期，分布广阔的北非古河流系统很可能被当时剧烈增加的非洲季风降水疏浚和激活。这些激活的（古）淡水河道对新石器时代文明的位置和分布有非常大的影响，而且很可能为现代人类走出非洲的迁徙创造了条件。此外，我们还通过东西向贯穿东地中海的一系列沉积物钻孔来分析这些河流物质的具体来源和空间分布。

在**第三章**中，通过元素地球化学、粘土矿物学、粒度分布端元模拟、以及浮游有孔虫氧同位素等多指标的综合研究，我们不仅可以约束东地中海陆源碎屑供应的变化，而且还可以揭示和表征沿着北非大陆边缘的（古）河流输入。在一个北非大陆尺度上，我们发现了不同的古河流系统之间的相关性；也就是说，自南向北流向地中海的和自东向西流向大西洋的古河流输入记录具有高度的相似性。这表明两者具有共同的上游汇水源区，即都是发源于撒哈拉中部的山脉，并且受控于相似的气候机制。通过结合其他的水文指标记录，我们认为撒哈拉地区湿润面积的大小（包括湖泊、沼泽、和河流等），对北非的古河流系统的疏通和输入有重要的控制作用，并且受地下水的调节，响应于受日照辐射量控制的西非季风降雨。

在**第四章**中，我们把研究的范围扩大到整个东地中海，而且主要针对另一个重要的腐泥层 S5。 与全新世腐泥层 S1 类似，S5 形成于倒数第二个间冰期的极盛期。在东地中海的盆地尺度上，我们利用多种地球化学的指标重建了腐泥层 S5 时期河流物质的源区和分布，并且与腐泥层 S1 时期和现代的情况作对比。这样全面且具体的认识，不仅能够帮助我们更好地理解腐泥层的形成机制和古气候水文条件变化，而且对早期人类的迁徙和聚集有指示性的意义。另一方面，我们证实了

综合地应用主量元素、稀土元素、以及 Sr 和 Nd 同位素的方法有效性。尤其是对于东地中海的物源研究，陆源碎屑沉积物的元素信息非常实用。

绝大多数使用 Sr 同位素和浓度作为物源指标的研究中，去钙沉积物组分中重晶石残留的 Sr 的影响都被忽略了。利用地中海沉积物作为示范性研究，在**第五章**中，我们证实了在传统去钙沉积物组分中重晶石 Sr 的存在，而且这个因素必须被考虑在相关的物源研究中。研究结果显示，重晶石含量>400 ppm 的海洋沉积物应该进行相关的校正。如果同时还存在陆源碎屑沉积物中的 $^{87}Sr/^{86}Sr$ 值>0.713，以及 Sr/Al 的比值较低（<0.0010）的情况，那么对于陆源碎屑 Sr 的校正是非常必要的。对于具有极高重晶石含量（>1500 ppm）的海洋沉积物，这种特殊情况则必须在传统的去钙处理后，再进行 NH_4Cl 淋滤以去除残留的生源 Sr。

在**第六章**中，我们首次重建了东地中海海水 Nd 同位素值在全新世腐泥层 S1 时期的情况。已有证据表明，鱼骸和有孔虫可靠地记录了底层水体的 Nd 同位素信号；而且我们的样品来自 9 个珍贵的沉积物钻孔，在空间和深度上覆盖了整个东地中海。此外，我们还使用了 2 个地中海钻孔中沉积物 HCl 淋滤液的 Nd 同位素数据。这些数据使得我们能够分析水团的来源和混合情况，并进一步评估地中海的温盐环流。研究结果表明，在约 800 米的深度以下，东地中海的水体是基本停滞的，并且这种状况存在于整个腐泥层 S1 时期。东地中海的水体停滞状况很可能在早于腐泥层 S1 的形成数千年时就开始发育，而与腐泥层 S1 的结束基本同步。另外，我们的结果显示，东地中海和西地中海的水体交换在腐泥层 S1 时期大幅减少。在此期间，东地中海的中层水减少，而深层水则很可能停止形成，但西地中海的环流应该仍然运行如常。这种关于东、西地中海深部环流特征的差异表明，深水停滞很可能是腐泥层形成的先决条件。

Acknowledgements

I would like to thank the Netherlands as a country, where I met my wife and have our son, and will get a PhD. Doing a PhD program is just like on a voyage. You may have to go through a storm, against the rain, the wind, and the dark, but always have hope in your heart as you know that there must be a blue sky at the end of a storm. It is the following people making this voyage possible, achievable, and not alone.

I would like to express my sincerest gratitude to my promotor, Gert de Lange, who offered me the opportunity to undertake the PhD program. To me, this is a life-changing event. From the first day on, you gave me all the necessary freedom and supports to develop my own ideas and research routes. You have always been encouraging me to discuss, to question, and to present. The discussions with you, as well as your thorough and critical reviews on the many versions of the manuscripts, have helped to me to think broader and deeper rather than the “tunnel vision” I would have often had. Thanks for the opportunities, for the introduction to the world of science, and for the delicious food (to Francoise) and the tasting wine in your garden (and office). In particular, I wish to thank Francoise and you for providing the helps regarding our son. In addition, thank you for taking care of my plants.

As for the origin of the PhD program, the China Scholarship Council (CSC) is acknowledged for the financial supports. Specifically, thanks are given to Zhifei Liu, the supervisor of my master study, for the support and recommendation in my application for the CSC–UU scholarship.

I am grateful to the reading committee, Katharina Pahnke, Gert-Jan Reichart, Zhifei Liu, Caroline Slomp, and Jack Middelburg for taking time out of their busy schedules to read my work critically and to oppose me at the public defense, which is my honor.

I own much gratitude to my co-authors, Philipp Böning, Katharina Pahnke, Kazuyo Tachikawa, Zhifei Liu, Jan-Berend Stuut, Yulong Zhao, Antonio Schirone, Amalia Filippidi, Gareth Davies, and Annie Michard. It is due to the fruitful collaborations and your substantial contributions so that I am able to complete this thesis. In addition, I thank my co-workers whose works weren’t included in the thesis but will be written up and published later. Especially, Insinga Donatella and Paola Petrosino are thankful for providing the tephra

analyses, Gert-Jan Reichart for the XRF core scanner analyses, and Haowen Dang for the δ18O chronology of CP11PC, respectively.

Thank you my paranymphs, Amalia Filippidi and Xiaochen Liu. Amalia, you have been helping me not only in the lab but also arranging the various activities for me. For these I am very grateful. As a co-author of Chapter 4, you will definitely be responsible for all the difficult questions at the defense ☺) Xiaochen, I feel lucky to have you in the group. We are on the same wavelength and can easily communicate with each other in a “common language”. You are such a resourceful man and I thank you for the helps from time to time.

I thank everyone in the Geochemistry group for the enjoyable years. I will never forget the Geochemist Poems and the “rubbish gifts” in the Sinterklaas parties. Matthias, Mathilde, and Nikki, thank you for hosting the Sinterklaas parties. Marie-Louise, I still remember the Sinterklaas you acted and your slave Peter ☺. The same thanks also go to Alwina, Alejandra, Anne, Fatimah, Itzel, and Tom for creating the warm and cheerful atmosphere. Also deserving a thank-you are my roommates through the years, Rick, Marie-Louise, Amalia, Marieke, and Matthias; it’s been my pleasure. Jack, thank you for the “nominally” supervision of the last stage of my PhD and the New-Year Borrels. Caroline, it’s my honor to be your teaching-assistant. I thank Gert-Jan for the Paleoceanography MSc course when I was a green PhD student. Shaun, it was nice to have you as the course partner and then being colleagues after years. Nikki, thank you for the good-bye card. Annuska, thank you for the new-born flowers. Niels, thank you for asking me to play football from time to time (and now my left knee is twisted and need a surgery ☺). Thanks are also given to Peter, Pien, José, Thilo, Mariette, Lex, Arthur, Amir, Jie, Shuang, Xiangbin, Anna, Regina, Wytze, Martijn, Linda, Olaf, Lauriane, and everyone else in the group as well as our friends from Spain, Carmina, Nieves, and Luis. I am very grateful.

I thank the staff at the Earth Sciences. Many thanks are given to Dineke van de Meent, Helen de Waard, Arnold van Dijk, Ton Zalm, Coen Mulder, Natasja Welters, Thom Claessen, Dominika Kasjaniuk, Bernadette Marchand, Tilly Bouten, Leonard Bik and etc. for the technical supports. Without your helps I will never be able to finish the PhD. Dineke, thank you for the patient guidance and the helps everywhere in the lab. Helen, Ton, and Coen, thank you for the efforts into the many ICP analyses and the reliable data, I really appreciate that. Arnold, thank you for the introduction of mass spectrometry and sharing me your knowledge of Chinese movies. In addition, I am also grateful to Pien van Minnen,

Annuska Exel, Marjolein Mullen-Pouw, Margot Stoete, Tamara Orhan, Wendy Hoevertsz, and Jan-Willem Blok for the helps with all the administrative challenges.

I paid two visits to the ICBM for Sr and Nd isotope analyses and I want to thank the Marine Isotope Geochemistry group for its great hospitality during my time spent at the University of Oldenburg. I thank Katharina Pahnke for the permissions and arrangements. I thank Philipp Böning for the high-quality isotopic analyses and the helps in finding accommodation. In particular, I am very grateful to Martina Schulz who not only instructed me column extractions but also performed these for me. I went to VU Amsterdam University for isotopic analyses. When I was there, the following people gave me many helps: Gareth Davies arranged the lab and schedule, Richard Smeets who assisted with chromatography, Mathijs van de Ven and Bas van der Wagt for the TIMS and MC-ICP-MS measurements, Xilin Sun is thanked for the dinner as well. Clay minerals analysis was performed by Yanli Li and Yulong Zhao at Tongji University in Shanghai, which was facilitated by Zhifei Liu. XRF core scanner has been done for core CP11PC at NIOZ, thanks for the helps from Rineke Gieles and permission from Gert-Jan Reichart. I am very grateful to these people.

I thank all the lecturers and attendees to the 10th Urbino Summer School. Tianyu Chen, Hui Tang, Jianghao Wang, Weimu Xu, Ruoyu Sun, Stefanie Kaboth, Mariko Harada, and Giovanni Baccolo, etc. thanks for making this experience unforgettable. I still remember how we were eager to the Chinese food and the delicious, Italian flavor sleeve-fish. Some of them I also meet and had great times later in Vienna (EGU2014) and in Prague (Goldschmidt2015). I thank Qiong Wu and Quan Chen for hosting me when I was in Paris. I cannot forget the heavy sampling party in Bremen, with Haowen Dang Zhongjing Cheng, Stephan Steinke, Huangmin Ge, and Enqing Huang (remember the Amsterdam Downtown Tour afterwards?). I thank you all for the great times we had, which highlighted my PhD.

I also want to thank the amazing football teammates: Moji, Andre, Ralph, Jinfeng, Matthias, Rick, Niels, Arjen, Amir, Xiaoguang, Sander, Thomas, Peter, Wytze, etc., you made the life on Friday not lonely. Besides, I thank the local Chinese football team: Utrecht United. Siyi, Jinfeng, Ruixue, Leihua, Wei Xiao, Hongkai, Feilong, Chen Chen, Lou Bo, Liao Lei, Chunhui, and everyone else in the team, thank you for the cheerful Sundays.

I would like to thank my Chinese friends in the Netherlands Dali, Jingchao, Zhang Miao, Luwen, Bao Xue, Liu Ying and Huang Ping, Shaohui, Xiaoguan, Zhang Jie, Zhou Wen and Qianqian, Kangming and Xu Li, Jianye, Xiaochen and Feifei, Jinfeng, Chaozhong, Li Shuai, Jin Shuang, Licheng, Haoran, and many other people, you make Utrecht a comfortable place to work, as well as a joyful place to live. I really appreciate that and wish you all good luck.

Back home in China, my family – my mother, brother Jiachen, and everyone else – have always been supportive of me throughout the past 30 years. There would be no thesis without your unconditional love and patience. I also want to thank my father-in-law and mother-in-law for the unwavering supports. I would like to reserve the greatest thank-you of all to my wife, Xin Wang, without whose constant supports it is impossible to make all these wonderful things happen. I would like to save some compliments for our wedding day, but let me say already, thank you for everything in the last few years. At last and above all, I thank Qianyou for being our Qianyou.

Curriculum vitae

Jiawang Wu was born on the 14th of May, 1987, in Hainan, China. He grew up in Sanya, the southernmost city of China, where he completed his pre-university education in 2005. Then, Jiawang started studying Earth Sciences at Tongji University in Shanghai. He obtained his Bachelor's degree in June 2009, and was granted a direct admission to postgraduate study. Jiawang obtained his Master's degree in April 2012, with a specialization in marine geology and clay mineralogy. His MSc study explored the relationship between the continental silicate weathering and the climate changes in tropical regions, West Pacific, under the supervision of Prof. Zhifei Liu. The study is part of a 973 program of China, and the result was awarded as Excellent Graduate Thesis of Shanghai City. In September 2012, Jiawang started as a PhD student at the Department of Earth Sciences – Geochemistry, Utrecht University, supervised by Prof. Gert J. de Lange. Under the CSC–UU Program, his PhD project studied the North-African hydroclimate variability and its impacts on the eastern-Mediterranean sapropel formation and related seawater circulation, of which this thesis is the result.

Bibliography

Wu, J., Liu, Z., Stuut, J.-B.W, Zhao, Y., Schirone, A., de Lange, G.J., 2017. North-African paleodrainage discharges to the central Mediterranean during the last 18,000 years: a multiproxy characterization. Quaternary Science Reviews 163, 95–113.

Wu, J., Böning, P., Pahnke, K., Tachikawa, K., de Lange, G.J., 2016. Unraveling North-African riverine and aeolian contributions to central Mediterranean sediments during Holocene sapropel S1 formation. Quaternary Science Reviews 152, 31–48.

Wu, J., Liu, Z., Zhou, C., 2013. Provenance and supply of Fe-enriched terrigenous sediments in the western equatorial Pacific and their relation to precipitation variations during the late Quaternary. Global and Planetary Change 108, 56–71.

Wu, J., Liu, Z., Zhou, C., 2012. Late Quaternary glacial cycle and precessional period of clay mineral assemblages in the Western Pacific Warm Pool. Chinese Science Bulletin 57, 3748–3760.

吴家望, 刘志飞, 周超, 2012. 西太平洋暖池晚第四纪黏土矿物的冰期旋回和岁差周期. 科学通报 57, 2145–2157.

Wu, J., Filippidi, A., Davies, G.R., de Lange, G.J. Riverine supply to the eastern Mediterranean during last interglacial sapropel S5 formation: a basin-wide perspective (under review in Chemical Geology)

Dang, H., Jian, Z., Bassinot, F., **Wu, J.**, Wang, T., Kissel, C. Calibrations of *Pulleniatina obliquiloculata* Mg/Ca thermometry for the tropical Indo-Pacific upper-thermocline: a core-top study (under review in Geochemistry, Geophysics, Geosystems)

Wu, J., Pahnke, K., Böning, P., Michard, A., de Lange, G.J. Mediterranean seawater circulation for Holocene sapropel S1 period – reconstructed using Nd isotopes in fish debris and foraminifera (to submit)

Wu, J., de Lange, G.J. The effect of marine barite associated Sr on provenance studies using Sr concentration and isotopes: with pertinent examples from Mediterranean sediments (in preparation)